Entangled photon source for a long-distance quantum key distribution

by

Sungeun (Paul) Oh

A thesis
presented to the University of Waterloo
in fulfillment of the
thesis requirement for the degree of
Doctor of Philosophy
in
Physics

Waterloo, Ontario, Canada, 2024

Examining Committee Membership

The following served on the Examining Committee for this thesis. The decision of the Examining Committee is by majority vote.

External Examiner:	Fumihiro Kaneda Assistant Professor Dept. of Physics, Tohoku University
Supervisor(s):	Thomas Jennewein Adjunct Associate Professor Dept. of Physics and Astronomy, University of Waterloo
Internal Member:	Michal Bajcsy Associate Professor Dept. of Electrical and Computer Engineering, University of Waterloo
Internal-External Member:	Agata Branczyk Adjunct Associate Professor Dept. of Physics and Astronomy, University of Waterloo
Other Member(s):	Donna Strickland Professor Dept. of Physics and Astronomy, University of Waterloo

Author's Declaration

I hereby declare that I am the sole author of this thesis. This is a true copy of the thesis, including any required final revisions, as accepted by my examiners.

I understand that my thesis may be made electronically available to the public.

Abstract

Satellite-based Quantum Key Distribution (QKD) leverages quantum principles to offer unparalleled security and scalability for global quantum networks, making it a promising solution for next-generation secure communication systems. However, many technical challenges need to be overcome. This thesis focuses on theoretical modeling and experimental validation for long-distance QKD, as well as the development and testing of the quantum source necessary for its implementation, to take strides towards realization. While various approaches exist for demonstrating long-distance QKD, here we focus on discussing the approach of sending entangled photon pairs from an optical quantum ground station (OQGS), one through free-space on one end (uplink), and the other one through ground on the other end.

In the thesis, we first discuss the considerations relevant to establishing a long-distance quantum link. Since a substantial amount of research has already been conducted on optical fiber communication through ground-based methods, our focus is specifically directed towards ground-to-space (i.e., free space) quantum links. One of the most concerning aspects in free-space quantum communication is signal attenuation caused by environmental factors. We particularly examine pointing errors that arise from satellite tracking systems. To investigate this further, we designed a tracking system employing a specific tracking algorithm and conducted tracking tests to validate its accuracy, using the International Space Station (ISS) as a test subject. Our findings illustrate the potentially significant impact of inaccurate ground station-to-satellite alignment on link attenuation, according to our theoretical model. Given that photons serve as the signals for the QKD, we also investigate the background light noise resulting from light pollution around our Optical Quantum Ground Station (OQGS), which is another concerning aspect, as it could worsen the link attenuation. Consequently, we estimate the minimum photon pair rate required for successful QKD, taking into account both the obtained values from these measurements and the expected level of link loss.

Having determined the minimum photon pair rate and other requirements for the long-distance QKD, we proceed to fully elaborate on the development process of the Entangled Photon Source (EPS), which is one of the crucial devices for demonstrating entanglement-based QKD. Here, the thesis includes a detailed explanation for the customization of a crystal oven. It also explains the implementations of a beam displacer scheme and a Sagnac scheme to create a robust interferometer, responsible for creating quantum entanglement. In addition, we demonstrate a novel approach to effectively compensate for the major weaknesses of the interferometer, namely spatial and temporal walk-offs. Finally, we conduct the entanglement test and demonstrate its suitability for long-distance QKD. As a

side project, we investigate the performance degradation of nonlinear crystals in response to proton radiation, exploring the potential of deploying the EPS in space for downlink QKD in the future. This thesis provides a comprehensive analysis and testing of elements required for long-distance QKD, contributing to the advancement of future global quantum networks.

Acknowledgments

I would like to express my heartfelt gratitude to my supervisor, Dr. Thomas Jennewein, for accepting me as his student, providing both financial and intellectual research support, and empowering me to pursue a doctorate in Physics. Thank you so much, Thomas.

I sincerely thank my advisory committee members, Agata Branczyk, Michal Bajcsy, Donna Strickland for their guidance and feedback over the years. I also sincerely thank Fumihiro Kaneda for being the external examiner of my defense. Finally, thank you University of Waterloo. Thank you all again.

I would like to thank all my colleagues and friends whom I had the pleasure of meeting during my work and studies at IQC, as well as throughout my life in Waterloo. It is difficult to mention all of you individually in here, but I want to express how amazing you were to me.

I sincerely thank my parents, Hyejin Kang and Chulho Oh, who supported me throughout my life. I could not have achieved this far without their unconditional support. I feel very

어머니 (강혜진) 아버지 (오철호), 두분 감사드리고 사랑합니다. 덕분에 물리학 박사 되었습니다!

Mom (Hye-Jin) and Dad (Chul-Ho), I thank you so much and I love you. Because of you, I was able to accomplish it !

grateful to my cats, Reumi and Marlo, for bringing joy to my everyday life. Lastly and most importantly, I would like to thank my wife, Yukyung Jung, who has always been by my side.

우리 **르미**랑 우리 **말로** 사랑해
내 삶의 동반자이자 아내 **정유경**, 사랑해

My cats, Reumi and Marlo, I love you guys.
My wife, Yukyung Jung, I love you.

Dedication

I dedicate this work to all those in need. I tried my best to provide as much mathematical details as possible. Let us advance this world with Physics! For those who may be curious as they plan to write Ph.D thesis in the future, it took me approximately seven months in total to write this.

Table of Contents

List of Figures

List of Tables

List of Abbreviations

ADC Analog-to-Digital Converter 54

ADU Analog-to-Digital Unit 54, 55

APT Acquisition, Pointing and Tracking unit 37

BBO Beta Barium Borate 129, 134, 135, 139

BNC Bayonet Neill-Concelman 21

CHSH Clauser-Home-Shimony-Holt 13, 14, 16, 60, 61, 122

CSA Canadian Space Agency 19, 23, 135, 139

CW Continuous Wave xiv, 68, 69, 118, 120, 139

DC Direct Current 108

DNB Day/Night Band xiv, 51, 58, 59

DPSS Diode-Pumped Solid-State 72

ECI Earth Centered Inertial xii, 25, 27

EPS Entangled Photon Source xviii, 19, 62, 68, 69, 94, 120, 124, 126–128, 135, 138, 139

ESA European Space Agency 129

FOV Field Of View 50

FWHM Full Width Half Maximum xiv, 81, 82, 114, 127

GEO Geosynchronous Equatorial Orbit 129

GPS Global Positioning System 24, 35

GUI Graphical User Interface xiii, 37

HWP Half Waveplate xv, 88, 96, 97, 99

IR Infrared 45

ISS International Space Station xii, xiii, 23, 33–36, 48, 137

KTP Potassium Titanyl Phosphate 129, 134, 135, 139

LED Light-Emitting Diode xvii, 130, 132, 133

LEO Low-Earth Orbit 23, 24, 26, 27, 34, 39, 40, 129, 137

LLA Latitude, Longitude, Altitude xiii, 27, 37

LN Lithium Niobate 129, 131, 134, 135, 139

LP Linear Polarizer 88

MFR Mode Field Radius 114

NOAA National Oceanic and Atmospheric Administration 44

NORAD North American Aerospace Defense Command 24, 25

OQGS Optical Quantum Ground Station xiii, 19, 24, 26, 27, 45, 47, 48, 56, 57, 138

PBS Polarizing Beamsplitter 88

PEEK Polyether Ether Ketone 104, 105

PM Polarization Maintaining 17, 127

PPKTP Periodically Poled Potassium Titanyl Phosphate 126

PPLN Periodically Poled Lithium Niobate xvi, 66–70, 72, 78, 88, 92, 96–99, 102, 103, 105–110, 112, 121, 127, 138

QBER Quantum Bit Error Rate 20, 45, 47, 60, 127

QEYSSat Quantum Encryption and Science Satellite xii, 18–20, 23, 24, 36, 46, 47, 69, 127, 137

QKD Quantum Key Distribution xii, 7, 12, 14, 17–20, 23, 24, 45, 47, 60, 62, 64, 68, 128, 134, 135, 137, 139, 140

QPL Quantum Photonics Laboratory 23, 45, 126, 127

QPM Quasi-Phase Matching 65, 72, 83, 85, 86, 88, 102, 107, 124, 126, 138

RAC1 Research Advancement Centre 1 xiv, 44, 56–59

SDP Simplified Deep Space Perturbations 26

SGP Simplified General Perturbations xii, 24–26, 33–37, 137

SMF Single Mode Fiber 80, 86, 88, 90, 92, 121

SNSPD Superconducting Nanowire Single Photon Detector 20, 21, 45, 57, 64, 88, 121, 140

SPAD Silicon Photodiode Avalanche Detector 20, 21, 44, 45, 57, 64, 88, 121

SPDC Spontaneous Parametric Down Conversion xiv, 63, 66–71, 73, 76, 82–84, 86, 95, 96, 118

SPENVIS Space Environment Information System 129

TEM Transverse Electromagnetic Mode 69, 72

TLE Two-Line Elements xii, xiii, 24–27, 37

VIIRS Visible Infrared Imaging Radiometer Suite xiv, 57–59

Chapter 1

Introduction

1.1 The timeline at University of Waterloo

After obtaining a master's degree in Physics and serving in the military in South Korea, where I developed a strong appreciation for the importance of national and corporate communication security, I found myself intrigued by the field of quantum security networks. The satellite-based Quantum Key Distribution (QKD) project undertaken by the Canadian government in collaboration with the University of Waterloo caught my attention, leading me to join the Quantum Photonics Laboratory (QPL) in Institute for Quantum Computing (IQC) as an intern in June 2019. Under the leadership of Dr. Thomas Jennewein, the QPL was actively involved in the Quantum Encryption and Science Satellite (QEYSSat) mission, funded by Canadian Space Agency (CSA). During the three months of internship, I discovered that satellite-based QKD resonated deeply with my background knowledge, as I studied in Cosmology for my master's degree. This realization provided an ideal avenue for me, ultimately leading to my decision to pursue a Ph.D., starting in September 2019.

From June 2019 to December 2019, I was tasked with validating the satellite orbit tracking system necessary for the QEYSSat mission. The task had previously been undertaken by Simon Friesen, Younseok Lee and Brendon Higgins, who had been considering the Simplified General Perturbation (SGP) models, algorithms used for tracking satellites. I studied mathematical details of the SGP4 model, specifically designed for Low-Earth Orbit (LEO) satellites, and programmed the algorithm using Matlab software for automation. Subsequently, I dedicated several nights to tracking multiple LEO satellites currently in orbit and validating the algorithm's accuracy.

From September 2019 to September 2020, I conducted a light pollution analysis with the aim of estimating the level of background light noise hindering satellite-based QKD. Inititally, the project involved theoretical modelling with co-op student Veronica Chatrath from September to December 2019. Subsequently, I conducted night-time observations to validate the theoretical model for the noise that QEYSSat would encounter. Although the observations were conducted multiple times and we realized midway through that our approach was not robust enough to validate the model as initially intended, fortunately, the results obtained amidst the setbacks, while less significant, contributed to the validation of the light pollution analysis through alternative means. The project was later revisited by my colleague Paul Godin, co-op student Nouralhoda Bayat, and myself, with new methods implemented in September 2022. Observations and data collections were completed by February 2023.

From September 2020 to April 2021, I conducted a radiation test on nonlinear crystals. To conduct the test, I constructed a compact experimental setup capable of subjecting the crystals to radiation exposure while simultaneously measuring their optical transmittivity. In December 2020, my colleagues Joanna Krynski, Paul Godin and I visited TRIUMF, a particle accelerator centre in Vancouver, to evaluate the radiation damage to the nonlinear crystals, optical fibers(tested by Paul Godin) and photodetector (tested by Joanna Krynski). The data obtained from the test at TRIUMF was successfully brought back to our lab for analysis in the spring of 2021.

My main project during my PhD program was building an Entangled Photon Source (EPS). The project spanned from May 2020 to January 2024. Update reports were submitted to the CSA regularly to keep the pace on track. Most of the work in the first project year consisted of theoretical studies and research due to the COVID pandemic. Around March 2021, I began custom designing a crystal oven, one of the key components of the EPS. With assistance from Hiruy Haile who is an engineer at the Science Machine Shop at the University of Waterloo, I successfully constructed the oven after making several modifications and conducting performance tests. The customization was finished by January 2022. As COVID restrictions gradually eased, I initiated experimental preparations, and by January 2022, commenced full-scale experimentation and construction. In early 2022, during the peak of experimentation, frequent breakdowns occured in a photodetector, resulting in noticeable delays. Given my primary responsibility for its use, I had to take the lead in analyzing the causes of breakdowns and carrying out repairs, requiring a significant amount of time. However, with the occasional assistance of my dear colleagues Stephane Vinet, Rammy Tannous, Paul Godin and Garen Simpson, along with the proactive support of my supervisor Dr. Thomas Jennewein, the issues were successfully resolved. By incorporating my idea of simultaneously compensating for temporal and spatial walk-off

effects into our original EPS design, I was able to build our first EPS for the QEYSSat mission. In my opinion, it was a great accomplishment during my PhD research, as it required countless days and nights in the lab without giving up halfway!

I will now use "we" rather than "I" to follow scientific writing conventions. Each chapter is prefaced with a statement of contribution to give credit to those that were involved.

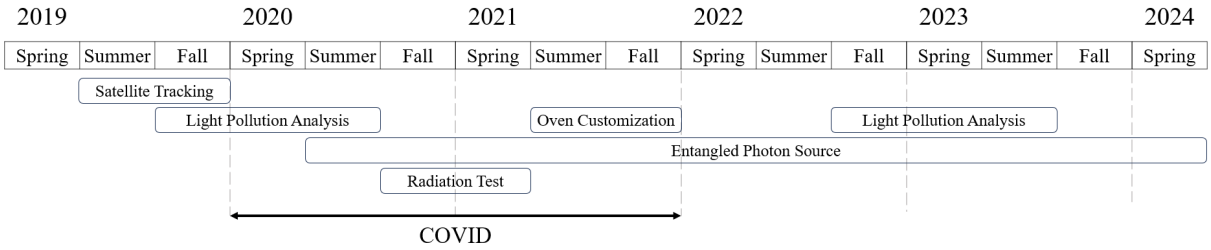

Figure 1.1: The timeline at University of Waterloo

1.2 Quantum Entanglement and Secure Network

Quantum mechanics brought about a revolutionary shift in technology of network, particularly by introducing the concept of a quantum security network. Cyber hacking is becoming more prevalent as increased connectivity provides a broader attack surface for cybercriminals. With sophisticated attack techniques, hackers can exploit vulnerabilities in various devices and systems. Cyberattacks render both the economy and national security more susceptible to threats. The persistance of hacking is largely attributed to the fact that conventional encryption keys are not truly random, but predictable [75]. The reason why particles from nature can be a powerful tool to generate random keys for a secure network is because of their probabilistic characteristics. The inherent quantum randomness exhibited by particles in nature makes them an ideal candidate for generating truly random keys, offering a promising solution to fortify network security.

While the majority of the physics community agrees that quantum communication is the next generation technology, we are confronted with a challenging reality. While the theoretical feasibility may seem plausible, validating it through experimentation and demonstrating its practical viability will demand significantly greater effort.

1.2.1 Formalism of Quantum States

J. Maxwell derived the famous Maxwell's equations which indicate that light is a wave. This is because the expression for the vector potential (from C.5) resembles the Laplace's wave equation.

$$\begin{aligned} \text{Vector potential}: \ \nabla^2 \vec{A} &= \frac{1}{c^2}\frac{\partial^2 \vec{A}}{\partial t^2} \\ \text{Laplace's wave equation}: \ \nabla^2 \psi &= \alpha^2 \frac{\partial^2 \psi}{\partial t^2} \end{aligned} \tag{1.1}$$

However, the fact that light is a wave could not solve the problem of ultraviolet catastrophe. The concept of quantization of energy of a particle was first suggested by M. Planck through solving the problem mathematically[83]. It then became recognized after A. Einstein observed the photoelectric effect through his experiment[39]. The fact that energy can be quantized is now widely accepted by many physicists. The fundamental energy can be expressed in many different ways, but the most popular expression contains the planck constant $h \approx 6.626 \times 10^{-34} J \cdot s$ and the frequency ν.

$$E = 0,\ h\nu,\ 2h\nu,\ 3h\nu\ \cdots \tag{1.2}$$

The idea of particle-wave duality rose after A. Compton observed the Compton effect through X-ray and γ-ray scattering experiments[33]. He realized that the change in wavelength very much resembles the change in momentum through a particle collision.

$$\begin{aligned} \text{(Compton) Ray Scattering} &: \lambda_f - \lambda_i = \lambda_c(1 - \cos(\theta) \\ \text{Particle Scattering} &: \frac{1}{p_f} - \frac{1}{p_i} = \frac{1}{m_e c}(1 - \cos(\theta) \end{aligned} \tag{1.3}$$

This showed that the Compton effect can be explained by assuming that the rays act as particles with discrete energy $E = h\nu$ and momentum $p = h/\lambda$. After all these mathematical realizations, E. Schrödinger derived a particle-version of the wave equation [92].

$$i\hbar\frac{\partial}{\partial t}\psi(\vec{r}, t) = H\psi(\vec{r}, t) \tag{1.4}$$

A simple solution to this equation is a plane wave. In order to determine the value that describes a physical quantity, the value must be a real number. However, every possible solution to the equation 1.4 has a complex term which does not allow us to study any physical quantities. The sense of frustration was soon alleviated by M. Born, who is famous for Born interpretation[18]. A convenient way to eliminate the complex term of a complex function is by taking the absolute square of it ($\psi\psi^*$). However, squaring a function has some mathematical meanings in the **Hilbert space**. In Hilbert space, every function represents an information (or an event, or a physical state) axis, and a collection of such states would describe all possible event. Using the Dirac's braket notation, the overall state can be expressed as

$$|\psi\rangle = \alpha\,|\psi_1\rangle + \beta\,|\psi_2\rangle + \gamma\,|\psi_3\rangle \tag{1.5}$$

where $\alpha, \beta, \gamma \in \mathbb{C}$ are the amount of information. Also, a complex conjugate of ψ can be written as $\psi^* = \langle\psi|$. Each information can be extracted by taking the inner product of its state and the overall state. For instance,

$$\langle\psi_1|\psi\rangle = \alpha\,\langle\psi_1|\psi_1\rangle + \beta\,\langle\psi_1|\psi_2\rangle + \gamma\,\langle\psi_1|\psi_3\rangle \tag{1.6}$$

Suppose all information is independent of each other (i.e, orthogonal to each other) such that we can write $\langle\psi_m|\psi_n\rangle = \delta_{mn}$. In Figure 1.2, we have a graphical representation of the overall state ψ that is decomposed into other three orthogonal states using equation 1.5

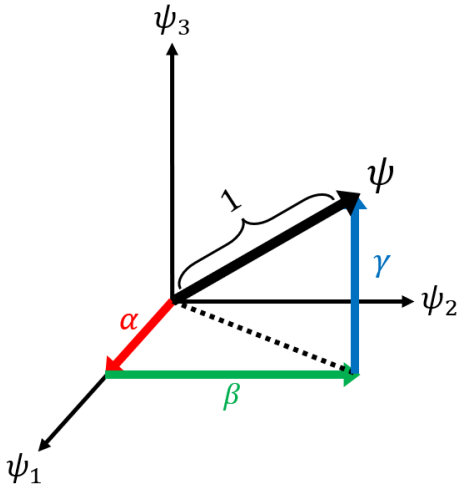

Figure 1.2: Graphical illustration of Hilbert space.

as an example. Note that Hilbert space does not restrict the number of states, and we are just showing the three dimensional case for convenience.

$$\langle\psi_1|\psi\rangle = \alpha\,\langle\psi_1|\psi_1\rangle + \alpha\,\cancelto{0}{\langle\psi_1|\psi_2\rangle} + \alpha\,\cancelto{0}{\langle\psi_1|\psi_3\rangle} = \alpha \tag{1.7}$$

Notice that the relationships between the states and the overall state look equivalent to the Pythagorean theorem, indicating that the absolute square of the information extracted from the inner product contributes additively to the overall state. This indicates that if we normalize the overall state by setting its length as 1, the absolute square of the inner product of the overall state can be written as follows.

$$|\langle\psi|\psi\rangle|^2 = |\alpha|^2\,|\langle\psi_1|\psi_1\rangle|^2 + |\beta|^2\,|\langle\psi_2|\psi_2\rangle|^2 + |\gamma|^2\,|\langle\psi_3|\psi_3\rangle|^2 \tag{1.8}$$

As ψ_1, ψ_2 and ψ_3 are orthogonal to each other, all the cross terms disappear, leaving us with three terms as shown. For instance, the probability of a particle being in the state ψ_1 is $|\alpha|^2$.

1.2.2 Quantum Key Distribution

Born gave one of the most important interpretations in the study of quantum mechanics, the probabilistic nature of waves, with the mathematical formalism of a probability distribution $p = |\,\langle\psi|\psi\rangle\,|^2$. Despite being a highly intriguing discovery, physicists struggled

with implementing the probabilistic characteristics of quantum mechanics until C. Bennett and G. Brassard made use of it by developing the idea of Quantum Key Distribution (QKD) in 1984 [15]. The fact that nature forbid any exact predictions on the quantum properties of a particle means that whichever particle state we obtain from the probability density is genuinely random. This already makes quantum computing distinct from classical computing.

$$\text{Classical bits}: \ 0 \text{ or } 1$$

$$\text{Quantum bits (qubits)}: \ |0\rangle \ \text{ or } \ |1\rangle \ \text{ or } \ \frac{1}{\sqrt{2}}\left(|0\rangle + |1\rangle\right) \ \text{ or } \ \frac{1}{\sqrt{2}}\left(|0\rangle - |1\rangle\right)$$

While classical bits can exist in either 0 or 1 state, qubits can exist in not only the 0 and 1, but also in superpositions of 0 and 1 states. Note that classical bits are fixed states, so we didn't use the Dirac's braket notation. Furthermore, particles can be entangled such that their states become correlated, regardless of the distance separating them. An example of a maximally entangled state of two particles (a and b) is

$$|\psi\rangle = \frac{1}{\sqrt{2}}\left(|0_a 0_b\rangle + |1_a 1_b\rangle\right) \tag{1.9}$$

For instance, if particle a is observed to be in the 0 state, particle b is inevitably in the 0 state as well. This conveys a profound meaning to us. **No-cloning theorem** states that it is impossible to create an identical copy of an arbitrary unknown quantum state [77, 57, 26]. Imagine that someone secretly tries to copy (i.e, hacking) a state $|\psi_1\rangle \to |\psi_1\rangle\,|\psi_2\rangle$, where $|\psi_1\rangle = |\psi_2\rangle = \alpha\,|0\rangle + \beta\,|1\rangle$. This is mathematically expressed as

$$\hat{L}\left(|\psi_1\rangle\,|0_2\rangle\right) = |\psi_1\rangle\,|\psi_2\rangle \tag{1.10}$$

where 0 state is regarded as a vacuum state, and there is a linear operator $\hat{L}$ that copies the information of the first state into the second state.

$$\begin{aligned} \text{LHS}: \quad \hat{L}\left(|\psi_1\rangle\,|0_2\rangle\right) &= \hat{L}\alpha\,|0_1 0_2\rangle + \hat{L}\beta\,|1_1 0_2\rangle \\ &= \alpha\,|0_1 0_2\rangle + \hat{L}\beta\,|1_1 1_2\rangle \\ \text{RHS}: \quad |\psi_1\rangle\,|\psi_2\rangle &= \alpha^2\,|0_1 0_2\rangle + \alpha\beta\,|0_1 1_2\rangle + \beta\alpha\,|1_1 0_2\rangle + \beta^2\,|1_1 1_2\rangle \end{aligned} \tag{1.11}$$

By investigating the left and the right hand sides separately, we can see that the only

condition that satisfies the equation is when $\alpha = \beta = 0$. This ensures that quantum information is absolutely unreplicable. Because of all these facts, quantum keys are very promising candidates for the robust security network.

1.2.3 Polarization Encoding

Physicists have devised various methods to encode quantum information. For quantum communication, we consider sending and receiving qubits, which becomes a compelling reason to utilize **photons**. There exist many different degrees of freedom in a photon where quantum information can be encoded. One option is the polarization of a photon describes the oscillation direction of the electric field (Also used for our entangled photon source that is going to be introduced in Chapter 3). We conveniently choose two linear polarization states, horizontal (H) and vertical (V) to be $|0\rangle$ and $|1\rangle$, respectively. The two transverse (i.e., on the H/V plane) polarizations are perpendicular to each other such that for any transverse polarization state we can use the following general expression.

$$|\psi\rangle = \cos\theta\,|H\rangle + \sin\theta\,|V\rangle \tag{1.12}$$

where θ is the angle from the horizontal polarization axis shown in Figure 1.3. Thus, the state $|\psi\rangle$ can become either horizontal or vertical polarization state by inserting $\theta = 0$ and $\theta = \pi/2$, respectively.

$$|\phi\,(\theta = 0)\rangle = |H\rangle \qquad |\phi\,(\theta = \pi/2)\rangle = |V\rangle \tag{1.13}$$

We can also have diagonal (D) and anti-diagonal (A) states, which are simply the V/H states that are rotated by 45°.

$$|D\rangle = \frac{1}{\sqrt{2}}\left(|H\rangle + |V\rangle\right) \qquad |A\rangle = \frac{1}{\sqrt{2}}\left(|H\rangle - |V\rangle\right) \tag{1.14}$$

They are also orthogonal to each other. Hence, we have two orthonormal polarization basis sets, H/V and D/A. Quantum states are probabilistic but we could still have an idea about what physical quantities we could expect from a certain state. Suppose we want to measure a physical quantity $\mathcal{O}$ that would tell us about the state of the photon. The expectation value of the physical quantity would be

$$\langle\hat{\mathcal{O}}\rangle = \int \psi^*\hat{\mathcal{O}}\psi\; d^3\vec{r} \tag{1.15}$$

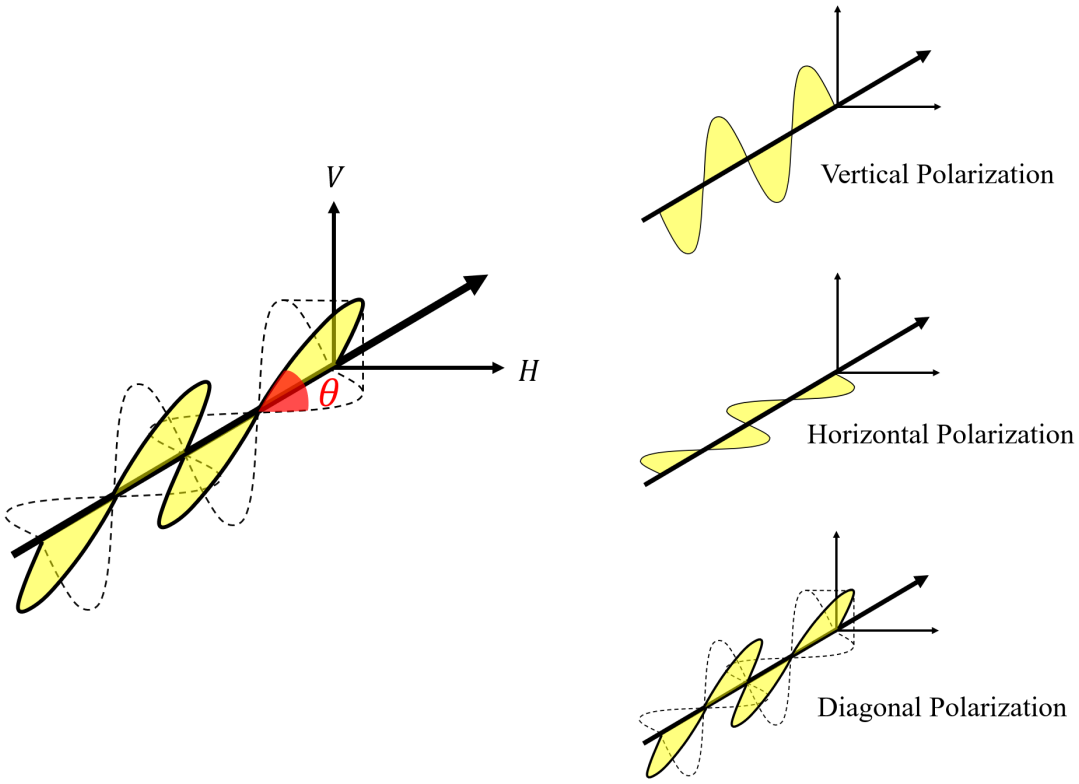

Figure 1.3: Graphical representations of different transverse polarizations of electromagnetic waves (light).

where the integral is taken over all $\mathbb{R}^3$. This is analogous to the general expression for the expectation value in statistics ($\langle x \rangle = \int p(x)x \; dx$), except we have an **operator** in between the two wave functions such that the operator is applied to the wave function to the right. This way, the operator is able to extract the information from the wave function. In Dirac notation, the equation 1.15 could be written as $\langle \psi | \hat{\mathcal{O}} | \psi \rangle$. We want the state to be an eigenstate of the operator (i.e, $\hat{\mathcal{O}} |\psi\rangle =_{\mathcal{O}} |\psi\rangle$) such that eigenvalues are generated without affecting the state. For simplicity, we consider a plane wave $\psi \propto exp(i\vec{k} \cdot \vec{r} - i\omega t)$. One applicable operator is an energy operator $\hat{E} = i\hbar\partial/\partial t$.

$$\langle \hat{E} \rangle = \int \psi^* \hat{E} \psi \; d^3\vec{r} = \hbar\omega \int \psi^* \psi \; d^3\vec{r} = E \tag{1.16}$$

As previously mentioned, energy can be quantized, which means it is treated as if it were countable objects, like the number of photons. In order to distinguish different polarizations, we could instead do a discrete summation $\hat{E} = \sum_i |\psi_i\rangle \, i\hbar\partial/\partial t \, \langle \psi_i |$ where $|\psi_i\rangle \langle \psi_i| = 1$. This way, probability of a single photon (E is normalized to 1) having certain polarizations can be calculated by applying projection operators.

$$\hat{\mathcal{O}}_H = |H\rangle \langle H| \quad \hat{\mathcal{O}}_V = |V\rangle \langle V| \quad \hat{\mathcal{O}}_D = |D\rangle \langle D| \quad \hat{\mathcal{O}}_A = |A\rangle \langle A| \tag{1.17}$$

1.2.4 The E91 Protocol

While Bennett and Brassard's invention of the BB84 protocol [15] was pioneering, we will turn our attention to a similar protocol called the **E91 protocol** [40], conceived by A. Ekert in 1991 (The reasons for choosing the E91 protocol are mentioned in Section 1.2.5). This protocol will be explained assuming the use of polarization encoding method. We consider an entangled photon source that produces pairs of photons entangled in polarization (Figure 1.4). The entangled photon pairs are sent to two receivers, Alice and Bob. Each receiver is given the two measurement bases (H/V and D/A) as tools to measure photon polarizations. Since they can choose their bases freely each time they measure a photon, it remains unknown whether they measured in the same basis unless they share the information with each other. After the two receivers have completed the polarization measurements, they communicate over a classical channel (i.e, regular communication channel) to reveal to each other only their sequences of bases used, not the measurement results. Statistically speaking, we can expect that roughly half of their sequences will match. Here, the receivers discard the mismatching bases because the results obtained in those bases would contain no information. For instance, Alice chose (+) basis and found that the photon has horizontal polarization, corresponding to the classical bit of 0. This means the photon on Bob's

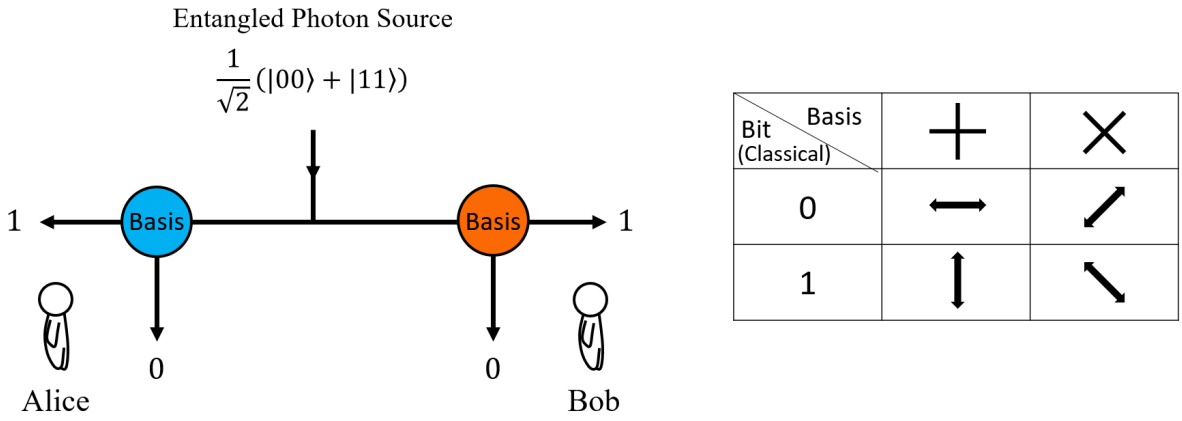

Figure 1.4: The E91 protocol. The entangled photon source sends out signal/idler photon pairs, and Alice and Bob measure them in the basis of their choice. The polarizations determined by the basis they used are interpreted as classical bits, either 0 or 1.

side should also have a horizontal polarization as it is entangled with the Alice's photon. However, if Bob used (×) basis and obtained the same classical bit, that classical bit contains no information. Calculating the probability of each outcome would allow us to understand the reason. As shown in Figure 1.5, when H/V basis (+) set is used, we could use the operators $\hat{\mathcal{O}}_H$ and $\hat{\mathcal{O}}_V$ to calculate the probability of obtaining the classical bit (0 or 1) when the other person's bit is determined. According to definition 1.17, each

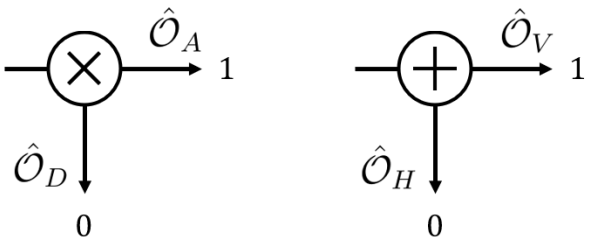

Figure 1.5: Each projection operator is responsible for one of the two polarizations that the basis can measure. D/A basis : $\hat{\mathcal{O}}_D$,$\hat{\mathcal{O}}_A$ and H/V basis : $\hat{\mathcal{O}}_H$,$\hat{\mathcal{O}}_V$

probability of Bob receiving the classical bit 0 or 1 when Alice's bit was 0 would be

$$\begin{aligned} &\text{Probability of Bob receiving 0}: \quad \langle H|\,\hat{\mathcal{O}}_D\,|H\rangle = \langle H|D\rangle\,\langle D|H\rangle = \frac{1}{2} = 50\% \\ &\text{Probability of Bob receiving 1}: \quad \langle H|\,\hat{\mathcal{O}}_A\,|H\rangle = \langle H|A\rangle\,\langle A|H\rangle = \frac{1}{2} = 50\% \end{aligned} \tag{1.18}$$

This implies that even if Bob obtains the same classical bit as Alice, it is a random outcome, not one obtained through entanglement. Therefore, only the bits obtained through the same bases are going to be valid as **quantum keys**. Some may wonder why we are using two basis sets in the first place if we are discarding half of the number of photons. If the choice of which basis set to use was predetermined and shared through classical communication, it would not only provide an opportunity for hackers to secretly steal the keys, but the receiver would also be unable to detect such an attack, as the number of keys received on both sides (0 and 1) would be equal. The ultimate intention of this random basis set selection is for the receiver to notice any attacks or interventions. Even if Alice and Bob use sequences of random basis sets, a hacker might steal some portion of the photons from one of the channels to extract the keys and send other photons as replacements to the receiver. However, this cannot be pretended that nothing has happened, as the receiver will notice a change. The photons replaced by the hacker are untangled such that the polarization states are random. This will affect half of the result that the receiver gets, which means half of the keys from the correct bases are also affected. If Alice and Bob decide to compare some portions of each other's final keys, they will observe roughly a 50% of error rate in their results. In the absence of any attacks, they would ideally have a 100% of matching result from the correct bases selections. Once they confirm that the entangled photons are delivered safely, they can use the obtained classical bits as their secretly shared keys. One could encrypt a binary file by overlapping with the secret keys, and send it to the other one who has the same key to decrypt the file. Of course, there exist various other challenges such as loss of information by the influence of external environmental factors, but these are areas that can be complemented through technological improvements. QKD itself has been proven in its potential.

1.2.5 Quantum Entanglement

Despite the random determination of polarization states for the photons received by Alice and Bob during measurement, it remains imperative that their photons stay correlated, thereby ensuring the meaningfulness of the measurements. In other words, although it is

purely random whether Alice and Bob measure $|0_a 0_b\rangle$ or $|1_a 1_b\rangle$ from an entangled state 1.9, it must still be the case that if Alice measures 0, then Bob must obtain 0, and if Alice measures 1, Bob must obtain 1. Meanwhile, it is possible for Alice and Bob to measure the same state simply by accident. To verify whether the photons measured by Alice and Bob are indeed entangled, one could use Clauser-Home-Shimony-Holt (CHSH) inequality, formulated in 1969 by Clauser, Horne, Shimony, and Holt. This inequality is a refinement of Bell's inequality, proposed in 1964 by John S. Bell [14]. The mathematical derivation begins by questioning whether there exists an unknown variable that influences the measurement results of Alice and Bob in such a way that understanding this variable could potentially allow us to predict the outcomes instead of merely accepting them as random determinations. Suppose Alice uses a basis α and Bob uses a basis β to measure the polarization of their photons. The measurement outcomes of Alice and Bob, somehow influenced by an unknown variable λ, can be written as $A(\alpha, \lambda)$ and $B(\beta, \lambda)$, respectively. If there were no such unknown variable, then, using bra-ket notation, the outcomes could have been written as $A(\alpha, \lambda) = \langle \alpha | \psi_{Alice} \rangle$ and $B(\beta, \lambda) = \langle \beta | \psi_{Bob} \rangle$. The correlation between Alice's and Bob's measurement outcomes, considering the influence of the unknown variable, can be expressed as

$$E(\alpha, \beta) = \int A(\alpha, \lambda) B(\beta, \lambda) \rho(\lambda) d\lambda \tag{1.19}$$

Here, we have a density function denoted as $\rho(\lambda)$, which satisfies $\int \rho(\lambda) d\lambda = 1$ and $\rho(\lambda) \geq 0$. Whether the two outcomes are correlated can be identified by comparing one correlation case $E(\alpha, \beta)$ with another $E(\alpha, \delta)$.

$$E(\alpha, \beta) - E(\alpha, \delta) = \int \left[A(\alpha, \lambda) B(\beta, \lambda) - A(\alpha, \lambda) B(\delta, \lambda) \right] \rho(\lambda) d\lambda$$

$$= \int A(\alpha, \lambda) B(\beta, \lambda) - A(\alpha, \lambda) B(\delta, \lambda)$$

$$\underbrace{-A(\alpha, \lambda) B(\beta, \lambda) A(\gamma, \lambda) B(\delta, \lambda) + A(\alpha, \lambda) B(\beta, \lambda) A(\gamma, \lambda) B(\delta, \lambda)}_{0} \rho(\lambda) d\lambda$$

$$= \int A(\alpha, \lambda) B(\beta, \lambda) \left[1 - A(\gamma, \lambda) B(\delta, \lambda) \right] \rho(\lambda) d\lambda - \int A(\alpha, \lambda) B(\delta, \lambda) \left[1 - A(\gamma, \lambda) B(\beta, \lambda) \right] \rho(\lambda) d\lambda \tag{1.20}$$

Note that here, we deliberately introduced other correlation cases $E(\gamma,\delta)$ and $E(\gamma,\beta)$. According to the triangle's inequality ($|\vec{a}+\vec{b}| \leq |\vec{a}|+|\vec{b}|$), we can write

$$|E(\alpha,\beta)-E(\alpha,\delta)| \leq \left|\int [1-A(\gamma,\lambda)\,B(\delta,\lambda)]\,\rho(\lambda)d\lambda\right| + \left|\int [1-A(\gamma,\lambda)\,B(\beta,\lambda)]\,\rho(\lambda)d\lambda\right| \tag{1.21}$$

where the front factors $A(\alpha,\lambda)\,B(\beta,\lambda)$ and $A(\alpha,\lambda)\,B(\delta,\lambda)$ are considered to be 1 (upper bound), as $|A| \leq 1$ and $|B| \leq 1$ according to equation 1.12. Since both terms on the right-hand side are guaranteed to be positive, we do not need the absolute-value brackets. Then equation 1.21 can be written as

$$|E(\alpha,\beta)-E(\alpha,\delta)| \leq 2-E(\gamma,\delta)-E(\gamma,\beta) = 2-[E(\gamma,\delta)+E(\gamma,\beta)] \tag{1.22}$$

Therefore, the CHSH inequality is

$$S = |E(\alpha,\beta)-E(\alpha,\delta)|+[E(\gamma,\delta)+E(\gamma,\beta)] \leq 2 \tag{1.23}$$

If this inequality is violated, it would indicate the absence of local hidden variables, and the presence of quantum entanglement. To understand how the CHSH inequality test is performed experimentally, we further examine the correlations of Alice's and Bob's measurement with equation 1.12 [29]. As discussed in section 1.2.4, we need at least two orthogonal bases (H/V and D/A) to demonstrate QKD. However, the CHSH inequality test requires at least four different bases (α,β,γ, and δ) to verify quantum entanglement. Each of the four bases correspond to a different polarization angle, since we are utilizing polarization states of photons. Each basis measures two different cases : detection and non-detection. Suppose Alice and Bob receive a maximally entangled photon pair which their state is expressed as follows.

$$|\psi\rangle = \frac{1}{\sqrt{2}}(|HH\rangle+|VV\rangle) \tag{1.24}$$

Alice uses basis α and Bob uses basis β, each consisting of two orthogonal measurement axes (illustrated in Figure 1.6). The outcomes from these axes can be mathematically described using eigenvectors

$$\begin{aligned}
|\alpha^+\rangle &= \cos\alpha\,|H\rangle+\sin\alpha\,|V\rangle \\
|\alpha^-\rangle &= -\sin\alpha\,|H\rangle+\cos\alpha\,|V\rangle \\
|\beta^+\rangle &= \cos\beta\,|H\rangle+\sin\beta\,|V\rangle \\
|\beta^-\rangle &= -\sin\beta\,|H\rangle+\cos\beta\,|V\rangle
\end{aligned} \tag{1.25}$$

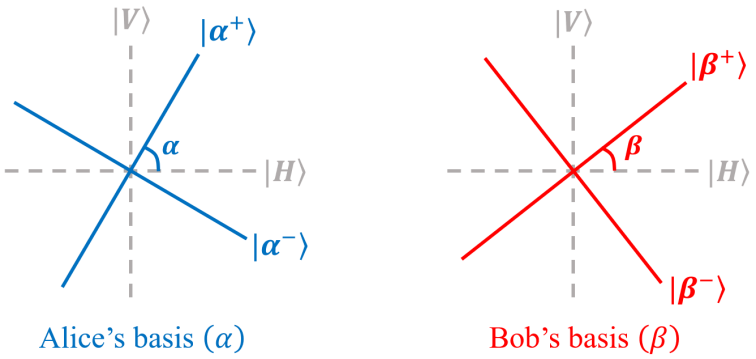

Figure 1.6: Two different bases chosen by Alice and Bob. The name of each basis corresponds to the rotation angle of its measurement axes.

with eigenvalues $\alpha = \pm 1$ and $\beta = \pm 1$. With these, we can define the following projection operators (which describe "measurements").

$$\begin{aligned} \hat{\mathcal{O}}_\alpha &= (+1)\left|\alpha^+\right\rangle\left\langle\alpha^+\right| + (-1)\left|\alpha^-\right\rangle\left\langle\alpha^-\right| \\ \hat{\mathcal{O}}_\beta &= (+1)\left|\beta^+\right\rangle\left\langle\beta^+\right| + (-1)\left|\beta^-\right\rangle\left\langle\beta^-\right| \end{aligned} \tag{1.26}$$

If Alice and Bob attempt to measure the polarizations of the photon pair simultaneously, then the correlation (expectation value) from bases α and β is

$$\begin{aligned} E(\alpha,\beta) &= \langle\psi|\,\hat{\mathcal{O}}_\alpha\hat{\mathcal{O}}_\beta\,|\psi\rangle \\ &= \left|\left\langle\alpha^+,\beta^+|\psi\right\rangle\right|^2 - \left|\left\langle\alpha^+,\beta^-|\psi\right\rangle\right|^2 - \left|\left\langle\alpha^-,\beta^+|\psi\right\rangle\right|^2 + \left|\left\langle\alpha^-,\beta^-|\psi\right\rangle\right|^2 \\ &= P_{++}(\alpha,\beta) - P_{+-}(\alpha,\beta) - P_{-+}(\alpha,\beta) + P_{--}(\alpha,\beta) \end{aligned} \tag{1.27}$$

where each term corresponds to the probability of a simultaneous detection (coincidence event).

$$\begin{aligned} P_{++}(\alpha,\beta) = P_{--}(\alpha,\beta) &= \frac{1}{2}\cos^2(\alpha-\beta) \\ P_{+-}(\alpha,\beta) = P_{-+}(\alpha,\beta) &= \frac{1}{2}\sin^2(\alpha-\beta) \end{aligned} \tag{1.28}$$

The number of coincidence events for each case is then $N_c(\alpha,\beta) = N_0 P(\alpha,\beta)$, where $N_0 = N_{++} + N_{+-} + N_{-+} + N_{--}$ is the number of coincidence events without any measurement bases (polarizers). Using equation 1.28 into equation 1.27, we obtain the following

expression for the photon correlation.

$$E(\alpha, \beta) = \cos[2(\beta - \alpha)] \tag{1.29}$$

Interestingly, if the correlation terms on the left-hand side of the inequality 1.23 are expressed as in the expression 1.29, it can lead to situations where the CHSH inequality is violated. Furthermore, if the difference between the basis angles of each correlation term is $\pi/8$, one observes a maximal violation.

$$\cos[2(\beta - \alpha)] = -\cos[2(\delta - \alpha)] = \cos[2(\delta - \gamma)] = \cos[2(\beta - \gamma)] = \frac{1}{\sqrt{2}} \tag{1.30}$$

This means that the CHSH inequality can be violated by quantum mechanics with a maximum value of $S_{QM} = 2\sqrt{2}$. Therefore, if we obtain a value between $2 \leq S_{exp} \leq 2\sqrt{2}$ in actual experiments, we can be confident that the two photons are quantum mechanically correlated regardless of the disitance between them, without the assistance of any local hidden variables. This CHSH test will be very useful in both Chapter 2 and Chapter 3.

1.3 Considerations For A Long-Distance Quantum Link

It is undeniable that QKD introduces a new wave in the future security network industry. To establish a long-distance quantum link, there exist numerous technological challenges that needs to be overcome. Developing quantum channels for long-distance quantum communication is one of the major challenges that requires an extensive research. When photons are transmitted over long distances, maintaining quantum information becomes challenging due to various environmental factors. We must clearly determine the most efficient pathways for transmitting quantum information and understand the factors to consider along those pathways. Subsequently, it is essential to establish a theoretical model outlining the minimum conditions required for achieving quantum communication. Once the requirements for the quantum channels are well understood, we look through selection processes of a quantum source capable of generating entangled photon pairs, and detection systems that can analyze the distributed quantum keys, considering the requirements.

1.3.1 Quantum Channels

There are currently two known media of transmitting photons over large distances : through optical fiber and free-space. Fiber-optic cables have been used globally to establish the worldwide internet infrastructure with the support of classical optical amplifiers and repeaters. However, optical fibers exhibit high attenuation due to absorption and scattering effects, posing significant challenges for quantum communication, especially over longer distances exceeding a few hundred kilometers [59, 52]. Quantum states of the quantum signals must not have any direct interactions with external environments, making the classical amplifiers or repeaters not feasible for quantum transmissions. Although technologies like quantum repeaters [25, 88] are currently being researched and developed, they have not yet advanced enough for commercial use. Thus, maintaining quantumness in long distances through optical fibers is very challenging at this stage. Moreover, if the polarization encoding method is used, one has to use a Polarization Maintaining (PM) optical fiber instead of the regular optical fiber. The PM fiber separates two polarizations into slow and fast modes to maintain them, but it also introduces a phase shift between the two. Extra efforts must be made to maintain the phase of the two overlapping polarization states.
On the other hand, the free-space channel not only makes it easier to maintain polarizations but also allows for longer-distance quantum communication compared to optical fiber, in terms of link attenuation. Note that polarization-encoded photons are even robust against atmospheric turbulence [48], unlike time-bin encoded photons which are highly vulnerable to atmospheric distortion, thereby potentially causing path distinguishabilities [43].

Free-space channels still face challenges posed by various atmospheric effects and equipment errors, but it is definitely more favorable than the optical fibers. The theoretical frameworks, experimental tests, and analytical insights pertaining to these challenges are detailed in Chapter 2.

Quantum Encryption and Science Satellite (QEYSSat)

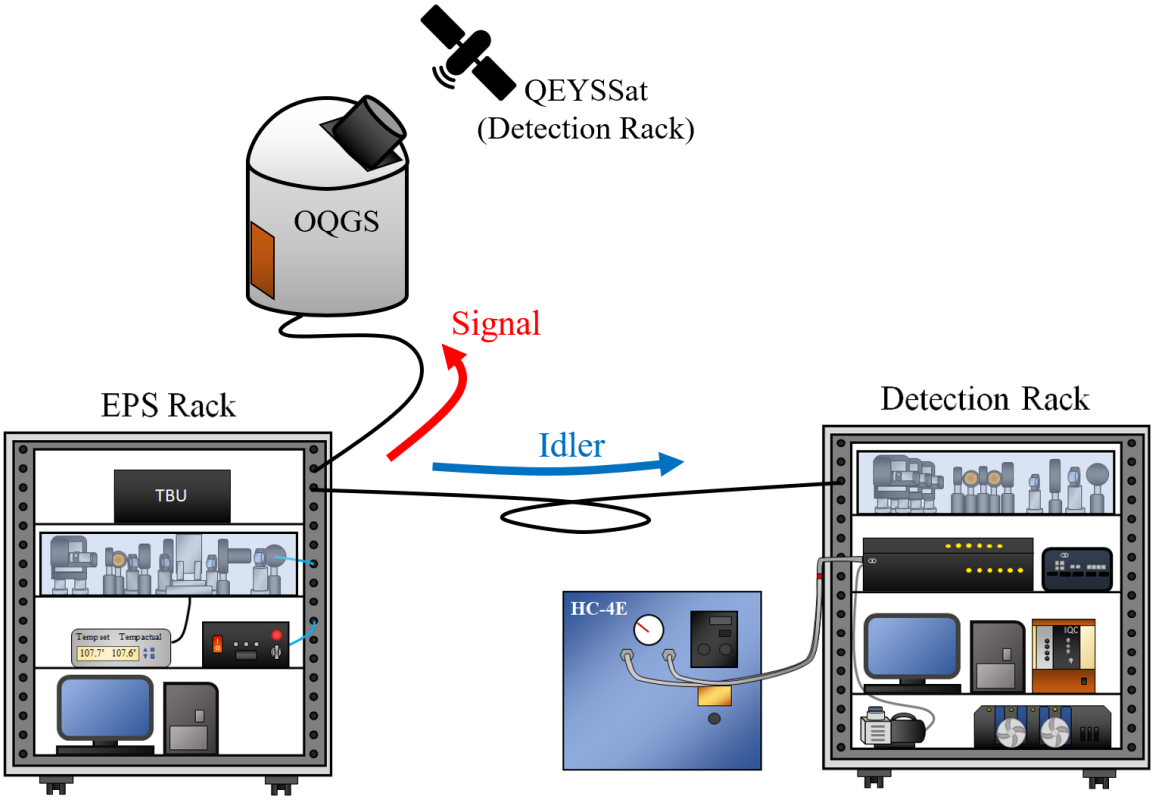

Figure 1.7: An illustration depicting the structure of the QKD system for the QEYSSat mission. The EPS rack which contains the EPS sends out signal/idler photons pairs. The signal photons are transmitted to the satellite (Alice) via OQGS. The idler photons are transmitted to the detection rack (Bob) through the ground.

The fact that signals transported through free-space would experience less attenuation than through the optical fiber, it may be deemed more efficient. However, it may not be suitable in urban areas where there exists physical obstacles and intense light pollution. In

such cases, transmission through optical fiber can be much more effective. We must also not forget that since signal transport through optical fiber can be more reliable than free-space transmission, using optical fiber transmission is sometimes essential. We are anticipating the need for a bridge connecting free-space and ground transmissions for quantum communication in the future. Quantum Encryption and Science Satellite (QEYSSat) is a mission funded by Canadian Space Agency (Canadian Space Agency (CSA)) led by Dr. Thomas Jennewein. The main goal is to demonstrate a long-distance QKD through ground-to-space quantum link, and prove the potential of establishing robust global quantum security networks [84, 4]. The design scheme for our ground-to-space QKD system is shown in Figure 1.7. In broad classification, the system consists of an EPS rack which contains the EPS that will provide entangled photon pairs (signal and idler photon make one entangled pair of photons), OQGS where signal photons will be sent to the satellite (Alice) through an optical telescope, and a detection rack that will receive and analyze the idler photons (Bob).

1.3.2 Quantum Source

Since the proposal of protocols like BB84 and E91, QKD has been extensively studied both theoretically and experimentally, resulting in the development of various demonstrational methods. The QKD protocol can be broadly divided into two schemes : the **prepare-and-measure** scheme and the **entanglement-based** scheme. These two schemes each have their own advantages and disadvantages.

The most crucial aspect in the prepare-and-measure scheme is the necessity of a single photon source. This is because the no-cloning theorem is effective only when the entities we encode are truly single photons. However, generating truly single photons is still in the development stage, and despite innovative ideas such as using quantum dots [95, 99, 103], achieving this state with a high efficiency remains quite challenging to date. A more practical source that has been widely explored involves using a weak coherent pulse [54], which faces an intrinsic limitation: it is not a single photon source but rather a source of single pulses. Suppose Alice, the sender, encodes information on each pulse in a coherent state $\left|\sqrt{\mu}e^{i\theta}\right\rangle$ with typically $\mu \ll 1$ photons. Since Bob (the receiver) or Eve (the hacker) has no information on the phase θ, they will observe a mixed state which its distribution follows Poissonian statistics with $P(n,\mu) = e^{-\mu}\mu^n/n!$ for n number of photons. In other words, this implies that Eve is no longer constrained by the no-cloning theorem [89], and can perform photon number splitting (PNS) attacks [71, 24]. Fortunately, this issue of potential hacking has theoretically been resolved by employing decoy state techniques [51, 68]. One drawback is, it introduces significant complexity, requiring the provision of additional states

and the emergence of lower bound conditions on the key rate [74]. Nevertheless, the decoy-state QKD has been demonstrated over almost a hundred kilometers through both optical fibers [104, 79] and free-space channels [91].

In this thesis, we choose the entanglement-based scheme that eliminates the need for us to rely on a true single photon source or a decoy state mechanism [94].[1] This is because the outcomes of the measurements did not exist before the measurements (basis-independent) [90], rendering the presence of multi-photon pairs insignificant for Eve. In summary, we plan to demonstrate long-distance entanglement-based QKD using the polarization encoding method for the E91 protocol. To achieve this goal, we need a quantum source capable of generating a sufficient amount of polarization-entangled photon pairs, essential for the successful long-distance QKD. The wavelength of photon pairs is determined by the results of studying the quantum channel, and once determined, it will dictate the wavelength of the pump laser capable of generating photon pairs at that wavelength. Also, the pair generation rate of the quantum source must be higher than the minimum required for the ground and free-space quantum link while maitaining Quantum Bit Error Rate (QBER) below the requirement for a secured QKD. We further discuss about the QBER in section 2.3.2.

1.3.3 Photon Detectors

Photon detectors are used to receive both signal and idler photons through optical fibers. Note that the photons are already in a polarization-measured state when they enter the optical fibers. The decision made later in Section 2.2.1, as a preview, is that we detect signal photons at 790 nm wavelength transmitted through free-space using Silicon Photodiode Avalanche Detector (SPAD) mounted on the satellite, and idler photons at 1550 nm wavelength transmitted through optical fiber using Superconducting Nanowire Single Photon Detector (SNSPD). SPAD utilizes a mechanism where the energy of incoming photons is amplified through a phenomenom called photo avalanche. When the amplified energy exceeds a certain bias voltage threshold, it is considered as a detection of one photon. For each photodetection event, the detectors employ 'gating', temporarily inducing a resistive state in the detection area, analogous to the motion of opening and closing a door (graphically described in Figure 1.8). Due to the photo avalanche mechanism, we must be cautious of residual photon remnants, referred to as 'after-pulses', whenever the next gating begins. These do not actually correspond to new photodetections, so it is essential

[1] While this thesis focuses on the entanglement-based scheme, QEYSSat considers both prepare-and-measure and entanglement-based schemes.

for SPAD to apply sufficient dead time (denoted as τ_j) to avoid multi-counting between incoming photons. SNSPD can efficiently detects photons in a superconducting state. However, it would require a recovery time from a normal conducting state every time it is hit by a photon. Deadtime of the SPAD (Excelitas Technologies, US) and the SNSPD (Quantum Opus, US) we use are 32 ns and 20 ns, respectively (information provided from the manufacturers [7, 6]). The numbers of signal and idler photodetections recorded by the detectors are going to be the raw single counts, N_s' and N_i'.

$$N_s = \frac{N_s'}{1 - N_s'\tau_s} - \frac{D_s}{1 - D_s\tau_s} \quad , \quad N_i = \frac{N_i'}{1 - N_i'\tau_i} - \frac{D_i}{1 - D_i\tau_i} \quad , \tag{1.31}$$

When we obtain the single count rates and, we need to also account for dark counts D_j that come from any electrical or quantum noises by subtracting them.

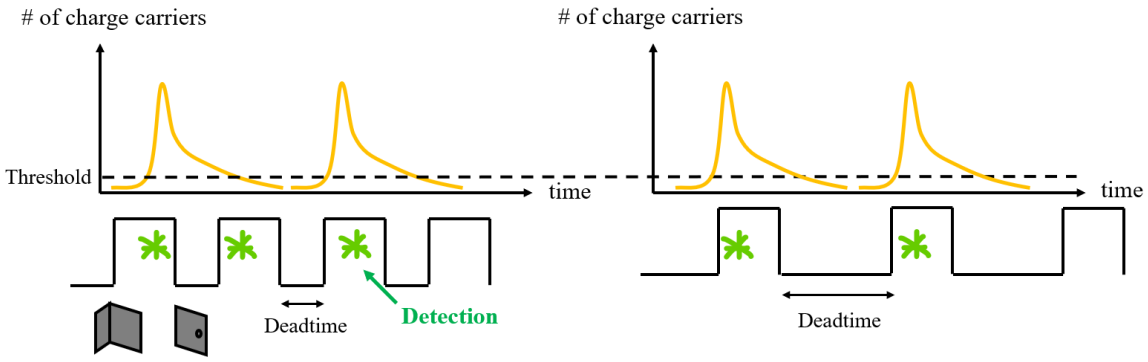

Figure 1.8: A graphical description of the after-pulsing effect with a short deadtime (left) is shown. The green stars are the clicks that indicate a photon detection within the pulse gate. When a photon is detected, the gate remains closed for the duration of the detector's deadtime. If the deadtime is not long enough, one photon will cause multiple clicks due to the avalanche effect, resulting in false single counts. In order to prevent the multi-counting from the after-pulsing effect, we need a dead time at least longer than the temporal width of the photons (right).

When two detectors capture photons, each sends a classical electrical signal to the time-tagging unit (either through Bayonet Neill-Concelman (BNC) cables or through free-space). If the two detectors transmit electrical signals simultaneously, the time-tagging unit considers it as a coincidence event[2]. The time-tagging unit obtains a coincidence

[2]Of course, any phyiscal time difference between the two detections should be initially compensated by introducing a delay time to one of the detectors.

rate, which refers to the number of coincidence events within a detection window, Δt. Figure 1.9 shows a histogram of the coincidence rates. Here, we need to also account for accidental coincidences $N_s N_i \Delta t$. Hence, the true coincidence rate is estimated by the following expressions

$$N_c \approx N_c' - N_s N_i \Delta t \tag{1.32}$$

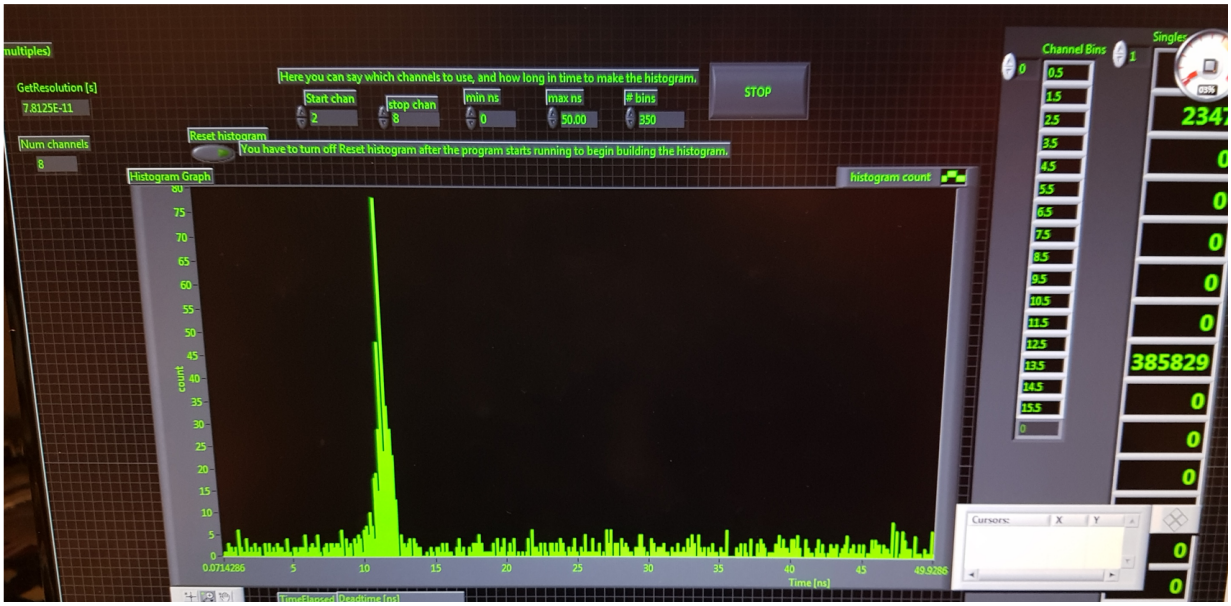

Figure 1.9: Histogram showing the coincidence events triggered by the signal and the idler photon. The arrival time difference (≈ 12 ns was adjusted by delaying one of the receiving channels. The horizontal and the vertical axes of the histogram represents the time delay and the number of the coincidence events, respectively.

Chapter 2

Ground-To-Space Quantum Link

QEYSSat mission plans to deploy quantum communication devices on a Low-Earth Orbit (LEO) satellite that is going to be launched in early 2025 (tentatively). The satellite is currenly under construction by Honeywell Aerospace. Our Quantum Photonics Laboratory (QPL) group is commissioned by CSA for building a ground station where our quantum source will be loaded to perform QKD. As the quantum source will be operating from the ground station, this is going to be an **Uplink** QKD [55]. Some of the required experimental conditions for a successful entanglement-based QKD demonstration have already been studied by our team [19, 20, 21]. In this chapter, we simulate a LEO satellite pass, then discuss about the environmental factors that need to be considered by making theoretical approaches in order to make the best decisions for the following conditions.

- Wavelengths of the signal and the idler photons
- Aperture sizes of the transmitter and the receiver telescopes
- Minimum production rate of the entangled photon pairs

We first model a typical LEO satellite pass to confirm whether it is possible to establish a quantum link, as well as to have a rough idea about the link duration. We test the model by tracking ISS which is a well-known LEO satellite. Once we confirm the feasibility of the quantum link, we also theoretically model the link attenuation and detrmine an optimal wavelength for the quantum signal. The link attenuation model will also give us an idea about the optimal aperture sizes for the transmitter and the receiver telescopes. Lastly, we investigate the background light pollution to estimate the amount of unwanted photons

that will be present at our desired wavelength, and obtain the lower bound for the minimum pair production rate of entangled photons required for the satellite QKD demonstration.

Statement of contribution

1. **Satellite Tracking Test :** Brendon Higgins conceived the idea of implementing SGP model. The coding task for simulating the model had previously been undertaken by Simon Friesen, Younseok Lee and Brendon Higgins. I completed the codes for path simulations, along with motorization of the telescope and tracking system. Additionally, I conducted satellite tracking and confirmed the tracking system.

2. **Link Attenuation Modelling :** Jean-Phillippe Bourgoin, Brendon Higgins and Prof. Thomas Jennewein initiated and established the modelling. I supplemented their approach and implemented for the photon pair rate estimation.

3. **Light Pollution Analysis :** Prof. Thomas Jennewein conceived the idea of conducting light pollution analysis by recognizing the significance of understanding the level of background noise. Veronica Chatrath and I initially conducted a theoretical study on light pollution and made preparations for its measurement. I conducted starlight measurements through astronomical observations. Nouralhoda Bayat, Paul Godin and I conducted the light pollution measurement. Katanya Kuntz participated in the analysis discussion.

2.1 LEO Satellite Pass Modelling

We explore the satellite path of the QEYSSat satellite orbiting in LEO when observed from the OQGS. Our focus is on the feasibility, the duration of the quantum link, the actual link distance and the potential error in the pointing capability of the transmitter telescope associated with it. This will also provide us with a better understanding of the level of link attenuation. We adopt the path calculation methods used by North American Aerospace Defense Command (NORAD) for LEO satellites [100, 13, 50, 35].

Two Line Elements

NORAD supplies satellite's Global Positioning System (GPS) information for thousands of satellites in a data format known as TLE set [8]. TLE consists of two lines and include

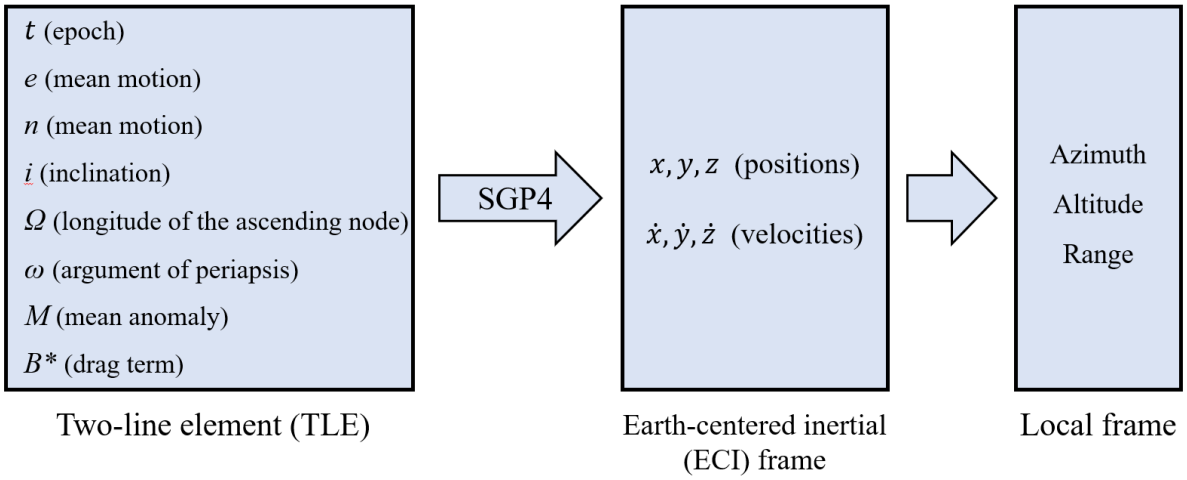

Figure 2.1: A flowchart of coordinate transformations for the satellite tracking test. The TLE are converted into ECI coordinates by applying the SGP4 model. Then the ECI coordinates are converted into the local coordinates; Azimuth, Altitude and Range, for maneuvering our Azi/Alt telescope.

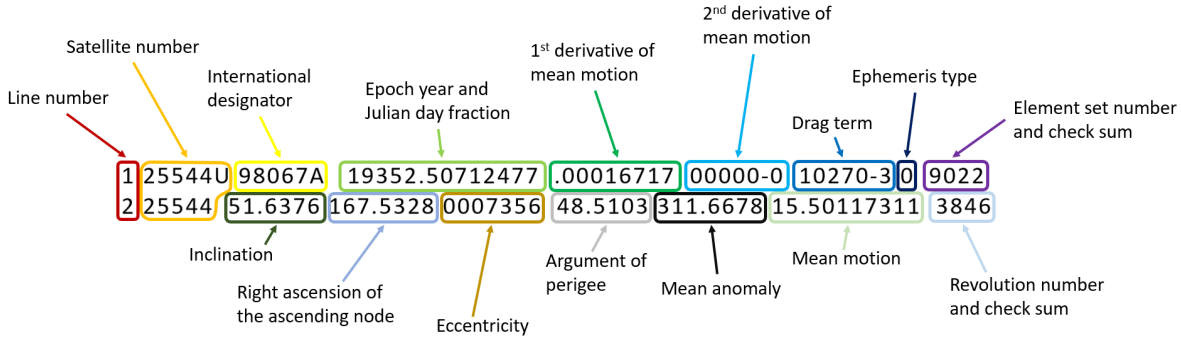

Figure 2.2: Compositions of TLE. The TLE can be collected from NORAD [8].

various physical quantities describing satellite orbits. Our orbital predictions require the following elements from TLE : Epoch t, eccentricity e, mean motion n, inclination i, longitude of the ascending node Ω, argument of periapsis ω, mean anomaly M and drag term B^*. Mean motion is simply one revolution divided by the satellite's orbital period.

$$n_0 = \frac{2\pi}{T} \tag{2.1}$$

SGP4 and Pointing algorithm

This algorithm controls the transmitter telescope integrated into OQGS. If the orbital period is less than 225 minutes, we use SGP4 algorithm [100, 13, 50, 35]. Otherwise, we use Simplified Deep Space Perturbations (SDP)4. SGP4 algorithm incorporates numerical analysis, including the utilization of the Jacobian matrix, and takes into account external factors such as atmospheric drag and gravity which is exceedingly challenging. Consequently, this complexity greatly complicates the derivation process. Hence, we endeavor to present the derivation with a focus on only essential aspects. We first obtain the original (at epoch) semimajor axis a_0'' and mean motion n_0'', using the given information from TLE.

$$\{Z_1 \ : \ e_0, n_0, i_0\} \quad \longrightarrow \quad \{Z_2 \ : \ Z_1, a_0'', n_0''\} \tag{2.2}$$

Using Kepler's third law, the semimajor axis a_1 of an elliptical orbit can be expressed in terms of the mean motion.

$$a_1 = \left(k_E^2 \frac{T^2}{4\pi^2}\right)^{1/3} = \left(\frac{k_E}{n_o}\right)^{2/3} \tag{2.3}$$

where we have the constant parameter, $k_E = \sqrt{GM} = 7.43669161 \times 10^{-2} (er/min)^{3/2}$. Given that Earth is not a perfect sphere due to its rotation, the gravitational potential is not uniform across the its surface. Furthermore, the gravitational potential experiences continuous perturbation from the orbiting moon. As a result, precise orbital calculations for LEO satellites, whose its orbits are typically significantly affected by gravitational variations, must meticulously consider these changes in gravity. One can account for gravitational perturbation by using zonal harmonics, denoted as J_i. The perturbation component δ_1 is computed as follows.

$$\delta_1 = \frac{3}{2}\left(\frac{R_E}{a_1^2}\right)^2 J_2 \frac{P_2(\cos i_0)}{(1-e_0^2)^{3/2}} = \frac{3}{2}\frac{k_2}{a_1^2}\frac{(3\cos^2 i_0 - 1)}{(1-e_0^2)^{3/2}} \tag{2.4}$$

where we have another constant parameter, $k_2 = \frac{1}{2}J_2R_E^2 = 5.413080\times10^{-4}$. Using equation 2.3 and 2.4, we obtain the corrected expressions as follow.

$$\begin{aligned} a_0 &= a_1\left(1 - \frac{1}{3}\delta_1 - \delta_1^2 - \frac{134}{81}\delta_1^3\right) \\ \delta_0 &= \frac{3}{2}\frac{k_2}{a_0^2}\frac{(3\cos^2 i_0 - 1)}{(1-e_0^2)^{3/2}} \end{aligned} \tag{2.5}$$

The original (at epoch) mean motion $n_0'' = n_0/(1+\delta_0)$ and semimajor axis $a_0'' = a_0/(1-\delta_0)$ can be recovered this way. Although the air density is much lower than near the Earth's surface, the atmospheric layers in which LEO satellites travel still exert strong enough air resistance to generate drag [5]. We will now predict the future parameters at time t, with consideration of the long-term influences of atmospheric drag and gravitation.

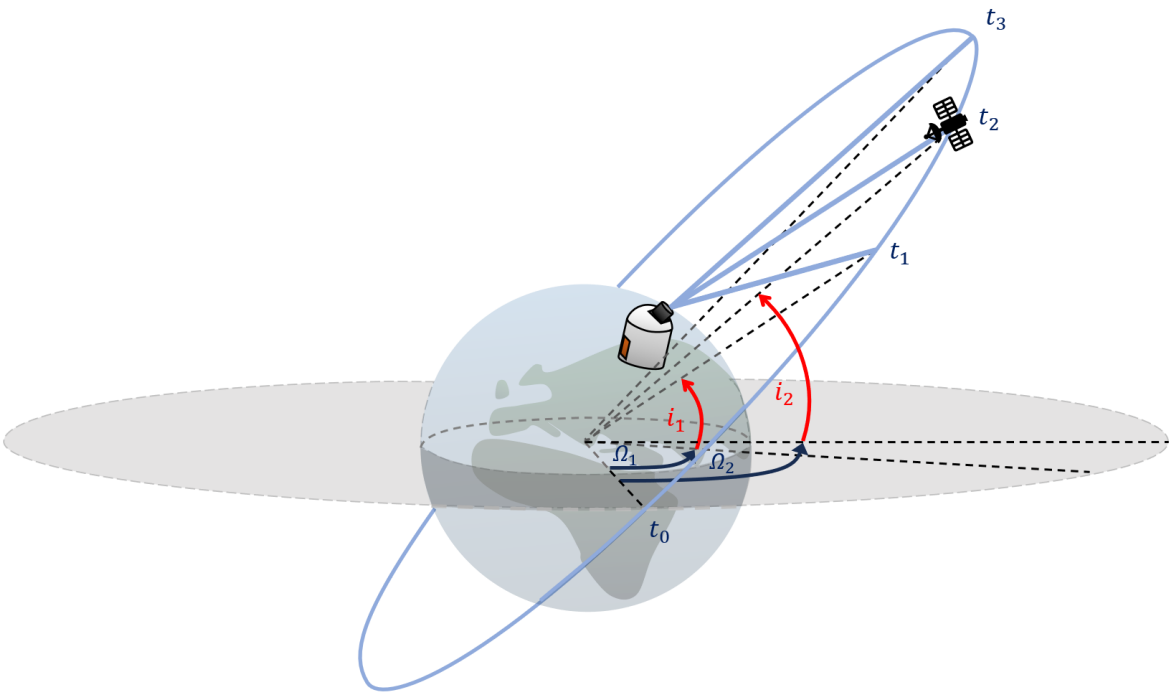

Figure 2.3: A diagram illustrating the satellite orbit in the ECI frame. t_0 is the Epoch time provided by TLE. We transform this frame into the local frame by applying the LLA coordinates of our OQGS.

$$\{Z_3 \ : \ Z_2, B^*, M_0, \omega_0, \Omega_0\} \quad \longrightarrow \quad \{Z_4 \ : \ Z_3, M, \omega, \Omega, a, e, n, L\} \tag{2.6}$$

We first define the following parameters.

$$\theta = \cos i_0 \ , \quad \xi = \frac{1}{a_0'' - s} \ , \quad p_0 = \left(1 - e_0^2\right)^{\frac{1}{2}} \ , \quad \eta = a_0'' e_0 \xi \tag{2.7}$$

Then the drag terms are

$$\begin{aligned}
M_{drag} &= M_0 + \left[1 + \frac{3k_2\left(-1+3\theta^2\right)}{2a_0''^2 p_0^3} + \frac{3k_2^2\left(13-78\theta^2+137\theta^4\right)}{16a_0''^4 p_0^7}\right] n_0''\left(t-t_0\right) \\
\omega_{drag} &= \omega_0 + \left[-\frac{3k_2\left(1-5\theta^2\right)}{2a_0''^2 p_0^4} + \frac{3k_2^2\left(7-114\theta^2+395\theta^4\right)}{16a_0''^4 p_0^8} + \frac{5k_4\left(3-36\theta^2+49\theta^4\right)}{4a_0''^4 p_0^8}\right] n_0''\left(t-t_0\right) \\
\Omega_{drag} &= \Omega_0 + \left[-\frac{3k_2\theta}{a_0''^2 p_0^4} + \frac{3k_2^2\left(4\theta-19\theta^3\right)}{2a_0''^4 p_0^8} + \frac{5k_4\theta\left(3-7\theta^2\right)}{2a_0''^4\theta_0^8}\right] n_0''\left(t-t_0\right) \\
\delta M &= -\frac{2}{3}\left(q_0-s\right)^4 B^* \xi^4 \frac{R_E}{e_0\eta}\left[\left(1+\eta\cos M_{drag}\right)^3 - \left(1+\eta\cos M_0\right)^3\right]
\end{aligned} \tag{2.8}$$

where $k_4 = -\frac{3}{8}J_4 R_E^4 = 6.2098875 \times 10^{-7}$, and $s = 1.01222928(er)$ $(q_0 - s)^4 = 1.88027916 \times 10^{-9}(er)^4$. Also, $(t - t_0)$ is the time since epoch. We introduce the following constants

$$\begin{aligned}
C_1 &= \left(q_0-s\right)^4 \xi^4 n_0''\left(1-\eta^2\right)^{-\frac{7}{2}}\left[a_0''\left(1+\frac{3}{2}\eta^2+4e_0\eta+e_0\eta^3\right)\right. \\
&\quad \left. +\frac{3}{2}\frac{k_2\xi}{\left(1-\eta^2\right)}\left(-\frac{1}{2}+\frac{3}{2}\theta^2\right)\left(8+24\eta^2+3\eta^4\right)\right] \\
C_2 &= B^* C_1 \\
C_3 &= \frac{\left(q_0-s\right)^4 \xi^5 A_{3,0} n_0'' R_E \sin i_0}{k_2 e_0}
\end{aligned} \tag{2.9}$$

where $A_{3,0} = -J_3 R_E^3$, and $J_3 = -2.53881 \times 10^{-6}$. These constants are used to calculate for the future angular parameters after $(t - t_0)$.

$$\begin{aligned}
M &= M_{drag} + \delta M + \delta\omega \\
\omega &= \omega_{drag} - \delta M - \delta\omega \\
\Omega &= \Omega_{drag} - \frac{21}{2}\frac{n_0'' k_2 \theta}{a_0''^2 p_0^2} C_2\left(t-t_0\right)^2
\end{aligned} \tag{2.10}$$

with $\delta\omega = B^* C_3 \cos\omega_0 (t - t_0)$. We further define the following constants.

$$
\begin{aligned}
C_4 &= 2n_0'' (q_0 - s)^4 \xi^4 a_0'' p_0^2 \left(1 - \eta^2\right)^{-\frac{7}{2}} \left(\left[2\eta (1 + e_0\eta) + \frac{e_0}{2} + \frac{\eta^3}{2} \right] - \frac{2k_2\xi}{a_0'' (1 - \eta^2)} \left[3\left(1 - 3\theta^2\right) \right.\right. \\
&\quad \left.\left. \times \left(1 + \frac{3}{2}\eta^2 - 2e_0\eta - \frac{1}{2}e_0\eta^3 \right) + \frac{3}{4}\left(1 - \theta^2\right)\left(2\eta^2 - e_0\eta - e_0\eta^3\right)\cos 2\omega_0 \right] \right) \\
C_5 &= 2 (q_0 - s)^4 \xi^4 a_0'' p_0^2 \left(1 - \eta^2\right)^{-\frac{7}{2}} \left[1 + \frac{11}{4}\eta (\eta + e_0) + e_0\eta^3 \right] \\
C_6 &= 4a_0''\xi C_2^2 \\
C_7 &= \frac{4}{3} a_0''\xi^2 (17a_0'' + s) C_2^3 \\
C_8 &= \frac{2}{3} a_0''\xi^3 (221a_0'' + 31s) C_2^4
\end{aligned}
\tag{2.11}
$$

The future parameters a, e and n after $(t - t_0)$ are then

$$
\begin{aligned}
a &= a_0'' \left[1 - C_2 (t - t_0) - C_6 (t - t_0)^2 - C_7 (t - t_0)^3 - C_8 (t - t_0)^4 \right]^2 \\
e &= e_0 - B^* C_4 (t - t_0) - B^* C_5 (\sin M - \sin M_0) \\
n &= k_E a^{-\frac{3}{2}}
\end{aligned}
\tag{2.12}
$$

Also, the overall rotation angle after $(t - t_0)$ is

$$
\begin{aligned}
L = M + \omega + \Omega + n_0'' \left[\frac{3}{2} C_2 (t - t_0)^2 + \left(C_6 + 2C_2^2\right)(t - t_0)^3 + \frac{1}{4}\left(3C_7 + 12C_2C_6 + 10C_2^3\right)(t - t_0)^4 \right. \\
\left. + \frac{1}{5}\left(3C_8 + 12C_2C_7 + 6C_6^2 + 30C_2^2C_6 + 15C_2^4\right)(t - t_0)^5 \right]
\end{aligned}
\tag{2.13}
$$

We also need to consider perturbations in the orbital period. This is essential because the satellite will progressively increase over time due to these perturbations. The perturbations are speculated to arise from potential influences attributed to higher-order perturbation terms. Perturbations in the orbital period will be calculated, segmented into long-period and short-period perturbations. Long-period perturbations have a period longer than the orbital period, while short-period perturbations have a period shorter than the orbital

period. We first incorporate long-period perturbations.

$$\{Z_4\} \quad \longrightarrow \quad \{Z_5 \ : \ Z_4, (E+\omega)\} \tag{2.14}$$

First, the following parameters are defined.

$$\begin{aligned} a_x &= e\cos\omega \\ a_y &= e\sin\omega + \frac{A_{3,0}\sin i_0}{4k_2 a p^2} \\ L_{total} &= L_s + \frac{A_{3,0}\sin i_0}{8k_2 a p^2}\left(\frac{3+5\theta}{1+\theta}\right) a_x \end{aligned} \tag{2.15}$$

where $p = (1-e^2)^{\frac{1}{2}}$. Then we solve Kepler's equation by iterating for the rotation angle from the epoch. The initial iteration value is set as $(E+\omega_1)_1 = L_{total} - \Omega$.

$$(E+\omega)_{i+1} = (E+\omega)_i + \frac{L_{tota} - \Omega - a_y\cos(E+\omega)_i + a_x\sin(E+\omega)_i - (E+\omega)_i}{1 - a_y\sin(E+\omega)_i - a_x\cos(E+\omega)_i} \tag{2.16}$$

Depending on the desired level of accuracy, we can perform iterations accordingly. Once we have the rotation angle from the epoch $(E+\omega)_N$ after N iterations, we consider the short-period perturbations.

$$\{Z_5\} \quad \longrightarrow \quad \{Z_6 \ : \ Z_5, r, u, \Delta r, \Delta u, \Delta\Omega, \Delta i, \Delta\dot{r}, \Delta\dot{f}\} \tag{2.17}$$

We rewrite equation 2.15 using the iterated value from equation 2.16.

$$\begin{aligned} e\cos E &= a_x\cos(E+\omega)_N + a_y\sin(E+\omega)_N \\ e\sin E &= a_x\sin(E+\omega)_N - a_y\cos(E+\omega)_N \\ e_N &= \left(a_x^2 + a_y^2\right)^{\frac{1}{2}} \\ p_N &= a\left(1-e_N^2\right) \end{aligned} \tag{2.18}$$

Using these, we first calculate for the following parameters.

$$
\begin{aligned}
r &= a\left(1 - e\cos E\right) \\
\dot{r} &= k_E \frac{\sqrt{a}}{r} e \sin E \\
\dot{f} &= k_E \frac{p_N^{\frac{1}{2}}}{r} \\
\cos u &= \frac{a}{r}\left[\cos\left(E+\omega\right) - a_x - \frac{a_y e \sin E}{1+\sqrt{1-e_N^2}}\right] \\
\sin u &= \frac{a}{r}\left[\sin\left(E+\omega\right) - a_y - \frac{a_x e \sin E}{1+\sqrt{1-e_N^2}}\right] \\
u &= \tan^{-1}\left(\frac{\sin u}{\cos u}\right)
\end{aligned}
\tag{2.19}
$$

The inclusion of both $\sin u$ and $\cos u$ makes it necessary to determine the paratemer u from numerical analysis. The variables that represent short-period perturbations incorporate Δ into their names, as follows.

$$
\begin{aligned}
\Delta r &= \frac{k_2}{2p_N}\left(1-\theta^2\right)\cos 2u \\
\Delta u &= -\frac{k_2}{4p_N}\left(7\theta^2-1\right)\sin 2u \\
\Delta\Omega &= \frac{3k_2\theta}{2p_N^2}\sin 2u \\
\Delta i &= \frac{3k_2\theta}{2p_N^2}\sin i_0 \cos 2u \\
\Delta\dot{r} &= -\frac{k_2 n}{p_N}\left(1-\theta^2\right)\sin 2u \\
\Delta\dot{f} &= \frac{k_2 n}{p_N}\left[\left(1-\theta^2\right)\cos 2u - \frac{3}{2}\left(1-3\theta^2\right)\right]
\end{aligned}
\tag{2.20}
$$

We finally arrive at the final expressions for the orbit parameters at time t_k.

$$\begin{aligned} r_k &= r\left[1 - \frac{3}{2}k_2\frac{\sqrt{1-e_N^2}}{p_N^2}\left(3\theta^2 - 1\right)\right] + \Delta r \\ u_k &= u + \Delta u \\ \Omega_k &= \Omega + \Delta\Omega \\ i_k &= i + \Delta i \\ \dot{r}_k &= \dot{r} + \Delta\dot{r} \\ \dot{f}_k &= \dot{f} + \Delta\dot{f} \end{aligned} \tag{2.21}$$

We further simplify by defining position and velocity vectors.

$$\{Z_7 \ : \ Z_6, r_k, u_k, \Omega_k, i_k, \dot{r}_k, \dot{f}_k\} \quad \longrightarrow \quad \{\vec{r}, \dot{\vec{r}}\} \tag{2.22}$$

First, we use the angle parameters to create unit orientation vectors.

$$\begin{aligned} M &= \vec{\mu}\sin u_k + \vec{\nu}\cos u_k \\ N &= \vec{\mu}\cos u_k - \vec{\nu}\sin u_k \end{aligned} \tag{2.23}$$

where

$$\vec{\mu} = \begin{bmatrix} \mu_x = -\sin\Omega_k\cos i_k \\ \mu_y = \cos\Omega_k\cos i_k \\ \mu_z = \sin i_k \end{bmatrix} \quad , \quad \vec{\nu} = \begin{bmatrix} \nu_x = \cos\Omega_k \\ \nu_y = \sin\Omega_k \\ \nu_z = 0 \end{bmatrix} \tag{2.24}$$

This allows us to predict the satellite's path in Cartesian coordinates.

$$\boxed{\vec{r} = r_k M \quad , \quad \dot{\vec{r}} = \dot{r}_k M + \dot{f}_k N}$$

If predictions are continually made from the previous iterated value, errors will accumulate over time. Therefore, as illustrated in Figure 2.3, the iteration at time t_k is always computed from the Epoch (t_0).

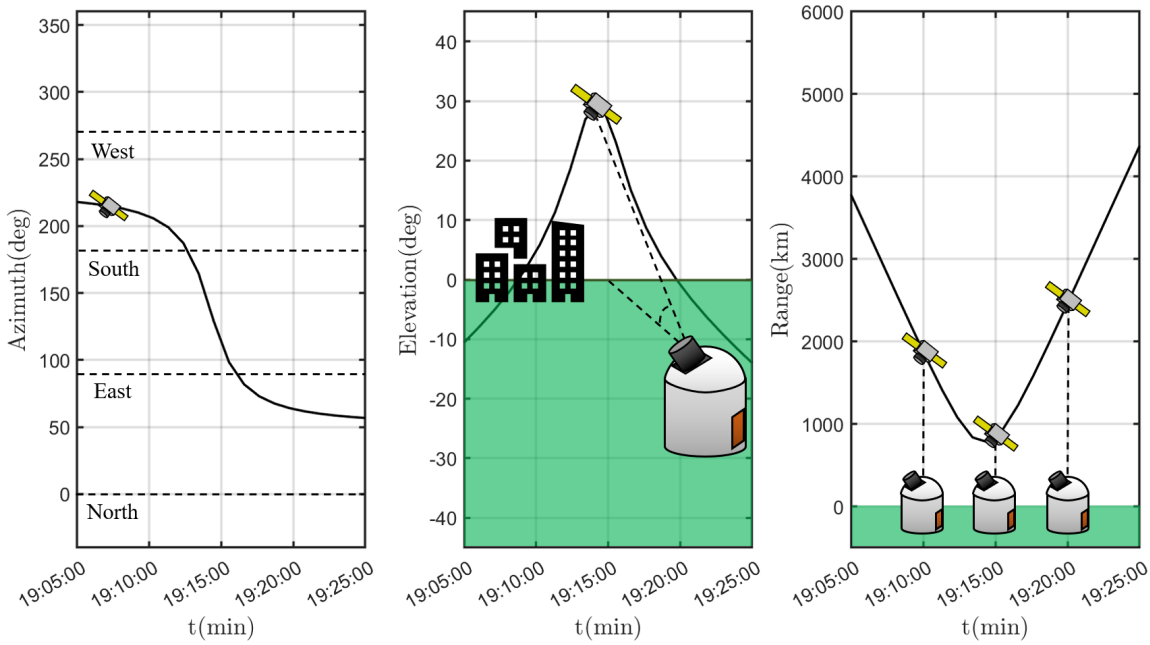

Figure 2.4: Three graphs predicting the path of the ISS in local coordinates using SGP4 algorithm. According to the calculations, the ISS is expected to be closest around 7:15pm, at which time it will be visible from the south, and its altitude will reach its peak.

2.1.1 Tracking Tests and Results

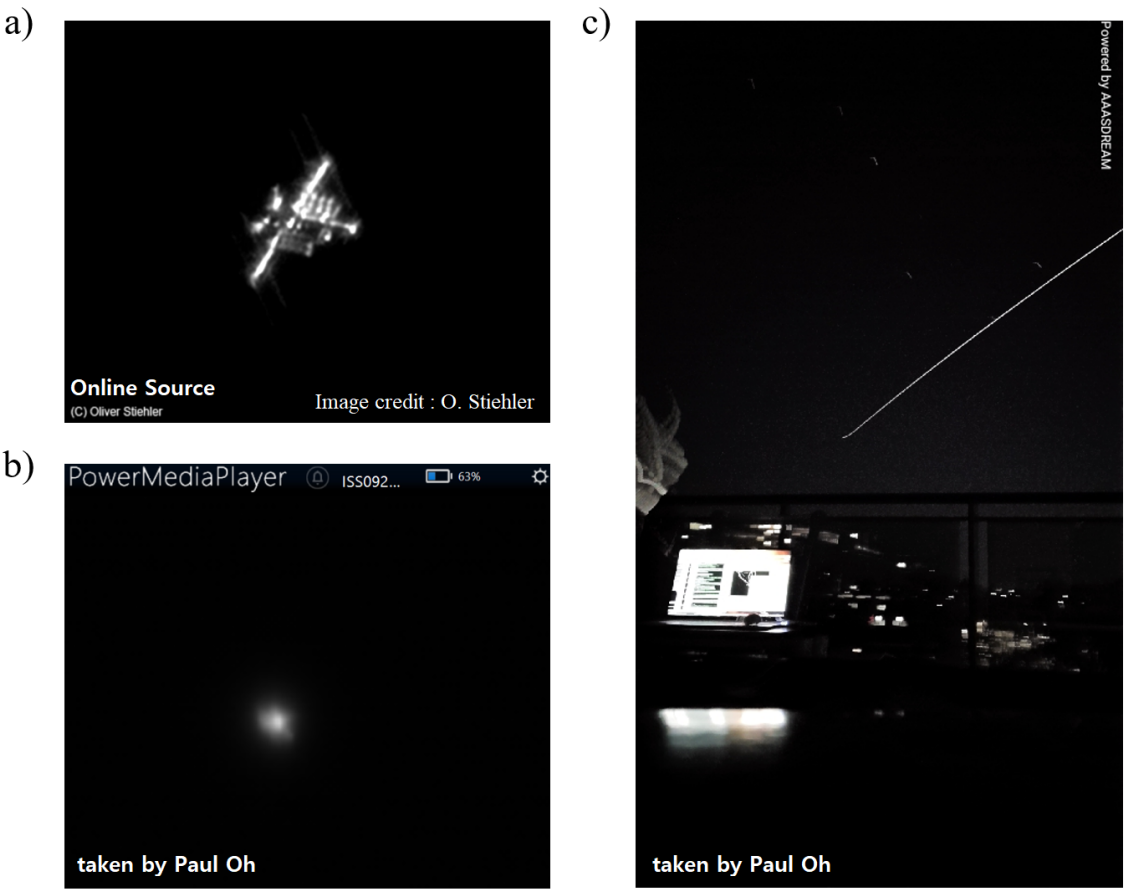

Figure 2.5: a) Picture taken by an amateur photographer (Image credit : O. Stiehler) just to compare with b) ISS taken by Sungeun (Paul) Oh during tracking. c) A timelapse photo showing the trail of ISS taken by Sungeun (Paul) Oh during tracking.

To confirm the precision of our use of the SGP4 algorithm, we attempted tracking the ISS, one of the most prominent and easily visible LEO satellites. The choice of selecting the ISS is based on its apparent magnitude, which can reach as low as -4, making it brighter than most satellites and even most stars. Its substantial size makes it easily observable when passing through the sky. Additionally, it is known to have an altitude of approximately 400 km, further contributing to its visibility. While Figure 2.5a is the image sourced online, Figure 2.5b is the sharpest image captured while tracking the ISS

on September 22nd, 2019. The photo was obtained using the Sharpcap software. Figure 2.5c is a photo taken in timelapse, capturing the path of the ISS as it moved, creating the appearance of a lingering trace in the sky. As we can see in the photo, other stars in the sky appear much dimmer compared to the ISS.
The ISS was tracked from University of Waterloo (Latitude : 43.4712^o, Longitude : -80.5442^o, Altitude (sea level) : 336 m). We used an Orion Goscope 80mm refractor telescope (Orion Telescope, US) mounted on NexStar GT mount (Celestron, Taiwan) to track the ISS. QHY-5-II-M camera (QHYCCD, China) was used for monitoring the tracking, and also for capturing some nice photos of the ISS. Figure2.6 shows the tracking result

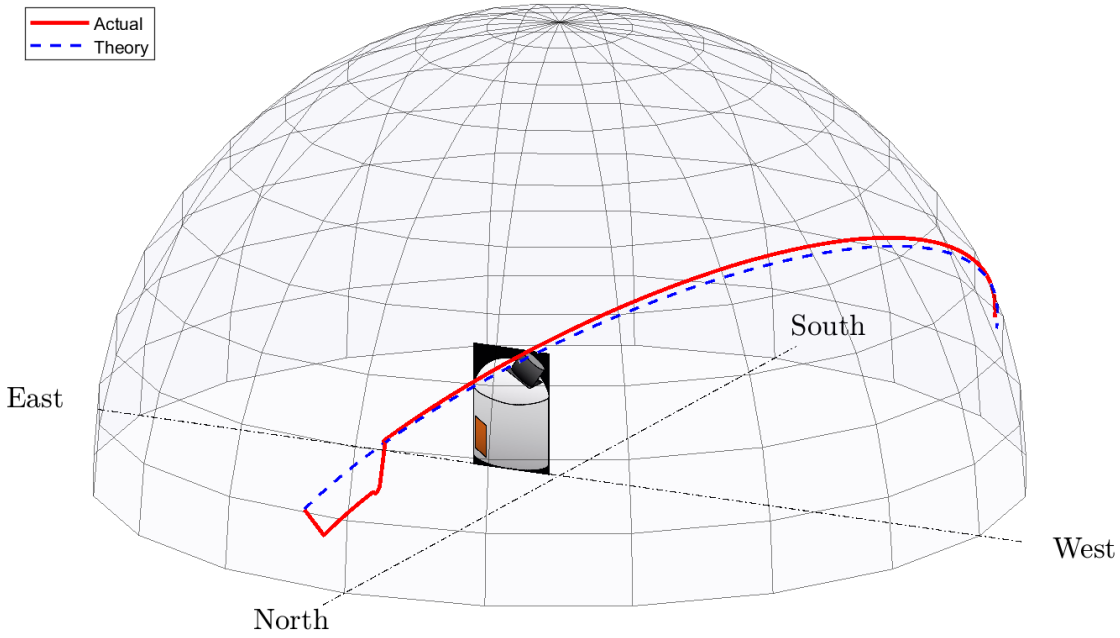

Figure 2.6: The result of the ISS tracking test done in October 2019, represented in 3-D graph. The ISS flew from North to South, circling around the West. The blue dashed line indicates the predicted path by SGP4. The red solid line represents the actual position of the ISS captured by our telescope as it was observed. As evident in the graph, manual adjustments were applied during the initial tracking phase.

obtained from a successful ISS tracking test performed in October 28th, 2019. Here, it is worth noting that the GPS values obtained from online sources for the tracking site may lack the desired accuracy. Additionally, we acknowledge the imperfect alignment of the

telescope with the initial position where the satellite appears. Consequently, the predictions derived from the SGP4 algorithm for the initial position and time are not considered crucial. Instead, we priortize monitoring changes in the satellite's position vector. Hence, the position offset present at the initiation of the tracking was manually adjusted. Following this adjustment, the ISS tracking proceeded reasonably well in accordance with our predictions. The raw data of the telescope's coordinate is shown in Appendix M. The pointing error σ_p was estimated based on the differences in the rates of change of azimuth and altitude between the SGP4 model predictions and the experimentally obtained values.

$$\sigma_p \approx \frac{1}{2}\left(\sigma_{p,azi} + \sigma_{p,alt}\right) = \frac{1}{2}\left[\left|\frac{\partial\theta_{azi,SGP4}}{\partial t} - \frac{\partial\theta_{azi,exp}}{\partial t}\right| + \left|\frac{\partial\theta_{alt,SGP4}}{\partial t} - \frac{\partial\theta_{alt,exp}}{\partial t}\right|\right]\Delta t \quad (2.25)$$

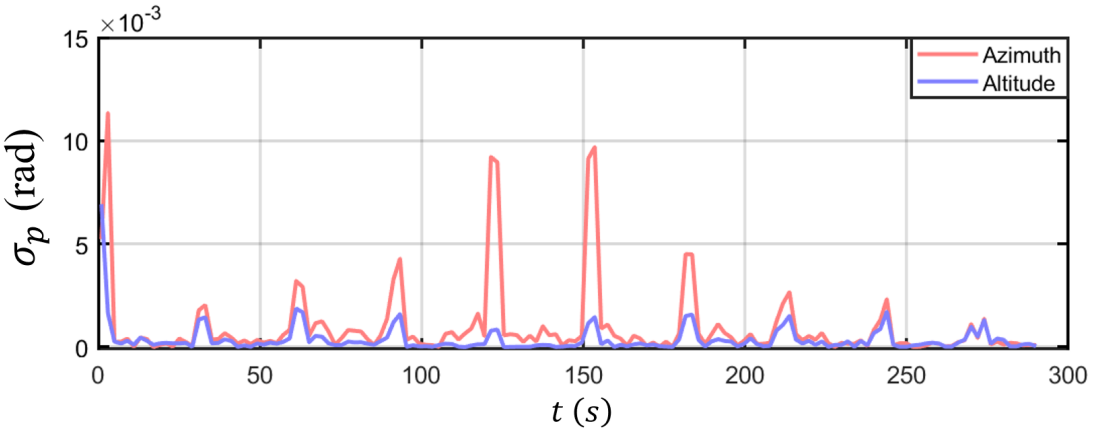

Figure 2.7: Graph showing pointing errors in azimuth (red) and altitude (blue). The periodic peaks are indicative of periodic adjustments to compensate for drift caused by the high slew rate of the motor mount.

The pointing error calculated from the tracking test was approximately $\sigma_p \approx 5.96 \times 10^{-4}$ rads.[1] With the validation of our satellite pass model, the ISS was within a distance of 1000 km (from the tracking site) for only about 2 minutes. Furthermore, through multiple tests, it has been observed that the ISS consistently becomes visible within altitude angles ranging from 30 to 50 degrees. We anticipate that QEYSSat will have a comparable pass duration.

[1] We expect to have a much lower pointing error from the actual tracking system for the QEYSSat [84].

Lastly to mention, we have developed a GUI (see Figure 2.8) that generates the satellite path in LLA coordinates using the SGP4 model. This is particularly useful as our ground station will be equipped with an Acquisition, Pointing and Tracking unit (APT) unit, which requires coordinates in this format.

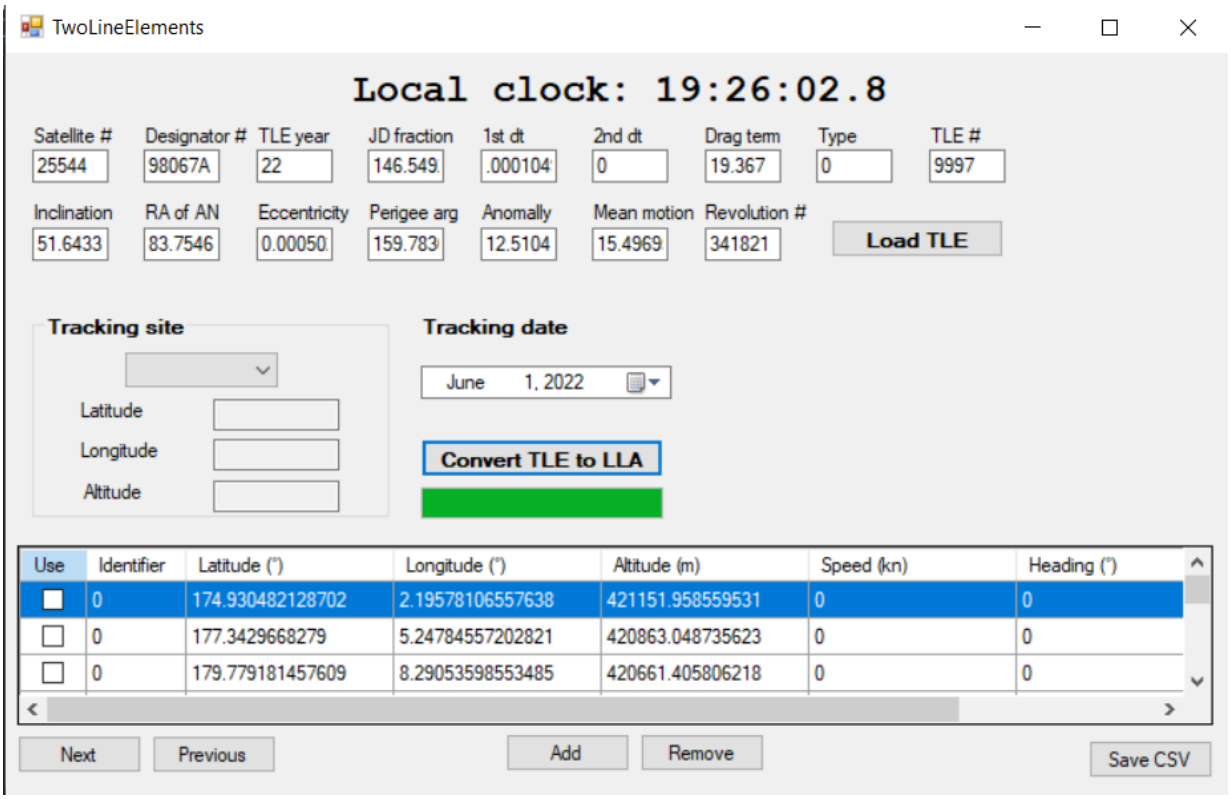

Figure 2.8: A GUI developed in C# coding that allows users to upload TLE data, convert it into LLA coordinates, and automatically feed it into the pointing system.

2.2 Link Attenuation Modelling

In this section, we show modelling of link attenuation [19, 20, 21], which will ultimately contribute to determining the minimum pair rate discussed later. In the ground-to-space quantum link, there are several types of errors that contribute to the overall link loss $\mathcal{L}$ (in decibels); geometric, atmospheric and mechanical system errors.

$$\mathcal{L} = \mathcal{L}_{geo} + \mathcal{L}_{atm} + \mathcal{L}_{mech} \tag{2.26}$$

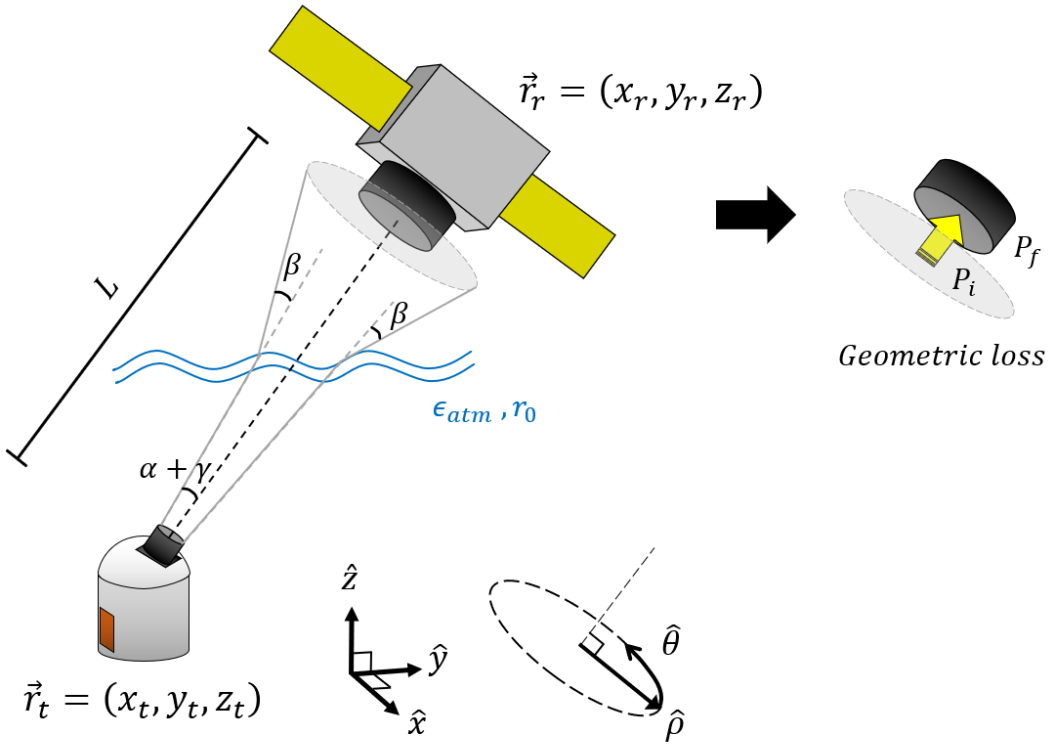

Figure 2.9: An illustration of how geometric attenuation is calculated using the ratio between the diffracted area (in light grey) and the area of the receiver telescope (in dark grey). The geometric attenuation of a quantum link can be computed in a manner similar to the method for determining fiber coupling efficiency.

The losses are additive, since each loss is a logarithm of the attenuation factor $A = P_i/P_f$.

$$\mathcal{L} = 10 \log_{10} \left(\frac{P_i}{P_f} \right) \tag{2.27}$$

where P_i and P_f are initial and final optical power, respectively. A high attenuation factor means a high link loss.

Geometric Attenuation

We derive the link loss caused by geometric attenuation using equation 2.27. We consider a ground-to-space quantum **uplink**, with an atmosphere present (Figure 2.9). When a beam encounters an obstacle or passes through an aperture, **diffraction** occurs, causing the beam to disperse and change its direction. In this case, the transmitter telescope with an aperture size (diameter) of D_t would cause diffractions. As we are using a laser beam as the quantum signal, we could assume gaussian wave propagating along the distance L. P_i is then the total incoming power from our quantum source. For now, we shall make an assumption that the power is not reduced by any attenuation factors throughout the transmission, such that the power right before the receiving telescope is still P_i. This way, the attenuation factor can be computed in a manner similar to the method for determining fiber coupling efficiency shown in the Appendix D.15. The fact that it is not the power but the intensity that is reduced by the diffraction, a perfect transmission (i.e, $A = 1$) is achieved only if the receiver telescope's aperture is large enough to collect all the power. We consider a realistic case where the receiver telescope captures only an optical power of P_f due to its limited aperture size. Dividing the full amount of power by the actually received amount of power will indeed yield the attenuation factor. Let us consider a LEO based satellite passing by the optical ground station located at $\vec{r}_t$, where quantum signals are transmitted through a transmitter telescope. A satellite carries a receiver telescope, and tries to receive signals at the location $\vec{r}_r$. The subscript t refers to the tramsmitter and r refers to the receiver. Also note that $\vec{r}_t$ and $\vec{r}_r$ are 2-D matrices that contain discretized points of each telescope aperture. The initial optical power P_i at the transmitter telescope can be calculated by integrating the initial intensity $I_{t,0}(\vec{r}_t)$ at the transmitter telescope over its area.

$$P_i = \int d\rho I_{t,0}(\vec{r}_t) dx dy = \pi R_t^2 I_{t,0}(\vec{r}_t) \tag{2.28}$$

where R_t is the receiver telescope's aperture radius. However, we would like to have the expression in terms of the initial intensity at the receiver telescope $I_{t,0}(\vec{r}_r)$. The intensity

received at the receiver telescope (with an aperture radius of R_r) can be calculated using Rayleigh-Sommerfield diffraction [70].

$$I_{t,1}(\vec{r}_r) = \frac{L^2}{\lambda^2}\left|\int\int \frac{\sqrt{I_{t,0}(\vec{r}_t)}}{|\vec{r}_r - \vec{r}_t|^2}\exp\left(\frac{2\pi i\,|\vec{r}_r - \vec{r}_t|}{\lambda}\right)\rho d\rho d\theta\right|^2 \tag{2.29}$$

and λ is the photon wavelength. The fact that the beam's profile is circularly symmetric, and the aperture sizes are small compared to the link distance ($L \gg D_t, D_r$) such that $L = |\vec{r}_r - \vec{r}_t|$, the expression can be greatly simplified.

$$I_{t,0}(\vec{r}_r) \approx \frac{\pi R_t^2}{L^2\lambda^2} I_{t,0}(\vec{r}_t) = \frac{1}{\pi L^2 \alpha^2} I_{t,0}(\vec{r}_t) \tag{2.30}$$

Here, we have a diffraction angle $\alpha = \lambda/(\pi D_t)$ by small angle approximation. This indicates that the intensity is reduced by the factor of the expanded area with a radius of $R \sim L\alpha$. Using this relation, the initial power at the receiver telescope is

$$P_i \approx \pi L^2 \alpha^2 I_{t,0}(\vec{r}_r) \tag{2.31}$$

Atmophseric turbulence has a greater impact on the beam propagation the closer it is to the Earth. Although the satellite is in LEO [53], it is much higher in altitude compared to the atmosphere. This implies that the impact could be particularly significant in the context of an uplink transmission. As the beam travels through the atmosphere, it will suffer from the atmospheric turbulence which will result in extra diffractions with an angle of β. By averaging over a longer time period than the turbulence period, we could have a two-dimensional Gaussian distribution of the turbulence (also see Figure 2.10).

$$g_{turb}(\rho) = \frac{1}{2\pi\sigma_{turb}^2} e^{-\rho^2/2\sigma_{turb}^2} \tag{2.32}$$

Using the Hufnagel-Valley model of atmospheric turbulence [96], the standard deviation σ_{turb} (which is equivalent to the half of the beam width) of the distribution at the receiver telescope is

$$\sigma_{turb} = \frac{L\lambda}{\pi r_0} \tag{2.33}$$

where r_0 is the Fried parameter (amount of turbulence in length) expressed as

$$r_0 = \left[0.424\csc(\delta)\left(\frac{2\pi}{\lambda}\right)^2 \int_0^h C_n^2(z)\left(\frac{h-z}{h}\right)^{\frac{5}{3}} dz\right]^{-\frac{3}{5}} \tag{2.34}$$

which is widely used in the research field of atmospheric turbulence. h and δ are the altitude and the elevation angle of the satellite, respectively. We also have the turbulence strength constant $C_n^2(z)$ (for a typical nighttime at sea level)[17], given by

$$C_n^2(z) = 1.7 \cdot 10^{-14} e^{-\frac{z}{100}} + 0.00359 \left(z \cdot 10^{-5}\right)^{10} e^{-\frac{z}{1000}} + 2.7 \cdot 10^{-16} e^{-\frac{z}{1500}} \tag{2.35}$$

The distribution of the turbulence can be convoluted on the transverse plane with the

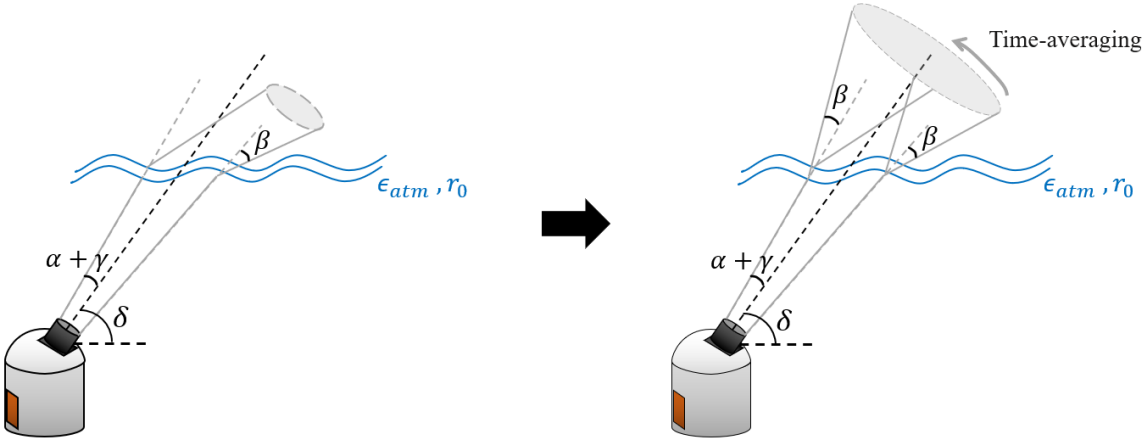

Figure 2.10: A figure describing how atmospheric turbulence effects are translated into the expansion of the transmission area. The atmosphere is described by the extinction coefficient ϵ_{atm} and the Fried parameter r_0. By averaging over a longer time period than the duration of the turbulence, we see an area resembling the diffracted area illustrated in Figure 2.9.

diffracted intensity to consider both the atmospheric turbulence and the diffraction.

$$I_{t,2}(\vec{r}_r) = (I_{t,1} \star g_{turb})(\rho, \theta) = \int_0^{2\pi} d\theta' \int_0^{\infty} I_{t,1}(\rho') g_{turb}(\rho - \rho') d\rho' \tag{2.36}$$

However, if we roughly assume that the turbulences distribute the intensity equally around the expanded area, the amount of contribution to the beam expansion is

$$\int I_{t,1} dx dy \approx \pi \sigma_{turb}^2 I_{t,1} \approx \pi L^2 \beta^2 I_{t,1} \tag{2.37}$$

where $\sigma_{trub} \sim L\beta$. $\beta = \lambda/(\pi r_0)$ is the angular expansion (see Figure 2.10. Instead of the convolution, we could simply add this term into equation 2.31.

$$P_i \approx \pi L^2 \left(\alpha^2 + \beta^2\right) I_{t,0}(\vec{r}_r) \tag{2.38}$$

Lastly, we consider an intensity loss from **pointing errors**. This is an amount of error from inaccuracy in pointing the satellite. Similar to the distribution of the turbulence, we could have another two-dimensional Gaussian distribution for the pointing error.

$$g_p(\rho) = \frac{1}{2\pi\sigma_p^2} e^{-\rho^2/2\sigma_p^2} \tag{2.39}$$

where σ_p is one standard deviation of the pointing error. By convoluting it with $I_{t,2}(\vec{r}_r)$, we have the final intensity at the receiver telescope.

$$I_{t,3}(\vec{r}_r) = (I_{t,2} \star g_p)(\rho, \theta) \tag{2.40}$$

Similar to the atmospheric turbulence, by roughly assuming that the error in the pointing motion distribute the intensity equally around the expanded area, the expansion can also be added into equation 2.31 in the similar manner.

$$P_i \approx \pi L^2 \left(\alpha^2 + \beta^2 + \gamma^2\right) I_{t,0}(\vec{r}_r) \tag{2.41}$$

where we have the pointing error angle γ. The angle from the pointing error depends on the performance of the satellite tracking system, which can be obtained experimentally. One would agree that the factor $\pi L^2 (\alpha^2 + \beta^2 + \gamma^2)$ represents the diverged area at the receiver telescope by the diffraction, the atmospheric turbulence and the pointing error. The final optical power received by the receiver telescope is simply the intensity at the receiver telescope integrated over its area $P_f = \pi R_r^2 I_{t,0}(\vec{r}_r)$. By applying equation 2.27 we obtain the expression of the overall geometric loss.

$$\mathcal{L}_{geo} \approx 10 \log_{10} \left(\frac{L^2 (\alpha^2 + \beta^2 + \gamma^2)}{R_r^2} \right) \tag{2.42}$$

Atmospheric Attenuation

In the absence of the atmosphere (ideally, vacuum), the optical power for a perfect transmission should remain unchanged $P_{i,t} = P_{i,r}$ as previously mentioned. Since there is air,we have to take **atmospheric absorption and scattering** effect into consideration. The power is attenuated by a factor of ϵ_{atm} (in decibels). We have already considered the area of

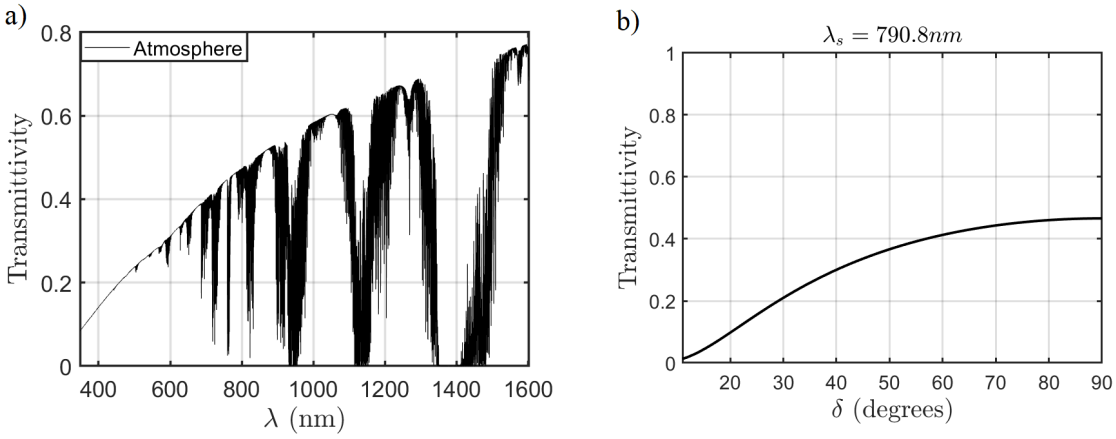

Figure 2.11: (a) Atmospheric transmittance at a typical rural area assuming measured towards zenith. This prediction was generated by a commercial program MODTRAN [20]. The dips are where light is observed by the molecules in the atmosphere. (b) Transmittance at 790.8 nm of wavelength for different elevation angle δ. The reason that we are interested in this wavelength is explained in section 2.2.1.

the optical power, so the area S_r is kept fixed. The loss from the atmospheric attenuation is then

$$\mathcal{L}_{atm} = 10\log_{10}\left(\frac{I_{t,0}(\vec{r}_t)S_r}{I_{t,0}(\vec{r}_r)S_r}\right)$$

$$= 10\log_{10}\left(\frac{I_{t,0}(\vec{r}_t)S_r}{I_{t,0}(\vec{r}_t)S_r \cdot 10^{-\frac{\epsilon_{atm}}{10}}}\right) = \epsilon_{atm}$$

Based on the satellite tracking result, we anticipated the minimum elevation angle (worst case scenario) to be approximately $\delta \approx 30^o$. The atmospheric transmittance at $\lambda_s = 790.8$ nm for this angle is estimated to be reduced by $\epsilon \approx 6.6$dB.

Mechanical System Attenuation

We also consider the optical losses from the transmitter system μ_t and the receiver system μ_r. The final power is simply $P_f = \mu_t\mu_r P_i$ such that

$$\mathcal{L}_{mech} = 10\log_{10}\left(\frac{1}{\mu_t\mu_r}\right) \tag{2.43}$$

At present, it is difficult to precisely estimate the optical losses of both systems. Therefore, we will make positive assumptions by adopting $\mu_t = 1$ (ideal) and $\mu_r = 0.55$ (the detection efficiency of SPAD at $\lambda_s = 790.8\,\text{nm}$) [7], as these factors can improve in the future.

2.2.1 Wavelength Selections For The EPS

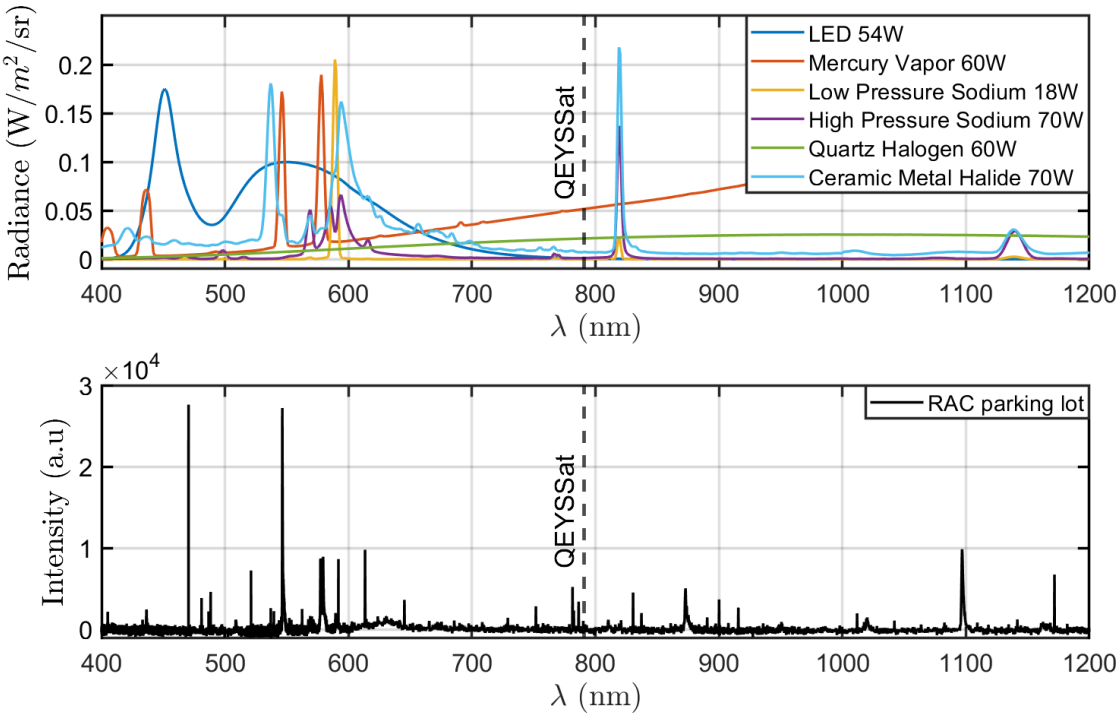

Figure 2.12: (Top) Spectral data of different street lamps retrieved from National Oceanic and Atmospheric Administration (NOAA) website [1]. (Bottom) Spectral data obtained using a mini portable spectrometer (OceanOptics, US) at the RAC1 parking lot. The spectrum is also used in section 2.3.1 (Figure 2.23) for estimating light pollution.

To select a wavelength suitable for the free-space quantum link, we need to take into account various considerations. As defined earlier, the divergence angles α, β and γ in equation 2.42 are inversely proportional to the wavelength. Therefore, it can be inferred that as the wavelength increases, the attenuation increases quadratically. Just considering this aspect, one might think it is preferable to choose a lower wavelength. Yet, as seen

in Figure 2.11, a decrease in wavelength corresponds to an almost quadratic reduction in atmospheric transmittance. Next, we consider technical limitations. The currently widely used detectors include SPAD and SNSPD. Typically, SPAD efficiently detects photons in the near-Infrared (IR) range $750-1500\,\text{nm}$, and SNSPD detects photons in a wider near-IR range[2]. While SNSPD is significantly more efficient than SPAD in terms of performance, the drawbacks is that it needs to be cooled down to extremely low temperatures. The associated increased complexity renders it unsuitable for satellite integration, highlighting a limitation. Therefore, the wavelength selected for the free-space quantum link is ideally in the acceptable wavelength range for the SPAD. We need to also consider light pollution. In the context of QKD, the most crucial consideration is the Quantum Bit Error Rate (QBER). If light generated from an external source arrives at the detector with the same wavelength as the signal photon, it can have a significantly adverse impact on the QBER. The spectral graphs in Figure 2.12 (top) shows that typical street lamps are predominantly concentrated within the wavelength spectrum ranging from 400 to 700 nm. This is also evident in the (bottom) graph in Figure 2.12, showing the spectrum taken in the nearby parking lot next to the future OQGS construction site. Having considered all these factors, 790.8 nm was chosen as the wavelength for the signal photons. For the idler photons transmitted through the ground, we can consider wavelengths that can leverage the already-present and widely-used telecom infrastructure. The wavelength of 1550 nm not only satisfies the requirements but also represents a suitable wavelength that can be efficiently detected by SNSPD. In fact, these signal/idler wavelengths choices are not significantly different from those already chosen by our QPL team for the airborne experiment in 2016 [84].

2.2.2 Aperture Size Selections

By combining all equations 2.42, 2.43 and 2.43, we obtain an expression for the overall attenuation factor.

$$\text{Overall Attenuation}: \quad A \approx \frac{L^2\left(\alpha^2+\beta^2+\gamma^2\right)10^{\frac{\epsilon_{atm}}{10}}}{\mu_t\mu_r R_r^2} \tag{2.44}$$

Equation 2.44 also gives us a sense of the aperture sizes (diameters) of the transmitter and receiver telescopes. As the beam travels through free space towards the satellite, it continues to diverge as discussed earlier. Therefore, a larger aperture size for the receiver

[2]Definitions of those ranges could slightly differ by manufacturers.

telescope is preferable. However, since the feasibility of this is entirely contingent upon whether the satellite can accommodate such dimensions, we focus more on the transmitter telescope's aperture size. Figure 2.13 illustrates the attenuation factor values based on the

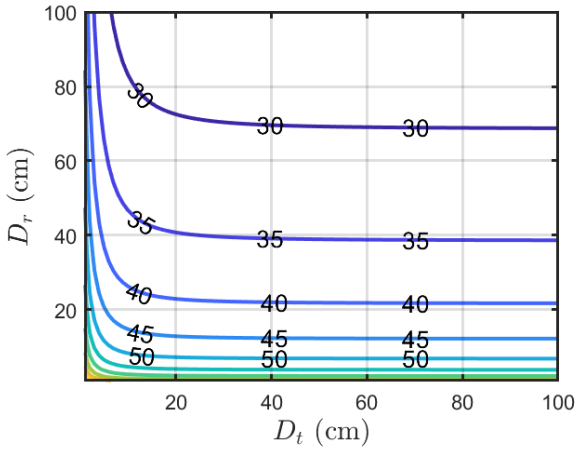

Figure 2.13: A color plot illustrating the variation in attenuation (calculated in dB) relative to changes in both the diameters of the transmitter D_t and the receiver D_r telescopes. The values on the curves represent the amount of attenuation (in decibel).

aperture sizes of the transmitter and receiver telescopes, using the following values.

- $\lambda_s = 790.8\,\text{nm}$ (from section 2.2.1)
- $L = 1000\,\text{km}$ (from section 2.1.1)
- $\gamma = 2\mu\text{rad}$ (from J-P. Bourgoin (2013) [20])[3]
- $r_0 = 6.7\,\text{cm}$ (from equation 2.34)
- $\epsilon_{atm} = 6.6\text{dB}$ (from section 2.2)
- $\delta = 30^o$ (from section 2.1.1)
- $T_t = 1$ and $T_r = 0.55$ (from section 2.2)

[3]Since the pointing error calculated from the tracking test (section 2.1.1) was overestimated due to experimentation with a cheap motor mount that has a poor performance, here we adopt the $\gamma = 2\mu rad$ that was considered in this paper. It is reasonable to use this value, as this paper also relates to the QEYSSat mission.

It is observed that once the transmitter aperture size exceeds 20 cm, the attenuation factor is no longer influenced. Hence, we choose the aperture size of 20 cm for our transmitter telescope.

2.2.3 Link Attenuation

We anticipate that the size of the receiver telescope to be installed on the QEYSSat will be around $D_r = 30\,\text{cm}$ [20]. By using the same values from Figure 2.13, we can obtain the overall link loss of $\mathcal{L} \approx 37.7$ dB. This loss is equivalent to roughly 8 km of a typical optical fiber channel for the 790 nm of wavelength [3]. If we use the pointing error obtained from the tracking test with the cheap motor mount ($\sigma_p = 5.96 \times 10^{-4}$rads), the link loss becomes $\mathcal{L} \approx 71.4$ dB which is significantly larger. From this, we can infer that the precision in the tracking system has a significant impact on the quantum link. Furthermore, as these values are calculated assuming the satellite is at zenith, the link loss could potentially worsen even further.

2.3 Background Noise Modelling

With the recent push for long-distance free-space QKD there has been a rising interest for the installation of OQGS. While several factors must be taken into account when establishing an OQGS, such as proximity to existing fiber optic infrastructure, a primary determinant for QKD effectiveness is the minimization of QBER. The QBER represents the fraction of incorrectly detected quantum bits in a sequence. Since our focus is on the uplink QKD at night, where the satellite faces the Earth and receives quantum signals from OQGS. When considering the sources of background light (noise) that would affect uplink QKD at nighttime, two main sources can be identified : the reflected moonlight denoted as N_{ML} (sunlight reflected off the Moon, being reflected again off the Earth's atmosphere) [20]; and the light pollution denoted as N_{LP}[42, 85]. The total number of background photon counts can be written as follows.

$$N_{BG} = N_{ML} + N_{LP} \tag{2.45}$$

Of particular concern is the impact of the noises within targeted communication wavelength ranges. Just by looking at Figure 2.14a, one can infer the significant impact of noise from reflected moonlight. Also, recent reports have highlighted a noticeable increase in artificial light at night [64]. Our aim is to establish an upper bound on the current challenges posed

by background noises at these OQGS sites, thereby laying the groundwork for enhanced satellite quantum communication strategies.

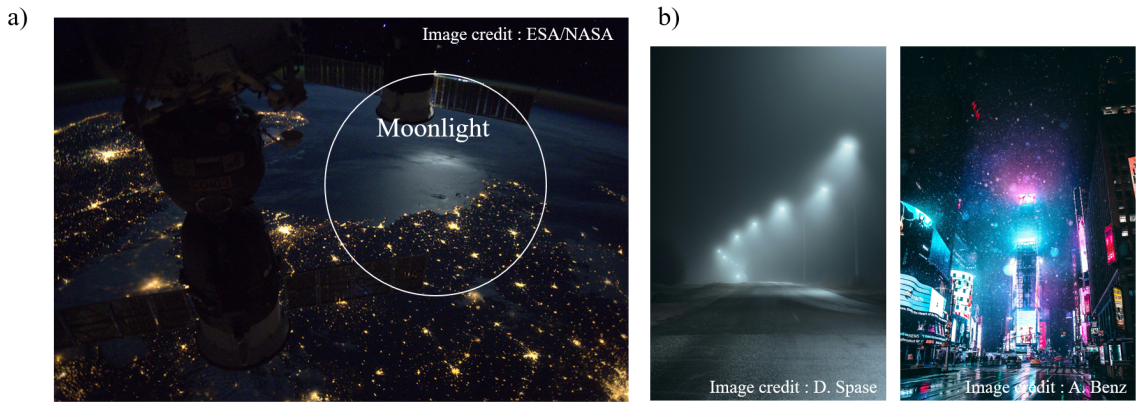

Figure 2.14: a) Photo of Earth taken from ISS (image credit : ESA/NASA). We see moonlight glowing on the ocean, along with artificial light from the land. b) Some cool pictures taken by amateur photographers showing artificial light (image credit : D. Spase(left) A. Benz(right)).

Moonlight

To estimate the amount of noise from moonlight, we initially calculate the number of photons emitted by sunlight using the spectral blackbody radiation[4] at a fixed temperature [82, 63].

$$B_\lambda(\lambda, T_\odot) = \frac{2hc^2}{\lambda^5} \frac{1}{e^{\left(\frac{hc}{\lambda k T_\odot}\right)} - 1} \tag{2.46}$$

where effective surface temperature of $T_\odot = 5772\text{K}$ of the sun is used [102]. We shall go through the mathematical methodology while referring to Figure 2.15. As illustrated in Figure 2.15b, the blackbody radiance $B_\lambda(\lambda, T)d\lambda$ corresponds to the radiance of a stream of light emitted from a source that reaches a target. One can define number radiant intensity $\mathcal{I}_\odot$ (radiant intensity in terms of the number of photons instead of energy) of the Sun by integrating equation 2.46 that is being divided by its energy $E_\lambda = hc/\lambda$ over the filtered

[4]Spectral blackbody radiation : Blackbody radiation per unit wavelength.

wavelength region (we used a bandpass filter that accepts (790 ± 5)nm), then over the photon emitting area.

$$\mathcal{I}_\odot = \int \frac{B_\lambda(\lambda, T_\odot)}{E_\lambda} d\lambda dA = A_\odot \int_{(790-5)nm}^{(790+5)nm} \frac{2c}{\lambda^4} \frac{1}{e^{\left(\frac{hc}{\lambda k T_\odot}\right)} - 1} d\lambda \tag{2.47}$$

The area is simply $A_\odot = \pi R_\odot^2$ where $R_\odot = 6.96 \times 10^5 km$ is the radius of the Sun [102]. In order to get the total number of photons per second N_M that reach the Moon, we must again integrate equation 2.47 over the solid angle of the Moon seen from the Sun (as illustrated in Figure 2.15c).

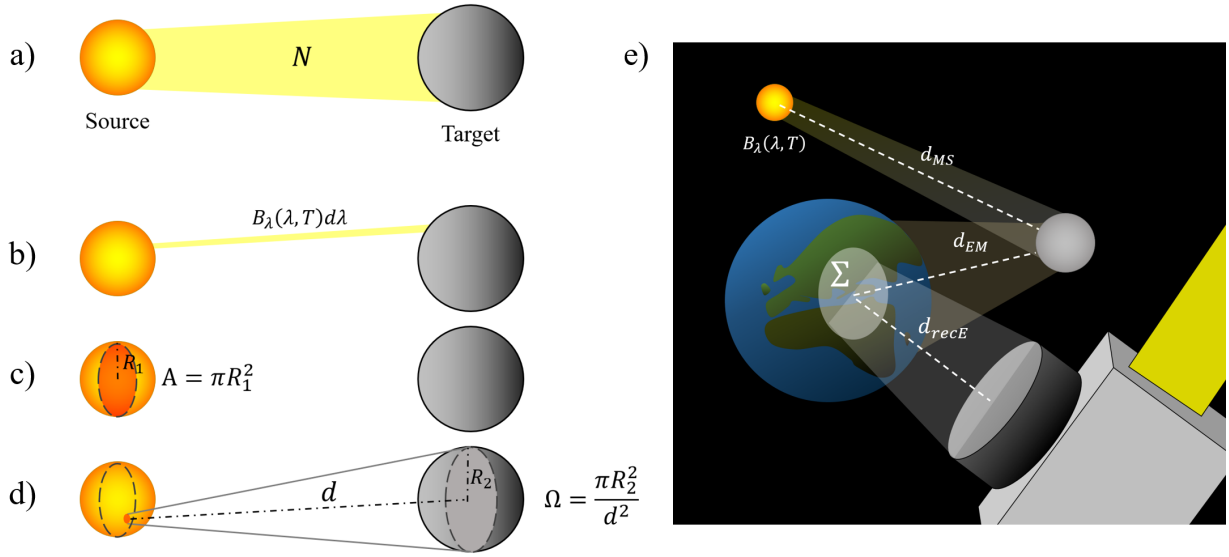

Figure 2.15: An illustration of the method for calculating the moonlight : a) Suppose we want to calculate the number of photons, denoted as N, emitted from a source and reaching a target. b) We first calculate a stream of light using spectral blackbody radiation function. The number radiance is obtained by dividing the radiation function by its energy, and integrating it over the wavelength range of interest. c) Next, we integrate the number radiance over the area of the source to obtain the number radiant intensity, denoted as $\mathcal{I}$. d) Finally we integrate $\mathcal{I}$ over the solid angle of the target as seen from the source, to obtain N.

$$N_M = \mathcal{I}_\odot \Omega_M \tag{2.48}$$

The solid angle of the Moon is $\Omega_M = \pi R_M^2 / d_{MS}^2$ where $R_M = 1.74 \times 10^3 km$ is the radius of the Moon and $d_{MS} \approx d_{ES} = 1.5 \times 10^8 km$ is the distance between the Sun and the Moon which can be approximated as the distance between the Sun and the Earth [102]. When these photons undergo reflection on the Moon's surface, we can assume Lambertian diffusion [17]. This means that regardless of the direction from which light hits the Moon's surface and reflects, it diffuses in all directions. We obtain the number radiant intensity from the Moon $\mathcal{I}_M$ (Hz/sr) by normalizing it with π (because $\cos\theta$ integrates to π over the hemisphere), and also considering the the Moon's albedo, denoted as a_M.

$$\mathcal{I}_M = \frac{a_M}{\pi} N_M \tag{2.49}$$

Note that the amount of light reflected off the Moon's surface could highly depend on the lunar phase. Here, we consider the Moon's albedo as $a_M = 0.136$ which was measured at the lunar phase angle $\theta = 7^o$ (almost a full moon case, corresponding to high background noise) [72].

The satellite will not receive the full amount of photons due to the limited Field Of View (FOV) of its receiver telescope. We must consider that we only receive photons from the area on Earth (shown as Σ in Figure 2.15e) that corresponds to the satellite's FOV.

$$\Sigma \approx \pi \left(FOV \cdot d_{recE} \right)^2 \tag{2.50}$$

We use FOV$= 50 \mu rad$ (which we expect our receiving telescope to have), allowing us small angle approximation. We assume $d_{recE} = 500\,\text{km}$ as the distance between the Earth's surface and the satellite. The number of photons per second N_E that reach the Earth is then

$$N_E = \mathcal{I}_M \Omega_E \tag{2.51}$$

where we have $\Omega_E = \Sigma / d_{EM}^2$, and $d_{EM} = 3.545 \times 10^5 km$ [102] is the perigee distance between surfaces of the Earth and the Moon (to consider the worst case scenario). Similarly to what was done in equation 2.49, the number radiant intensity from the Earth can be expressed also assuming Lambertian diffusion.

$$\mathcal{I}_E = \left(10^{-\frac{\epsilon_{atm}}{10}} \csc\left(\delta\right) \right)^2 \frac{a_E}{\pi} N_E \tag{2.52}$$

We consider a typical value of $a_E = 0.29$ for the Earth's albedo [32]. $\mathcal{I}_E$ differs from $\mathcal{I}_M$ in that it includes an extinction coefficient of the atmosphere previously discussed in 2.2. The extinction term is squared to accounts for the entry and exit of light into the atmosphere when being reflected. Finally, the number of photons per second N_{ML} that reach the receiver telescope is

$$N_{ML} = \mathcal{I}_E \Omega_{rec} \tag{2.53}$$

where we have $\Omega_{rec} = \pi R_{rec}^2/d_{recE}^2$. $R_{rec} = 5\,\text{cm}$ is used as the radius of the receiver telescope. Using all the values mentioned here, the dark counts resulting from moonlight are calculated to be $N_{ML} = 137\ s^{-1}$. Considering that the weather on Earth can vary the extinction coefficient, if we do not consider atmospheric extinction at all (worst case scenario), the calculation results in $N_{ML} = 863\ s^{-1}$.

Light Pollution

Background noise from artificial light pollution can be calculated using a method similar to the previous method (for Moonlight), but with a simpler process, since there are no intermediate sources for bouncing.

$$N_{LP} = 10^{-\frac{\epsilon_{atm}}{10}} \int_{(790-5)nm}^{(790+5)nm} \frac{B_{\lambda;\text{Sources}}}{E_\lambda} d\lambda dA d\Omega \tag{2.54}$$

The spectral radiation function, divided by its corresponding energy, is integrated over the filtered wavelength region, the area of the sources, and the solid angle of the receiver telescope as seen from Earth. Atmospheric extinction is also considered here, but since it is the case of light passing through, the factor of 2 is not included in the formula. The amount of light pollution can vary greatly depending on the region, as light sources may differ from one city to another. However, to provide a rough estimate, some research papers reporting on light pollution in urban areas through moonlight-free nighttime observation have shown radiance in the DNB ranging between $40 \sim 180\text{nW/cm}^2\text{/sr}$ [27, 41].

2.3.1 Background Noise Measurements

Starlight analysis

While it was not possible to directly measure the quantity of photons received from Moonlight through observation, we attempted to estimate the number of photons received from a star using the blackbody radiation function as a means of validating the amount of light received. We use equation 2.54, considering the photons to have passed through the atmosphere once. Another reason we apply equation 2.54 for the downlink (the receiver being on Earth) is that we assume normal incidence of light from the star. In this case, the

Figure 2.16: (a,b) Photos of the experimental setup for the background noise outdoor measurements. (c) Photo of a star (Arcturus), taken by Sungeun (Paul) Oh on a clear night for starlight analysis.

integration over the area and the solid angle yields the same result regardless of whether one is considered the source or the target.

$$A\Omega = A_1 \frac{A_2}{d_{12}^2} = \frac{A_1}{d_{12}^2} A_2 \tag{2.55}$$

One can obtain the number radiant intensity of a star by performing numerical integration of the number radiance function. If the filter bandwidth is narrow, as shown in Figure 2.17, the numerical integration could be simplified by calculating the trapezoidal area underneath the function. Orion GoScope refractor telescope (Orion, US) with an aperture size of 8 cm is used for star observation. The telescope is maneuvered automatically by the Nexstar GT telescope mount (Celestron, US) to locate stars. The eyepiece of the telescope is replaced with the electronic filter wheel (ZWO ASI, China) and a ASI183mm Pro (ZWO ASI, China) camera which is a monochromatic complementary metal-Oxide semiconductor (CMOS) camera [62]. The filter wheel consists of four different bandpass filters. This configuration of the telescope is illustrated in Figure 2.18. The telescope mount is programmed using Matlab software (MathWorks, US) to automatically point towards the stars. We entered Python code into SharpCap software (SharpCap, UK) to control camera settings and the filter wheel (illustrated in Figure 2.19. There have been several observation attempts to measure the photon counts received from the stars. However, due to unstable weather conditions, we only present data obtained by measuring Vega using a $(790 \pm 10)nm$ bandpass filter (Thorlab, US). We conduct a technical analysis based on

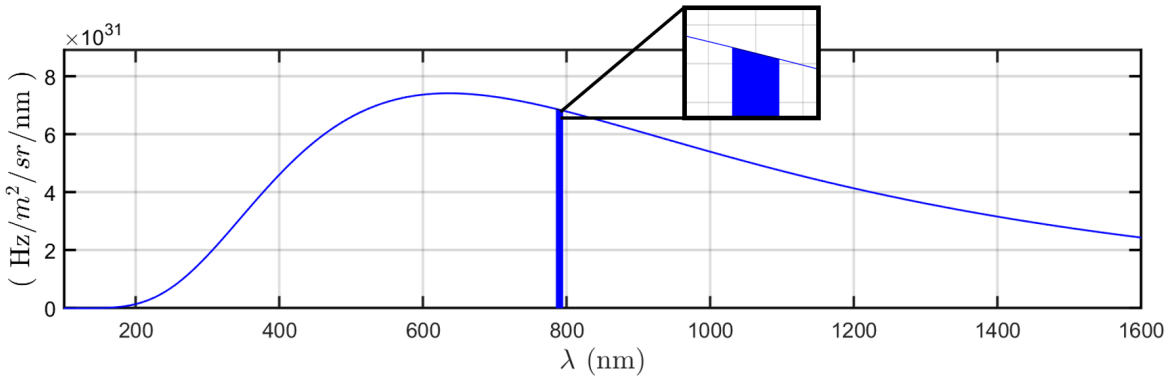

Figure 2.17: A spectral number radiance plot as a function of the wavelength. The zoomed-in section shows how one can approximate the area as a trapezoid when numerically integrating the function.

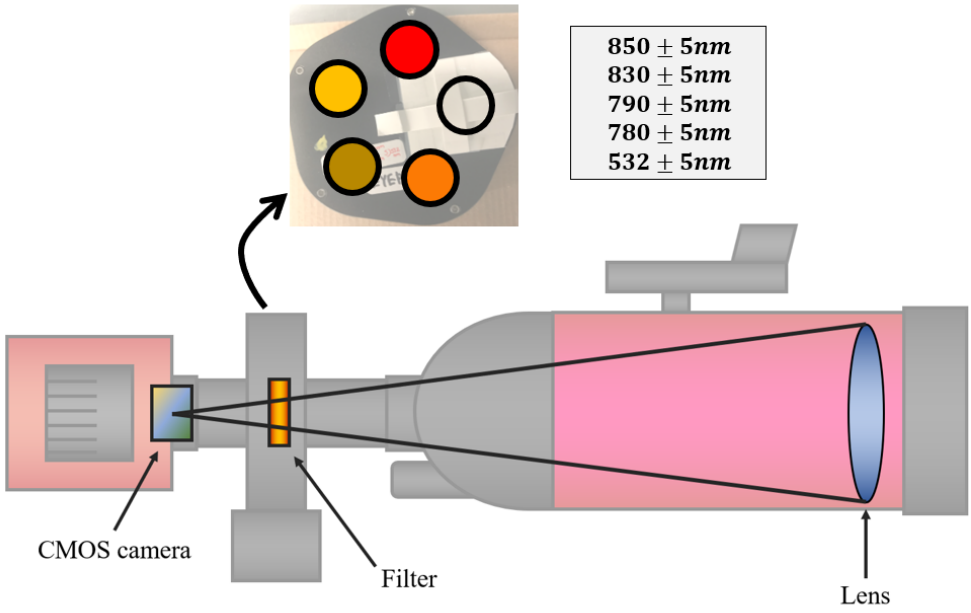

Figure 2.18: A diagram illustrating the structure of the measurement device for the observation. Starting from the right, we attached them in the following sequence: Orion GoScope refractor telescope (Orion, US), electronic filter wheel (ZWO ASI, China), and ASI183mm Pro (ZWO ASI, China) camera.

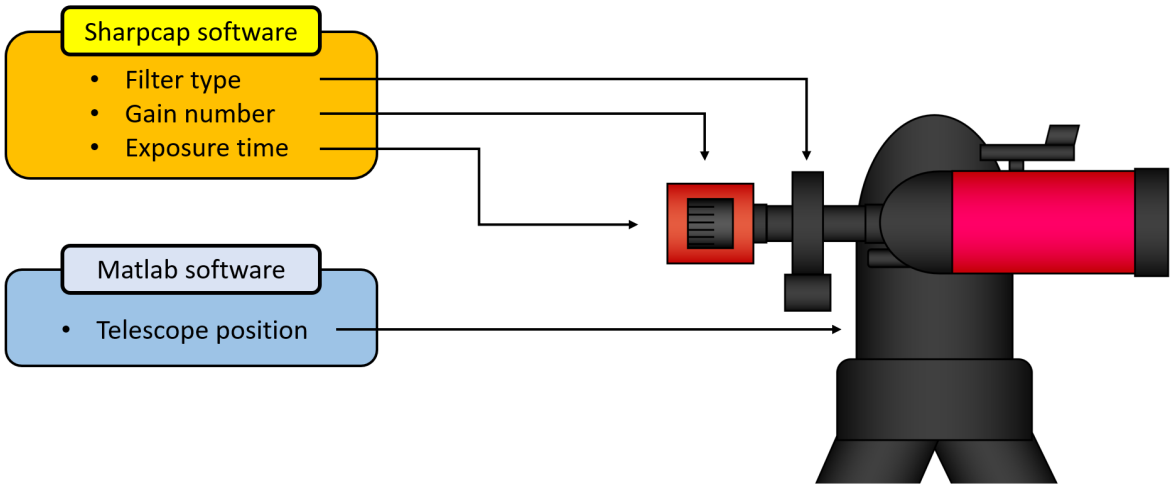

Figure 2.19: A schematic flowchart showing how the measurement device is controlled during the experiment. We used two different software programs (without any particular reasons) to control the telescope, electronic filter wheel, and camera.

the specifications of the camera provided on the website of the ZWO ASI company [62]. For the observation, a gain of 0 was set[5], allowing for a full electron well capacity of 15000 electrons per pixel. The camera employs a 12-bit Analog-to-Digital Converter (ADC) value, dividing the brightness level of each pixel into $2^{12} = 4096$ Analog-to-Digital Unit (ADU). Consequently, the brightness level increases for every accumulation of approximately 3.66 electrons. Figure 2.20 shows the image of Vega taken with an exposure time of $\Delta t = 0.1\,\mathrm{s}$. The pixels that contain Vega display a total accumulated brightness value of 5944 ADU. The pixel with the highest value is 909 ADU (as shown in Excel), which the value appears as 56 in the DS9 software due to the MONO16 setting ($909/16 \approx 56$). To retrieve the actual number of photons, we use the following equation.

$$N_{exp} = \left(3.66 \frac{e^-}{ADU}\right) \frac{\#\ ADU}{\eta_d \Delta t} \tag{2.56}$$

By considering the camera's detection efficiency of $\eta_d = 0.38$ at 790 nm, it was calculated that $N_{exp} = 5.7 \times 10^5 \mathrm{Hz}$ of photons from Vega reached the telescope lens. The theoretically

[5]The gain value here simply represents a set level, and is unrelated to the actual physical concept of gain.

estimated value (including the atmospheric effect) is $N_{theo} = 9.7 \times 10^5$Hz. Considering the many approximations and assumptions made, the values being within the same order of magnitude suggests a reasonable level of agreement between the experimental and theoretical results. Another reason for not being able to compare the results with other stars is

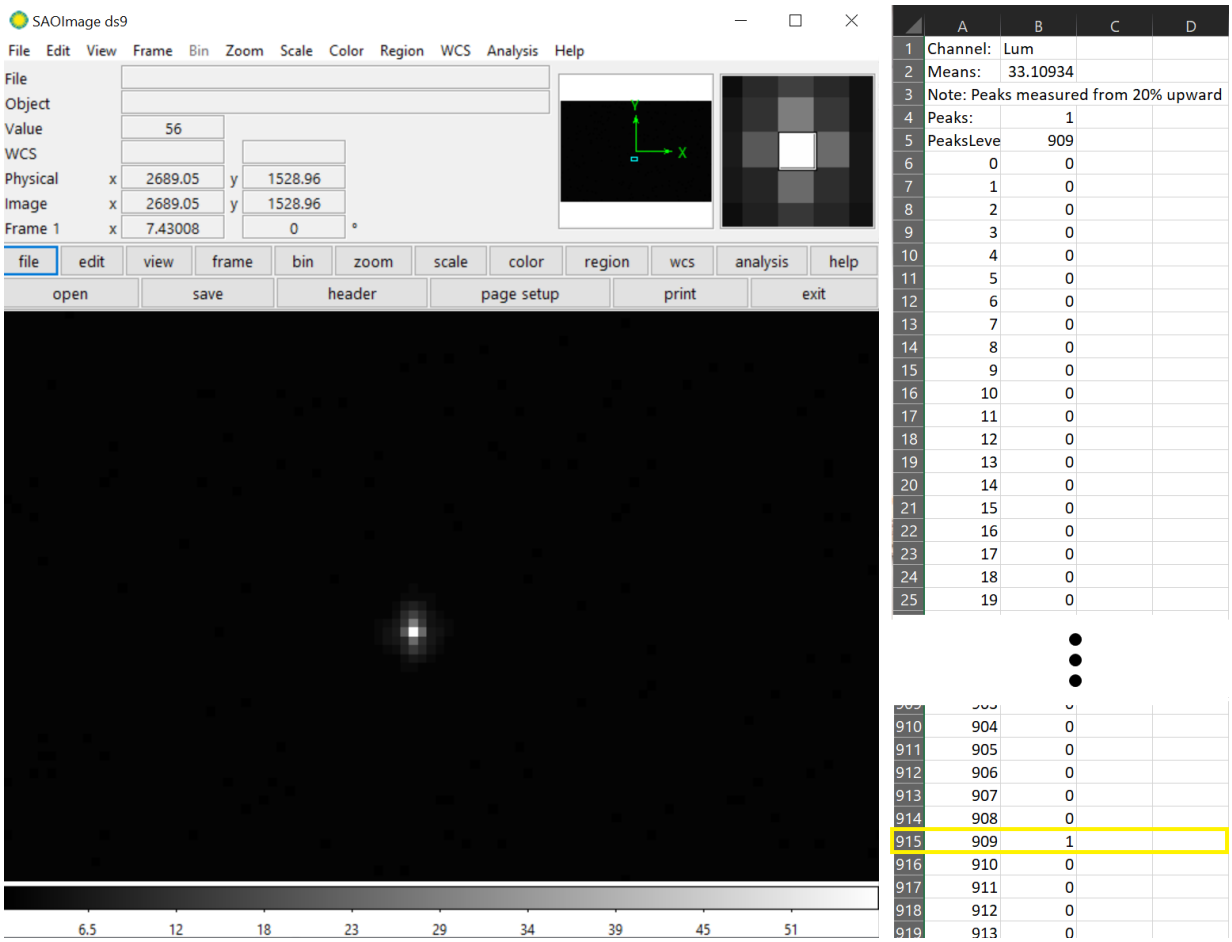

Figure 2.20: The photo of Vega being analyzed using the SAOImageDS9 program [56]. We see a pixel peaking at 909 ADU, which the value is displayed as 56 in the DS9 software. This is because one of the settings (MONO16) divides the peak level by 16. To highlight the cell that has the peak value, the middle section of the Excel sheet was taken out of the screenshot.

that the majority of stars observable through our telescope are not single entities; rather, they exist in binary or multiple systems, making them unsuitable for applying the black-

body function[6]. As the photon count of Vega has been confirmed to some extent, it would be beneficial to calculate the number of photons reaching a satellite when these photons are reflected by the Earth's atmosphere. The starlight calculation method is similar to the method used for calculating moonlight, but excluding the intermediate source, the moon. From what was observed through the telescope, we theoretically predict that the satellite's receiver telescope receives only about 1.4×10^{-4} photons per second from Vega. Vega is one of the brightest stars in the night sky, so we can infer that the contributions of starlight to the background noise will be extremely small.

Light pollution analysis

We also measure artificial light pollution in the area where the Waterloo OQGS (ON, Canada) is located. Our OQGS is planned to be built in the near future on the rooftop of RAC1, which is located near the University of Waterloo (Canada). The primary source

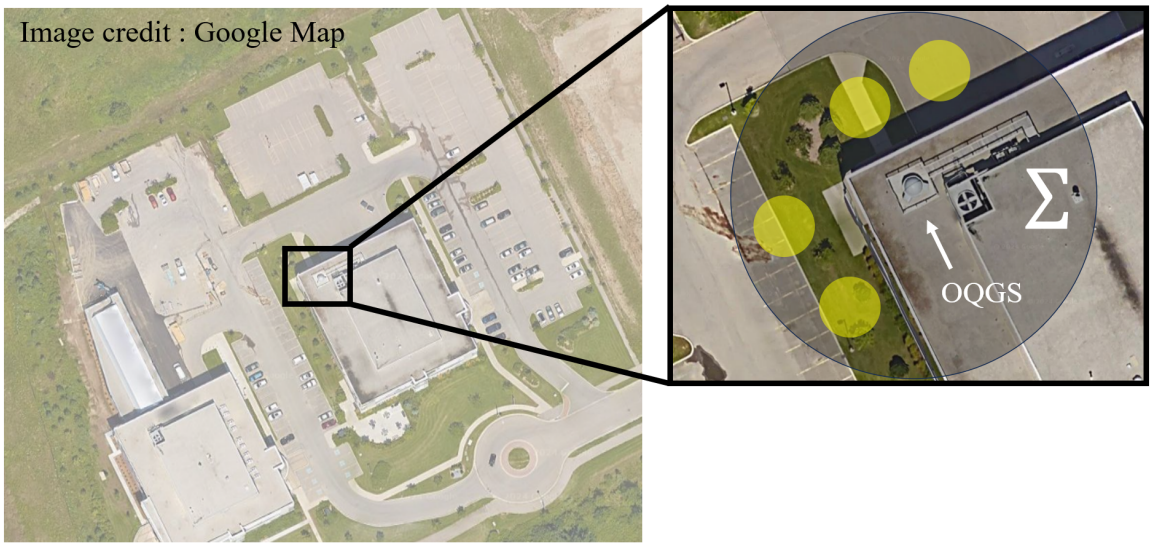

Figure 2.21: A satellite image (Image credit : Google Map) of where OQGS is located. The highlighted grey area, denoted as Σ, within the zoomed-in section represents the area of the parking lot as seen from the satellite. Each highlighted yellow region, denoted as A_p, within this grey area is where light pollution measurements were done.

[6]This was only realized much later! It was a sad realization that not only several months of effort became somewhat meaningless but also one needs a clear understanding before performing any experiments.

from which light pollution is expected to emanate from is the parking lot of the RAC1 building (Figure 2.21). Investigating the exact number of street lamps or the amount of light from buildings around the OQGS can be a complex task. Therefore, to validate our results, we rely on data obtained from VIIRS satellite. VIIRS satellite collects visible and infrared images and global observations of the land, atmosphere, cryosphere and oceans [11]. We measured light pollution in the parking lot area using two different approahces. Note that we need both approaches to validate our observation results. The measurements were performed during a new moon phase on March 20, 2023, and during a near full moon on February 28, 2023. One approach involves using an optical fiber and a photodetector

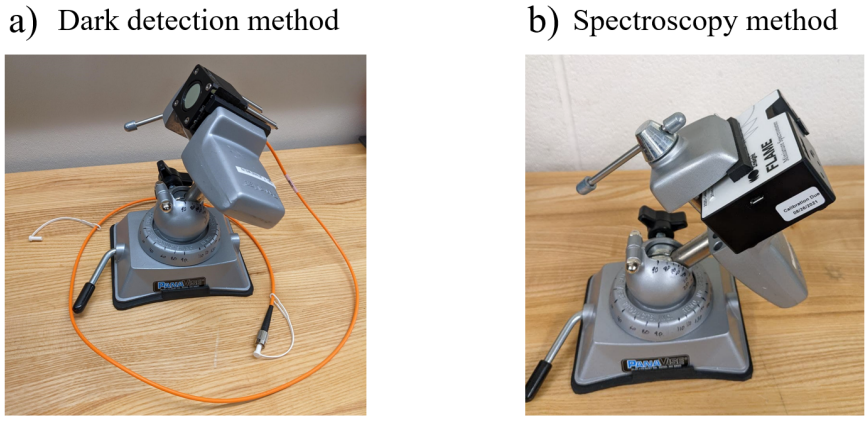

Figure 2.22: a) Light pollution measurement device for the dark detection method. A multimode fiber, a bandpass filter (790 ± 5nm), a rotating clamp and a SPAD detector are used to measure the background counts. b) Light pollution measurement device for the spectroscopy method. A mini spectrometer and a rotating clamp are used to take the spectra of light coming from the parking lot area. Both photos are taken by my colleague, Paul Godin.

(see Figure 2.22a). We attached a bare multimode optical fiber to a rotation-capable clamp. A bandpass filter (790 ± 5nm) is also mounted to collect photons only in that wavelength range. The other end of the fiber is connected to a photodetector. For the detector, we chose a simpler SPAD rather than the cryogenically cooled SNSPD for conducting outdoor tests and measurements. The fiber is oriented vertically downward from the rooftop of the RAC1 building to face the parking lot and collect photons emitted from it. Here, we can assume that atmospheric effects are negligible at this short distance. The number radiance

$\mathcal{B}_p$ (Hz/m^2/sr) of the parking lot can be written as

$$\mathcal{B}_p = \frac{N_{roof}}{\Omega_f A_p} \tag{2.57}$$

$\Omega_f = \pi R_f^2/d_p^2$ is the solid angle of the fiber as seen from the parking lot, where R_f is the radius of the fiber core and d_p is the distance between the fiber and the parking lot (equivalent to the height of the rooftop. $A_p = \pi\left(d_p \sin \mathrm{NA}\right)^2$ is the area of the parking lot as seen from the rooftop by the fiber, where NA is the numerical aperture of the fiber. Hence, we can estimate $\mathcal{B}_p$ once we obtain the photon counts N_{roof} collected from the rooftop, through the fiber, and by the detector. In order to compare with the VIIRS data, we need to calculate the number of photons reaching the VIIRS satellite. We first multiply $\mathcal{B}_p$ by the solid angle $\Omega_{sat} = \pi\left(R_{sat}/d_{sat}\right)^2$ of the receiver camera of the VIIRS satellite, where $R_{sat} = 9.5\,\mathrm{cm}$ and $d_{sat} = 830\,\mathrm{km}$ are the radius of the receiver camera and the distance between the parking lot and the satellite, respectively [38]. Then we multiply again by the area of the parking lot $\Sigma = \pi\left(FOV \cdot d_{sat}\right)^2$ as seen from the satellite at zenith.

$$N_{D.method} = 10^{-\frac{\epsilon_{atm}}{10}} \csc^2(\delta)\, \mathcal{B}_p \Omega_{sat} \Sigma \tag{2.58}$$

We consider atmospheric effect as well as the elevation of the satellite. The cosecant

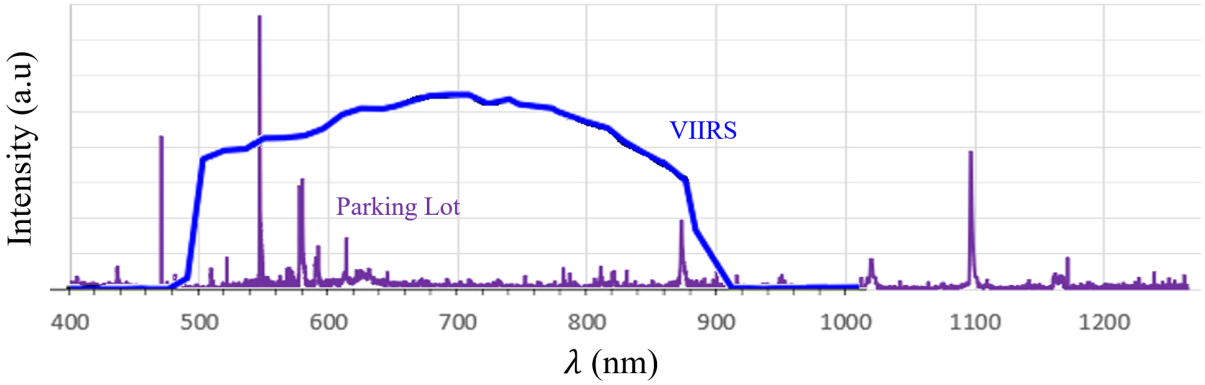

Figure 2.23: The sensitivity spectrum of the DNB sensor that is used by VIIRS (plotted in blue) [101]. The dark subtracted spectrum of the RAC1 parking lot taken from the rooftop (plotted in purple).

term is multiplied twice : once for the atmospheric term and once for the area term. VIIRS satellite uses wide-band filters to capture data [9], while we use a narrow-band filter

(790 ± 5)nm for our measurements, rendering the comparison of data inaccurate. Therefore, we adopt another approach, which involves using a spectrometer (see Figure 2.22b). We conduct RAC1 parking lot scans by attaching a mini spectrometer (Ocean Insight, US) to a rotation-capable clamp. We obtain the spectrum by directing the spectrometer towards the parking lot, again from the rooftop of the RAC1 building, with the fiber input port of the spectrometer kept open to expose it to the scanning area. Figure 2.23 shows

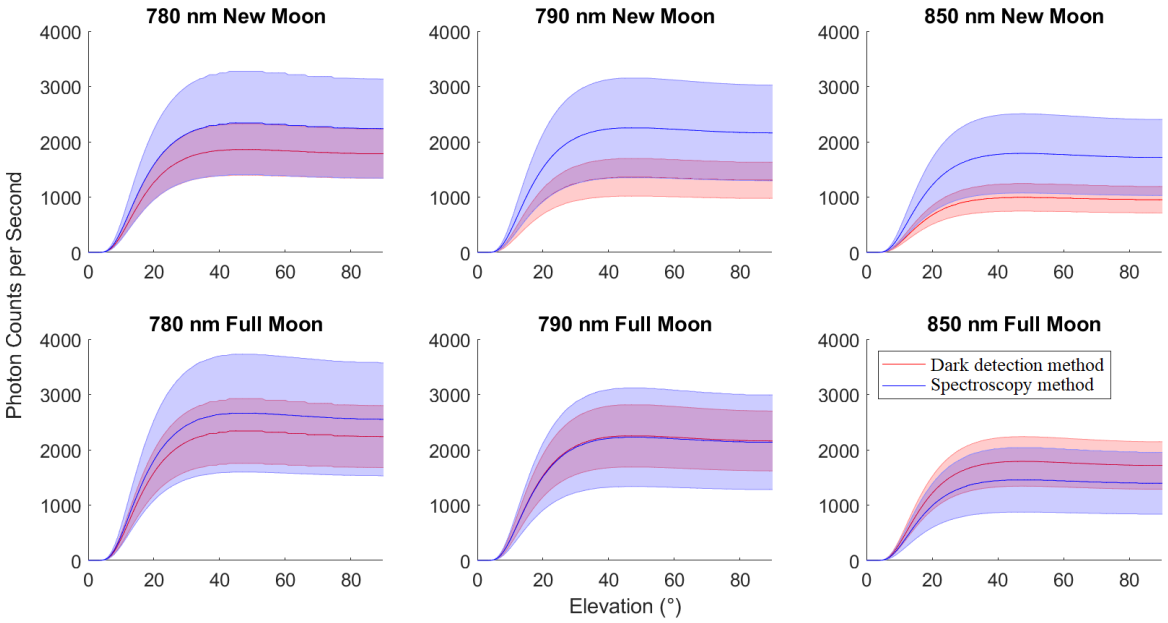

Figure 2.24: Six graphs showing the analysis results using 'dark detection method' and 'spectroscopy method'. We measured during the new moon and full moon phases using bands of (780 ± 5)nm, (790 ± 5)nm, and (850 ± 5)nm. The graphs display an uncertainty range of $\pm 25\%$. The graphs are generated by my colleague, Paul Godin.

the dark subtracted spectrum of the parking lot (shown in purple) captured with an exposure time of 10 seconds and averaged over 5 measurements. We multiply the spectrum by the VIIRS DNB spectrum (shown in blue), obtained from the VIIRS website [10, 9]. After multiplying the two spectra, we select only the wavelength region corresponding to the VIIRS DNB and determine the portion within the (790 ± 5)nm range. As a result, it is expected that when the VIIRS satellite scans the parking lot using the DNB filter, the number of photons received within our narrow-band region would account for 0.42% of the total, which can be used as a calibration factor. Finally, by obtaining the brightless level of the parking lot provided by the satellite on the date of our observation, and multiplying it

by the calibration factor, we can compare it with the photon number values previously obtained through the first approach. The calculation results shown in Figure 2.24 takes into account an uncertainty range of ±25%. The uncertainty is considered because the number radiance $\mathcal{B}_p$ is calculated from the experimentally measured N_{roof} that only corresponds to the background noise in the yellow regions shown in Figure 2.21 rather than from the entire region Σ. Nevertheless, Figure 2.24 shows that the photon counts obtained from both approaches are within the same order of magnitude, indicating a reasonable level of agreement between them. We can finally approximate the total background noise from these experimental investigations.

$$N_{BG} \approx 863\,\text{Hz}(N_{ML}) + 2000\,\text{Hz}(N_{LP}) \approx 3000\,\text{Hz}. \tag{2.59}$$

2.3.2 Minimum Photon Pair Rate Estimation

In practical terms, it is not possible to send perfectly entangled photon pairs every single time. Occasionally, photons may be transmitted without any correlation, which corresponds to an error in QKD. However, the good news is that a certain degree error tolerance is acceptable in QKD, and perfect photon correlation is not necessarily required. We use CHSH inequality [30, 81] to mathematically determine the maximum acceptable error level to ensure secure QKD. For a successful QKD demonstration, it is crucial that the signal and idler photons exhibit strong correlation upon reaching Alice and Bob. The degree of correlation preservation during their transport through the quantum link can be assessed by the entanglement visibility.

$$V = \frac{N_{\text{expected}} - N_{\text{unexpected}}}{N_{\text{expected}} + N_{\text{unexpected}}} \tag{2.60}$$

N_{expected} is the number of expected coincidence detection event from Alice and Bob. The $N_{\text{unexpected}}$ unexpected coincidence events may originate from sources associated with background noise. The QBER can also be obtained from the entanglement visibility.

$$\text{QBER} = \frac{N_{\text{unexpected}}}{N_{\text{expected}} + N_{\text{unexpected}}} = \frac{1 - V}{2} \tag{2.61}$$

If all the coincidence detections are as expected, we will have $V = 1$ (which means 100%) and QBER $= 0$. The decrease in visibility can be interpreted as the depolarization of the entangled photon states. Depolarization occurs when the entangled states transition to completely mixed states. In terms of the projection operator, the depolarizing channel

could be described as follows [66].

$$|\psi\rangle\langle\psi| \longrightarrow (1-p)\,|\psi\rangle\langle\psi| + \frac{p}{4}\mathbb{I} \tag{2.62}$$

where $p = 1 - V$ is the probability of depolarization. We can address such scenarios by adding the depolarization feature into equations 1.28.

$$\begin{aligned} N_{++}(\alpha,\beta) = N_{--}(\alpha,\beta) &= \frac{1-p}{2}N_0\cos^2(\alpha-\beta) + \frac{p}{4}N_0 \\ N_{+-}(\alpha,\beta) = N_{-+}(\alpha,\beta) &= \frac{1-p}{2}N_0\sin^2(\alpha-\beta) + \frac{p}{4}N_0 \end{aligned} \tag{2.63}$$

Referring to equations 1.23 and 1.27, the statistical value S can be experimentally obtained by measuring the followinig coincidence counts.

$$\begin{aligned} S_{exp} =& \frac{N_{\alpha^+\beta^+} - N_{\alpha^+\beta^-} - N_{\alpha^-\beta^+} + N_{\alpha^-\beta^-}}{N_{\alpha^+\beta^+} + N_{\alpha^+\beta^-} + N_{\alpha^-\beta^+} + N_{\alpha^-\beta^-}} - \frac{N_{\alpha^+\delta^+} - N_{\alpha^+\delta^-} - N_{\alpha^-\delta^+} + N_{\alpha^-\delta^-}}{N_{\alpha^+\delta^+} + N_{\alpha^+\delta^-} + N_{\alpha^-\delta^+} + N_{\alpha^-\delta^-}} \\ &+ \frac{N_{\gamma^+\delta^+} - N_{\gamma^+\delta^-} - N_{\gamma^-\delta^+} + N_{\gamma^-\delta^-}}{N_{\gamma^+\delta^+} + N_{\gamma^+\delta^-} + N_{\gamma^-\delta^+} + N_{\gamma^-\delta^-}} + \frac{N_{\gamma^+\beta^+} - N_{\gamma^+\beta^-} - N_{\gamma^-\beta^+} + N_{\gamma^-\beta^-}}{N_{\gamma^+\beta^+} + N_{\gamma^+\beta^-} + N_{\gamma^-\beta^+} + N_{\gamma^-\beta^-}} \end{aligned} \tag{2.64}$$

where we attempt to maximally violate the CHSH inequality by choosing $\alpha = 0^o$, $\beta = 22.5^o$, $\gamma = 45^o$ and $\delta = 67,5^o$. As we previously discussed in section 1.2.5, the maximal violation of CHSH is $S_{QM} = 2\sqrt{2}$ whereas the classical upper bound is $S_{CM} = 2$. In actual experiment, we must consider statistical fluctuations. Let us claim that the CHSH inequality is violated when S_{exp} deviates from S_{CM} by a minimum of three standard deviations (i.e., $\approx 99.7\%$ confidence level).[7]

$$S_{exp} - 3\Delta S_{exp} > S_{CM} \tag{2.65}$$

We can use error propagation to derive the statistical fluctuations [76].

$$\Delta S_{exp} = \sqrt{\sum_i \sum_j \left(\frac{\partial S}{\partial N_{i,j}}\right)^2 N_{i,j}} \tag{2.66}$$

Note that we assume Poissionian statistics such that the uncertainty of the coincidence count is $\Delta N = \sqrt{N}$. For instance, the partial derivatives with respect to α and β are

$$\begin{aligned} \frac{\partial S}{\partial N_{\alpha^+\beta^+}} = \frac{\partial S}{\partial N_{\alpha^-\beta^-}} &= \frac{2\left(N_{\alpha^+\beta^-} + N_{\alpha^-\beta^+}\right)}{\left(N_{\alpha^+\beta^+} + N_{\alpha^+\beta^-} + N_{\alpha^-\beta^+} + N_{\alpha^-\beta^-}\right)^2} \\ \frac{\partial S}{\partial N_{\alpha^+\beta^-}} = -\frac{\partial S}{\partial N_{\alpha^-\beta^+}} &= \frac{2\left(N_{\alpha^+\beta^+} + N_{\alpha^-\beta^-}\right)}{\left(N_{\alpha^+\beta^+} + N_{\alpha^+\beta^-} + N_{\alpha^-\beta^+} + N_{\alpha^-\beta^-}\right)^2} \end{aligned} \tag{2.67}$$

[7] The choice of three standard deviations is purely arbitrary on our part.

Hence, the fluctuation term with α, β is

$$\sum_{\alpha}\sum_{\beta}\left(\frac{\partial S}{\partial N_{\alpha,\beta}}\right)^{2} N_{\alpha,\beta} = \frac{4\left(N_{\alpha^{+}\beta^{+}} + N_{\alpha^{-}\beta^{-}}\right)\left(N_{\alpha^{+}\beta^{-}} + N_{\alpha^{-}\beta^{+}}\right)}{\left(N_{\alpha^{+}\beta^{+}} + N_{\alpha^{+}\beta^{-}} + N_{\alpha^{-}\beta^{+}} + N_{\alpha^{-}\beta^{-}}\right)^{2}} \tag{2.68}$$

By putting equations 2.63 into equation 2.68 and choosing the angles previously mentioned, equation 2.66 becomes

$$\Delta S_{exp} = 2\sqrt{\frac{\frac{1}{2} - \frac{p^{2}}{2} + p}{N_{0}}} = 4\sqrt{\frac{1 - \frac{V^{2}}{2}}{N_{total}}} \tag{2.69}$$

Here, we assumed that the coincidence events for each correlation measurement are the same $(N_0(\alpha,\beta) = N_0(\alpha,\delta) = N_0(\gamma,\delta) = N_0(\gamma,\beta) = N_0 = N_{total}/4)$. The total coincidence events include both the expected and the unexpected cases.

$$N_{total} = N_{expected} + N_{unexpected} \tag{2.70}$$

Finally, the violation inequality 2.65 can be written as follows.

$$2\sqrt{2}V - 12\sqrt{\frac{1 - \frac{V^{2}}{2}}{N_{total}}} > 2 \tag{2.71}$$

As the visibility varies between 0 and 1, we can write $S_{exp} = S_{CHSH}V = 2\sqrt{2}V$. This means that if the visibility is 1, the statistical value becomes $2\sqrt{2}$, indicating the violation of the inequality. Given the assumption that the unexpected coincidence events predominantly originate from background noise, we can utilize our experimental values obtained (equation 2.45) to approximate the minimum (or sufficient) number of expected counts (or number of entangled photon pairs) necessary for establishing a long-distance quantum link. Also, we utilize the link loss obtained from Section 2.2.3, as we are referring to the visibility after traveling through free-space.

$$V = \frac{\left(N_{pair}10^{-\frac{\mathcal{L}}{10}}\right) - N_{BG}}{\left(N_{pair}10^{-\frac{\mathcal{L}}{10}}\right) + N_{BG}} \tag{2.72}$$

By plugging in the values $N_{BG} = 3000\,\text{Hz}$ and $\mathcal{L} = 37.7\text{dB}$, the required photon pair rate for the successful satellite-based QKD is $N_{pair} > 114\,\text{MHz}$. For the sake of simplicity, let us assume that our minimum pair rate for our EPS is 100 MHz.

Chapter 3

Polarization-Based Entangled Photon Source

We first discuss the quantum source for creating photon pairs implemented according to equation 1.9. Certain crucial components are necessary to construct a quantum source capable of producing entangled photon pairs. First of all, to make use of the quantum entanglement of photons (wave packets), they must be in a coherent state. Whatever properties of the wave packets are chosen as the quantum state, they must be able to overlap completely in order to become entangled. This requirement is met by a laser device. Lasers not only confine photons to coherent states but also have the capability to emit a substantially large amount of photons. Next, we need a system capable of creating photon

Figure 3.1: A schematic diagram showing the process of generating entangled states. We utilize nonlinear materials that can perform SPDC. The entanglement of photon pairs is achieved by building an interferometer.

pairs from the photons. While there are various ideas for the system, our approach involves performing Spontaneous Parametric Down Conversion (SPDC) using nonlinear materials. Given the availability of photon pairs, the final step would be to perfectly overlap them.

In this chapter, we present the development and testing of a polarization-based entangled photon source suitable for the long-distance QKD. All data analysis presented in this chapter is conducted using the following devices : SPAD for single photon detections of signal photons, SNSPD for single photon detections of idler photons, and a time-tagging unit for coincidence detections.

Statement of contribution

1. **Design of Entangled Photon Source :** Younseok Lee and Prof. Thomas Jennewein conceived the idea of using two beam displacers and a Sagnac loop to create an interferometer. I wrote Matlab codes for all necessary simulations presented in this chapter. I constructed the entangled photon source, incorporating my novel compensation method. Then I demonstrated the quantum entanglement experimentally.

2. **Construction of crystal oven :** I designed and constructed a crystal oven that can hold two crystals perpendicular to each other. I confirmed its performance experimentally.

3.1 Photon Pair Generation

3.1.1 Spontaneous Parametric Down Conversion

A photon, as it passes through a nonlinear medium, often undergoes interactions, leading to a process known as frequency conversion [23]. One example is when a photon subsequently splits into two correlated photons, each designated as the signal (s) and idler (i) photons, while conserving the total energy.

$$\omega_p = \omega_s + \omega_i \tag{3.1}$$

The original photon is designated as the pump (p) photon. For this interaction to occur, the phase of the atomic dipoles of the medium must match the phase of the pump field, such that the field radiated by each the dipole adds constructively in the propagation direction of the pump field [23]. However, in any material, refractive indices affect the wave vectors ($k = n\omega/c$) of the fields, leading to a wave vector mismatch ($\Delta k \neq 0$), which ultimately results in a phase mismatch. This phase shift increases with the length of the medium L.

$$\phi = \Delta k L \tag{3.2}$$

Due to this reason, a phase-matching condition is necessary to enhance the nonlinear optical processes. While encountering a phase shift is inevitable, we can exploit the fact that a phase shift of 2π is equivalent to zero phase (refer to Figure 3.2). An additional

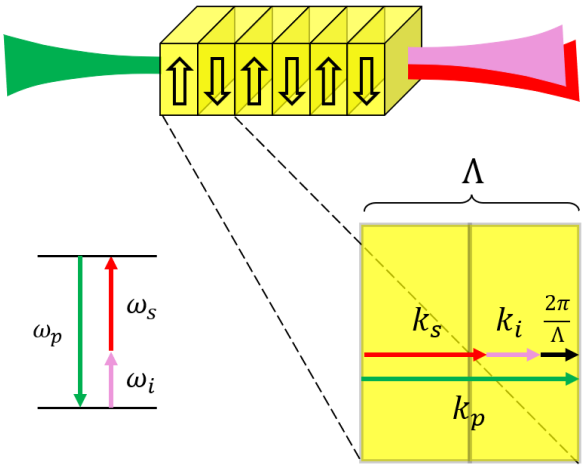

Figure 3.2: Figure illustrating the quasi-phase matching condition in the periodically poled nonlinear crystal. The poling period Λ is determined to conserve the wave number, enabling the production of signal and idler photons with wave numbers k_s and k_i from the pump photon with wave number k_p. Simultaneously, the energies must always be conserved (i.e, $\hbar\omega_p = \hbar\omega_s + \hbar\omega_i$).

wave vector of $k = 2\pi/\Lambda$ could complete the phase shift of 2π, thereby fixing the phase mismatch. This technique, known as **Quasi-Phase Matching (QPM)**, is widely used in nonlinear optical experiments. In experiments, we address the issue by periodically alternating the sign of the nonlinear susceptibility in the material, deliberately creating the additional wave vector.

$$\Delta k = k_p - k_s - k_i - \frac{2\pi}{\Lambda} \tag{3.3}$$

The poling period, Λ, is the physical length as shown in Figure 3.2. With a correct phase compensation, we could obtain $\Delta k = 0$ that would allow constructive interference over the propagation distance, effectively enabling nonlinear interactions. Using equation 3.1,

equation 3.3 becomes

$$\begin{aligned}\Delta k &= \frac{n_p\omega_p}{c} - \frac{n_s\omega_s}{c} - \frac{n_i}{c}(\omega_p - \omega_s) - \frac{2\pi}{\Lambda} \\ &= \frac{(n_p - n_i)}{c}\omega_p + \frac{(n_i - n_s)}{c}\omega_s - \frac{2\pi}{\Lambda}\end{aligned} \tag{3.4}$$

We use this equation to identify the required poling period of the material. It is worth noting that the refractive indices are wavelength and temperature dependent,

$$n \to n(\lambda, T) \tag{3.5}$$

which are usually described by Sellmeier equation which contains different coefficients for different materials. The associated bandwidths can be estimated by the first-order Taylor expansion of equation 3.3.

$$\Delta k \approx \left.\frac{\partial k_p}{\partial \omega}\right|_{\omega_p} \Delta\omega_p - \left.\frac{\partial k_s}{\partial \omega}\right|_{\omega_s} \Delta\omega_s - \left.\frac{\partial k_i}{\partial \omega}\right|_{\omega_i} \Delta\omega_s = \frac{2\pi}{L} \tag{3.6}$$

we could also write it in terms of the propagation constant, $\beta' = \partial k/\partial\omega\,|_{\omega}$. By using equation A.2, equation 3.6 can be rearranged to express the wavelength bandwidths of the signal and the idler photons.

$$\Delta\lambda_{s,i} = \frac{\lambda_{s,i}^2}{c}\left|\frac{1}{L(\beta_i' - \beta_s')} - \frac{(\beta_p' - \beta_{i,s}')}{(\beta_i' - \beta_s')}\frac{c\Delta\lambda_p}{\lambda_p^2}\right| \tag{3.7}$$

According to equation 3.7, the bandwidth decreases with increasing crystal length. When signal travels through free-space, chromatic dispersion can decohere the phases of the signal photons. To mitigate the dispersion, it is advantageous to have a narrow initial bandwidth. We purchased two identical 5% MgO-doped PPLN bulk crystals (Covesion Ltd., UK) to perform type-0 SPDC. Each is responsible for down-converting one polarization state. The birefringence of a Lithium Niobate crystal is highly temperature-dependent, which allows easy phase-matching by keeping it untilted while varying the temperature of the crystal [47]. Because the separation between signal and idler wavelengths is large, we use MgO-doped ones which allow a wider wavelength operation [2]. The detailed specifications of the purchased crystal are shown in Appendix.B. By running simulations (shown in Figure 3.3), we identified that the poling period of $\Lambda = 7.10\,\mu\text{m}$ that is provided by the

manufacturer at a temperature of 107.6 °C satisfies the condition for a pump photon at a wavelength of 523.64 nm and signal and idler photons at wavelengths of 790.8 nm and 1550 nm, respectively. When choosing the length of the crystals, we need to consider our desired photon bandwidth for the signal photons. As the length of the crystal increases,

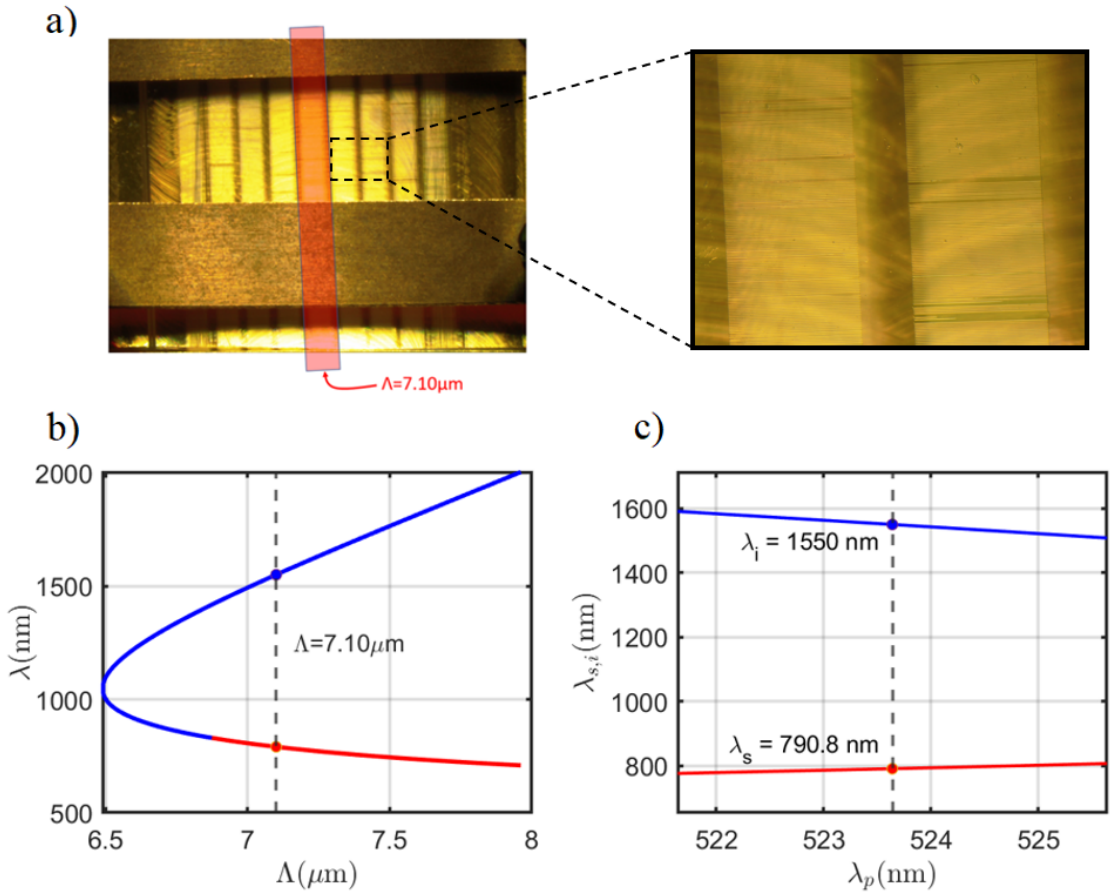

Figure 3.3: A Non-degenerate SPDC process in a periodically poled nonlinear crystal. a) Photo of the purchased PPLN crystal with nine different gratings (zoomed-in photo on its right). Only one ($\Lambda = 7.10\,\mu$m) of the gratings is considered. b) shows different wavelength outcomes from type-0 SPDC over different poling periods. c) shows the non-degenerate SPDC wavelength outcomes over different pump wavelength. The poling period is fixed to 7.10 µm.

the photon bandwidths become narrower according to equation 3.7. We aim for the photon bandwidth to be less than 1 nm to minimize chromatic dispersion effect for the free-space

channel. Maintaining low dispersion is crucial, as a highly dispersive photon field is more vulnerable to the atmospheric effects. Narrow bandwidths reduce the dispersion effects in the channel, resulting in a longer coherence time.[1] Another reason for desiring a narrow photon bandwidth is that it allows us to use a narrow bandpass filter so that any unwanted light (with a different wavelength) is easily blocked. To generate photons with such a narrow bandwidth, the crystal length needs to be at least on the order of a centimeter. The two PPLN crystals that we purchased both have a length (in the propagation direction of pump field) of 10 mm, which was a good compromise for the photon bandwidths, SPDC efficiency and commercial availability.

3.1.2 Continuous Wave

Equation 3.7 indicates that the production of photon pairs with narrow bandwidths can be achieved not only by using a long crystal length, but also by using pump photons with narrow bandwidths. This leads us to favor a CW laser, typically emitting a near single-frequency beam in commercial models (refer to Appendix A). CW lasers also offer several advantages in long-distance QKD. While timing of the pulses may be important, especially in methods like time-bin encoding, polarization encoding methods do not necessitate pulsed photons. Therefore, it is preferable to use a CW laser, since it has the

Part #	Manufacturer	Max power (stability)	λ (nm)	$\Delta\lambda$ (nm)	M^2	PM fiber coupled	User interface	Price (USD)	Final decision
FPYL-523.5-200T-LN-FCPM	Frankfurt Laser	200mW (<1%)	523.5±0.5	0.1nm	1.2	✓	RS232	13,295	✓
CL523-400	Crystalaser	200mW (<5%)	523.5±0.5	0.15nm	1.1	✓	✗	19,670	
MGL-N-523.5	CNI laser	200mW (<5%)	523.5±1.0	0.2nm	1.5	✓	RS232	9,540	

Table 3.1: List of CW lasers that sufficiently meet the majority of the requirements for the EPS.

capability of continuously producing a lot higher number of photons compared to pulsed lasers. Moreover, CW waves cause less damage to the optics than pulses, which is the

[1] A prolonged coherence time also provides the flexibility to anticipate potential temporal discrepancies on the entanglement of photons.

preferable since we need the minimum pair rate of 100 MHz (calculated from section 2.3.2) for QEYSSat mission. We searched for laser products capable of achieving near Transverse Electromagnetic Mode (TEM)00 mode at 523 nm with a power output of up to 200 mW.[2] Table 3.1 displays a list of initially selected candidate CW lasers. While all these lasers have great specifications, a CW laser from Frankfurt Laser (Germany) stood out notably for its exceptional power stability and spectral bandwidth. For our EPS, we decided to purchase this laser which produces single-frequency beam at 523.64 nm of wavelength.

3.1.3 Characterization Tests and Results

Figure 3.4 shows the spectrum of the CW laser where the actual values for the central wavelengths and the bandwidths of signal and idler photons were found to be $\lambda_p = 523.64\,\text{nm}$ and $\Delta\lambda_p = 0.0077\,\text{nm}$, respectively. These values are used in the calculations presented in the following sections. We also conducted a characterization test of the PPLN crystal we

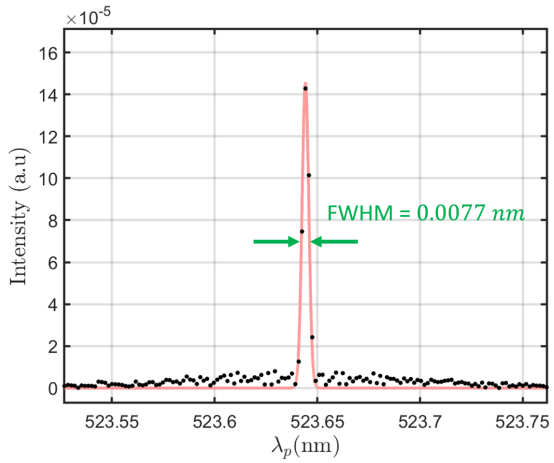

Figure 3.4: Characterization of the CW laser beam. The spectrum of the beam was analyzed using Gaussian fit. The central wavelength of the pump beam and its bandwidth are identified to be $\lambda_p = 523.64\,\text{nm}$ and $\Delta\lambda_p = 0.0077\,\text{nm}$, respectively.

purchased by measuring the central wavelengths and bandwidths of the signal and idler photons generated from SPDC while changing the temperature of the crystal by 2 °C. The wavelengths and bandwidths are calculated by fitting Gaussian profiles to the spectra obtained using a spectrometer (Teledyne Princeton Instruments, US). The results are plotted

[2]The reason for the desired power output is explained in section 3.3.7.

in Figure 3.5 The experimental results agreed with the expected wavelengths and bandwidths of the signal and idler photons, calculated using equation 3.7. were generated from the PPLN crystal.

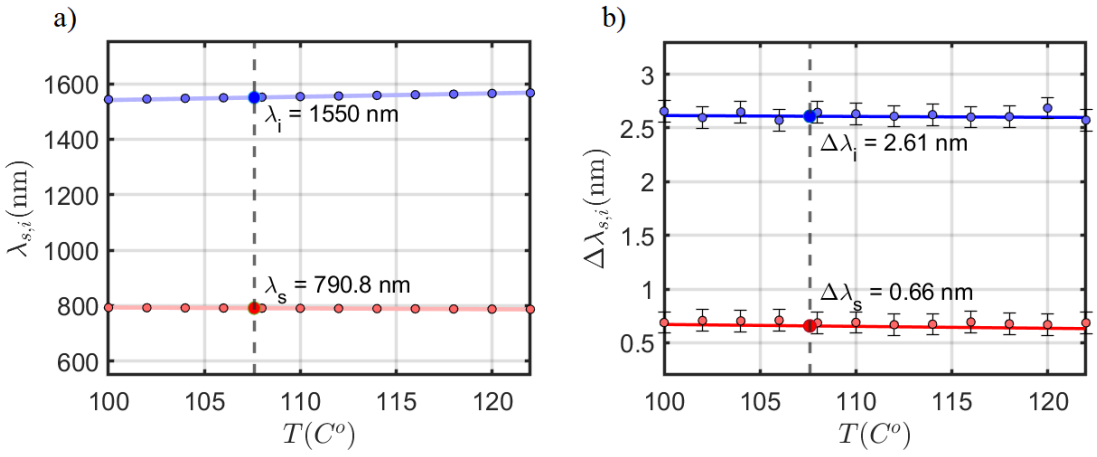

Figure 3.5: The solid lines depicted in both plots represent theoretical values, while the dots correspond to actual experimental data points. a) shows the non-degenerate SPDC wavelength outcomes over different temperature. The error bars on this plot are too small to be visible. b) shows the wavelength bandwidths that correspond to the central wavelengths shown in plot a).[3]

3.2 Photon Emission Rates

There have been many studies indicating that the photon pair rate and mode-coupling (heralding) efficiency are influenced by the degree of focusing of the pump beam into the crystal and the beam waists of the signal and the idler beams [67, 36]. We mathematically derive the emission rate of the single photons and photon pairs produced through SPDC process in a bulk crystal [16] for given beam waists. Then, we demonstrate how different beam waist combinations affect the photon emission rate and the mode-coupling efficiency.

3.2.1 Theoretical Calculations

Periodic Poling

The significance of the crystal's second-order nonlinear susceptibility, denoted as χ'', lies in its substantial impact on the rate of photon pair generation. This importance stems from its dual role : not only does it establish the quasi-phase matching condition, as shown earlier, but it also includes the nonlinear coefficient, denoted as d_{eff}, which dictates the degree of interaction enhancement derived from this condition. To incorporate the nonlinear susceptibility into the pair rate calculations, we shall express it mathematically. Note that although nonlinear susceptibility is a frequency-dependent parameter, the frequency bandwidths of the photons we are dealing with are small enough compared to their optical frequencies to assume our susceptibility to be frequency-independent. To achieve continuous enhancement in pair generation by making the quasi-phase matching condition, it is necessary to periodically alternate the sign of the nonlinear susceptibility, as depicted in Figure 3.2. Due to technical characteristics of the ferroelectrical poling process, the grating engraved on the crystal will contribute to nonlinear interaction in the form of a square wave. Thus, we apply Fourier series $F(z)$ for the square wave to describe spatial variation of the poling.

$$\chi''(\vec{r}) = 2d_{eff}F(z) = 2d_{eff}\left(\sum_{m=-\infty}^{\infty}\frac{2}{m\pi}\ sin\left(\frac{m\pi L_{coh}}{\Lambda}\right)e^{ik_m z}\right) \tag{3.8}$$

The second-order nonlinear susceptibility $\chi''(\vec{r})$ depends on the nonlinear coefficient $2d_{eff}$[4], the crystal's poling period Λ and the coherence length of the wave L_{coh}. The wave number

[4]The factor of 2 comes from the fact that we are using equations D.1 as the expressions for the electric fields, such that the nonlinear polarization is defined as $P^n = 2^{n-1}d_{eff} : E_1E_2\cdots E_n$. The nonlinear coefficient should be just d_{eff} if one considers $\vec{E} = \frac{1}{2}\left[\vec{E}^{(+)} + \vec{E}^{(-)}\right]$ instead of $\vec{E} = \vec{E}^{(+)} + \vec{E}^{(-)}$.

$k_m = 2\pi m/\Lambda$ takes the role of achieving the desired QPM condition. Assuming that the crystal's poling period exactly matches half of our desired coherence length ($L_{coh} = \Lambda/2$), the sine term becomes $sin\,(\pi m/2)$ such that only the odd terms survive.

$$\chi''(\vec{r}) = 2d_{eff}\left(\frac{4}{\pi}\sum_{m=0}^{\infty}\frac{(-1)^m}{(2m+1)}e^{ik_m z}\right) \tag{3.9}$$

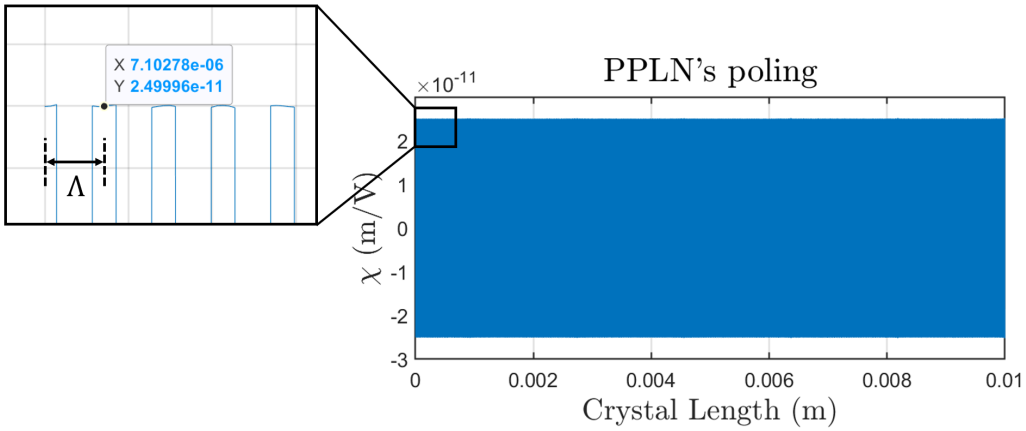

Figure 3.6: The graph represents the result of summation over 10,000 iterations for the nonlinear susceptibility. We use the following values provided by the company (Covesion Ltd.) from which our PPLN crystals were purchased : $\Lambda = 7.10\,\mu m$, $d_{eff} = 25\,pm/V$.

Interaction Hamiltonian

We consider a coherent paraxial gaussian wave, as we use the pump beam at 523.64 nm that is provided by a single frequency Diode-Pumped Solid-State (DPSS) laser. We assume that it is propagating along the z axis, with its beam waist positioned at the origin. The beam comes out of a single mode fiber (i.e, near TEM00 mode), and is focused at the PPLN crystals by a focal lens. We also assume that the PPLN crystals are optically uniform media as they are positioned in a way that the beam propagates along the extraordinary axis of the crystals. We first simplify equation D.14 by defining a q parameter, $q = 2i(z + z_R)/k$.

The negative single frequency (creation) electric field can be written as

$$E_j^{(-)}(\vec{r},t) = -i\sqrt{\frac{\hbar\omega_j}{2\epsilon_0 n_j^2 L_c}}\sqrt{\frac{2}{\pi W_j^2}}\frac{W_j^2}{q_j^*}\hat{a}_j^\dagger e^{-\frac{\rho^2}{q_j^*}-ik_j z+i\omega_j t}\hat{e}_j \qquad j = s \text{ (signal)}, i \text{ (idler)} \tag{3.10}$$

where $\hat{e}$ is a linear polarization unit vector. Note that the constant factor $1/iz_R$ at the front was taken out and absorbed by the volume constant for convenience, and the fresnel factor, $1/n$ is included. We are interested in the parametric interaction inside the crystal, so we use the crystal length as the normalization constant for the length term, $1/\sqrt{L_c}$. Lastly, we are considering an electric field for all values of k_s and k_i, in order to calculate for the total single mode pair emission rates. This expression is going to be used for the signal and the idler beam.

On the other side, the pump beam isn't the outcome of the SPDC process, but rather produced by the laser. Also, we are considering the case where the pump photons are destroyed to produce signal and idler photons. Hence, we use the positive frequency version of equation 3.10. We assume a strong pump field created by the laser which allows us to treat it classically. Thus, E_0 could be rewritten using the classical pump power expression $P = cn_p\epsilon_0 |E_0|^2 A/2$ with the cross-sectional area of the beam $A = \pi W_p^2/2$ and $E_0^{(+)} = E_0/2$.

$$E^{(+)}(\vec{r},t) = i\sqrt{\frac{P}{2\epsilon_0 n_p c}}\sqrt{\frac{2}{\pi W_p^2}}\frac{W_p^2}{q_p}e^{-\frac{\rho^2}{q_p}+ikz-i\omega_p t}\hat{e}_p \tag{3.11}$$

The pump power can be expressed in terms of the pump photons

$$P = \sum_{k_p} N_p \hbar\omega_p J^2(\omega_p)\frac{c}{n_p L_c} \tag{3.12}$$

where N_p is simply the number of pump photons, and $\int J^2(\omega_p)d\omega = 1$ is the spectral function. Note that $\sqrt{N_p}J(\omega_p)$ would correspond to the annihilation operator $\hat{a}$. In practical scenarios, the pump field encompasses several frequency modes, necessitating the presence of summation in the equation. However, the interaction length (crystal length) L_c greatly exceeds the wavelength of the pump beam, allowing us to turn the discrete summations into integrals.

$$\sum_{k_p} \approx \frac{L_c}{2\pi}\int dk_p = \frac{n_p L_c}{2\pi c}\int d\omega_p \tag{3.13}$$

$$E^{(+)}(\vec{r},t) = \int d\omega_p i \sqrt{\frac{N_p \hbar \omega_p}{4\pi\epsilon_0 n_p c}} \sqrt{\frac{2}{\pi W_p^2}} \frac{W_p^2}{q_p} J(\omega_p) e^{-\frac{\rho^2}{q_p} + ikz - i\omega_p t} \hat{e}_p \tag{3.14}$$

The time dependent Hamiltonian operator, $\hat{H}_{spdc}(t)$, describes the parametric interaction between the pump field (p) and the signal (s) and idler (s) fields.

$$\hat{H}_{spdc}(t) = \int \hat{E}_p^{(+)} \hat{P}_{s,i}''^{(-)} d^3\vec{r} = \int 2\epsilon_0 \chi''(\vec{r}) \hat{E}_p^{(+)}(\vec{r},t) \hat{E}_s^{(-)}(\vec{r},t) \hat{E}_i^{(-)}(\vec{r},t)\ d^3\vec{r} \tag{3.15}$$

The factor of 2 is from the consideration of permutation symmetry of the second order nonlinear term. By putting 3.10, 3.11 and 3.8 into 3.15, we obtain the following expression

$$\hat{H}_{spdc}(t) = 2d_{eff} \frac{4}{\pi} \sum_{m=0}^{\infty} \frac{(-1)^m}{2m+1} \int d\omega_p \left(-i \sqrt{\frac{2N_p \hbar^3 \omega_p \omega_s \omega_i}{\pi^4 \epsilon_0 n_p n_s^2 n_i^2 c L_c^2}} \right) J(\omega_p) \hat{a}_s^\dagger \hat{a}_i^\dagger e^{-i\Delta\omega t} \Phi(\Delta k) + h.c \tag{3.16}$$

which includes the spatial overlap function $\Phi(\Delta k)$,

$$\Phi(\Delta k) = \int_0^\infty \rho\ d\rho \int_0^{2\pi} d\theta \int_{-\frac{L_c}{2}}^{\frac{L_c}{2}} dz\ \frac{W_p W_s W_i}{q_p q_s^* q_i^*} e^{-\rho^2 \left(\frac{1}{q_p} + \frac{1}{q_s^*} + \frac{1}{q_i^*} \right) + i\Delta k z} \tag{3.17}$$

where $\Delta k = k_p - k_s - k_i - 2\pi(2m+1)/\Lambda$.

Spatial Overlap

By integrating equation 3.17 over the transverse (ρ, θ) plane, the spatial overlap function becomes

$$\Phi(\Delta k) = \int_{-\frac{L_c}{2}}^{\frac{L_c}{2}} dz\ \frac{\pi W_p W_s W_i}{q_s^* q_i^* + q_p q_s^* + q_p q_i^*}\ e^{i\Delta k z} \tag{3.18}$$

The depth of focus is two times the Rayleigh length ($2z_R = kW^2$) which is twice the Rayleigh range, and the beam outside the Rayleigh range is said to be "out of focus" [87]. We define two dimensionless parameters, $l = 2z/L_c$ and $1/\xi = kW^2/L_c$. In particular, ξ is known as the focal parameter which indicates the strength of beam focusing. For instance, $\xi \gg 1$ means the beam is strongly focused, and $\xi \ll 1$ means the beam is weakly focused relative to the crystal length (co-linear beams). Then the q parameter becomes

$q_j = \frac{L_c}{k_j}\left(\frac{1}{\xi_j} + il\right)$. By replacing the q parameters, the denominator of the function may be written as

$$q_s q_i + q_p^* q_s + q_p^* q_i = \frac{L_c^2}{k_p k_s k_i}\left[\left(\frac{k_p}{\xi_s\xi_i} + \frac{k_s}{\xi_p\xi_i} + \frac{k_i}{\xi_p\xi_s}\right) - il\left(\frac{k_p - \delta k}{\xi_p} + \frac{k_s - \delta k}{\xi_s} + \frac{k_i - \delta k}{\xi_i}\right) - l^2\delta k\right] \tag{3.19}$$

where $\delta k = k_p - k_s - k_i$.
To further simplify the expression, we define

$$\begin{aligned} A_\pm =& 1 + \frac{k_s\xi_s}{k_p\xi_p} \pm \frac{k_i\xi_i}{k_p\xi_p} \\ B_\pm =& \left(1 - \frac{\delta k}{k_p}\right)\left(1 + \frac{(k_s + \delta k)\xi_p}{(k_p - \delta k)\xi_s} \pm \frac{(k_i + \delta k)\xi_p}{(k_p - \delta k)\xi_i}\right) \end{aligned} \tag{3.20}$$

such that

$$\frac{q_s^* q_i^* + q_p q_s^* + q_p q_i^*}{W_p W_s W_i} = \sqrt{\frac{\xi_p\xi_s\xi_i}{k_p k_s k_i}} L_c \left[\frac{k_p}{\xi_s\xi_i} A_+ - il\frac{k_p}{\xi_p} B_+ - l^2\delta k\right] \tag{3.21}$$

We now introduce an aggregate focal parameter, $\xi_\pm \equiv (\xi_s\xi_i/\xi_p)\, B_\pm/A_\pm$, that contains all three focal parameters for the pump, signal and idler modes. Then the inverse of equation 3.21 can be written as follows.

$$\frac{W_p W_s W_i}{q_s^* q_i^* + q_p q_s^* + q_p q_i^*} = \sqrt{\frac{k_s k_i}{k_p}} \frac{1}{\sqrt{L_c}} \frac{1}{\sqrt{A_+ B_+}} \frac{\sqrt{\xi_+}}{(1 - il\xi_+ - C_+\xi_+^2 l^2)} \tag{3.22}$$

where $C_\pm = \frac{\delta k \xi_p^2 A_\pm}{k_p \xi_s \xi_i B_\pm^2}$. The motivation behind all the derivations that have been shown so far was to enable the study of each term in the final expression separately. Also, note that the negative versions (A_-, B_-, C_- and ξ_-) will appear in the calculation of the single photon emission rate in the next section.

$$\Phi(\Delta k) = \frac{\pi}{2}\sqrt{\frac{k_s k_i}{k_p}}\sqrt{\frac{L_c}{A_+ B_+}} \int_{-1}^{1} dl\ \frac{\sqrt{\xi_+}}{(1 - il\xi_+ - C_+\xi_+^2 l^2)} e^{i\frac{\phi}{2}l} \tag{3.23}$$

Note that the differential was transformed as $dz \to (L_c/2)\, dl$, and so did the limits of the integral. In the case where $\xi_+ \ll 1$, the photon fields can be approximated as plane waves, and the spatial overlap function becomes proportional to the standard phase matching function.

$$\Phi(\Delta k) \propto sinc\left(\frac{\Delta k L}{2}\right) \tag{3.24}$$

If ξ_+ is not small enough,

Photon Pair Emission Rate

Suppose the nonlinear SPDC process was successful in the crystal. Using E.3, the resulted state from an initial state $|i\rangle = |1_p, 0_s, 0_i\rangle$ (generated by the pump laser) can be expressed as

$$|\psi_{spdc}(t)\rangle = -\frac{i}{\hbar}\int_0^t dt\ \hat{H}_{spdc}(t)\,|i\rangle \tag{3.25}$$

To calculate the photon pair emission rate, we first need to determine the probability of generating one of the paired photons under the assumption that the other photon of the paired photon has been generated. The Fermi's Golden Rule (refer to Appendix E) allows one to determine the transition rate if the density of energy states ρ is regarded as constant due to the narrow range of the energy. Here, we won't make such an approximation, but rather accounts for the frequency dependency, keeping the density of states inside the integral in equation E.7. The probability of finding the idler mode k_i in the final state $|f\rangle = |0_p, 1_s, 1_i\rangle = \hat{a}_p\hat{a}_s^\dagger\hat{a}_i^\dagger\,|1_p, 0_s, 0_i\rangle$ for each signal mode k_s can be determined by the probability density function of SPDC summed over all possible idler modes.

$$P_{k_i}(k_s) = \sum_{k_i} |\langle f\,|\,\psi_{spdc}(t)\rangle|^2 \tag{3.26}$$

Then we integrate it again over all values of the signal mode k_s to find the total photon pair probability P_c.

$$P_{pair} = \sum_{k_s} P_{k_i}(k_s) \tag{3.27}$$

Consequently, the pair probability can be considered as a coincident photodetection probability (assuming no detection loss). Analogous to the approximation made for the pump mode earlier, the signal and idler wavelengths are also much shorter than the interaction length (or the bandwidths are narrow enough that the coherence lengths are much longer than the interaction length) such that we can apply the same approximation as follows.

$$\sum_{k_s}\sum_{k_i} \approx \left(\frac{L_c}{2\pi}\right)^2 \int dk_s dk_i = \frac{n_s n_i L_c^2}{4\pi^2 c^2}\int d\omega_s d\omega_i \tag{3.28}$$

Then the coincidence probability from the SPDC is

$$P_{pair} = \left(\frac{4}{\pi}\sum_{m=0}^{\infty}\frac{(-1)^m}{2m+1}\right)^2 \left(\frac{32 d_{eff}^2 \pi^2 N_p \hbar L}{\epsilon_0 n_p^2 \lambda_s^2 \lambda_i^2}\right) \frac{1}{A_+ B_+} \int d\omega_s d\omega_i J^2(\omega_p) \times \left| \int_{-1}^{1} dl \; \frac{\sqrt{\xi_+}}{(1 - il\xi_+ - C_+ \xi_+^2 l^2)} e^{i\frac{\phi}{2}l} \right|^2 \tag{3.29}$$

If the frequency bandwidths of the photons are much smaller than the optical frequencies, we could further assume that the followings are constant [16].

$$A_\pm, \; B_\pm, \; \xi_p, \; \xi_s, \; \xi_i \tag{3.30}$$

This relates to the approximation that the frequency dependence of the pair rate is essentially determined by the pump spectral function, $J(\omega_p)$, and the phase mismatch δk. In order to work with the two dominant factors, one could transform the differentials into a favorable form. First, by putting equation 3.2 into 3.1 (including the Fourier term), we obtain an expression for the phase shift.

$$\phi = \left[\omega_s(n_p - n_s) + \omega_i(n_p - n_i) - \frac{2\pi(2m+1)}{\Lambda}\right]\frac{L_c}{c} \tag{3.31}$$

The phase shift can be distorted by the presence of various frequency components within the signal and idler photon bandwidths. The further these frequency components stray from their nominal frequencies, the more severe the phase distortion happens. As illustrated in Figure 3.7, we can assume the wave mismatch to have a linear frequency dependence with a group index $n' = n - \lambda dn/d\lambda$.

$$\delta k \approx \frac{n'}{c}\delta\omega \tag{3.32}$$

By this assumption, we could approximate the phase mismatch as follows.

$$\phi \approx \phi_0 + \left[\delta\omega_s\left(n_p' - n_s'\right) + \delta\omega_i\left(n_p' - n_i'\right)\right]\frac{L_c}{c} \tag{3.33}$$

The fourier term essentially contributes to worsening the phase mismatch ϕ_0 at nominal frequency. Hence, we consider this contribution as part of the deviation of the frequency components. We could let a Jacobian matrix

$$J = \begin{bmatrix} \frac{d\phi}{d\omega_s} & \frac{d\phi}{d\omega_i} \\ \frac{d\omega_p}{d\omega_s} & \frac{d\omega_p}{d\omega_i} \end{bmatrix} = \begin{bmatrix} \frac{L_c}{c}(n_p' - n_s') & \frac{L_c}{c}(n_p' - n_i') \\ 1 & 1 \end{bmatrix}$$

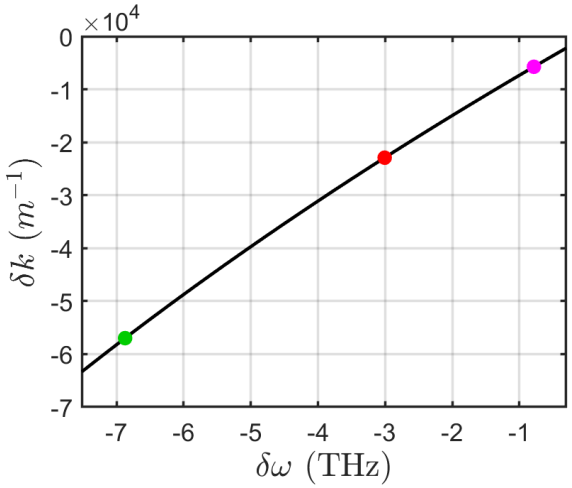

Figure 3.7: Linear frequency dependency in the wave mismatch. Depending on the crystal's sellmeier equation, this could not always be the case. In our case with PPLN crystal.

to transform $d\omega_s d\omega_i \rightarrow d\phi d\omega_p$.

$$d\omega_s d\omega_i = \frac{1}{|J|}\, d\phi d\omega_p = \frac{c}{L_c \left|n_i' - n_s'\right|} d\phi d\omega_p \tag{3.34}$$

We can now replace the differentials with what we have derived.

$$P_{pair} = \frac{32 d_{eff}^2 \pi^2 N_p \hbar c}{\epsilon_0 n_p^2 \left|n_i' - n_s'\right| \lambda_s^2 \lambda_i^2} \frac{1}{A_+ B_+} \int d\phi \left| \int_{-1}^{1} dl \, \frac{\sqrt{\xi_+}}{(1 - il\xi_+ - C_+ \xi_+^2 l^2)} e^{i\frac{\phi}{2}l} \right|^2 \tag{3.35}$$

As $\int J^2(\omega_p) d\omega = 1$, the pump spectral function disappears. We can also integrate the phase term as it becomes a function $\left(\int e^{\frac{i\phi}{2}(l-l')} d\phi = 4\pi\delta(l - l')\right)$. Finally, by replacing N_p with $P\lambda_p / 2\pi c\hbar$, we obtain the expression for the photon pair emission rate R_{pair} (in Hz).

$$R_{pair} = \frac{64\pi^2 d_{eff}^2 \lambda_p}{\epsilon_0 n_p^2 \left|n_i' - n_s'\right| \lambda_s^2 \lambda_i^2} \frac{P\xi}{A_+ B_+} \int_{-1}^{1} dl \, \frac{1}{(1 - il\xi_+ - C_+ \xi_+^2 l^2)\,(1 + il\xi_+ - C_+ \xi_+^2 l^2)} \tag{3.36}$$

Single Photon Emission Rate

When we refer to the photon pair emission rate, we calculate the pair probability of collecting pairs at a specific spatial mode, typically the fundamental mode (since collecting higher-order spatial modes could result in collecting the lower modes as well). However, one could derive the single photon emission rate (signal photon for instance) by summing the pair probability density function over all spatial modes for the **idler** photon. Then equation 3.15 becomes

$$\hat{H}_{spdc}(t) = \int 2\epsilon_0 \chi''(\vec{r}) \hat{E}_p^{(+)}(\vec{r},t) \hat{E}_s^{(-)}(\vec{r},t) E_{i:n,l}^{(-)}(\vec{r},t)\ d^3\vec{r} \tag{3.37}$$

where the idler photon field is expressed by the Laguerre Gauss modes.

$$E_{i:n,l}^{(-)}(\vec{r},t) = -i\sqrt{\frac{\hbar\omega_i}{\pi\epsilon_0 n_i^2 L_c}} \left(\frac{W_i}{q_i}\right)^{l+1} \left(\frac{q_i^*}{q_i}\right)^n L_n^l \left(\frac{2W_i^2\rho^2}{|q_i|^2}\right) e^{-\frac{\rho^2}{q_i} + ik_i z + il\phi} \hat{e}_i \tag{3.38}$$

L_n^l is the associated Laguerre polynomial, and $\rho = \sqrt{x^2+y^2}$ and $\tan\phi = x/y$. As we have been considering paraxial Gaussian beam, one could assume the idler mode to be azimuthally symmetric ($l = 0$). With such an assumption, equation 3.17 becomes

$$\Phi_n(\Delta k) = \int_0^\infty \rho\ d\rho \int_0^{2\pi} d\theta \int_{-\frac{L_c}{2}}^{\frac{L_c}{2}} dz\ \frac{W_p W_s W_i}{q_p q_s^* q_i^*} \left(\frac{q_i}{q_i^*}\right)^n L_n\left(\frac{2W_i^2\rho^2}{|q_i|^2}\right) e^{-\rho^2\left(\frac{1}{q_p}+\frac{1}{q_s^*}+\frac{1}{q_i^*}\right)+i\Delta k z} \tag{3.39}$$

with a simplified version of the Laguerre polynomial, $L_n(x) = \sum_{m=0}^n (-1)^m \frac{n!}{(n-m)!m!m!} x^m$. With a bit of work, the overlap function becomes

$$\Phi_n(\Delta k) = \int_{-\frac{L_c}{2}}^{\frac{L_c}{2}} dz\ \frac{\pi W_p W_s W_i}{q_s^* q_i^* + q_p q_s^* + q_p q_i^*} \left(\frac{q_s^* q_i + q_p q_i - q_p q_s^*}{q_s^* q_i^* + q_p q_i^* + q_p q_s^*}\right)^n\ e^{i\Delta k z} \tag{3.40}$$

The probability density function $P_{n,spdc}(t)$ would have the same expression as 3.35, except the spatial overlap $\Phi^2(\Delta k)$ is now $\Phi_n^2(\Delta k)$. In case of $n = l = 0$, we see that equation 3.40 gives us back the spatial overlap of the fundamental Gaussian mode (equation 3.18). Referring to the previous derivation, the expression for the single photon rate in terms of

the focal parameters would be as follows.

$$R_s = \frac{64\pi^2 d_{eff}^2 \lambda_p}{\epsilon_0 n_p^2 \left|n_i' - n_s'\right| \lambda_s^2 \lambda_i^2} \frac{P\xi_+}{A_+ B_+} \int_{-1}^{1} dl \; \frac{1}{\left(1 - il\xi_+ - C_+\xi_+^2 l^2\right)\left(1 + il\xi_+ - C_+\xi_+^2 l^2\right)} \times \sum_{n=0}^{\infty} \left[\frac{A_- B_-}{A_+ B_+} \frac{\left(1 - il\xi_- - C_-\xi_-^2 l^2\right)}{\left(1 - il\xi_+ - C_+\xi_+^2 l^2\right)} \frac{\left(1 + il\xi_- - C_-\xi_-^2 l^2\right)}{\left(1 + il\xi_+ - C_+\xi_+^2 l^2\right)} \right]^n \tag{3.41}$$

Again, with $n = l = 0$, equation 3.41 becomes equivalent to equation 3.36. This implies that if one uses a Single Mode Fiber (SMF) to collect the signal or the idler photons, the single photon emission rate is going to be exactly the photon pair emission rate.

Theoretical Analysis and Discussions

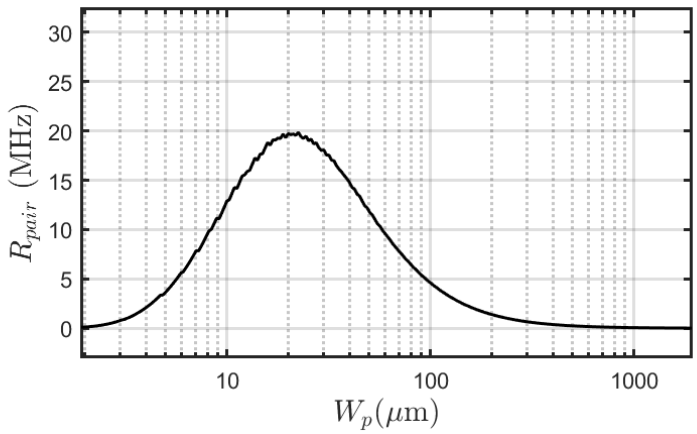

Figure 3.8: Photon pair emission rate R_{pair} as a function of the beam radius of the pump W_p.

We examine how the focusing of the beam affects the photon emission rate by increasing the aggregate focal parameter ξ_+. As we aim to increase the aggregate focal parameter

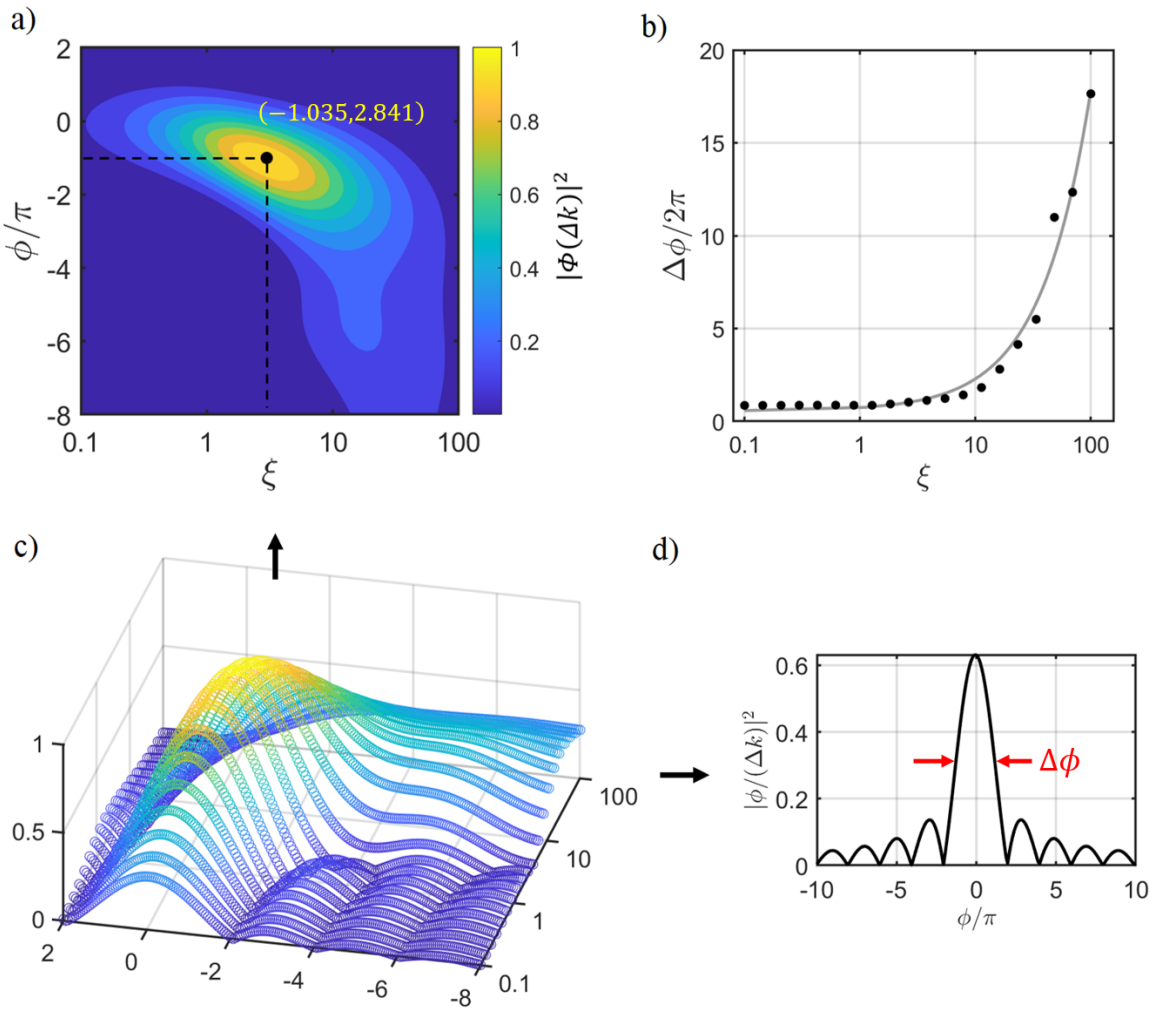

Figure 3.9: (a) A contour plot of the normalized joint spectral function (brightness) for different phases per half cycle ϕ/π and focal parameters ξ. The brightness is maximized at $(\phi/\pi, \xi) = (-1.035, 2.841)$. (b) The phase bandwidth $\Delta\phi$ plotted for each ξ. The phase bandwidth for each ξ is obtained by numerically calculating the FWHM of $|\phi(\Delta k)|^2$ from (a). (c) A 3-d plot of (a). (d) One layer of (c) which could correspond to the sinc function with a FWHM of $\Delta\phi$ in co-linear case.

rather than individual focal parameters (ξ_p, ξ_s, ξ_i), we preferably decrease the pump beam radius (implying increase in the ξ_p) and let the signal and idler beam radii adjust accordingly such that ξ_+ increases. Using equation 3.36, we obtain the plot shown in Figure 3.8. Interestingly, there exists a maximum pair rate. In our case, at 1.0 mW of pump power, the maximum pair rate can go as high as $R_{pair} \approx 20$ MHz at $W_p = 21.8\mu m$, while $W_s = 19.2\mu m$ and $W_i = 22.2\mu m$ are determined to be the optimal values for the signal and idler beam radii, respectively. To find the reason, we investigate the spatial overlap $\Phi(\Delta k)$. As evident from equation 3.24, the photon pair rate is proportional to the joint spectral function $|\phi(\Delta k)|^2 = sinc^2(\phi/2)$ under the approximation of $\xi_+ \ll 1$. Hence, it would be interesting to examine the spatial overlap from equation 3.23 without such an approximation. In Figure 3.9a, a contour plot illustrating the normalized joint spectral function with respect to the phase and the focal parameter is presented. Interestingly, there exists a maximum focal condition $(\phi/\pi, \xi) = (-1.035, 2.841)$, which is also confirmed by several papers [16, 23, 22]. By carefully selecting the focal parameters of pump, signal and idler

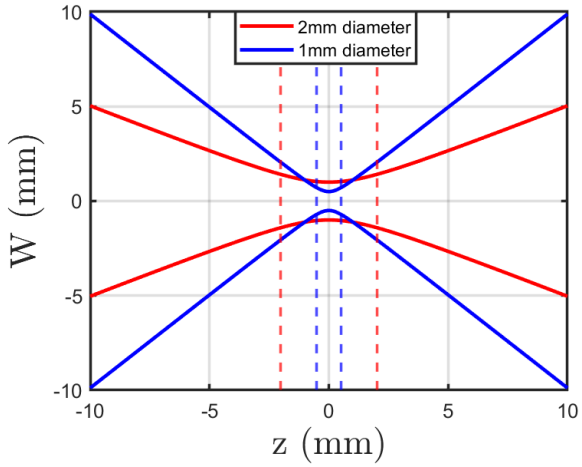

Figure 3.10: Graphical representation of the focusing of a Gaussian beam. The beam being focused to the sizes of 1 mm (blue) and 2 mm (red) of beam waist is shown as an example, under the assumption of the same focal condition. The dotted lines represent the Rayleigh lengths of the beams. Initially (assuming the beams are focused from either left or right), the blue beam is larger than the red beam. However, within the Rayleigh length region of the blue beam, it becomes narrower than the red beam.

modes, one could optimize the emission rate of the SPDC process. In the meantime, if we plot the phase bandwidth $\Delta\phi$, determined numerically from Figure3.9a through the calculation of the FWHM of $|\phi(\Delta k)|^2$ for each ξ_+, we see the phase bandwidth starting to

exponentially broaden from around $\xi \approx 10$ (a strong focusing condition where the Rayleigh length is 10 times shorter than the crystal length). This indicates a pronounced deviation from an optimal QPM condition. There exists an optimal aggregate focal parameter, and once we surpass this optimal parameter, the pair rate begins to decrease. The reason for the increase in the phase bandwidth with strong focusing is that the focusing causes the light to become non-colinear [28, 16]. According to the descriptions of the paraxial Gaussian beam (equations (i) and (iv) shown in Figure D.1), the beam radius at a far distance ($z \gg z_R$) can be approximated as $W(z) \sim W_0(z/z_R) = \theta_0 z$, where θ_0 is the beam divergence angle. Thus, the angle can be expressed as

$$\theta_0 = \frac{\lambda}{\pi W_0} \tag{3.42}$$

Figure 3.10 compares the cases where a Gaussian beam is focused to sizes of different sizes of beam waist as an example. In accordance with the profound symmetry of nature, a beam strongly focused at a large angle diverges by the same large angle. Thus, in identical focal condition, a beam initially larger in size than another beam will become smaller within its Rayleigh length, despite its initial size being larger than the narrower beam. Stronger focusing leads to a smaller beam waist, which in turn results in greater divergence. This is precisely the reason for the significant mismatch of QPM that occurs with a high aggregate focal parameter. Suppose we choose a very weak focal condition $\xi_+ \ll 1$, such as it is similar to the case where $C_+ \approx 0$ (near-degenerate SPDC where $\delta k/k_{p,s,i}$ are typically small). Then by letting $x = \xi l$ and $dx = \xi dl$, the integral part of the 3.36 can be simplified as follow

$$\begin{aligned}\left|\int_{-1}^{1} dl \int_{-1}^{1} dl' \frac{\sqrt{\xi}}{(1 - il\xi)} \frac{\sqrt{\xi}}{(1 + il'\xi)}\right| &= \int_{-1}^{1} \frac{\xi}{(1 + l^2\xi^2)}\, dl \\ &= 2 \arctan(\xi)\end{aligned}$$

where we used the delta function . Using the approximation, equation 3.36 becomes

$$R_{pair} \approx P \frac{128\pi^2 d_{eff}^2 \lambda_p}{\epsilon_0 n_p^2 \left|n_i' - n_s'\right| \lambda_s^2 \lambda_i^2} \frac{\arctan(\xi)}{A_+ B_+} \tag{3.43}$$

The single photon emission rate from the signal mode can also be simplified.

$$R_s \approx P \frac{128\pi^2 d_{eff}^2 \lambda_p \hbar}{\epsilon_0 n_p^2 \left|n_i' - n_s'\right| \lambda_s^2 \lambda_i^2} \frac{\arctan\left(\frac{C_{2,s}}{C_{1,s}} \xi_s\right)}{C_{1,s} C_{2,s}} \tag{3.44}$$

where

$$C_{1,s} = 2\sqrt{\left(1 + \frac{k_s}{k_p}\frac{\xi_s}{\xi_p}\right)\frac{k_i}{k_p}}$$

$$C_{2,s} = 2\left(1 - \frac{\delta k}{k_p}\right)\sqrt{\left(1 + \frac{k_s + \delta k}{k_p - \delta k}\frac{\xi_p}{\xi_s}\right)\frac{k_i + \delta k}{k_p - \delta k}}$$

Equations 3.43 and 3.45 highlight that both the single and pair rates increase with shorter wavelengths of the signal and idler photons or with longer wavelength of the pump photon. They are also linearly proportional to the pump power. Strong overall focusing increases the rate under the approximation of $C_+ \approx 0$. Using equations 3.43 and 3.45, one can also determine the pair-to-single ratios (mode-coupling efficiencies), denoted as $\mu_{s,i} \equiv R_{pair}/R_{i,s}$. The mode-coupling efficiencies indicate how likely it is to receive the signal/idler photon mode, when receiving anidler/signal photon. The overall mode-coupling efficiency (multiplicative average) is $\mu_{pair} \equiv R_{pair}/\sqrt{R_s R_i}$. One can determine the upper bounds of single and pair rates by optimizing certain factors in equations 3.43 and 3.45. Firstly, the inverse of the tangent in both equations 3.43 and 3.45 asymptotically approaches $\pi/2$. Next, to optimize the spatial overlap by the beam waists, we focus on maximizing $1/\sqrt{A_+ B_+}$. We can simplify equation 3.20 by introducing new parameters to separate the focal parameters from the constants.

$$X_j = \frac{k_j}{k_p}\sqrt{\frac{1 + \delta k/k_j}{1 - \delta k/k_p}} \quad , \quad r_j = \frac{\xi_j}{\xi_p}\sqrt{\frac{1 - \delta k/k_p}{1 + \delta k/k_j}} \qquad j = \text{ signal}(s),\ \text{idler}(i) \tag{3.45}$$

Using equation 3.45, equation 3.20 can be written as

$$A_+ B_+ = \left(1 - \frac{\delta k}{k_p}\right)(1 + X_s r_s + X_i r_i)\left(1 + \frac{X_s}{r_s} + \frac{X_i}{r_i}\right) \tag{3.46}$$

Figure 3.11 shows that the term is maximized when $r_s = r_i = 1$. Hence, in the case of $\delta k/k_j \ll 1$ (near-degenerate SPDC), we have $A_+ B_+ \approx 4$. Hence, we can write upper bounds for the pair rate and the single rate as follow.

$$R_{pair} \leq P\frac{32\pi^3 d_{eff}^2 \lambda_p}{\epsilon_0 n_p^2 \left|n_i' - n_s'\right| \lambda_s^2 \lambda_i^2}$$

$$R_s \leq P\frac{128\pi^3 d_{eff}^2 \lambda_p}{3\epsilon_0 n_p^2 \left|n_i' - n_s'\right| \lambda_s^2 \lambda_i^2}$$

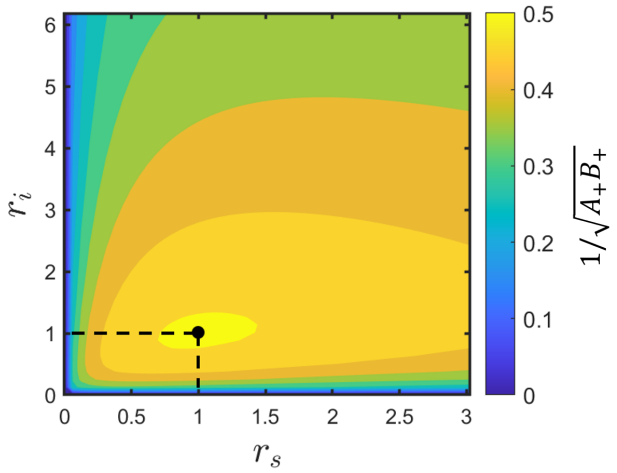

Figure 3.11: Contour plots of the term, $1/\sqrt{A_+B_+}$. It shows that it is maximized at $r_s = r_i = 1$.

Setting aside the upper bound for now, we revisit equations 3.43 and 3.45. Upon examination, we can see that both the pair and single rates depend on the aggregate focal parameter ξ_+. Hence, we explore various combinations of ξ_p, ξ_s and ξ_i by subsituting them into the mentioned equations. By doing so, we find the optimal focusing condition for a given ξ_p [5], that maximizes the R_{pair}. Subsequently, we compile these optimal conditions, and plot them as a function of the pump beam's radius, W_p, which is inversely proportional to ξ_p. Figure 3.12 shows the numerical results of the aforementioned analysis (we are only interested in the solid lines at the moment). It is evident from Figure 3.12a that with increasing ξ_+ (strong overall focusing), the pair rate also increases. This characteristic can be understood visually in Figure 3.13. When the beam is strongly focused, we essentially confine a given number of pump photons into a narrower space for interaction. Consequently, spatial overlap is naturally enhanced, and so is the pair rate. However, the overall mode-coupling efficiency μ_{pair} decreases as a trade-off. This decrease is due to the disturbance (or mismatch) of the QPM condition caused by the shift in phase under different focal conditions, such that the enhancement in the pair rate is slower compared to the enhancement in the single rate. The overall mode-coupling efficiency seems to approach 71% according to the theory. This roughly agrees with the theoretical upper bounds that we have derived (equation 3.47), in which the upper bound of the overall mode-coupling

[5] We chose to analyze with respect to ξ_p for no particular reason. The analysis can also be performed with respect to the other two focal parameters, ξ_s and ξ_i.

efficiency is $(R_{pair}/R_s)_{max} = 75\%$. In fact, the 75% of efficiency was the degenerate SPDC case, where the disturbance of QPM condition would be minimal. However, once again, we

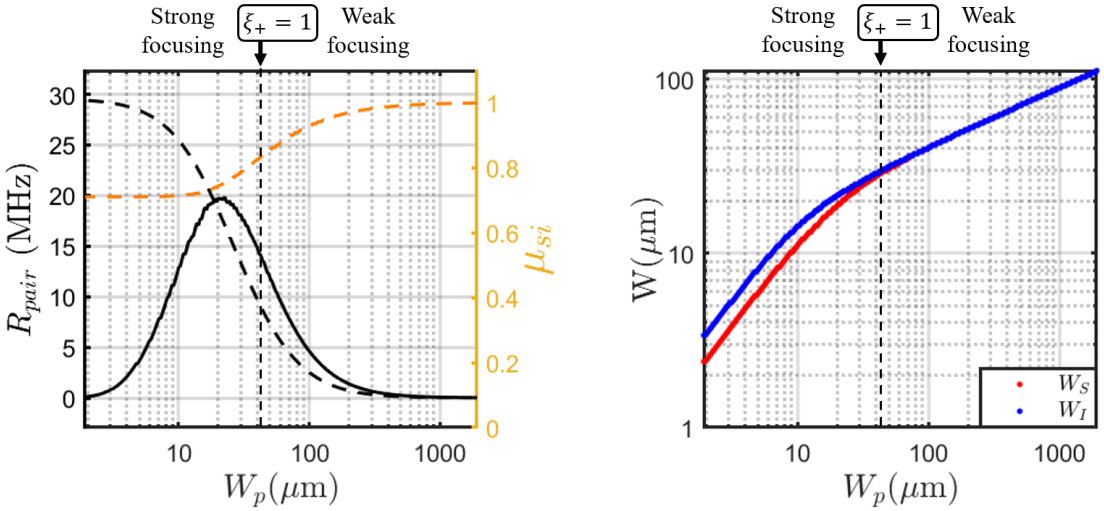

Figure 3.12: (a) Optimal photon pair emission rate (black dashed curve) and the corresponding overall mode-coupling efficiency (orange dashed curve) over different pump beam radii at 1.0 mW of pump power. The black dashed curve is the pair rate calculated without the approximation of $C_+ \approx 0$. The black solid curve is the same curve from Figure 3.8. (b) The optimal focal parameters (translated into the beam radius) of the pump, signal and idler modes that gave the results in (a).

utilize SMFs, meaning we are not concerned about the mode-coupling efficiency. When deriving equations 3.36 and 3.41, we mentioned that we made the approximation of $C_+ \approx 0$. In the case of a highly non-degenerate SPDC, with a strong focal condition, such an approximation may no longer be valid, potentially leading to worse outcomes than expected. This also applies to degenerate SPDC, although occurring in a distant future upon increasing ξ compared to the non-degenerate case. In our case, where we have the QPM condition of 523.64 nm $\rightarrow$ 790.8 nm + 1550 nm, this invalidation happens quite early, and the pair rate does not actually approach $\pi/2$, but degrades. Therefore, the asymptotic behavior shown in Figure3.12a is, in reality, not perfectly accurate, especially in our case of non-degenerate SPDC. In our case, equation 3.43 is valid with an uncertainty of $\pm 20\%$ from $\xi_+ > 0.1$. This implication also helps us understand Figure 3.12b. As depicted, in a strong focusing regime, the optimal beam radius values for the signal and idler beams exhibit peculiar behavior due to sudden phase broadening caused by strong focusing. The

analysis showed that with a right focal condition, $R_{pair} = 100\,\text{MHz}$ can be achieved even with 5 mW of pump power.

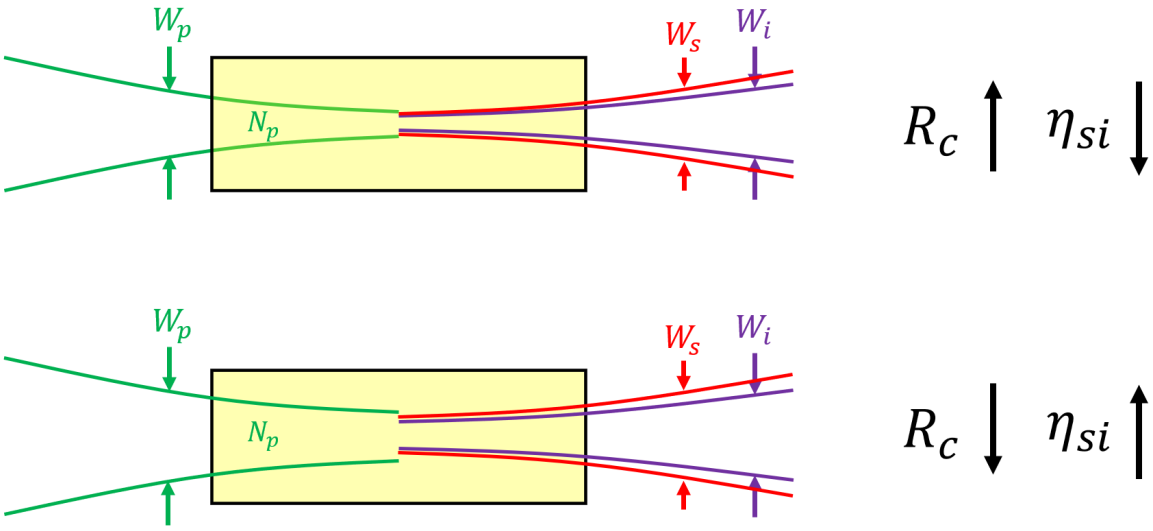

Figure 3.13: Visualizations of three paraxial Gaussian beams with radii W_p, W_s, and W_i inside the nonlinear crystal. Strong focusing of the beams increases the photon pair emission rate while the mode-coupling efficiency drops. Weak focusing of the beams results in the opposite phenomenon.

3.2.2 Measurements and Results

Experiments are conducted to verify the variation in the pair rate R_{pair} under different focal conditions as indicated by equation 3.36. Figure 3.14 shows the design and the experimental setup to verify the theoretically derived photon emission rates for a given beam waist combination. The CW laser provides the pump beam at 523.64 nm wavelength through a SMF. The pump beam is collimated by an aspheric lens (8 mm), and is linearly polarized before being focused to the PPLN crystal by a plano-convex lens. In the actual experimental setup, the linear polarizer was replaced with a zeroth-order HWP and a Polarizing Beamsplitter (PBS). The two schemes are equivalent nonetheless (Linear Polarizer (LP)=HWP+PBS). Additionally, an additional HWP* was placed between the pump-side lens and the PPLN crystal in order to verify the consistency in the pair emission rates for different polarization states; horizontal (H) and vertical (V). A 10 mm PPLN crystal is placed at where the pump beam is focused, and is temperature-controlled to achieve the QPM condition for 523.64 nm $\rightarrow$ 790.8 nm1550 nm. The signal beam passes through a dichroic mirror, while the idler beam reflects off the dichroic mirror. Each beam is collimated by a plano-convex lens. After ensuring that only the signal and idler photons are received using two bandpass filters (for each), both beams are then focused into the SMFs using aspheric lenses (11 mm for the signal and 15 mm for the idler). The SMF on the signal side sends signal photons to the SPAD, while the SMF on the idler side sends idler photons to the SNSPD. As explained in section 1.3.3, the two detectors send out electric signals to the time-tagging unit whenever they receive a photon. The time-tagging (coincidence) window is set to $\Delta t = 1.5$ ns, while a time delay is applied to adjust the arrival times of the electric signals from the two detectors. Once raw single and coincidence counts are measured, the actual single and coincidence counts are obtained through the dark subtraction method using equations 1.31 and 1.32. It is important to note that in a real experiment, one considers not only the mode-coupling efficiencies (μ_s, μ_i) but also the detection efficiencies (η_s, η_i) for the signal and idler photons.[6] With the assumption that photons in all spatial mode are detected, the theoretical expectations are the followings :

$$\begin{aligned} \text{Single count rate (signal)} &: \quad N_s = \eta_s R_s = \frac{\eta_s}{\mu_s} R_{pair} \\ \text{Single count rate (idler)} &: \quad N_i = \eta_i R_i = \frac{\eta_i}{\mu_i} R_{pair} \\ \text{Coincidence rate} &: \quad N_c = \eta_s \eta_i R_{pair} \end{aligned} \tag{3.47}$$

[6] Detection efficiency is quite often also called heralding efficiency. One must not be confused with the mode-coupling and detection efficiencies.

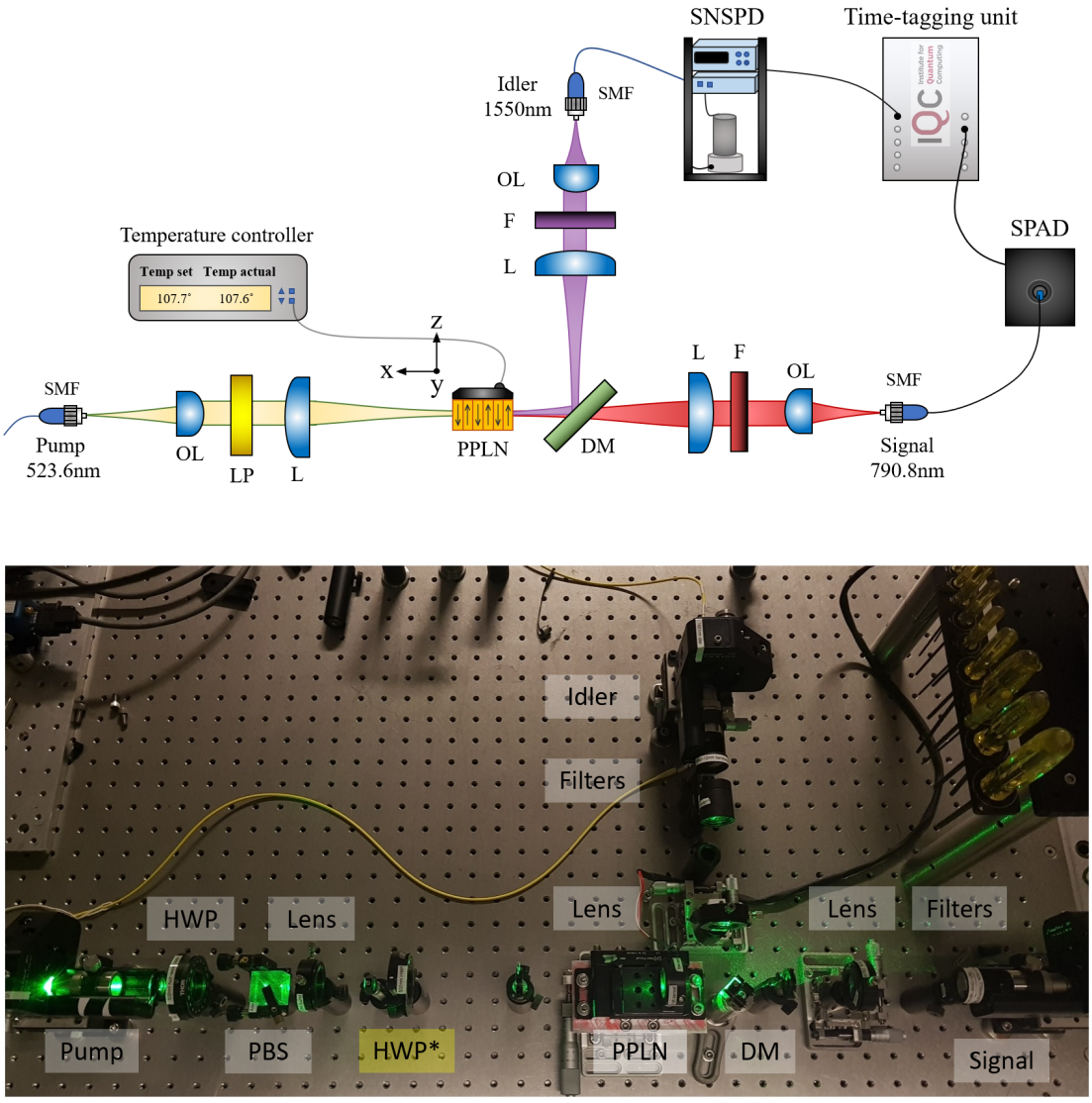

Figure 3.14: Experimental design for the optimization test (top figure) and the actual experimental setup (bottom figure). Optical components are : Objective lens (OL), Half waveplate (HWP/HWP*), Polarizing beamsplitter (PBS), Linear polarizer (LP), Lens (L), Periodically poled Lithium Niobate crystal (PPLN), Dichroic mirror (DM), Bandpass filter (F), Single-mode fiber (SMF).

As we use SMFs to collect the signal and idler photons, we can assume $\mu_s = \mu_i = 1$ such that $R_{pair} = R_s = R_i$. The detection efficiencies must includes transmittivity of all optical components (including the detectors' efficiencies) along the optical path. These values are predicted based on the specifications of the optical components provided by the manufacturers. The detection efficiencies are expected to be $\eta_s = 47.45\%$ for the signal beam and $\eta_i = 39.37\%$ for the idler beam. We first demonstrate whether strong focusing leads to an increase in the pair rate. The lens focal lengths for the signal and idler beam are fixed at $f_s = 15\,\text{cm}$ and $f_i = 10\,\text{cm}$, respectively. Then we vary the lens focal length for the pump beam to see the changes in the pair rates. Figure 3.15 shows the photon

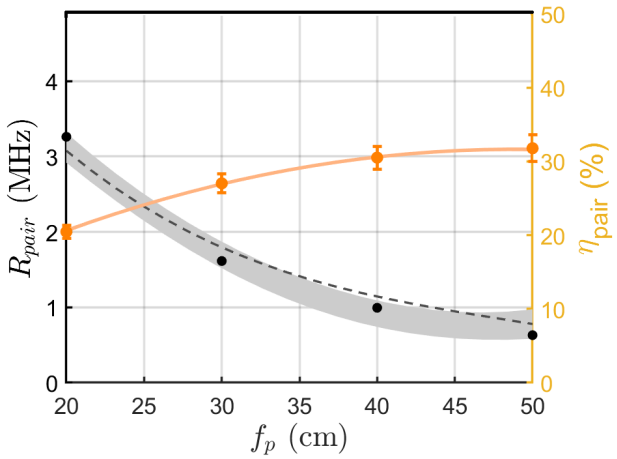

Figure 3.15: Photon pair emission rates (left axis) and their corresponding pair mode-coupling efficiencies (right axis) across different lens focal lengths for the pump beam with 1.0 mW of power. Background noises and the detection efficiencies are considered. Both errors are calculated by applying Poissonian statistics (the error bars of the R_{pair} were too small to be visible). Both shaded regions represent the 95% confidence interval of the fitted curves. The dashed curve is the theoretical curve of the photon pair emission rate.

pair emission rates and the mode-coupling efficiencies calculated from the experimentally obtained single and coincidence counts. We can see that the theoretically model (dashed curve) and the experimentally obtained pair rates are in good agreement with each other. The overall heralding efficiency η_{pair} is expected to remain constant, but the graph shows that efficiency drops as the pump lens focal length increases. This is suspected to be due to saturation of the detector and time-tagger. We also verify the linear relationship between the power of the pump and the pair rate, as implied in equation 3.36. The lens focal length for the pump beam is fixed at $f_p = 50\,\text{cm}$, while those for the signal and idler beams are

varied to see the changes in the pair rates. As shown in Figure 3.17, variations in the focal lengths of the pump, signal and idler lenses translate into the resulting spot sizes at the crystal. When determining the spot sizes, we use the paraxial approximation (Appendix D), which is also applied in our theoretical model. We perform measurements of the

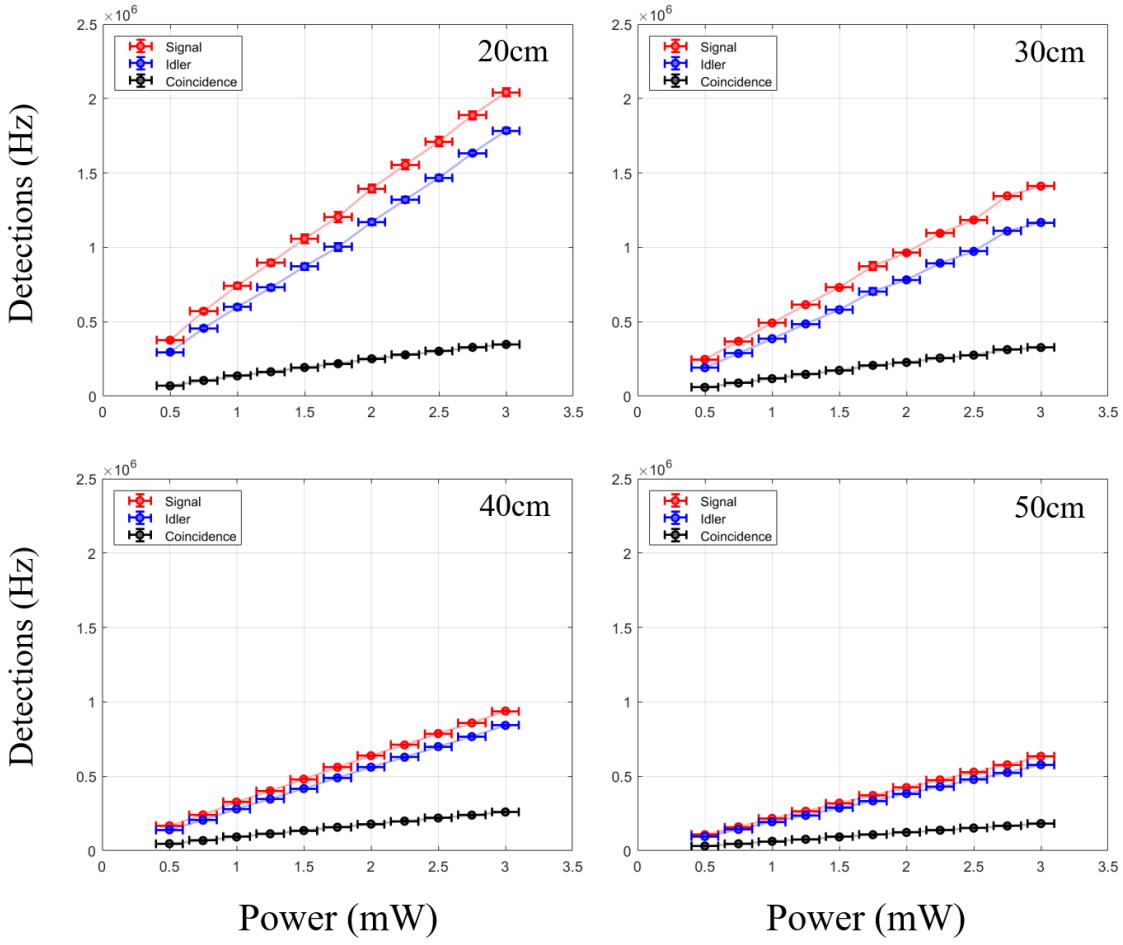

Figure 3.16: Single and coincidence rates over different pump power for each measurement with different pump focal lengths; 20 cm, 30 cm, 40 cm, 50 cm.

single counts of the signal and idler photons, as well as the coincidence counts, for each lens combination corresponding to a specific aggregate focal condition. Each aggregate focal condition is measured multiple times to average the results. This overall process is repeated for verifying various lens combinations (see Figure 3.18). The experimentally obtained data are plotted as a contour in Figure 3.18. The theoretical expectations well

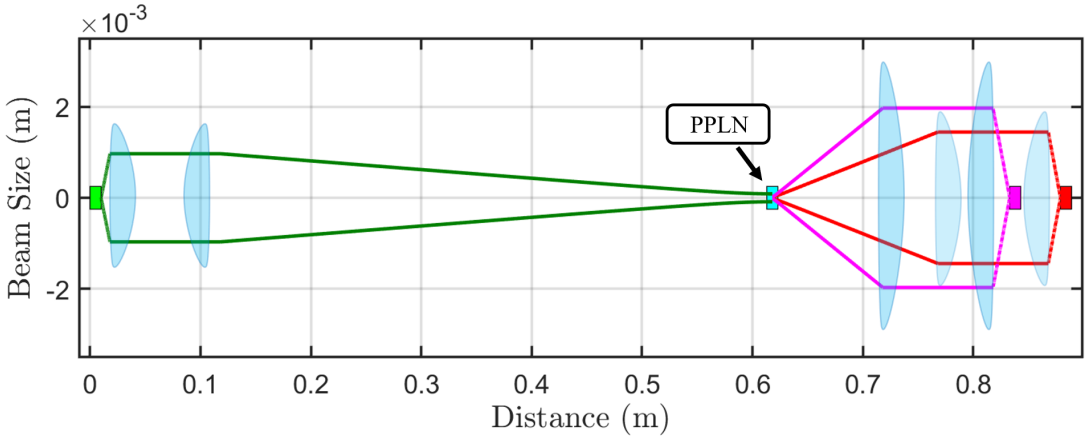

Figure 3.17: Ray diagrams showing the pump (green), signal (red) and idler (purple) beams. The SMFs are drawn as boxes on both ends of the graph. The PPLN crystal is also shown at the focal points of the three beams.

agreed with with actual data trend observed through the experiment (data is shown in Appendix N). Both theory and experimental results from Figure 3.18 tell us that what the pair rate relies on is not the individual focal parameters for the pump, signal and idler modes, but rather the aggregate focal parameter. If the ξ_p is determined by the pump beam radius, then we need to find ξ_s and ξ_i that can optimize ξ along with it.

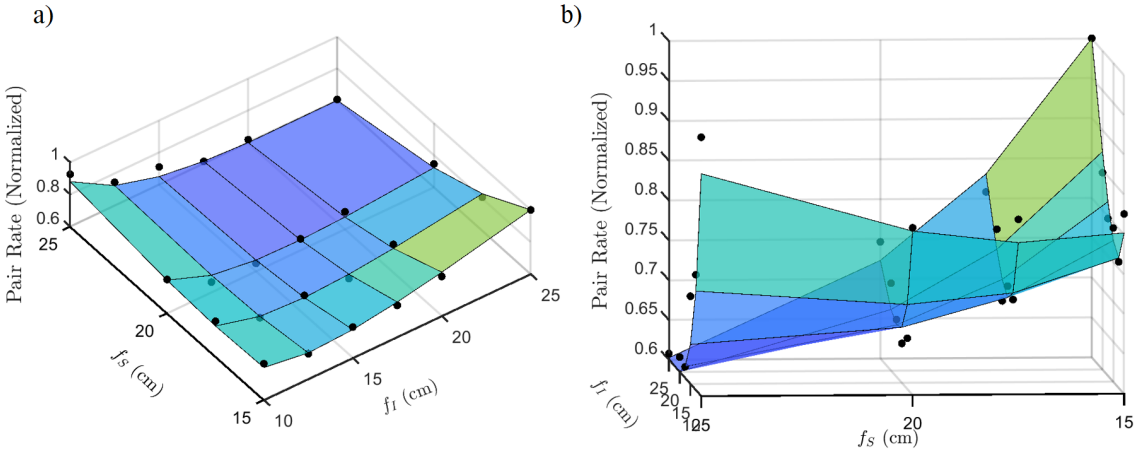

Figure 3.18: Contour plots of the photon pair rates with different signal and idler lens combinations. (a) seen from above. (b) seen from side. The meshes are the theoretical expectations, and the dots are the experimentally obtained data. The vertical axis corresponds to the normalized pair rate, and the horizontal axes are the lenses' focal lengths. Focal lengths for the signal beam : 15 cm, 17.5 cm, 20 cm, 25 cm. Focal lengths for the idler beam : 10 cm, 12.5 cm, 15 cm, 17.5 cm, 20 cm, 25 cm. Pump focal length was fixed to 50 cm. In (b), pair rates for different pump focal lengths are shown : 20 cm, 30 cm, 40 cm, 50 cm

3.3 Entangled Photon Source

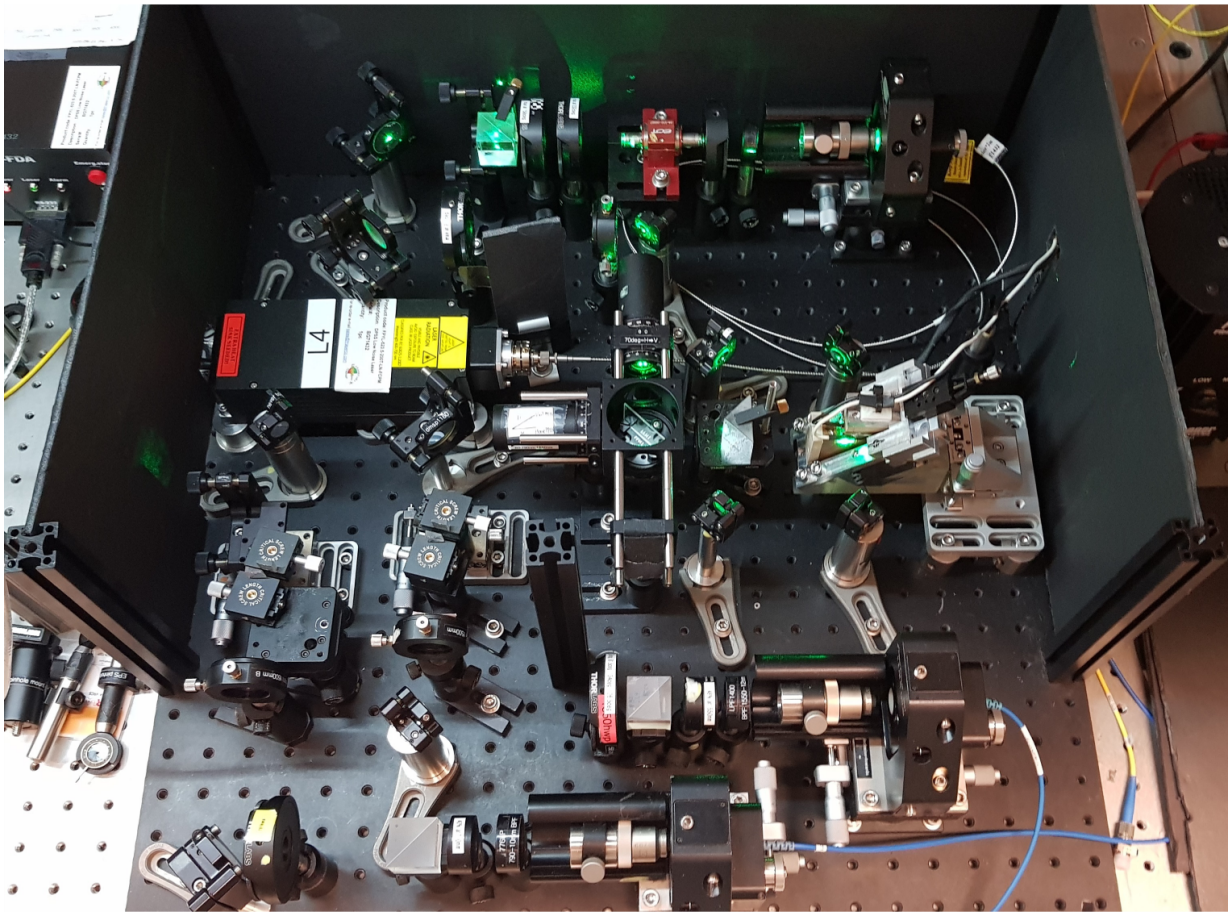

Figure 3.19: The EPS setup (Completed in January 2024).

3.3.1 Hybrid Interferometer

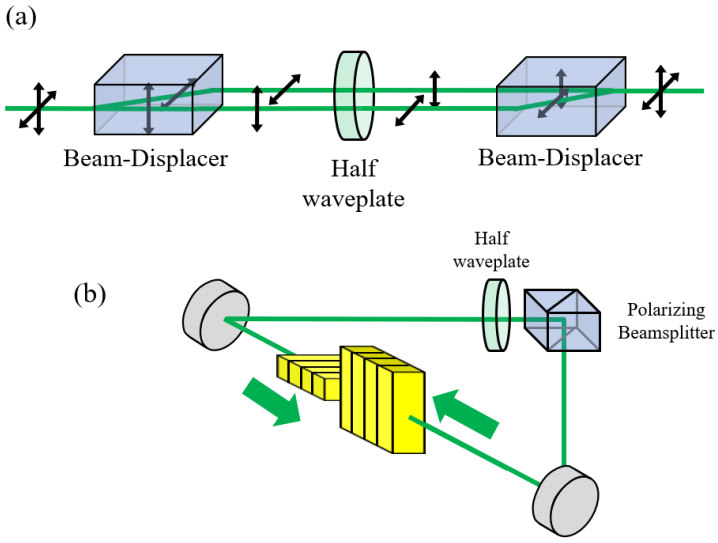

Figure 3.20: a) Interferometer using two beam displacers and a half waveplate. b) Sagnac loop with two crystals placed in the middle. The arrows indicate the propagation directions of the pump beam that is separated from the polarizing beamsplitter.

The most crucial process of entanglement is the perfect merging of two down-converted photon beams. The "**perfect merging of two beams**" means an impeccable alignment that takes into account all natural aspects, including spatial overlap, temporal overlap, wavelength overlap and phase overlap. Since we have the type-0 SPDC process, we consider signal(s)-idler(i) photon pairs with the same polarization. The Bell state for such a case is written as follows[7].

$$|\text{Bell}\rangle = \frac{1}{\sqrt{2}}\left(|V_s V_i\rangle + e^{i(\phi_r+\Delta\phi_r)}\,|H_s H_i\rangle\right) \tag{3.48}$$

The overall relative phase between the $|VV\rangle$ and the $|HH\rangle$ states can be represented as a combination of the relative phase resulting from the path difference (denoted as ϕ_r) and the relative phase variation induced by temperature fluctuation (denoted as $\Delta\phi_r$). The relative phase variation is essentially a component of the relative phase resulting from the path difference, given that we are addressing how temperature fluctuation contributes

[7]One could favorably have the phase term beside either one of the pair states.

to the additional path difference. However, the purpose of distinguishing between the two phases is simply to examine them separately in this chapter. The relative phase should ideally be zero in order to have each pair state have the same probability of being obtained (i.e, perfect merging of two beams). We utilize a Mach-Zehnder interferometer type, an optical setup employing two optical components to divide and recombine a beam of light. While a typical Mach-Zehnder interferometer uses two beam splitters [80, 58], we specifically opt for a Mach-Zehnder interferometer employing two beam displacers capable of splitting and recombining two orthogonally polarized beams (refer to Figure 3.20a) [93, 65]. One additional condition to note is that a HWP must be inserted between the two beam displacers in order to have two identical path lengths. Having a HWP in the middle allows the beam that originally traveled straight through and the displaced light to switch roles (refer to Figure 3.21).

We argue that this scheme is more favorable than typical ones, not only due to the simplification of the alignment procedure[8], but primarily because employing two identical beam displacers could be interpreted as incorporating the **Sagnac loop** using two separate optical components instead of a single optical component. The Sagnac loop offers the advantage of a self-compensating effect [46] (which will be explained shortly). However, due to the typical use of only one optical component (polarizing beamsplitter) [44], as shown in Figure 3.20b, there are current technological limitations for three different waves (pump, signal and idler) to efficiently pass through and reflect off this single optical component. On the other hand, two beam displacers, despite being two optical components, are equivalent to the Sagnac type as they separate the beam in parallel when the beam enters them perpendicular to their surfaces, ensuring identical beam path lengths. Additionally, we place a dichroic mirror between the two beam displacers. This arrangement ensures that when the pump beam split by the first beam displacer passes through their respective PPLN crystals, only the down-converted signal and idler photons pass through the dichroic mirror and are recombined at the second beam displacer. Hence, this scheme allows for the effective transmissions of all three waves by applying separate coatings corresponding to the wavelengths of the beams passing through the two beam displacers [65]. The main benefit of having the Sagnac loop is its self-compensating effect. Starting with self-compensation for ϕ_r, if the beams travelling through the Sagnac loop do not undergo a wavelength change through processes like SPDC, the difference in the length of the two paths would be zero, resulting in ϕ_r being zero as well[9]. Of course this is an oversimplified situation, as there

[8]The alignment procedure becomes simple when two beams propagate in parallel with each other. If the two beams separated by the first beam displacer are not perfectly recombined at the second beam displacer, we know that the alignment is not perfect.

[9]Conversely, a Mach-Zehnder interferometer with two beam splitters would introduce a comparably

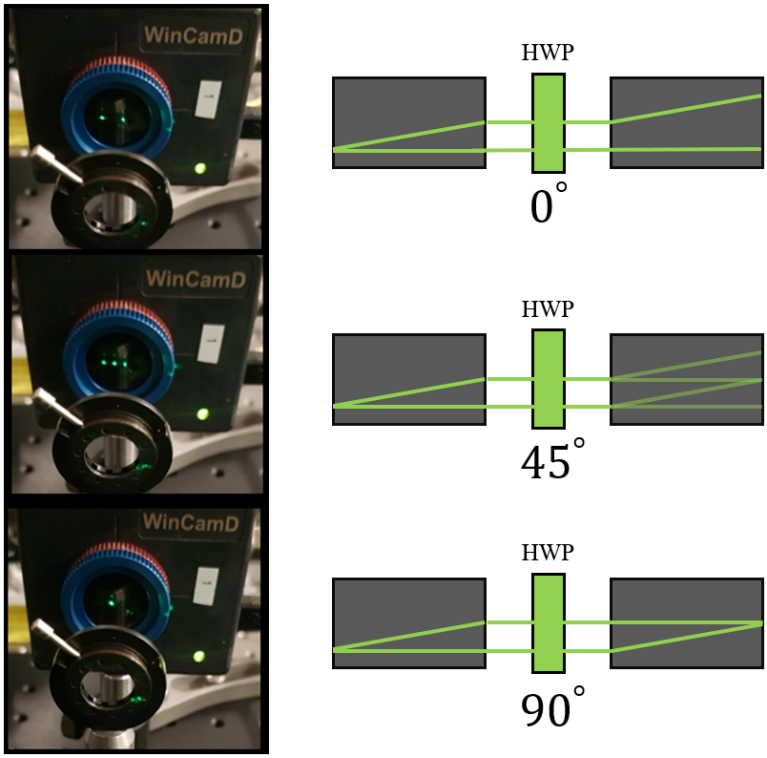

Figure 3.21: Images and diagrams demonstrating how the rotation angle of the HWP alters the displacement of the beam path. Three different cases with different polarization angles (with respect to the fast axis of the waveplate) are shown. The actual rotation angles of the HWP is half of the polarization angles.

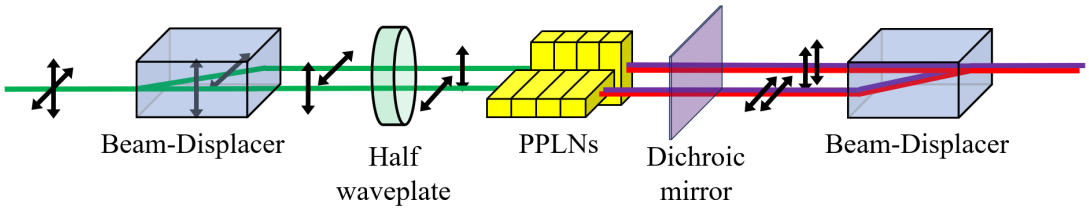

Figure 3.22: Interferometer using the beam displacer scheme. The split pump beam (green) passes through PPLN crystals and is down converted into signal (red) and idler (purple) beams, which are recombined at the second beam displacer.

will be a path difference when the pump beam is converted into the signal and idler beam with different wavelengths during their travel. Nevertheless, it remains true that Sagnac loop provides a clearer understanding of the phase between the two recombined beams, and this is further discussed in the following section. Moving on to self-compensation for $\Delta\phi_r$, this phase considers a non-vacuum environment where any thermal fluctuations may occur. In fact as explained in the earlier section, our PPLN crystals are heated by an oven, undeniably indicating the presence of thermal fluctuations. For each of the separated beam paths (denoted with subscripts, CW (clock-wise) and CCW (counter clock-wise), as it is equivalent to the Sagnac loop), the phase is expressed as follows.

$$\begin{aligned}\Delta\phi_{CW} &= \delta\phi_e(\lambda_p, T) + \delta\phi_o(\lambda_s, T) + \delta\phi_o(\lambda_i, T) \\ \Delta\phi_{CCW} &= \delta\phi_o(\lambda_p, T) + \delta\phi_e(\lambda_s, T) + \delta\phi_e(\lambda_i, T)\end{aligned} \tag{3.49}$$

Each term can be written as

$$\delta\phi = \sum_j \frac{2\pi L_j}{\lambda}\left(\frac{\partial n_j}{\partial T} + n_j\alpha\right)\Delta T \tag{3.50}$$

where we consider the phase shifts introduced by all the transmissive optical components (each indexed with j) within the Sagnac loop, each with a length of L_j. The thermo-optic coefficients $\partial n_j/\partial T$ and the thermal expansion coefficient $\alpha_{e,o}$ are normally provided by the manufacturer (See Appendix. B for the information)[10]. Using equation 3.49, the relative phase from temperature fluctuations is

$$\begin{aligned}\Delta\phi_r &= \Delta\phi_{CW} - \Delta\phi_{CCW} \\ &= \delta\phi_r(\lambda_p, T) - \delta\phi_r(\lambda_s, T) - \delta\phi_r(\lambda_i, T)\end{aligned} \tag{3.51}$$

where $\delta\phi_r = \delta\phi_e - \delta\phi_o$. If the three phase terms in equation 3.51 are all added together, compensation by other external factors would be required. However, with the polarization flip using the HWP (one of the crucial aspects that make this process equivalent to the Sagnac loop), one of the terms among the three can be subtracted. When the SPDC process occurs in the PPLN crystal, the beam is greatly influenced by the properties of the crystal. To ensure that two separated beams propagate in a more similar environment, we employ additional Sagnac Loop (refer to Figure 3.20). Aligning the two PPLN crystals

large amount of uncertainty in the lengths of the two separated paths that the beam takes within the interferometer.

[10]The first and the second terms inside the bracket in equation 3.50 correspond to the changes in the refractive index and the material length, respectively.

perpendicular to each other at the center of the loop almost eliminates phase differences caused by each crystal. This is because both beams from opposite directions would gain both ordinary and extraordinary phases by going through the two crystals. The thermo-optic coefficient for the effective extraordinary ray is derived from the formula of the effective refractive index 3.56.

$$\frac{\partial n_{eff}}{\partial T} = \frac{n_o \dfrac{\partial n_e}{\partial T} + n_e \dfrac{\partial n_o}{\partial T}}{\sqrt{n_o^2 \sin^2\theta_{eff} + n_e^2 \cos^2\theta_{eff}}} + 2n_o n_e \frac{n_o \dfrac{\partial n_o}{\partial T} \sin^2\theta_{eff} + n_e \dfrac{\partial n_e}{\partial T} \cos^2\theta_{eff}}{\left(n_o^2 \sin^2\theta_{eff} + n_e^2 \cos^2\theta_{eff}\right)^{3/2}} \tag{3.52}$$

We make the assumption that the phases introduced by the half waveplate and the dichroic mirror are negligible in comparison to those induced by the beam displacers, due to their much smaller thicknesses. Each phase term in equation 3.51 is calculated to be $\delta\phi_r(\lambda_p, T) = 6.22\pi$, $\delta\phi_r(\lambda_s, T) = 4.09\pi$ and $\delta\phi_r(\lambda_i, T) = 2.08\pi$. Hence, the relative phase is $\Delta\phi_r = 0.052\pi$, ensuring sufficient phase stability. However, no self-compensation effect would

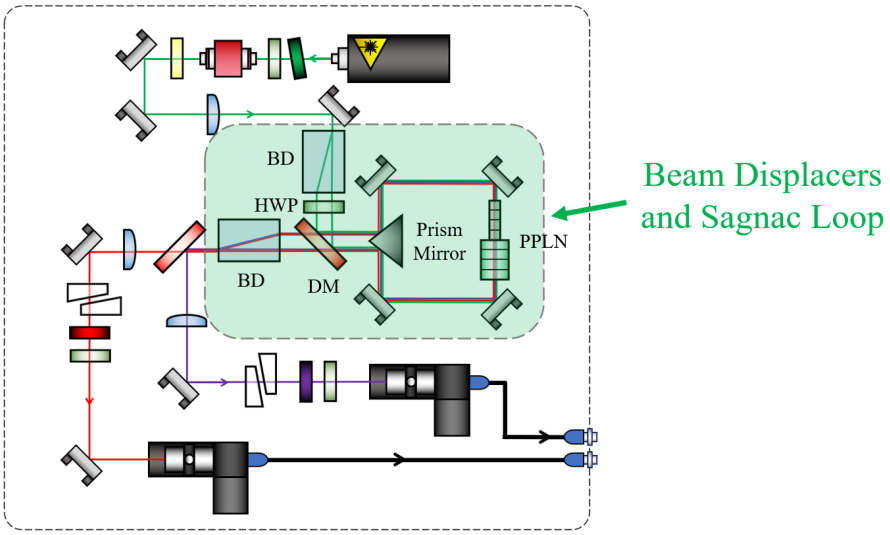

Figure 3.23: A diagram illustrating the integration of othe two beam displacers (BD) and a Sagnac loop concept in the setup. The highlighted green area includes the beam displacers and a Sagnac loop. A dichroic mirror (DM) is placed after the HWP to allow the pump beam to enter the Sagnac loop. A prism mirror further split the pump beam to create the Sagnac loop. The signal and idler photons that are generated from the PPLN crystals exit the Sagnac loop, pass through the dichroic mirror, and merge at the second beam displacer.

introduce a phase shift of $\Delta\phi_r = 12.39\pi$. As a result, while self-compensation may not

be entirely perfect, it certainly helps quantum states remain usable for a long enough period of time. Given that we will be providing high pump power, it would be a good idea to disperse the returning pump beam to minimize the damage to the optics. If we solely apply the beam-displacing interferometer scheme, the returning pump beam that has not undergone down-conversion will be recombined at the first beam displacer. However, one remarkable feature is that, with the presence of additional Sagnac loop, the beam disperses upon returning to the first beam displacer, as illustrated in Figure 3.21. If we use this hybrid interferometer, which combines the beam-displacing interferometer with the Sagnac loop, entanglement can be achieved much more efficiently. The loop can be situated anywhere along the beam path between the half waveplate and the second beam displacer. Lastly, without the loop, it is difficult to mount two crystals side by side between the beam displacers unless the beam separation is large enough.

3.3.2 Construction of Crystal Oven

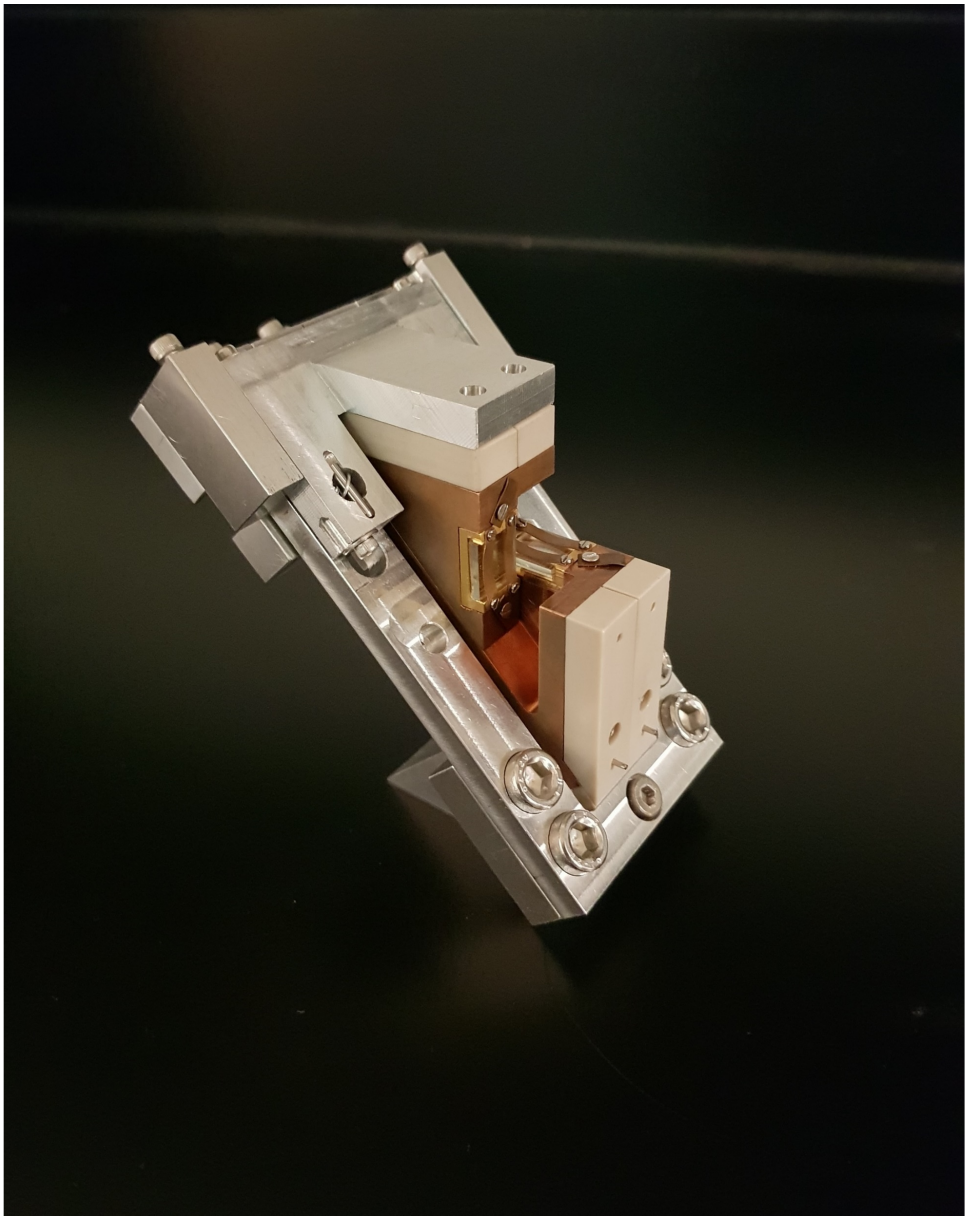

Figure 3.24: Photo of the custom designed crystal oven (Assembly completed in December 2021).

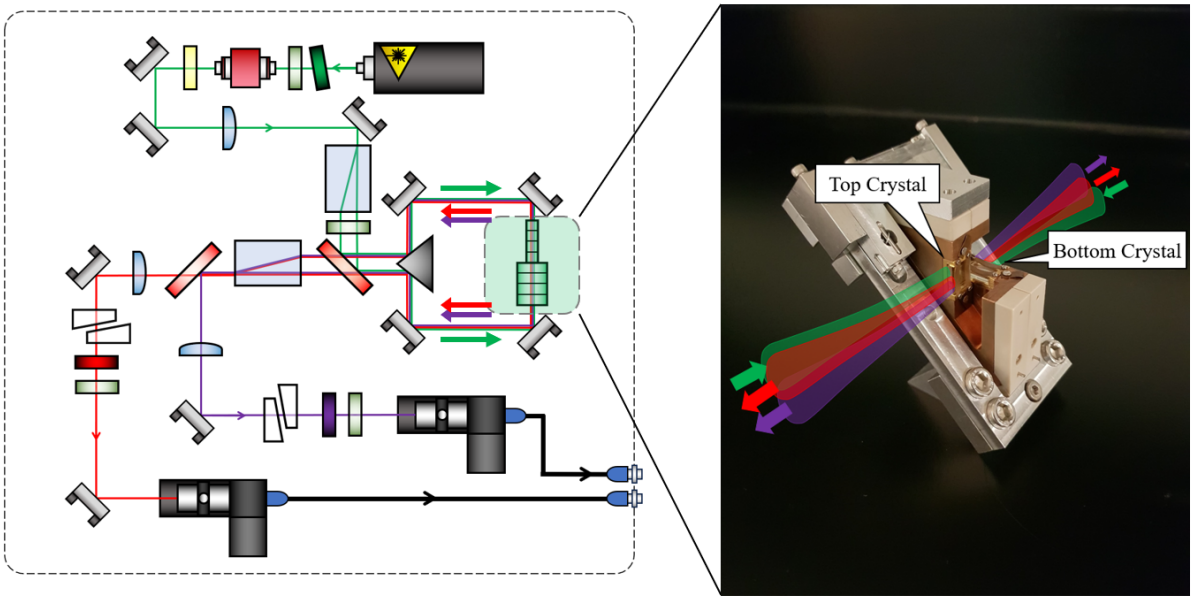

Figure 3.25: Left : A schematic diagram of the entangled photon source. The highlighted green box is where two PPLN crystals are mounted on the customized oven. Right : A picture of the custom designed crystal oven with two PPLN crystals mounted in a perpendicular orientation to each other. As shown in the picture, two pump beams (green) enter from both sides, and subsequently, signal beam (red) and idler beam (purple) are emitted from both sides as well.

As seen in Figure3.3a , our PPLN crystals have gratings with nine different poling periods. We present a custom-made crystal oven that enables the use of all these gratings. It is installed in the middle of the Sagnac loop of our EPS, as illustrated in Figure 3.25. The oven ensures that two crystals are closely aligned perpendicular to each other, and generates QPM conditions at different temperatures through temperature variation. The oven was manufactured and improved at the University of Waterloo Science Machine Shop from February 2021 over the course of a year with the design was created using Fusion360 (Autodesk, US) software. The design drawings are shown in Appendix. P.
We ensured that the two PPLN crystals we have were manufactured in the same batch by the company. Assuming they were produced in this manner, we implemented a diagonal translational movement for one of the crystals, enabling both crystals, oriented perpendicular to each other, to utilize all nine gratings (refer to Figure3.26). The front face size of each grating is a square with dimensions of 0.5 mm in both width and height, and there is a 0.2 mm spacing between adjacent gratings. This suggested considering the possibility of a

diagonal translation of at least 8.63 mm. Copper was chosen as the material for mounting the crystals due to its effective heat conduction and generally affordable cost, making it suitable for use as a mounting plate. Another reason for using this material is the intention to mount the plate in the existing oven (PV20, Covesion Ltd. US), which is also made of Copper, designed to accommodate a single PPLN crystal. The two crystals are each

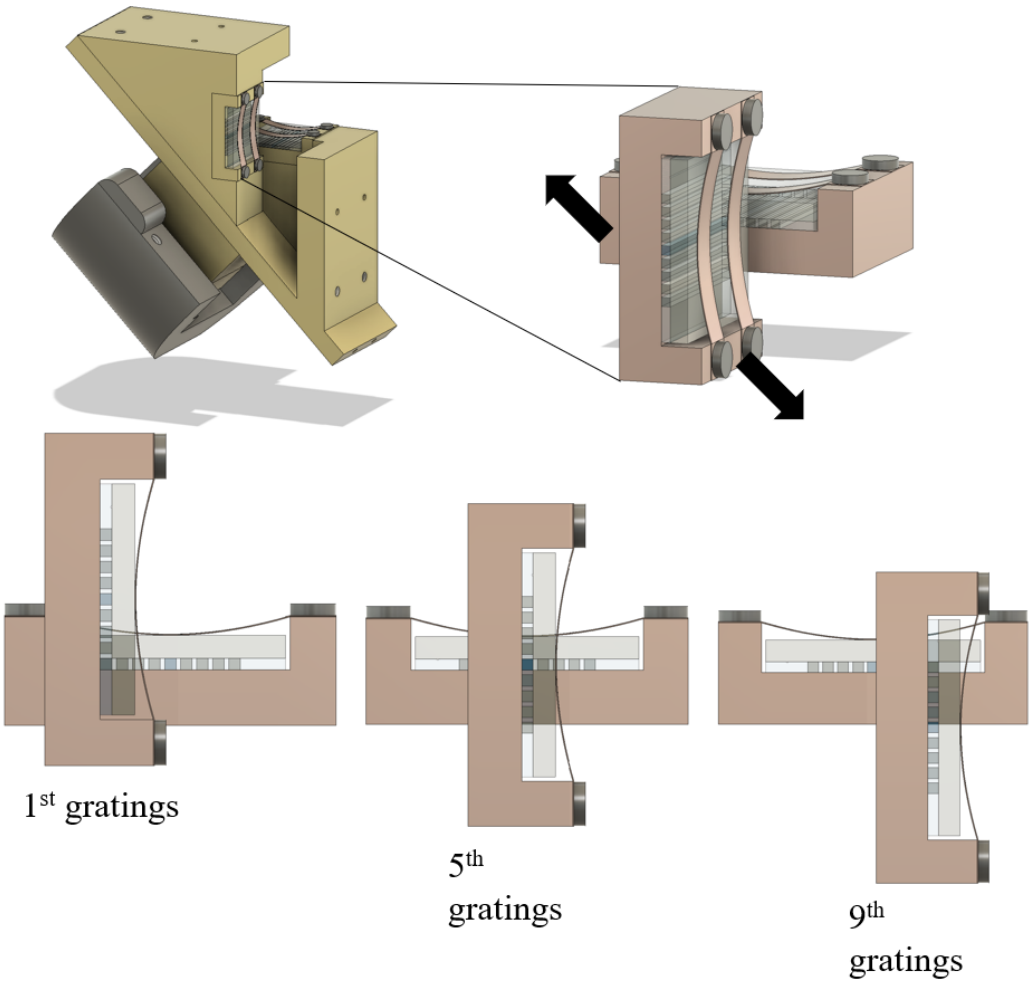

Figure 3.26: Top: A 3-D image showing how the two PPLN crystals are mounted on the customized oven. Only the copper plates and the oven of the customized oven are shown here. The image on the right is an enlarged view of the two PPLN crystals. Bottom : Schematic diagrams illustrating the diagonal translation of the vertically mounted PPLN crystal (Front faces of the crystals are shown).

mounted on a top plate and a bottom plate, secured in place with dowel pins. To ensure efficient heat distribution throughout the entire crystal, the design features a Copper plate with precisely carved spaces tailored to accommodate the size of the crystals. The bottom plate is jointed to the existing oven with dowel pins. The top plate is configured to slide diagonally, as it is not jointed to the bottom plate. To enable a good diagonal translational

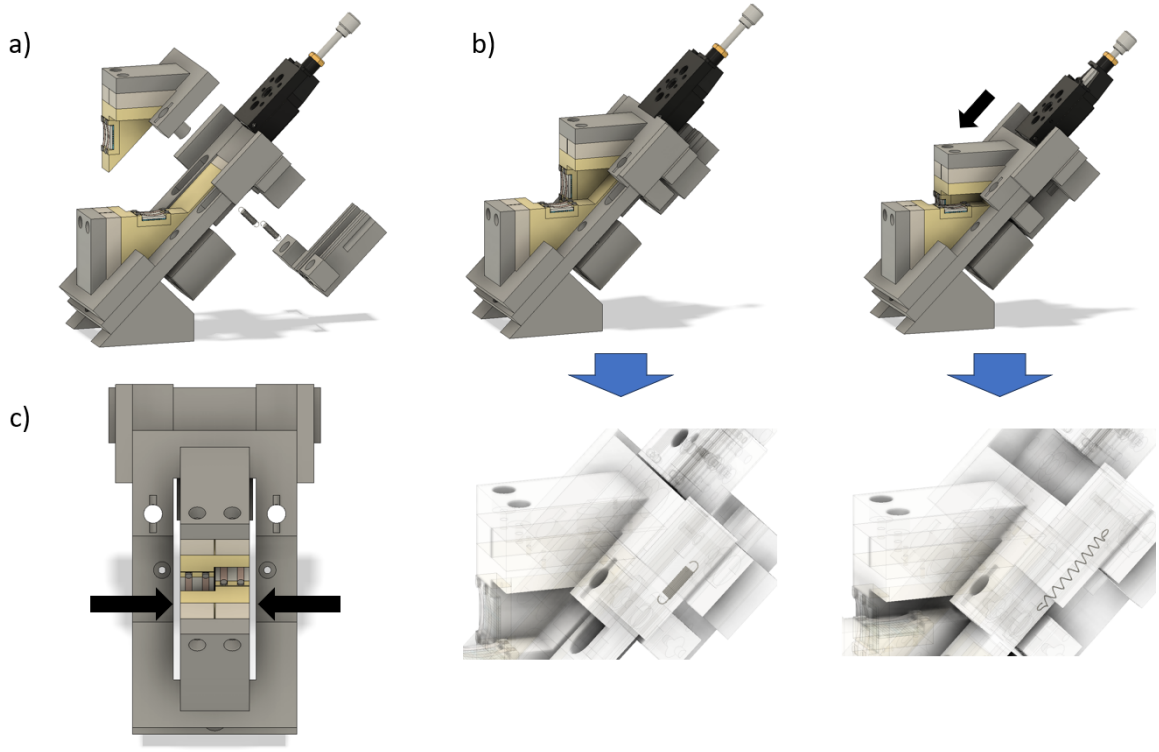

Figure 3.27: a) The top Copper plate is attached to the Polyether Ether Ketone (PEEK) bars, which in turn are attached to the upper Aluminum slider. Another Aluminum slider is positioned beneath the sliding surface, pulling the upper slider downward with springs. b) The two engaged sliders allow diagonal sliding. The origin position of the sliders is at the top. They slide downward by the micrometer attached to the sliding plate and return upward to the original position by the spring situated inside. c) To prevent heat transfer through direct and extensive contact with the Aluminum structure, we kept a thin 2 nm gap between the crystal oven and the Aluminum structure. PEEK bars are placed between the upper and lower ends of the Copper plate's slide, connecting the Copper and Aluminum plates. This allows for a balanced junction between the Copper plate and the Aluminum structure using a narrower area.

movement of the top plate, it is crucial that the top plate is well-aligned with the bottom plate, ensuring minimal lateral movement. Furthermore, a micrometer with precision is required to execute the translation accurately. However, since the Copper plates heat up, it's essential for the structure securing and supporting these plates to be made of materials capable of effectively blocking heat (otherwise, the micrometer will also become hot to touch). For cost-effectiveness, we choose to utilize the readily available Aluminum for the structure at the Science Machine Shop, and block heat transfer between the Copper plates and the Aluminum structure by incorporating thermal insulators (refer to 3.27). PEEK serves as the thermal insulator due to its low thermal conductivity $\sim 0.25W/m/K$, in contrast to Copper with a thermal conductivity of $\sim 400W/m/K$ and Aluminum with a thermal conductivity of $\sim 300W/m/K$. The oven structure was designed with an overall symmetrical shape to ensure uniform heat transfer for both the top and bottom crystals (This is the reason why the bottom Copper plate has been enclosed with PEEK material on its side and covered with Aluminum, resembling the top Aluminum slider).

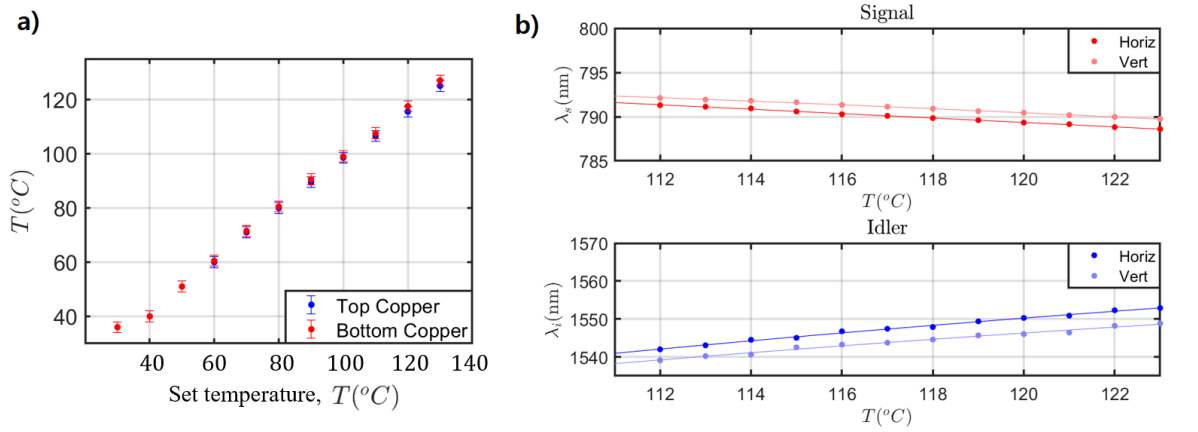

Figure 3.28: a) The plot shows how the temperature of two copper plates deviates when heated by the customized oven. The top copper plate, which is indirectly in contact with the oven, is slightly cooler than the bottom copper plate, which is directly in contact with the oven. b) Wavelength plots for signal (top) and idler (bottom) as a function of temperature. Signal wavelength from vertically oriented PPLN crystal is slightly higher than that from horizontally oriented PPLN crystal. Conversely, the idler wavelength from the vertically oriented crystal is lower than that from the horizontal one.

The crystal oven structure was designed with the expectation of uniform heat transfer. However, since the top copper plate is not actually mounted on the oven but rather placed

on top to allow sliding, the top crystal receives slightly less heat transfer compared to the bottom crystal, as shown in Figure 3.28a. It becomes apparent that with rising temperatures, the top and bottom copper plates progressively diverge such that the horizontally polarized (bottom crystal) and the vertically polarized signal and idler photons also diverge, as shown in Figure 3.28b. This raises a major concern. High-quality entanglement of photons relies on their indistinguishability. However, the slight difference in wavelengths between vertically and horizontally polarized photons will reduce their indistinguishability due to imperfect wavelength overlap. Our target operating temperature is 107.6 °C, and reaching this point exposes an approximately 2 °C difference between the two plates. To address this issue, a separate power resistor (VPG Inc., US). was attached to the top copper plate, supplying sufficient voltage to slightly elevate the temperature of the top crystal. When delivering additional heat to the top crystal through a power resistor, the bottom crystal also experiences a slight temperature increase. However, since this process compensates for the situation where the top crystal is at a lower temperature than the bottom crystal, it does not pose any issues.

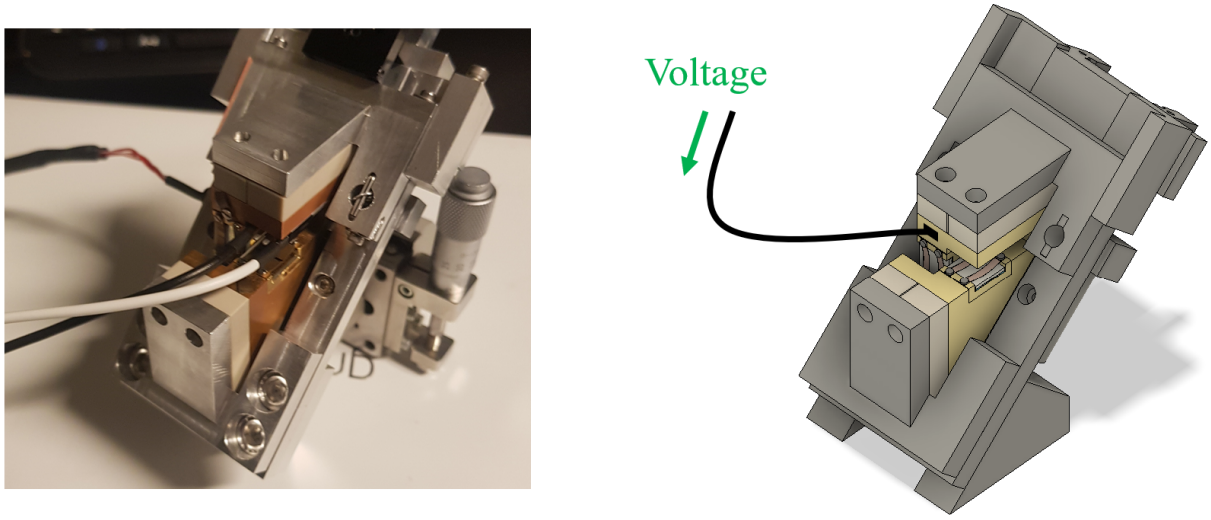

Figure 3.29: Left : A photo of the fully assembled customized oven with two PPLN crystals mounted. A power resistor is attached to the top copper plate (where the vertically oriented PPLN is mounted) in order to compensate for the slightly lower temperature. Right : A 3-D drawing of the fully assembled customized oven, showing how voltage is applied to the power resistor to generate extra heat.

3.3.3 Design Tests and Results

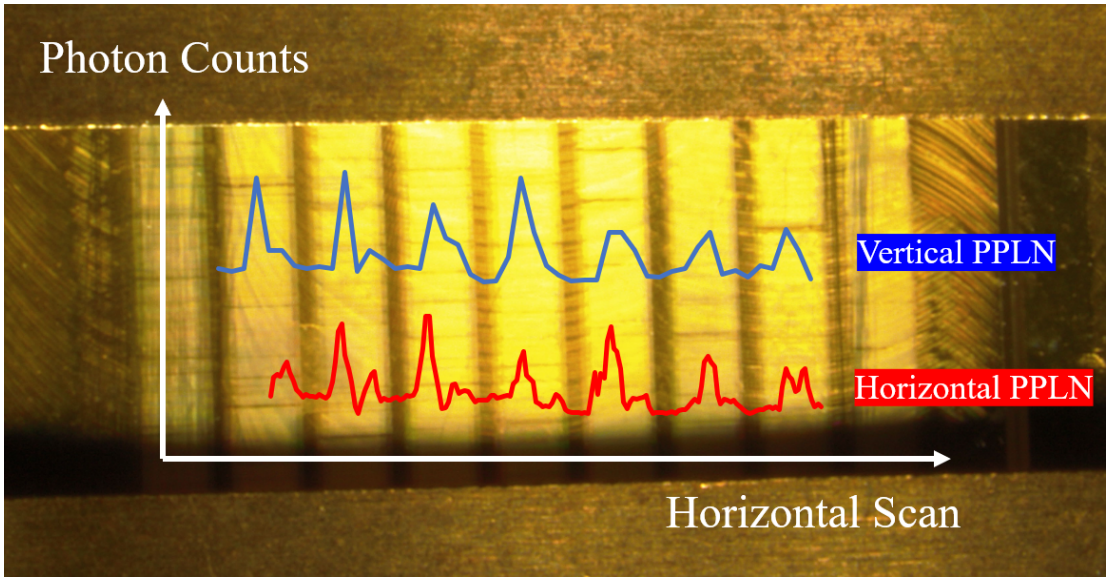

Figure 3.30: Photo of a zoomed-in PPLN crystal, with the photon counts measured simultaneously from the vertical and horizontal PPLN crystals plotted on the photo.

Figure 3.30 illustrates the measured verification of whether the crystals, placed perpendicular to each other, generate photons at all the different gratings through diagonal translation. Horizontal PPLN denotes the crystal mounted on the upper copper plate (that can undergo diagonal translation), while vertical PPLN refers to the crystal mounted on the lower copper plate. The analysis conducted on the signal photon counts (790.8 nm), measured using a single-mode fiber. The poling periods at both ends are extremely deviated from the QPM condition, and the temperature controller failed to adjust to the corresponding temperature, preventing the acquisition of a plot. Also, the slightly uneven peaks are presumed to be caused by imperfect poling, resulting in non-uniform domains. However, the diagonal translation demonstrates the ability to utilize almost all gratings in the two crystals. As of now, only the 5^{th} grating that is located at the center ($\Lambda = 7.10\,\mu m$) is used. Therefore, the remaining data analysis will be based on this specific grating. It is demonstrated that both crystals collectively emitted ~ 1.2 MHz for the signal photons when a pump power of 1.0 mW was applied. Although not shown in this figure, the single count rates were 400 kHz for the idler photons (1550 nm) from both crystals.
The crystal oven is connected to a temperature controller, TC200 (Thorlab Inc., US), for heating. The power resistor is that is attached to the top copper plate is separately con-

nected to a Direct Current (DC) power supply, E3630A (Agilent, US), receiving additional voltage power. Using a spectrometer, SpectraPro2750 (Teledyne Princeton Instruments, US), we observed the shift in the signal and idler waves with changes in temperature. When the wavelength of the signal photons emitted from the bottom crystal was 790.8 nm, the actual temperature reading on the temperature controller was 120 °C due to incomplete heat transfer (However, since the trend is consistent with Figure 3.5, we regard the temperature as 107.6 °C). Considering that heating with the power resistor also slightly increases the temperature of the bottom crystal, the experiment was conducted by providing additinoal voltage to the power resistor at a temperature below the actual value. At

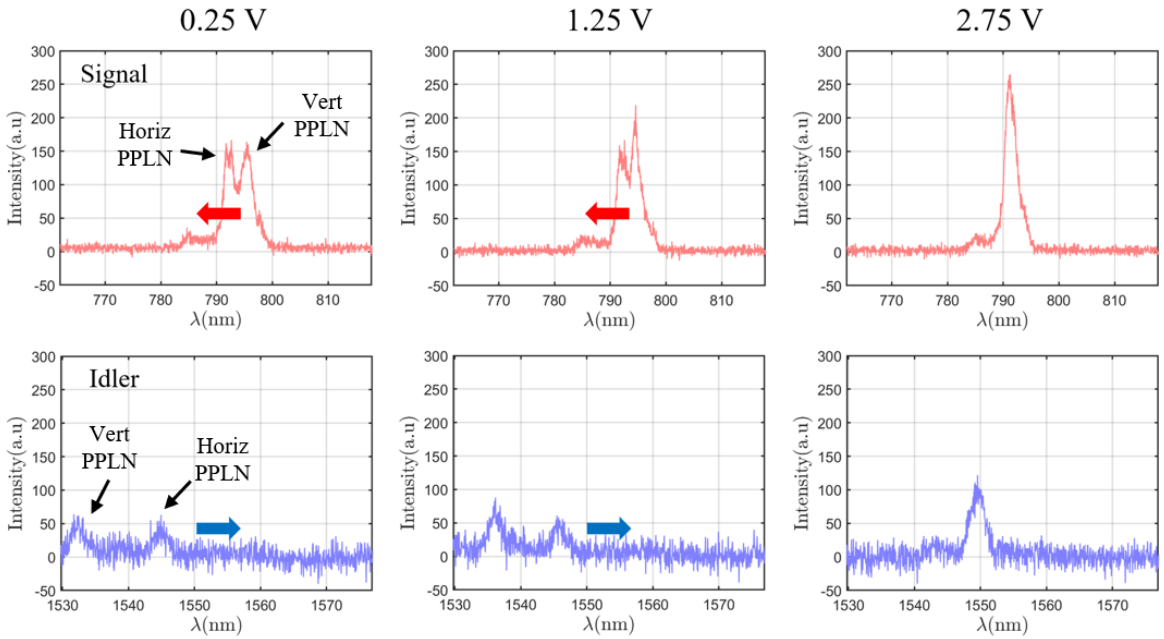

Figure 3.31: Graphs demonstrating the shift in signal and idler photon wavelengths from the two crystals based on the voltage fed into the power resistor. In the signal plots, the left peaks represent the photon wavelength generated from the horizontally placed PPLN, while the right peaks represent the photon wavelength generated from the vertically placed PPLN. Conversely, in the idler plots, the situation is reversed. As the voltage fed into the power resistor increases, it can be observed that the signal wavelengths shift to the left while the idler wavelengths shift to the right.

the lower temperature, we gradually increased the voltage power, aiming to identify the optimal temperature and voltage at which both the top and bottom crystals emit photons

of the same wavelength. As shown in Figure 3.33, increasing the applied voltages to the power resistor induces a shift in the wavelengths of the signal beams towards lower values, accompanied by a corresponding shift in the idler beams towards higher wavelengths. Such

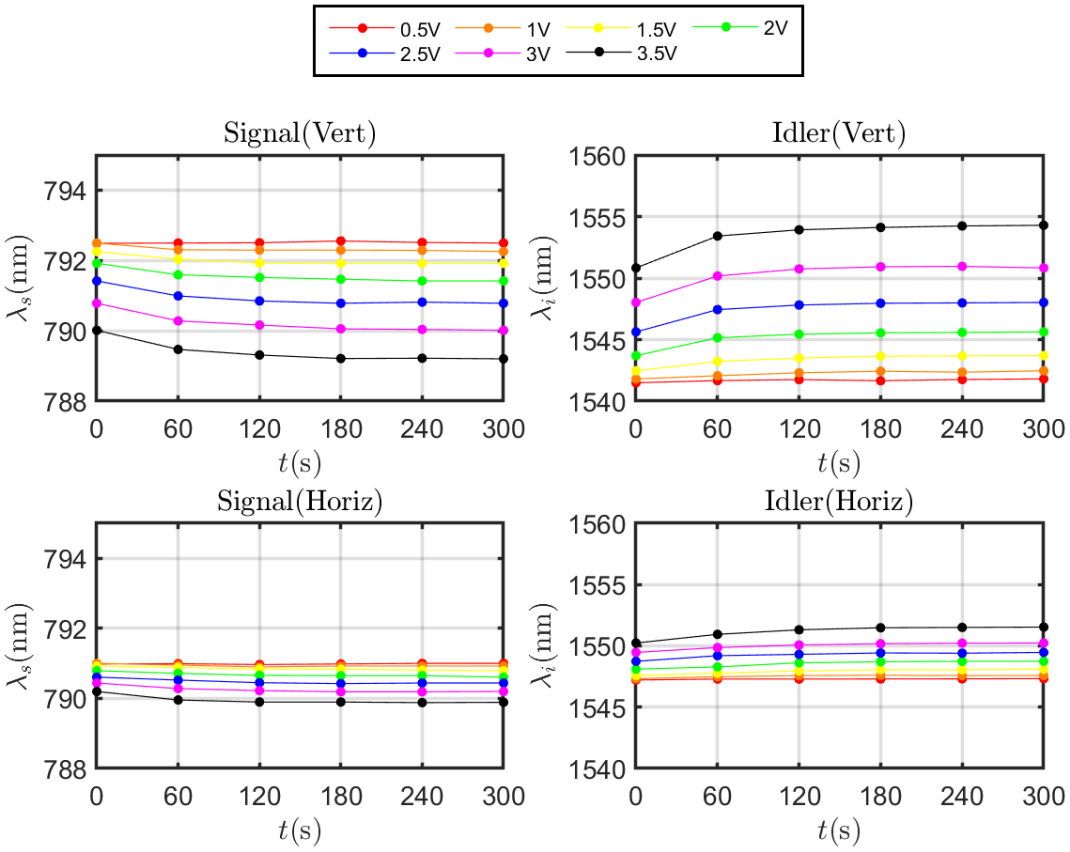

Figure 3.32: Graphs illustrating how the signal and idler photon wavelengths shift over time when the power resistor is fed with the voltage amounts indicated in the table above. In the titles of the graphs, 'Vert' and 'Horiz' denote the vertical and the horizontal PPLN crystals, respectively. As observed, the shift in signal and idler photon wavelengths from the vertical PPLN crystal is more dramatic compared to that from the horizontal PPLN, which makes sense since the voltage is fed to the vertical PPLN through the power resistor.

a trend aligns well with what we see from 3.5, with the unique distinction that, in this case, temperature is increased not through a temperature controller but by applying additional voltage to the power resistor. Another important observation is that, with each increase

in voltage power, it takes time for the temperature of both crystals to stabilize. Therefore, during temperature stabilization, temperature changes are measured at regular intervals to determine the asymptotic line and establish the average time required for stabilization. Looking at Figure 3.32, it can be observed that the wavelengths of signal and idler photons emitted from the bottom crystal generally stabilize after approximately ~ 3 minutes. The reason this makes sense is that the bottom crystal does not directly receive voltage power, resulting in relatively minor temperature changes. On the other hand, for the wavelengths of the signal and idler photons emitted from the top crystal, it can be observed that it takes approximately ~ 5 minutes for stabilization due to large temperature changes. Based on

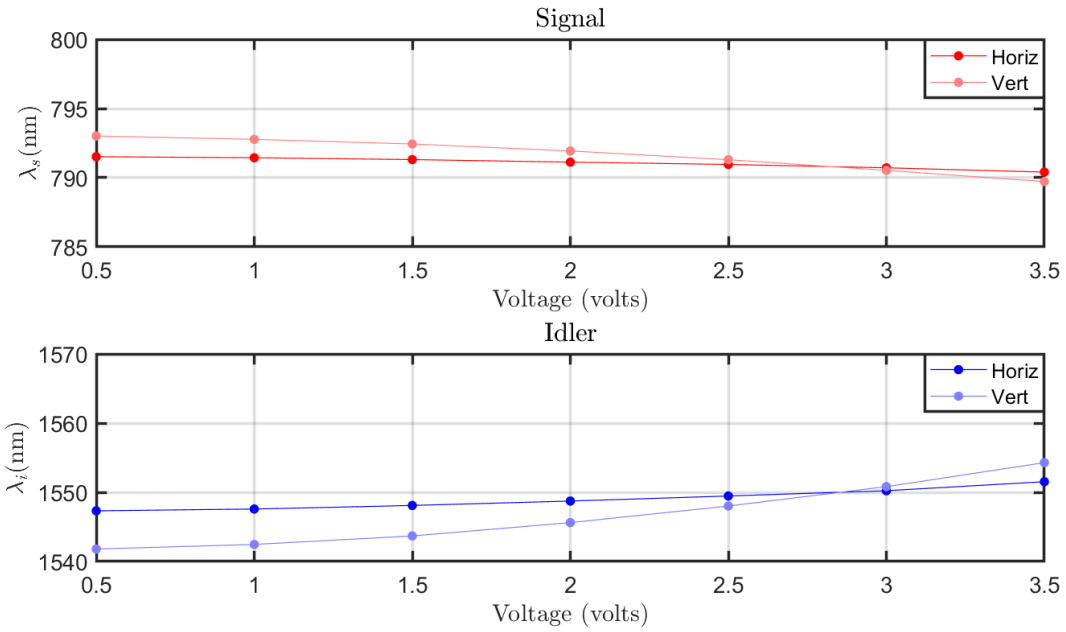

Figure 3.33: Two graphs showing variations in signal (top graph) and idler (bottom graph) photon wavelengths in response to varying voltage levels supplied to the power resistor. 'Vert' and 'Horiz' denote the vertical and the horizontal PPLN crystals, respectively. We observe that both the signal and idler photon wavelengths converge at 118.7 °C when $V = 2.83V$ is applied to the power resisitor.[11]

this observation, it seems appropriate that, when assuming an increase in voltage power by 0.5 V increments to search for the optimal temperature and voltage, waiting for a minimum of ~ 5 minutes before recording the data is advisable. After a prolonged and patient search, we identified that the two waves overlap at 118.7 °C when the additional voltage of

2.75 V is applied to the power resistor (refer to Figure 3.33). When comparing the graph shown in Figure 3.33 with the one presented in Figure 3.28b, it can be observed that the intention behind attaching the power resistor is well reflected.

3.3.4 Walk-offs from Hybrid Interferometer

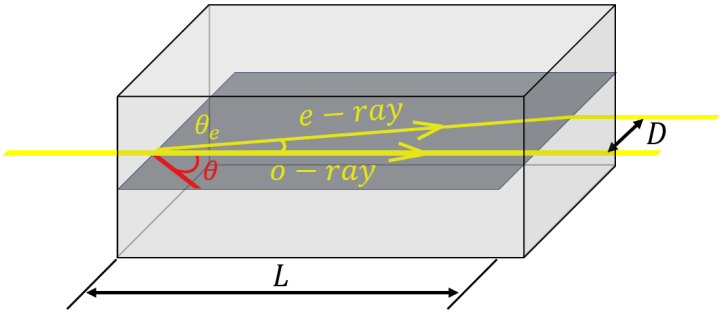

Figure 3.34: A diagram illustrating the displacement D of a beam in a beam displacer with a length L.

Even if the relative phase is minimized to some extent in the Sagnac loop, there is still phase introduced by the two beam displacers. As light propagates through the birefringent material, the component with a polarization that is non-orthogonal to the material's optic axis undergo displacement. This type of component ray is known as the extraordinary ray (with a subscript "e"). The component of the ray that maintains its original path is referred to as the ordinary ray (with a subscript "o"). The displacement amount can be determined from the angle of refraction of the e-ray, θ_e.

$$\tan\theta_e = \left(1 - \frac{n_o^2}{n_e^2}\right) \frac{\tan\theta}{1 + \frac{n_o^2}{n_e^2}\tan^2\theta} \tag{3.53}$$

θ is the angle between the optic axis and the normal to the surface of the medium for the incident rays (refer to Figure 3.34). Note that equation 3.53 applies specifically when the incident beam enters the medium perpendicular to the surface of the medium (the generic equation is a lot more complicated). The separation between the two rays created by the medium with a length of L is then $D = L\tan\theta_e$. We use the length of $L = 39.4\,\text{mm}$

that corresponds to the two beam displacers (Newlight Photonics inc, Canada) used in our setup to obtain the plot shown in Figure 3.35. The plot implies that a change in wavelength leads to a corresponding shift in displacement.

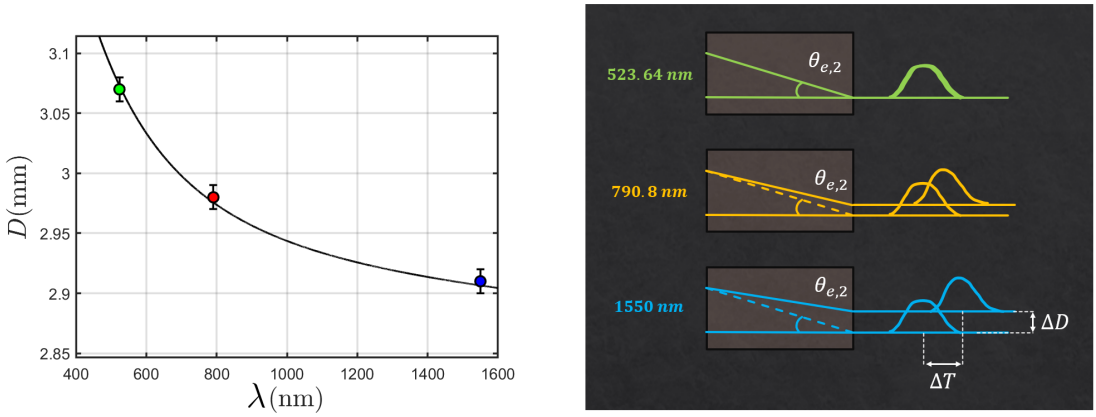

Figure 3.35: Left : Experimentally measured displacements of the pump, signal and idler beams plotted on the theoretical displacement curve as a function of wavelength. Right : Three diagrams illustrating how the pump, signal and idler beams undergo spatial ΔD and temporal ΔT walk-offs in the beam displacer. As seen, the degree of displacement decreases as the wavelength increases.

We are examining a scenario in which the initial beam with a wavelength of 523.64 nm, goes through a PPLN crystal, resulting in down-conversion to wavelengths of 790.8 nm and 1550 nm. Consequently, when the down-converted photons pass through the second beam displacer, they will not return to their original position, given that their wavelengths are no longer the pump wavelength. This deviation from the original position is reffered to as spatial walk-off, denoted by ΔD.

$$\Delta D_{s,i} = L \tan \theta^{p}_{e,2} - L \tan \theta^{s,i}_{e,1} \tag{3.54}$$

$\theta_{e,1}$ and $\theta_{e,2}$ are the refraction angles of the first and the second beam displacers, respectively. equation 3.54 theoretically gives us the spatial walk-offs of 0.10 mm for the signal beam and 0.17 mm for the idler beam.
If the wavelength has changed and the presence of spatial walk-off has been confirmed, then we may also question the existence of temporal walk-off. To calculate temporal walk-off,

one first needs to determine the group velocity[12].

$$v_{g,o} = \frac{c}{\mathcal{N}_o} = \frac{c}{n_o - \lambda \dfrac{dn_o}{d\lambda}} \quad , \quad v_{g,eff} = \frac{c}{\mathcal{N}_{eff}} = \frac{c}{n_{eff} - \lambda \dfrac{dn_{eff}}{d\lambda}} \tag{3.55}$$

where $\mathcal{N}$ are the group indices of the corresponding rays. $dn/d\lambda$ can be interpreted as the slope of the function $n(\lambda)$, and is calculated numerically. The ordinary and extraordinary rays exhibit different group velocities due to their distinct refractive indices. Therefore, one must be cautious when calculating the time difference. The refractive index affecting the o-ray, denoted as n_o, can be directly obtained from the Sellmeier's equation B.1. However, the refractive index affecting the e-ray is an effective refractive index which depends on the effective angle, $\theta_{eff} = \theta + \theta_e$.

$$n_{eff} = \frac{n_o n_e}{\sqrt{n_o^2 \sin^2 \theta_{eff} + n_e^2 \cos^2 \theta_{eff}}} \tag{3.56}$$

The time taken for the beam to pass through the beam disiplacer can be easily conceptualized through a geometric approach.

$$\begin{aligned} T^{s,i}_{o\to e} &= \frac{L}{v^p_{g,o}} + \frac{L}{v^{s,i}_{g,e} \cos \theta^{s,i}_{e,2}} \\ T^{s,i}_{e\to o} &= \frac{L}{v^p_{g,e} \cos \theta^p_{e,1}} + \frac{L}{v^{s,i}_{g,o}} \end{aligned} \tag{3.57}$$

$T_{o\to e}$ is the time taken by the ray, which initially travels straight and then becomes displaced. Similarly, $T_{e\to o}$ is the time taken by the ray, which initially becomes displaced then travels straight. The temporal walk-off is then the time difference between the two travel time.

$$\Delta T_{s,i} = T^{s,i}_{o\to e} - T^{s,i}_{e\to o} \tag{3.58}$$

equation 3.58 theoretically gives us the temporal walk-offs of 0.65 ps for the signal beam and 1.06 ps for the idler beam.

3.3.5 Walk-off Compensation Method

If we are to determine the spatial overlap (quality of the entanglement) of the beams, we can characterize the spatial modes of the ordinary and extraordinary rays with Gaussian

[12]One could also use the inverse of the propagation constant that we previously mentioned instead of the group velocity.

functions.

$$g(x,y) = \frac{1}{\sqrt{2\pi\sigma^2}} e^{-(x^2+y^2)/2\sigma^2} \tag{3.59}$$

The standard deviation can be obtained from FWHM$= 2\sqrt{2\ln 2}\sigma$. The FWHM of the signal and idler beams were measured to be 0.6 mm and 0.8 mm, respectively. The beam overlap is then the product of the two Gaussians integrated over the transverse plane (x,y).

$$\int_{-\infty}^{\infty} g_o(x,y) g_e(x - \Delta D_x, y - \Delta D_y) dx dy \tag{3.60}$$

The spatial overlap factors are calculated to be 52.4% for the signal photon, and 17.1% for the idler photon (this is in consideration of the additional walk-off mentioned in section 3.3.7).
We also determine the temporal overlap (quality of the entanglement) by characterizing the temporal modes of the ordinary and extraordinary rays also with equation 3.59. The standard deviation can be derived from the temporal width $\tau = 2\sqrt{2\ln 2}\sigma$, which in turn can be determined from the wavelength and its bandwidth (from FWHM).

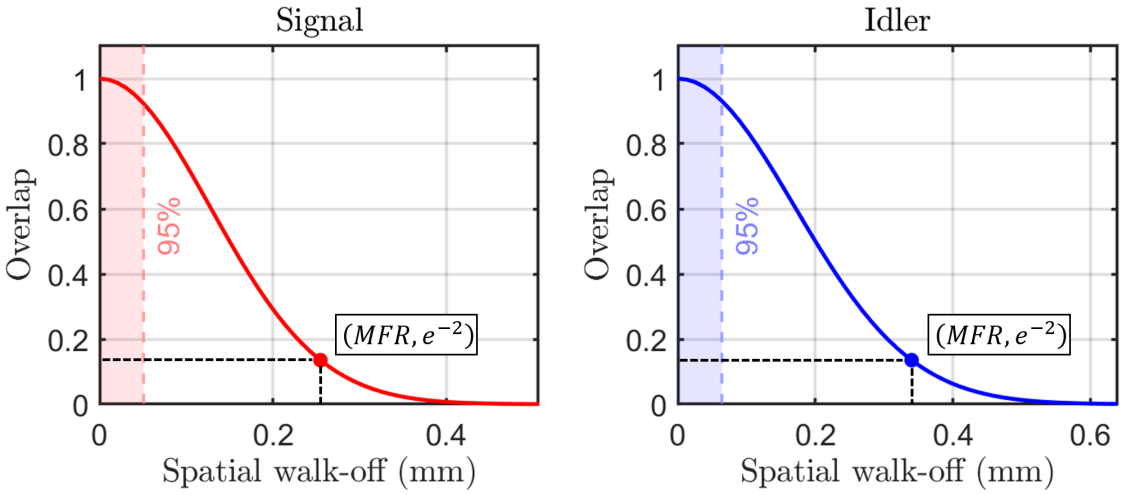

Figure 3.36: Theoretical Gaussian beam spatial overlap of signal photons with a Mode Field Radius (MFR) of 0.26 mm (left) and idler photons with a MFR of 0.34 mm (right) as a function of spatial walk-off, respectively. We see that the amount of spatial walk-off at the intensity of I_{max}/e^2 exactly corresponds to the MFR of the Gaussian intensity profiles.

$$\tau \approx \frac{\lambda^2}{c\Delta\lambda} \tag{3.61}$$

The bandwidths of the signal and the idler photons are measured to be $\Delta\lambda_s = 0.66\,\text{nm}$ and $\Delta\lambda_i = 2.61\,\text{nm}$, respectively. According to equation 3.61, the temporal widths (at 1/e) are $\tau_s = 2.68\,\text{ps}$ for the signal photon, and $\tau_i = 2.61\,\text{ps}$ for the idler photon. In a similar manner, by using equation 3.60, the temporal overlap of two Gaussian intensity profiles is calculated to be 88.8% for the signal photon, and 72.1% for the idler photon. The entanglement quality decreases as the two beams fail to overlap both spatially and temporally. This highlights the necessity for us to compensate for the spatial and temporal walk-offs. Say, our objective is to attain a beam overlap of over 95% in both temporal and spatial domains. In case of compensating only for the temporal walk-off, the solution is fairly straightforward. Temporal walk-off refers to the phenomenon where one beam arrives earlier than the other in a pair of beams. A simple temporal walk-off compensation is having another birefringent material (compensator) to slow down the leading beam. In our case, the leading beam in both the signal and idler paths is the ordinary beam. This means, either a negative uniaxial ($n_o > n_e$) compensator with its optic axis aligned with the oscillation direction of the slower ray, or a positive uniaxial ($n_e > n_o$) compensator with its optic axis aligned with the oscillation direction of the faster ray is needed for the temporal walk-off compensation. Suppose we use Calcites which have ordinary and extraordinary refractive indices of n_o and n_e, respectively. The length of the Calcite needed for the temporal walk-off compensation will be

$$L = |v_{g,e} - v_{g,o}|\,\Delta T \tag{3.62}$$

To simultaneously compensate for both spatial and temporal walk-offs, we developed a novel approach for compensation. Employing a separation between two crystal wedges proves to be an effective approach for achieving spatial compensation (See Figure 3.62). One side is flat, allowing the ray to enter perpendicularly. This simplifies calculations such as group velocity. Moreover, even if the ray exits the first wedge at a non-perpendicular angle, when it enters the second wedge that is identical in shape, it will regain its original propagation direction. This offers a great advantage. One important thing to remember is that the distance the two beams travel within the gap between the wedges is slightly different, due to the different refractive indices. This leads to either an increase or a decrease in the original temporal walk-off, and this should be taken into account when determining the thickness of the crystal. In our case, the o-ray is bent more than the e-ray, as Calcites are negative uniaxial crystals. Consequently, the o-ray travels a longer distance than the e-ray, resulting in a reduction of the temporal walk-off. Additionally, it

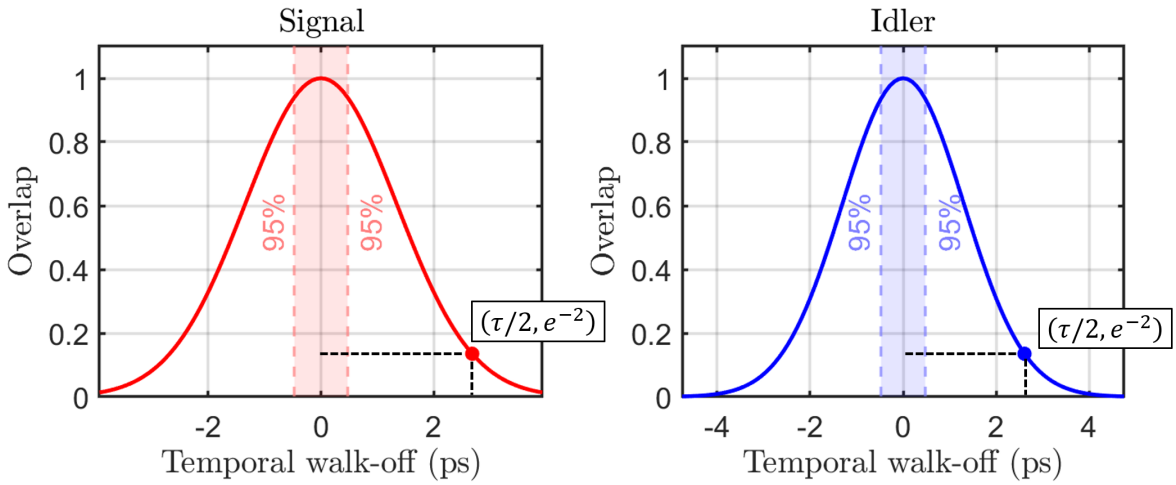

Figure 3.37: The left and right graphs illustrate the theoretical Gaussian beam overlap of signal beams and idler beams (each with two orthogonal polarization states) as a function of temporal walk-off, respectively We see that the amount of spatial walk-off at the intensity of I_{max}/e^2 exactly corresponds to the temporal width of the Gaussian intensity profiles.

is crucial to note that in the first Calcite wedge (on the left), the e-ray travels a slightly longer distance than the o-ray. We determine the lateral separation d needed for a perfect spatial overlap. We let the vertical shift of the o-ray be $b = a\tan(\theta_o - \phi)$ such that the vertical shift of the e-ray is $b - \Delta D$. In doing so, a relationship between the two vertical shifts can be established as follows.

$$a\tan(\theta_o - \phi) - \Delta D = (a - \Delta D\tan\phi)\tan(\theta_e - \phi) \tag{3.63}$$

$\theta_{o,e}$, ϕ and ΔD are known quantities, so we can rearrange equation 3.63 to determine a.

$$a = \frac{1 - \tan\phi\tan(\theta_e - \phi)}{\tan(\theta_o - \phi) - \tan(\theta_e - \phi)}\Delta D \tag{3.64}$$

Finally, we calculate the lateral separation d as follows.

$$d = a - b\tan\phi \tag{3.65}$$

We use two pairs of Calcites (Newlight Photonics inc, Canada) with a wedges angle $\phi = 15°$ (The angle can be chosen arbitrarily, as long as the rays do not bend excessively and refrain from entering the second wedge). The total path lengths traveled by each ray can

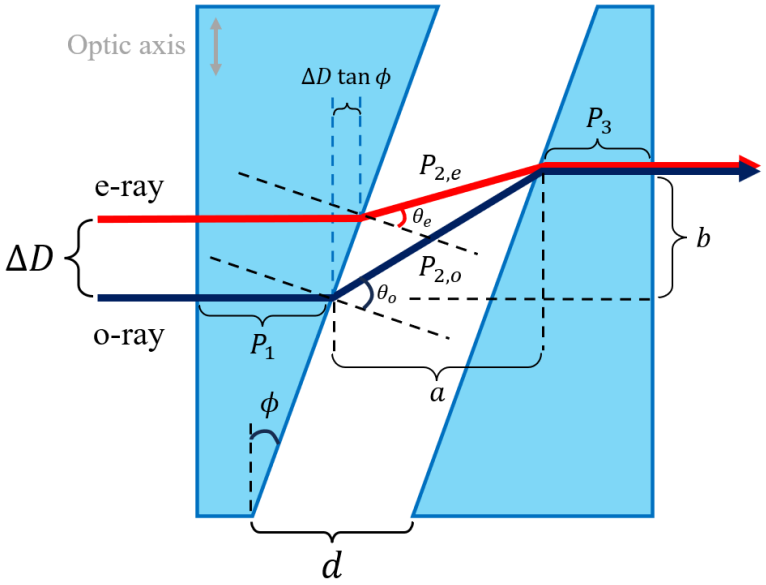

Figure 3.38: A schematic diagram of two Calcite wedges used to compensate for both spatial and temporal walk-offs. The optic axis of our Calcite wedges is aligned perpendicular to the direction of ray propagation such that both the ordinary (purple) and extraordinary (red) rays undergo no beam displacement when entering the Calcite perpendicularly. However, upon exiting the first wedge, the e-ray experiences more bending than the o-ray due to negative birefringence ($n_e < n_o$). The path lengths of the e-ray and the o-ray in between the two wedges are shown as $P_{2,e}$ and $P_{2,o}$, respectively. By identifying the correct lateral separation between the two wedges, we effectively merge the two rays at the second wedge. Temporal walk-offs are compensated by the thickness of the wedges.

be expressed as follows.

$$\begin{aligned} P(\text{o-ray}) &= P_1 + P_{2,o} + P_3 \\ P(\text{e-ray}) &= P_1 + \Delta D \tan\phi + P_{2,e} + P_3 \end{aligned} \tag{3.66}$$

We want the temporal walk-off to be canceled by the time delay created by P(o-ray) and P(e-ray). Hence, using equations 3.55, the temporal walk-off can be written as

$$\Delta T = \left[\frac{1}{v_{g,o}}\left(P_1 + P_3\right) + \frac{1}{c}P_{2,o}\right] - \left[\frac{1}{v_{g,e}}\left(P_1 + \Delta D \tan\phi + P_3\right) + \frac{1}{c}P_{2,e}\right] \tag{3.67}$$

3.3.6 Walk-off compensation Results

We can deduce from Figure 3.39 that to achieve the spatial overlap above 95%, a spatial walk-offs of approximately $\Delta D = 0.05\,\text{mm}$ and $\Delta D = 0.06\,\text{mm}$ is deemed acceptable for the signal and idler beams, respectively. In actual experiments, higher values of $\Delta D_s = 0.145\,\text{mm}$ and $\Delta D_i = 0.325\,\text{mm}$ are observed due to additional divergence at the two dichroic mirrors. The additional divergence could potentially introduce ambiguity in temporal walk-off compensation (fortunately, it seems to have had minimal, if any, impact on the trend). However, when compensating for the spatial walk-off, the additional divergence poses no issues and should simply be taken into account. The lateral separation needed for the signal and idler paths with the additional divergence considered are calculated to be $d_s = 2.75\,\text{mm}$ and $d_i = 6.60\,\text{mm}$, respectively. Figure 3.39 shows theoretical Gaussian beam overlap of signal photons and idler photons (each with two orthogonal polarization states) as a function of spatial walk-off, respectively. To validate the theoretical curve of the spatial overlap, we completely compensated for the spatial walk-off of the signal beam and varied the spatial walk-off of the idler beam while measuring coincidence counts. The spatial walk-off of the idler beam is varied by changing the lateral separation between the two Calcite wedges that are placed on the idler beam path. [13]Coincidence counts at each variation is measured. The peak experimental value plotted on the idler graph corresponds to when spatial walk-off is fully compensated for both the signal and idler beams, with the coincidence counts measuring $N_c = 33.3\,\text{kHz}$. This marks almost 8 times enhancement in the coincidence counts, as without compensation on the idler side (while the signal side remained fully compensated), the coincidence count was $N_c = 4.2\,\text{kHz}$. It is worth noting that SPDC occurs randomly in time when using a CW

[13]We choose to vary the idler beam primarily because the effect of the variation is more noticeable and easier with the idler beam path to validate the spatial overlap through the experiment.

laser as the pump field. Therefore, we focus on minimizing the relative temporal walk-off $|\Delta T_s - \Delta T_i|$ between the signal and the idler beams, rather than minimizing them individually. Since Calcites are placed in both beam paths for spatial compensation, we fix

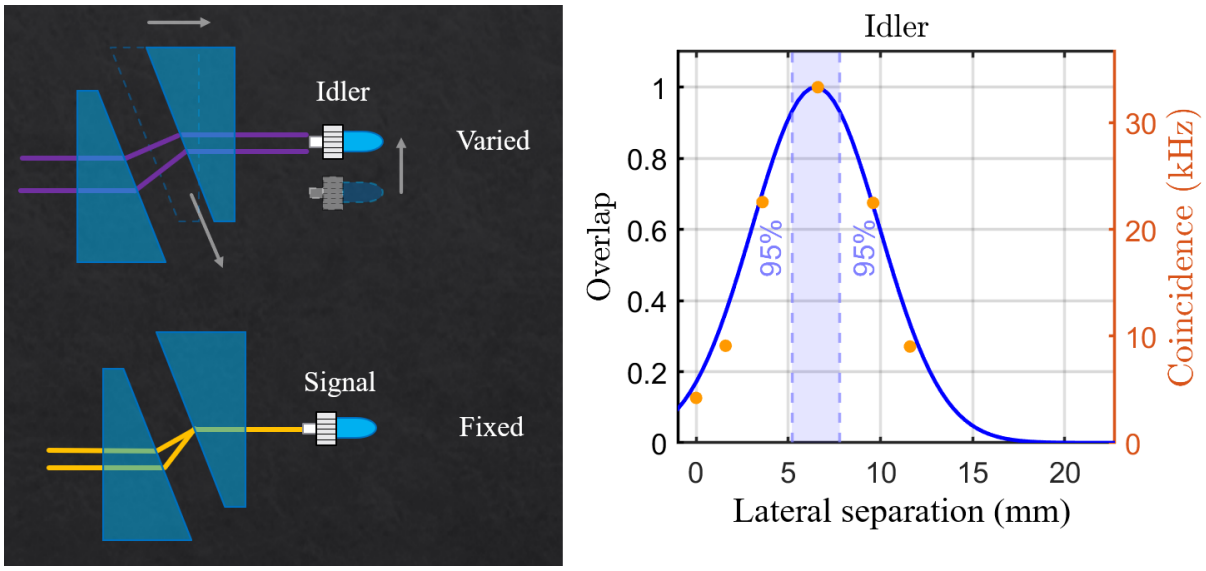

Figure 3.39: Theoretical Gaussian beam spatial overlap of idler photons (right) as a function of the lateral separation length between the two Calcites, respectively. We shift the position of one of the Calcite wedges on the idler side as illustrated in Figure (left). The lateral separation between the wedges is varied as 0 mm, 1.6 mm, 3.6 mm, 6.6 mm, 9.6 mm and 11.6 mm. The optical fiber collecting idler photons is realigned for each variation. The results are plotted (dots) on the same graph.

the thickness of the Calcite wedges in the signal path and adjust the temporal walk-off of the idler beam accordingly.[14] The adjustment can be done simply by allowing diagonal translation of the idler Calcite wedge as shown in Figure 3.39.

[14]We choose to vary the idler beam positions primarily due to a technical limitation. There was not much of space to move the optics diagonally in the signal beam path.

3.3.7 Polarization-Entanglement Test and Results

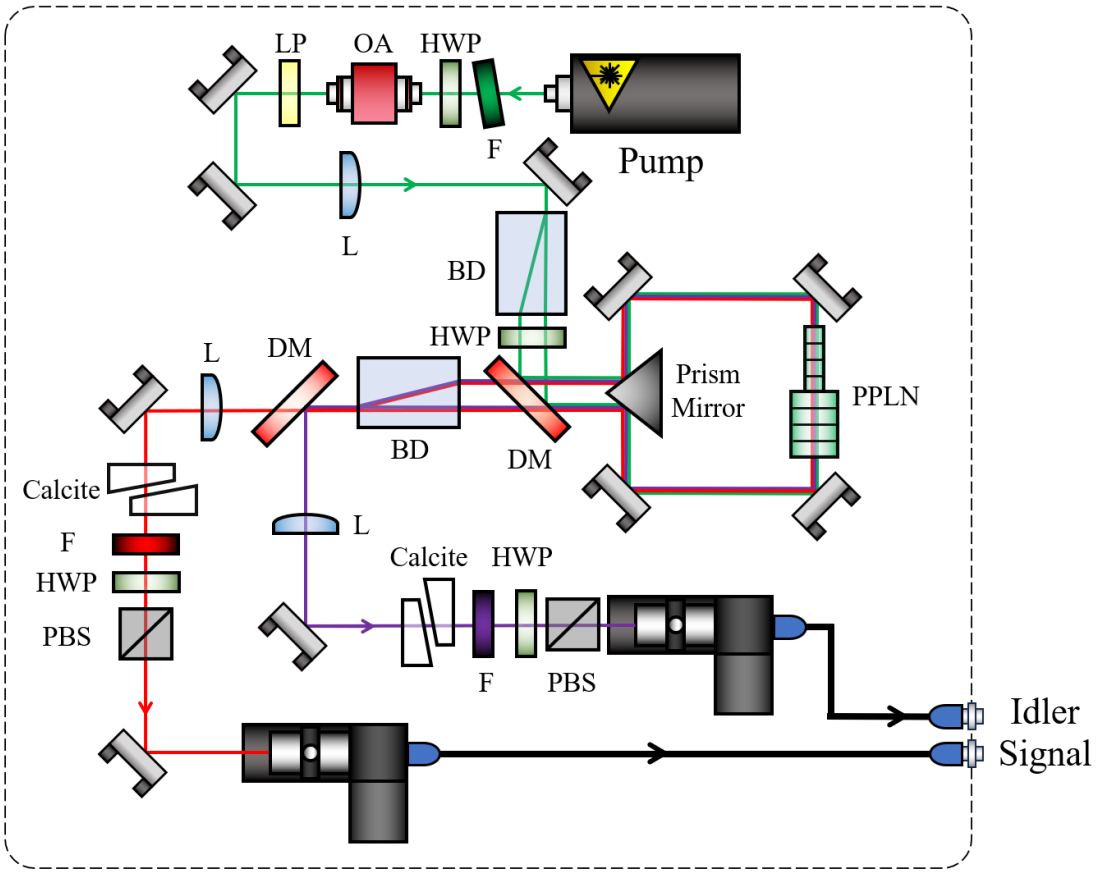

Figure 3.40: Design of EPS. Optical components are : Filter (F), Optical Isolator (OA), Linear Polarizer (LP), Lens (L), Beam Displacer (BD), Half waveplate (HWP), Dichroic Mirror (DM), Polarizing Beam splitter (PBS).

We demonstrate polarization-entanglement of photons with our entangled photon source, with the hybrid interferometer implemented (See Figure 3.40). We use the CW pump laser that operates at a wavelength of $523.6 \pm 0.1 nm$. The pump beam, collimated by an aspheric lens ($f_p = 8\,\text{mm}$) passes through several optical components to be diagonally polarized. It is then focused by the magnifying lens ($f_p = 40\,\text{cm}$) to the PPLN crystals in the Sagnac loop. The first beam displacer splits the diagonally polarized pump beam into two beams with horizontal and vertical polarization by displacing one of them that is extraordinary with respect to the displacer's optic axis. The polarization of the two beams is switched

by passing through a half waveplate before they enter the Sagnac loop. The first dichroic mirror reflects the pump beam into the Sagnac loop, while allowing the signal and idler beams that are produced from down conversion by the PPLN crystals to pass through and reach the second beam displacer. The two pairs of signal and idler beams combined by the second beam displacer are separated by the second dichroic mirror (signal beam is transmitted and idler beam is reflected). Along each beam path, there is another lens ($f_s = 60\,\text{cm}$ and $f_i = 50\,\text{cm}$) to re-collimate the beam before entering the Calcite wedges for walk-offs compensation. Note that the lenses must be placed before the wedges in order to prevent from the beam entering non-perpendicular to the wedges' surfaces. This is where we expect the signal and the idler photons to be entangled. We place a long-pass filter and

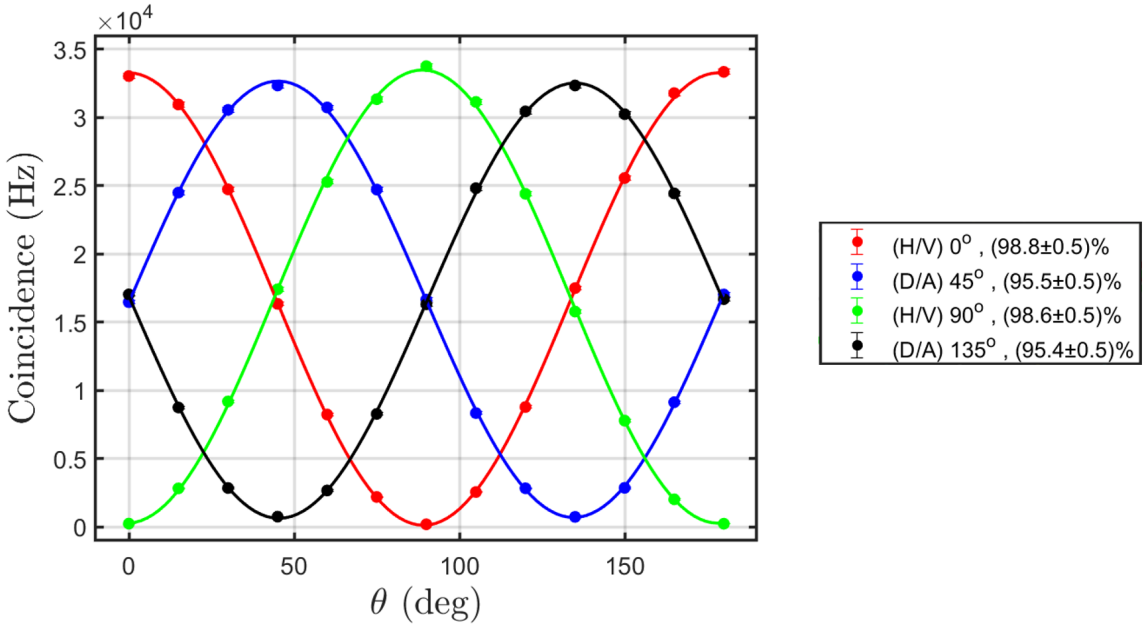

Figure 3.41: Polarization entanglement measurement results. The correlation measurement was conducted using four different polarization bases. The coincidence counts, measured at 1.0 mW of pump power while changing the polarization angle from 0^o to 180^o, are plotted on the graph.

a bandpass filter on each beam path to ensure that any noises are reduced. From here, the polarization-entanglement test is proceeded by measuring the polarization correlation of the Bell states. We place a half waveplate and a polarizing beam splitter on each arm (signal and idler). The arrived signal and idler photons are focused by the aspheric lenses ($f_s = 11\,\text{cm}$ and $f_i = 15\,\text{cm}$) and collected through the SMFs. SPAD and SNSPD are used

to collect signal and idler photons, respectively. The detection efficiencies from the signal and the idler beam paths are estimated to be $\eta_s = 0.38$ and $\eta_i = 0.217$ considering all the optical components along the ways including the detectors. These values are estimated based on the specifications of the optical components provided by the manufacturers. The coincidence counts within a 1.5 ns detection window are measured using a time-tagging unit. The correlations are measured by rotating the half waveplate on the signal arm while the half waveplate on the idler arm are fixed to 0^o (V basis), 45^o (A basis), 90^o (H basis) and 135^o (D basis). The measurements are done with the pump power of 1.0 mW, and the coincidence window of 1.5 ns. As the result shown in Figure 3.41, the visibilities (correlation quality) $V = (N_{c,max} - N_{c,min})/(N_{c,max} + N_{c,min})$ of the four basis, from the background subtracted coincidence rates are $V = (96.8 \pm 0.5)\%$, $V = (95.5 \pm 0.5)\%$, $V = (98.6 \pm 0.5)\%$ and $V = (95.4 \pm 0.5)\%$. In order to confirm the entanglement, we perform the CHSH test [30]. The CHSH inequality is expressed as

$$S = |E(\alpha, \beta) - E(\alpha, \delta) + E(\gamma, \delta) + E(\gamma, \beta)| \leq 2 \tag{3.68}$$

where we have the correlation estimates expressed as

$$E(\alpha, \beta) = \frac{N_c(\alpha, \beta) - N_c(\alpha, \beta + 90^o) - N_c(\alpha + 90^o, \beta) + N_c(\alpha + 90^o, \beta + 90^o)}{N_c(\alpha, \beta) + N_c(\alpha, \beta + 90^o) + N_c(\alpha + 90^o, \beta) + N_c(\alpha + 90^o, \beta + 90^o)} \tag{3.69}$$

We chose $\alpha = 0^o$, $\beta = 22.5^o$, $\gamma = 45^o$ and $\delta = 67, 5^o$ and confirmed that the inequality is strongly violated at $S = 2.75 \pm 0.03$ by 25 standard deviations, which also agrees nicely with the expected value from the average visibility $S_{exp} = 2\sqrt{2}V_{avg} \approx 2.75$, indicating the entanglement [81, 30]. We also examine the consistency of experimental data quality with increasing pump power levels. The experimental data includes the single counts of signal(N_s) and idler(R_i) photons, as well as coincidence counts(N_c) representing simultaneous detection of the signal and the idler photons. Detection saturation was observed during the experiment when the power exceeded 4 mW. To mitigate this effect, attenuators are installed at both ends of the signal and idler beams. Initially, single counts and coincidence counts are recorded with and without the attenuators, spanning power levels from 1.0 mW to 4 mW. From these measurements, a calibration factor is derived, which is then used to estimate counts at power levels of 5 mW and above based on the counts measured with the attenuators. The results are plotted in Figure 3.42a. At a pump power of 1.0 mW, the average background subtracted values for four different bases were $N_s = (460.7 \pm 3.5)$kHz, $N_i = (210.7 \pm 1.0)$kHz and $N = (33.33 \pm 0.05)$kHz. These are the values that also corresponds to the maximum counts shown in Figure 3.41. The measured pump-varied counts from all four bases demonstrate a consistent linear increase with increasing power. This observation supports the idea that there is a direct relationship

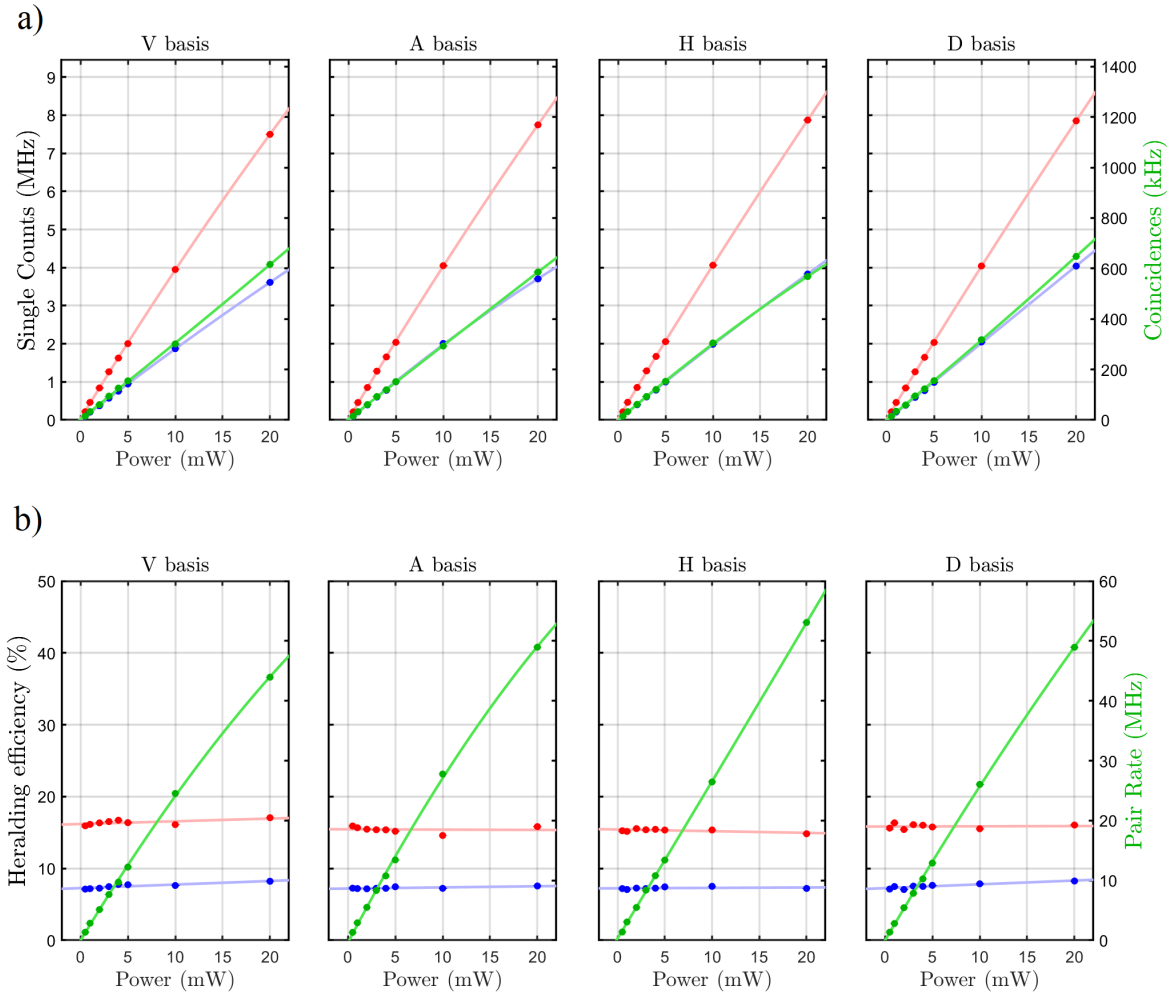

Figure 3.42: The single counts of both signal (red) and idler (blue) photons, as well as the coincidence (green) counts are measured from four different polarization basis while varying the pump power. After the necessary background subtractions, the data are plotted on these graphs. Graphs showing the photon pair emission rates R_{pair} (green), along with the heralding efficiencies of the signal photon η_s (blue) and the idler photon η_i (red) for different pump powers, calculated from the data shown in (a).

between pump power and photon rates, as predicted by equations 3.43 and 3.45. The calculated pair rates and the heralding efficiencies are plotted in Figure 3.42b. The pair rate at 1.0 mW was $R_{pair} = 2.92 \pm 0.12$ MHz which agrees with the theoretical prediction $R_{theo} = 2.82$ MHz. Also, signal and idler heralding efficiencies of $\eta_s = 15.8\%$ and $\eta_i = 7.2\%$, respectively. The pair rate from all four bases showed a linear increase with increasing pump power, while the heralding efficiencies remained fairly constant as one would expect. As derived from our theoretical model in Chapter 2, we have set a minimum requirement of 100 MHz pair rate for each polarization measurement basis to establish a long-distance quantum link. The trends of all four bases in Figure 3.42b indicate that such a pair rate is possibly achieved at the power level of 50 mW.

3.3.8 Discussion

The 100 MHz pair rate was deduced with the assumption that we start with near-100% visibility at the EPS. The average visibility obtained from the entanglement test using the four polarization bases is $(96.6 \pm 0.3)\%$, with a maximum visibility of 98.8% (H/V basis). It is important for us to examine how well these values are maintained as the power is increased. Figure 3.43 shows the decreasing trends in visibility from all four polarization bases measurements. In particular, the visibility of D/A bases drops below 90% when the pump power reaches 10 mW. One reason could be attributed to the issue of mode hopping effect that arises with increasing power. Figure 3.45 depicts the spectra of the pump, signal and idler photons obtained while increasing the pump power. The laser we use operates in not exactly a single frequency mode. Additionally, as evident in the spectra of the pump mode, increasing the power causes the pump wavelength to shift towards the right. As explained earlier in the process of obtaining the data shown in Figure 3.42, the mode hopping effect is observed in both the signal and idler modes when the pump power exceeds 4 mW. When we draw dashed lines representing the positions of the pump peak at the far left and far right in the spectra, assuming that our original temperature of 107.6 °C is maintained, we find that the the signal and idler wavelengths achieved by the QPM with the shifted pump wavelength exactly correspond to the peak positions shownw in the signal and idler spectra. From this observation, we can be confident that the mode hopping originated from the shift in the pump wavelength. The overall phase shift due to the wavelength shift of the pump wavelength affects the visibility in the following manner.[78]

$$V = \frac{1}{2}(1 + \cos \Delta\phi) \tag{3.70}$$

Figure 3.44 illustrates the impact of the phase change caused by the shift in the pump wavelength on the visibility. We see that, in fact, the visibility would drop below 90%

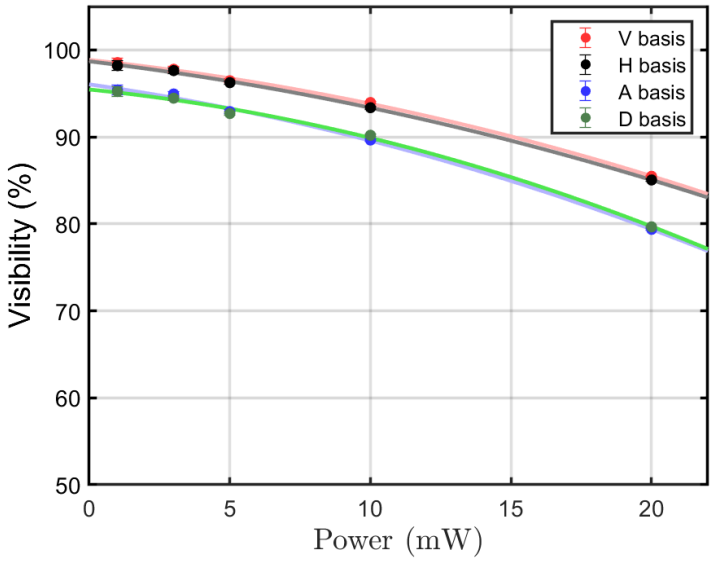

Figure 3.43: Graph showing the measured entanglement visibility across different pump powers for the four polarization bases.

when the pump wavelength is shifted by 0.05 nm. Considering the changes in phase and

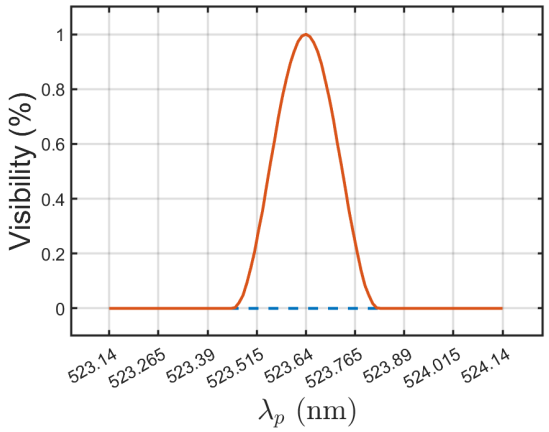

Figure 3.44: Graph showing a theoretical curve of the changes in entanglement visibility across different pump wavelength, assuming the peak visibility is 100% at $\lambda_p = 523.64$ nm.

walk-offs when the wavelengths of pump, signal and idler photons shift, we can conclude

that the drop in visibilities was an inevitable consequence. Therefore, the entanglement visibility could be improved by using either a single-frequency (more sharp bandwidth) laser or a narrower spectral filters or both. Another possible cause for the decrease in visibility could be the multi-photon pair generation events. The accidental-to-coincidence ratio (D basis, for instance) at 20 mW of pump power was calculated to be $N_s N_i \Delta t / N_c \approx 0.073$, indicating approximately 7.3% chances of an uncorrelated coincidence detection. Accidental coincidences may arise from detector dark counts, multi-photon pair generation [49]. The issue can also be addressed by using detectors and a time tagger with a better timing resolution (a narrower coincidence window).

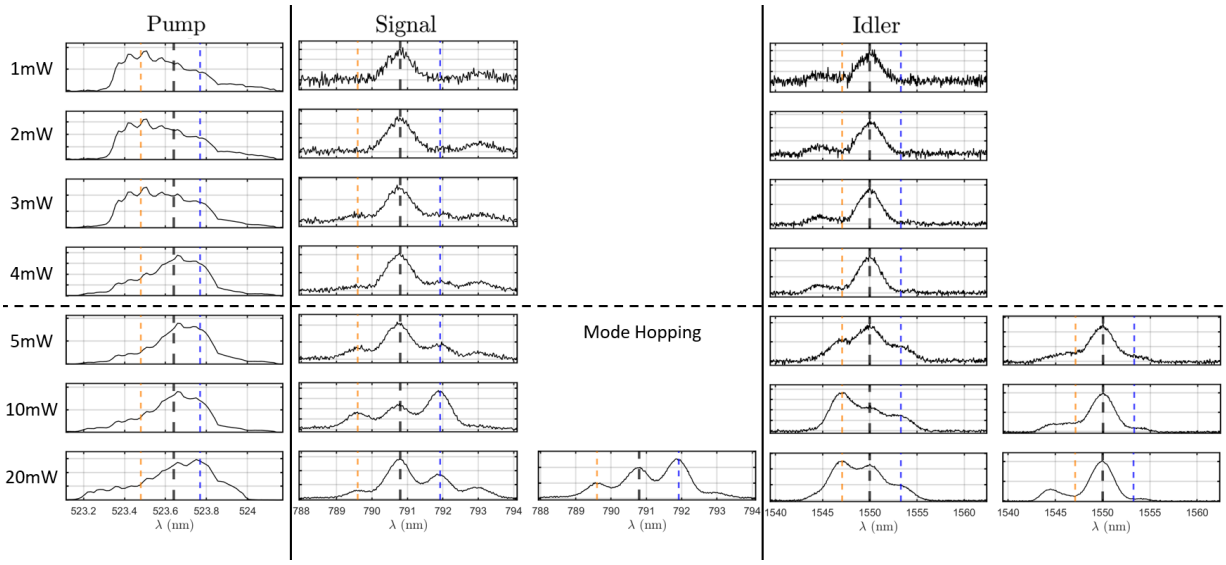

Figure 3.45: Spectra showing the mode hopping effects in the pump, signal, and idler modes across varying pump powers. The black dashed lines represent the positions of the pump, signal and idler photon wavelengths that we would expect from our QPM condition. Meanwhile, the orange dashed lines and the blue dashed lines represent the left and right positions where the unwanted peaks are observed. Two spectra captured at different time points are shown to illustrate the deformations caused by the mode hopping in the signal mode at 20 mW of pump power. Similarly, two spectra are shown for each 5 mW, 10 mW and 20 mW of pump power to show the mode hopping occuring in the idler mode.

Table 3.2 shows the performances of the different types of EPS built by the QPL team, including the EPS presented here (first item). The EPS made with a Periodically Poled Potassium Titanyl Phosphate (PPKTP) crystal and consisting of a Sagnac loop has a high heralding efficiency, and narrow bandwidths. However, the wavelengths of the signal and

Material (Type)	**Interferometer**	λ_s, λ_i	$\Delta\lambda_s, \Delta\lambda_i$	R_{pair} **(1mW)**	η_{pair}	**References**
PPLN (Type0)	BD & Sagnac	791nm, 1550nm	0.66nm, 2.61nm	2.92 MHz	11%	This work
PPKTP (Type2)	Sagnac	776nm, 842nm	0.3nm, 0.3nm	0.808 MHz	35%	[12]
PM fiber (Type1)	BD & Sagnac	764nm, 1220nm,	1.14nm, 4nm	0.001 MHz	22%	[65]
PPLN waveguide (Type0)	N/A	785nm, 834nm	2nm, 5nm	708 MHz	6%	[97]
PPKTP (Type0)	BD	780nm, 842nm	3nm, 3nm	0.3 MHz	19%	[69]

Table 3.2: Comparison of other EPS built by QPL team. The first item shows the EPS presented in this thesis; $\lambda_{S(I)}$ are the central wavelengths of signal (idler) photons; $\Delta\lambda_{S(I)}$ are their spectral bandwidths (from FWHM); R_{pair} is the photon pair emission rate; η_{pair} is the pair heralding efficiency.

idler photons are not suitable for QEYSSat. Furthermore, attaining a pair rate of 100 MHz would require a pump power of 124 mW, presenting a challenge ini finding a commercially available laser with such high power output and low noise characteristics comparable to our current laser. The EPS built using a PM fiber also exhibits an inadequate pair rate for QEYSSat, despite its production of degenerate photon wavelengths that are closest to our signal and idler photon wavelengths. The EPS built using a PPLN waveguide has the highest pair rate, even much higher than the pair rate achieved by our EPS. However, it not only has wide bandwidths (making it vulnerable to atmospheric effects due to large dispersion), but it has also shown a significant amount of fluorescence noise, which is a contributing factor to increasing the QBER.[97] As of now, although there are tasks (such as improving entanglement visibility) that were previously addressed, the EPS presented here shows specifications that make it the most suitable for use in QEYSSat compared to other EPSs listed on the table. It is worth noting that utilizing both the beam displacer scheme and the Sagnac loop scheme necessitate the integration of numerous optical components in constructing our EPS, thereby leading to an overall decrease in efficiency. Therefore, another improvement suggested for future enhancements of the EPS presented in this paper is the enhancement of pair heralding efficiency $\eta_{pair} = N_c/\sqrt{N_s N_i}$ by finding optical components with higher performances.

Chapter 4

Radiation Test

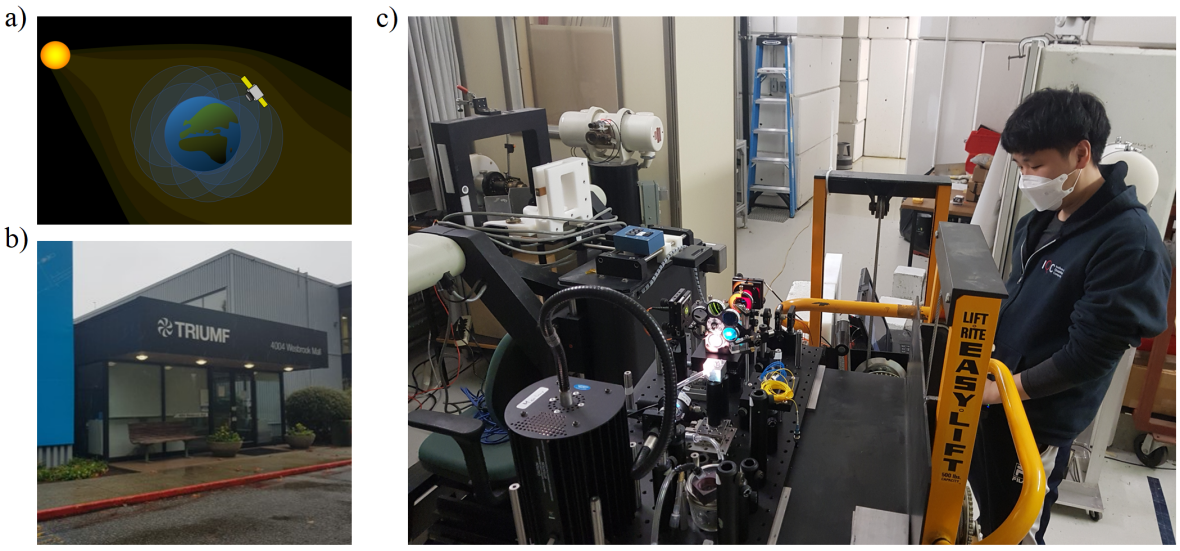

Figure 4.1: (a) A diagram illustrating the exposure of a satellite to various forms of space radiation, including solar radiation. (b) Entrance building of TRIUMF, Canada's particle accelerator centre. (c) The photo was taken during the radiation test conducted in the radiation chamber at TRIUMF in December 2020.

Although this thesis focuses solely on uplink QKD, our group is working towards future quantum communication missions involving the demonstration of downlink QKD [19]. To study downlink QKD, we shall consider the case where the EPS is integrated into the

satellite and deployed into space.

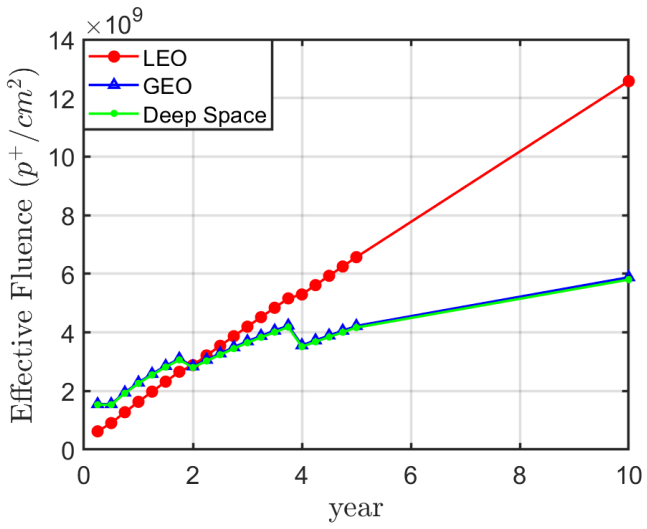

Figure 4.2: Effective proton fluence over time in space. The data is provided by the European Space Agency (ESA)'s Space Environment Information System (SPENVIS) system, which is an open-source of space radiation simulations [60]. The saw-tooth pattern observed in the graph arises from a change in the confidence intervals of the measurement model, which becomes smaller as the duration increases [98, 61].

As shown in Figure 4.2, the measurement of trapped ions reveals lower levels at high altitudes such as Geosynchronous Equatorial Orbit (GEO). Conversely, at lower altitudes like LEO, the detection of ions trapped by Earth's magnetic field, particularly protons, electrons, and heavy ions, is evident. This underscores the necessity for us to anticipate the operational performance of the quantum source, which incorporates a nonlinear optical material, when integrated into a LEO satellite in the future. In Vancouver, at TRIUMF, the cyclotron is capable of achieving a decade's worth of proton radiation exposure at LEO (i.e,$\sim 10^{10} protons/cm^2$) in a few minutes. Therefore, we conducted tests at this facility to assess the transmittivity changes of the nonlinear optical materials that could be used for the quantum source. We tested with three distinct nonlinear crystals : Beta Barium Borate (BBO), Potassium Titanyl Phosphate (KTP) and Lithium Niobate (LN). Given the substantial cost associated with utilizing TRIUMF's cyclotron, we have designed a crystal holder to maximize efficiency in testing, allowing for the most time-effective experiments.

Statement of contribution

1. **Radiation test :** Prof. Thomas Jennewein conceived the idea of conducting radiation test at TRIUMF (BC, Canada). I designed the test setup, and conducted the radiation test experimentally at TRIUMF. Joanna Krynski and Paul Godin assisted me with the experiment. I wrote Matlab codes to perform the analysis.

2. **Customization of crystal holder :** I designed and constructed a crystal holder that can hold three crystals using the air suction method. I confirmed its performance experimentally.

4.0.1 Experimental Setup

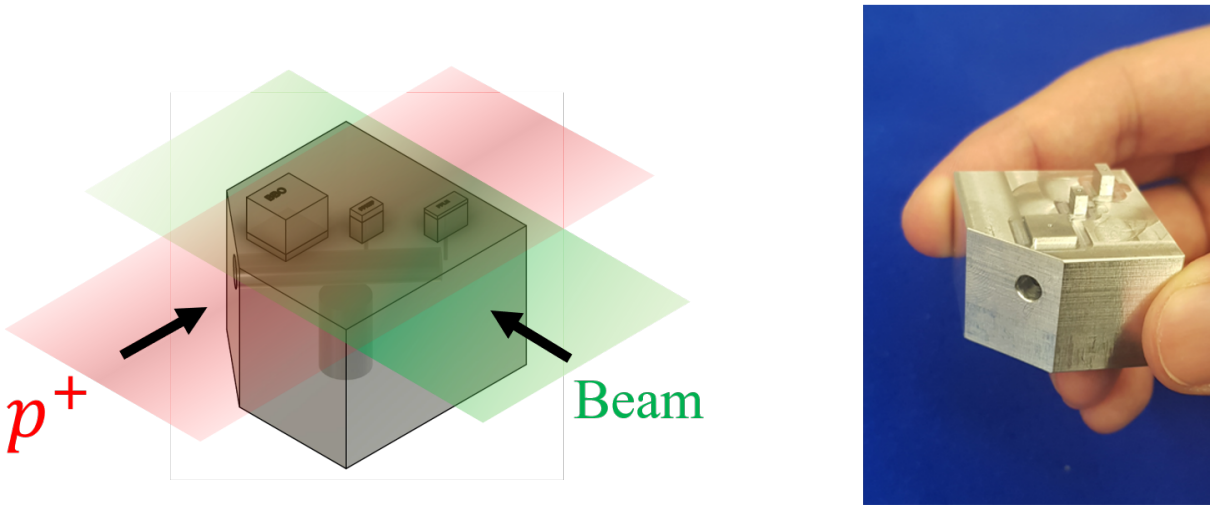

Figure 4.3: Left : A diagram illustrating the paths of the LED beam (green) and the proton radiation beam on the crystal holder. Right : Photo of the customized crystal holder.

Figure 4.3 illustrates our custom-made crystal oven. Three crystals are mounted diagonally in a row, and the heights of the bases on which the crystals are placed were carefully considered to ensure that the beam used to verify transmittivity passes through the central points of all three crystals. When verifying the transmittivity, the beam is focused on a single crystal at a time. Hence, a micrometer is used to remotely translate the crystal holder for each measurement. Due to the risk of crystals breaking when glued to the surface and later detached, we adopted a method of mounting them on the holder using air

suction. Small holes are drilled at the center of each of the three bases where the crystals are placed, creating passages that connect the three holes inside the holder. This allows air to be suctioned through those passages. Taking into account the maximum acceleration of the micrometer, which moves the crystal holder at $4mm/s^2$, we calculate the minimum air suction force required to withstand this acceleration. The calculation was done considering LN crystal which is the lighest among the three prepared crystals.

$$\vec{F}_{suction} > \vec{F}_{micrometer} - \vec{F}_{friction} \tag{4.1}$$

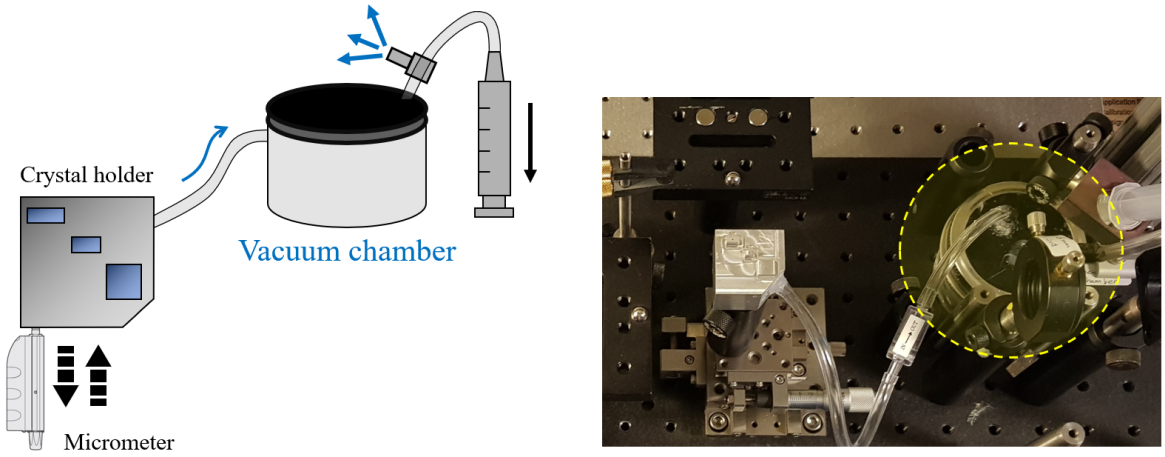

Figure 4.4: A diagram illustrating the mechanism of a custom-designed vacuum system (left). The actual photo of the vacuum chamber installed in the radiation test setup (right).

The crystal holder is connected to a 125 mL glass container through a plastic hose, and the glass container, which serves as a vacuum chamber, is connected to a syringe capable of extracting air (refer to Figure 4.4). The volume of the glass container was determined by the amount of pressure needed to generate the suction force, $\vec{F}_{suction}$. Since we are calculating the minimum suction force required to prevent the crystals from slipping, a rough upper bound calculation was sufficient for determining the volume of the container. To create a vacuum equivalent to the volume of the vacuum chamber, air is sucked in with a syringe until it is pumpable by hand, and then expelled through a T-valve.

We designed a measurement setup for the proton radiation exposure. Considering that a proton beam is incident in the direction shown in Figure 4.5, the transmittivity changes of crystals and optical components due to radiation are measured in real-time. For broad

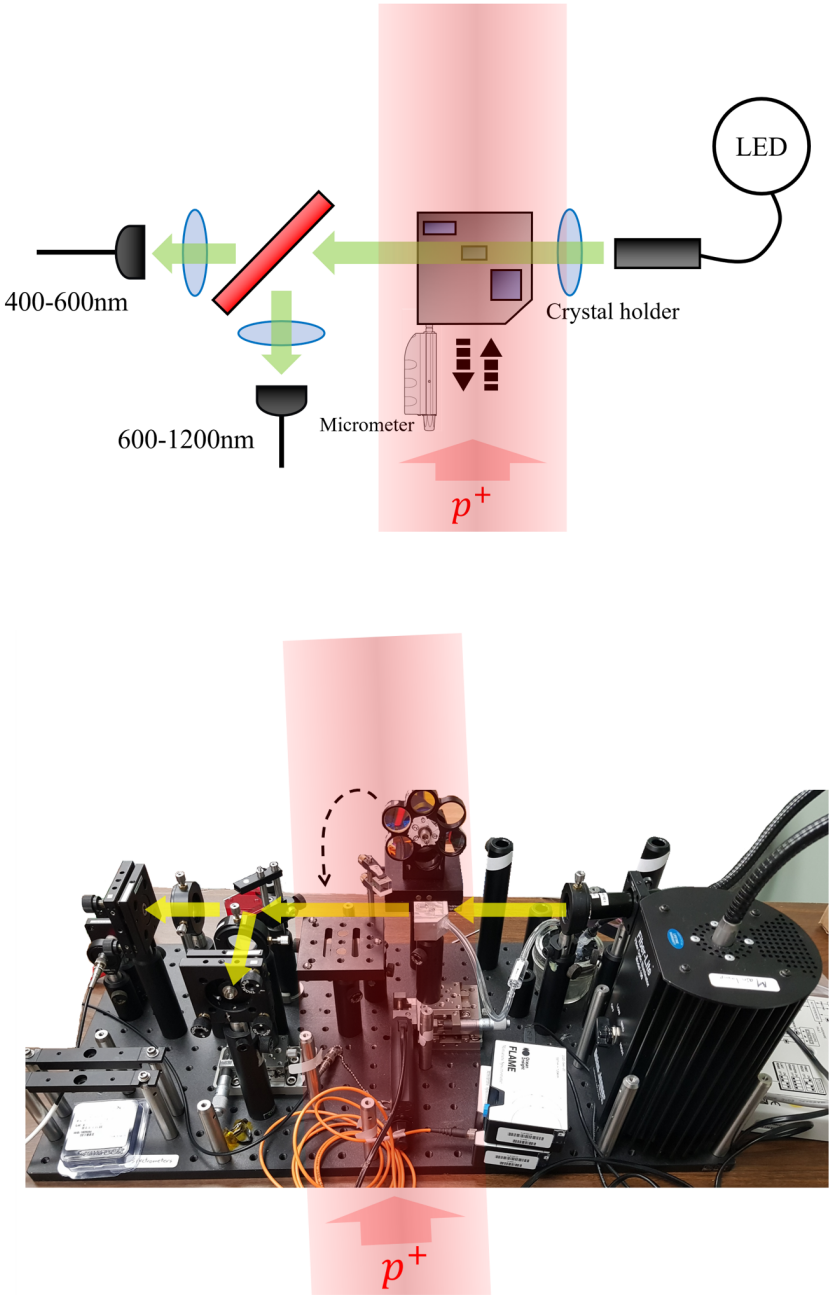

Figure 4.5: The top figure shows the design of the radiation test setup. The bottom figure shows the actual setup built for the test. The regions highlighted in red indicates the area of the path that has been exposed to proton radiation. The yellow and green arrows are the path of the LED light.

wavelength range scanning, an LED lamp was employed as the light source. Moreover, for precise transmittivity measurements, the beam from the LED lamp was focused at the location of the crystals by a focal lens. The transmittivity change is measured by two mini spectrometers (Ocean Insight, US). Due to the limited wavelength range of these two spectrometers, it is necessary to incorporate a dichroic mirror to split the beam passing through the crystal into two for the measurements. For precise measurements, background intensity measurements $I_{0,i}, I_{0,f}$ and intensity measurements with the crystals I_i, I_f are taken both before and after the radiation exposure. The relative transmission is then calculated by determining the ratio of the measurements after exposure to those taken before exposure.

$$T_{rel} = \frac{I_f/I_{0,f}}{I_i/I_{0,i}} \tag{4.2}$$

4.0.2 Radiation Damage Tests and Analysis

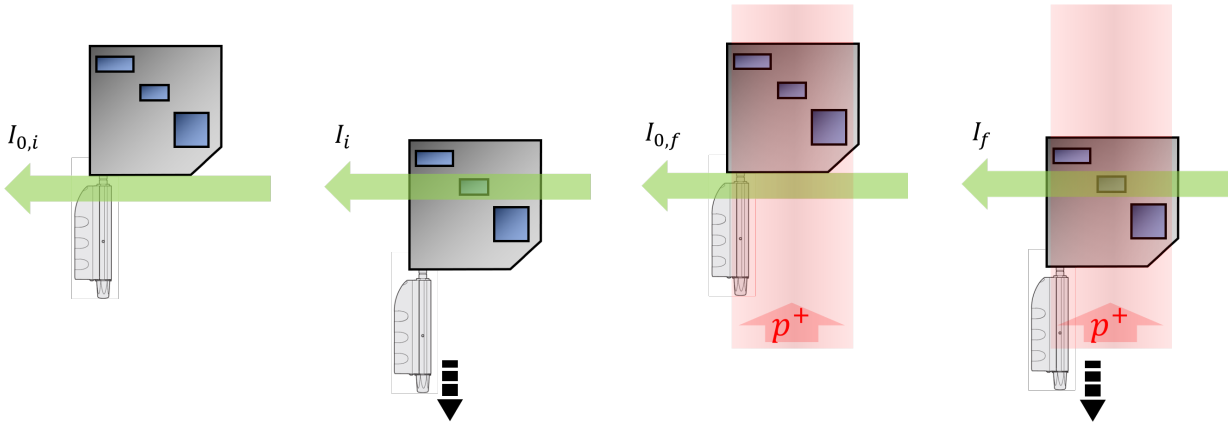

Figure 4.6: Scanning process of the crystals on the customized crystal holder.

We ran the experiment with the aim of exposing the optical setup to a proton radiation dose equivalent to the amount accumulated over 10 years in space (i.e, $\sim 10^{10}\ p^+/cm^2$ from Figure 4.2). The cyclotron delivered a proton beam at $116MeV$ energy through BL2C line. Testing with protons of such energy is reasonable, as it is known that the number of protons occupying space decreases significantly beyond $100MeV$ [73]. To observe changes in transmission, we exposed the setup to proton radiation amounts equivalent to 3 months, 6 months, and 1 year, followed by progressively increasing the exposure each subsequent

year until reaching a dose equivalent to 10 years' worth of proton radiation in space[1]. For safety reasons, our group conducted experiments remotely from outside the radiation chamber. For each radiation exposure, we used a micrometer to remotely translate the crystal holder, obtaining the spectrum of each crystal (illustrated in Figure 4.6).

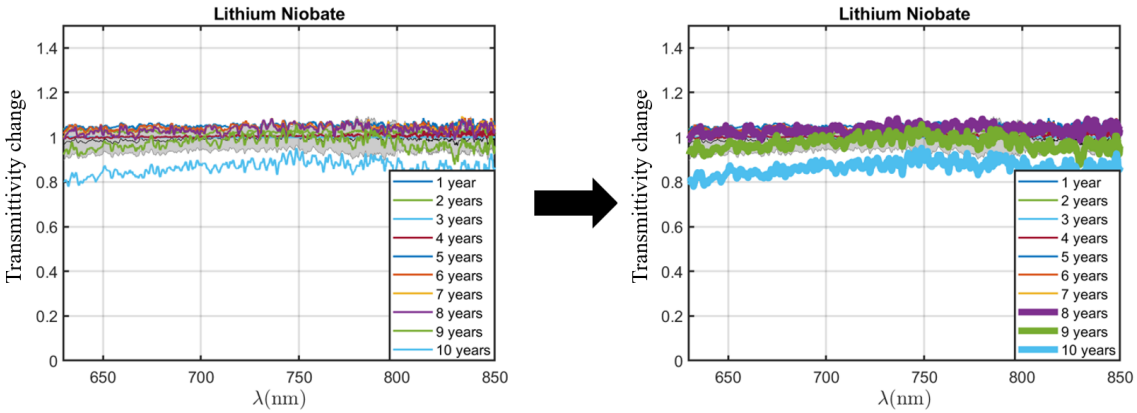

Figure 4.7: Graphs showing the changes in transmittivity of LN crystal due to proton radiation exposure, ranging from equivalent of 1 year to 10 years in space. The shaded region (left plot) is the 95% confidence interval of the transmittivity values from the 1^{st} year. The transmittivities corresponding the 8^{th}, 9^{th} and 10^{th} years are highlighted in the right plot to improve visibility of the lines.

The experimental results overall provided us with somewhat insignificant yet positive indications[2]. Figure 4.8 indicates that neither the BBO nor the KTP crystals exhibit performance degradation due to exposure of proton radiation equivalent to 10 years in space. Both the transmission quality of BBO and KTP crystals shows little variation, remaining within the 95% confidence interval of the transmittivity values from the 1^{st} year. Concerning the transmittivity change of LN, as shown in Figure 4.7, the transmission qualities up until the 9^{th} year show little variation that remains within the 95% confidence interval (shaded region in the left plot of Figure 4.7) of the transmittivity values from the 1^{st} year. The only year transmittivity line that falls distinctly outside the 95% confidence interval of the 1-year transmittivity line is from the 10-year spectrum. This implies that there should be no concerns regarding the future implementation of download QKD, where

[1]However, the proton radiation equivalent to durations of 3 and 6 months in space had minimal impact on the change in transmittivity of all three crystals. As a result, they are excluded from the graphs shown in Figure 4.7 and 4.8.

[2]The insignificance is also observed in other papers [86, 31].

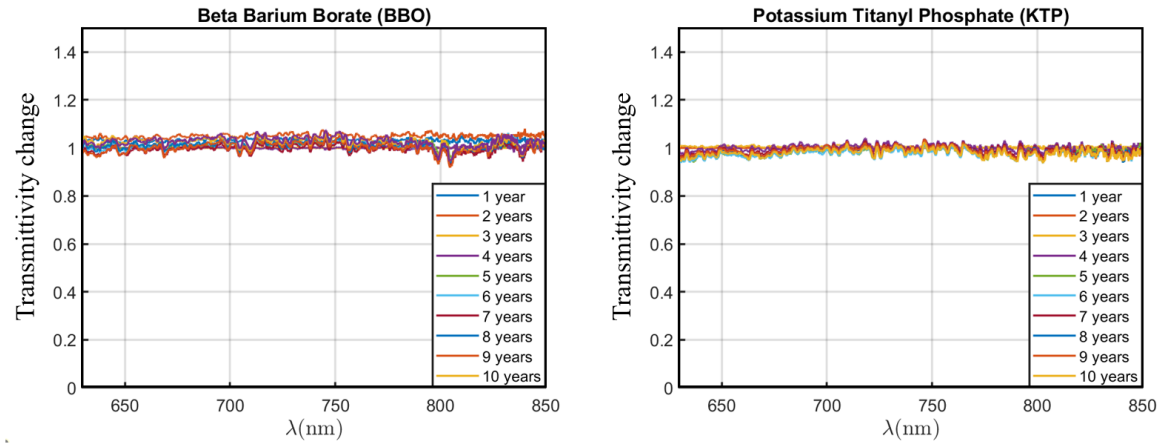

Figure 4.8: Graphs showing the changes in transmittivities of BBO and KTP crystal due to proton radiation exposure, ranging from equivalent of 1 year to 10 years in space.

the EPS, with the LN crystal mounted on it, will be deployed in space. This assumes that CSA intends to operate the downlink QKD for a similar duration of about 2 years as they plan for the uplink [4].

Figure 4.9: A proton-radiated photograph of the radiation test setup. The film was also exposed to the proton radiation by being positioned in front of the test setup, along the proton beam path.

Chapter 5

Conclusion and Outlook

The work presented in Chapter 2 focused on theoretical modelling and experimental validation of the long-distance quantum link. This study and testing contributed to understanding the link attenuation for the QEYSSat mission. We demonstrated the LEO satellite tracking test by tracking the ISS. Based on the remarkable alignment observed between the predicted path of the ISS using SGP4 and its actual trajectory, it became evident that the SGP4 algorithm is well-suited for tracking LEOsatellites, despite the substandard movement quality of the telescope motor mount that was used for the tests. The pointing error of the motor mount that we used was calculated to be 5.2×10^{-4} rads, which would result in approximately $\mathcal{L} \approx 72$ dB link attenuation. This indicates a significant contribution to the loss of quantum signal. By confirming experimentally that the ISS being within 1000 km (from the tracking site) lasts approximately 2 minutes, we expect QEYSSat to appear for around the same duration for the QKD demonstration. After conducting an analysis of atmospheric properties and considering technical constraints, it was determined that the optimal configuration for the ground-to-space QKD demonstration would involve a signal wavelength of 790 nm for free-space transmission, coupled with a wavelength of 1550 nm for ground-based transmission. Additionally, using these wavelengths along with the link length estimated from the tracking test, we determined the optimal aperture size of the transmitter telescope to be 20 cm. As a summary, having established all parameters (with the exception of adopting a reasonable value for the pointing error), the estimated overall quantum link loss is approximately 37.5 dB.

We also conducted light pollution measurement and analysis to investigate the amount background noise that could affect the visibility of the QKD. Firstly, rather than directly measuring the background noise originating from moonlight, we established the validity of using observations of light from stars to infer the amount of light present. This approach

provided some degree of assurance regarding the applicability of the blackbody radiation function. For instance, the theoretically estimated number of photons received from Vega is $N_{theo} = 9.7 \times 10^5$Hz, and the experimentally measured value was $N_{exp} = 5.7 \times 10^5$Hz, suggesting a reasonable level of agreement between the two values. Having gained some confidence in estimating the background photons from moonlight using blackbody function, we arrived at a worst-case scenario estimate of $N_{ML} = 863$ Hz for photons originating from moonlight. Also, we estimate that the photons that the receiver telescope in the satellite would receive are about 1.4×10^{-4} Hz, indicating that starlight is a negligible background source. Next, we experimentally examined the light pollution coming from the parking lot next to our OQGS. Using the two methods presented in Section 2.3.1, we were able to estimate that the light pollution within the wavelength range of 790 ± 5 nm emitted from the parking lot during a full moon is about $N_{LP} = 2000$ Hz. Combining the background noise from both moonlight and light pollution, we anticipate the receiver telescope to experience a background photon noise level of approximately 3000 Hz. In summary, Chapter 2 helped us to determine that the minimum required photon pair rate is 100 MHz.

In Chapter 3 we presented the complete development process of the EPS. Through experimental validation, our PPLN crystal experimentally demonstrated its ability to achieve a QPM condition of $523.64\,\text{nm} \rightarrow 790.8\,\text{nm} + 1550\,\text{nm}$. Also, the spectral bandwidths of the signal and idler photons were $\Delta\lambda_s = 0.66\,\text{nm}$ and $\Delta\lambda_i = 2.61\,\text{nm}$, respectively, nicely agreeing with our theoretical predictions. The customization process of the crystal oven and its functionalities are also presented. Although the initial intention of placing both crystals at the same temperature was not achieved due less heat transfer to the top copper plate than the bottom copper plate, the issue was resolved by attaching a power resistor to the top copper plate to feed extra voltage power, effectively equilizing the temperature of the two crystals. Simultaneous compensation for the spatial and temporal walk-offs using Calcite wedges has made a significant contribution to optimizing both the coincidence counts and the visibility. Prior to any compensation, the coincidence counts at $P = 1\,\text{mW}$ was $N_c = 4.2\,\text{kHz}$, which improved to $N_c = 33.3\,\text{kHz}$ after full spatial walk-off compensation. The visibility was also enhanced, reaching up to 95%, through simultaneous temporal compensation. The photon pair emission rate was calculated to be $R_{pair} = 2.92 \pm 0.12\,\text{MHz}$ which nicely agrees with the theoretical value of $R_{theo} = 2.82\,\text{MHz}$. However, at high power, the phase instability caused by the laser's mode hopping effect led to significant fluctuations in visibility, providing the necessity for a single-frequency laser to resolve this issue. Nevertheless, as seen in table 3.2, we can conclude that among the EPSs developed so far, this one is the most suitable source for ground-to-space quantum links.

Lastly, in Chapter 4, we tested how well crystals can maintain performance under proton radiation for potential downlink applications ini the future. Based on the experi-

mental results,it is conjectured that LN, BBO and KTP crystals will experience minimal performances degradation from proton radiation in space over several years. However, limitations in theoretical modelling implies that further validation for accurate assessment will be needed in the future.

The work presented in this thesis shows several advancements in the EPS for long-distance entanglement-based QKD. We plan to commercialize the EPS by enhancing the robustness and compactness of the interferometer, as illustrated in Figure 5.1. Our current EPS setup has a dimension of 24"×24". The miniaturized interferometer shown in Figure will have a dimension of 13"×15", such that it can be installed in the 19"×19" rack.

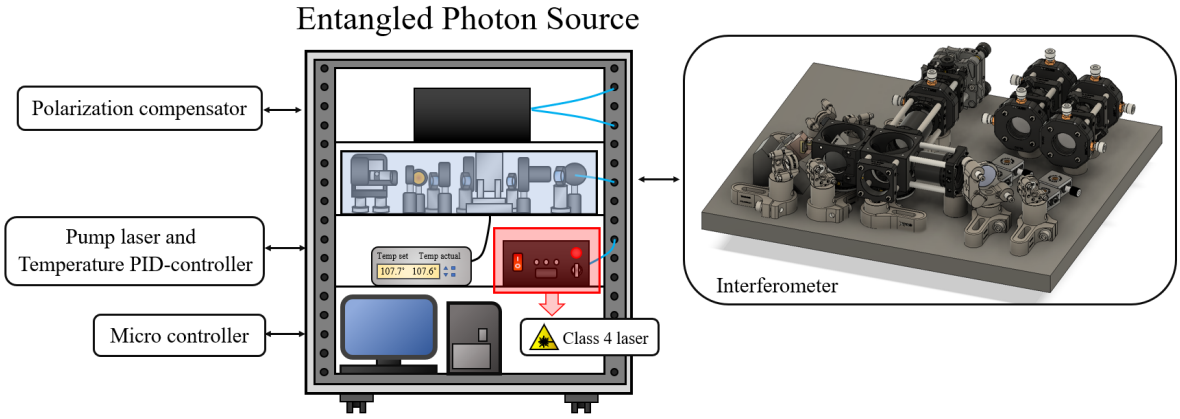

Figure 5.1: Schematic diagram detailing the construction plan for the EPS rack. The 3-D figure on the right depicts the miniaturized EPS design.

Note that this miniaturization plan also includes miniaturizing the custom-designed crystal oven. Additionally, with financial support from the CSA, we aim to procure optical components with enhanced specifications for the forthcoming prototype, thereby improving the performance of the EPS. The photon pair rate can improve upon the nonlinear coefficient of the crystal. Exploring methods to enhance the pair rate generation capability of crystals appears to be another important future task that we will have to consider. The EPS rack will encompass all necessary components for the EPS, including the CW laser and the temperature controller for the crystal oven. In the rack, the laser and the temperature controller will be controllable by a single computer. Finally, the photon pairs generated by the EPS will pass through a polarization compensator, also installed in the rack, to ensure correction of any polarization drift. Recently, our research team has agreed that due to significant losses in the fiber connecting the EPS and telescope, as well as losses due to the intensity pick-off, setting 100 MHz as a lower bound is overly optimistic.

Therefore, there is a need for further discussion in defining the lower bound in the future.

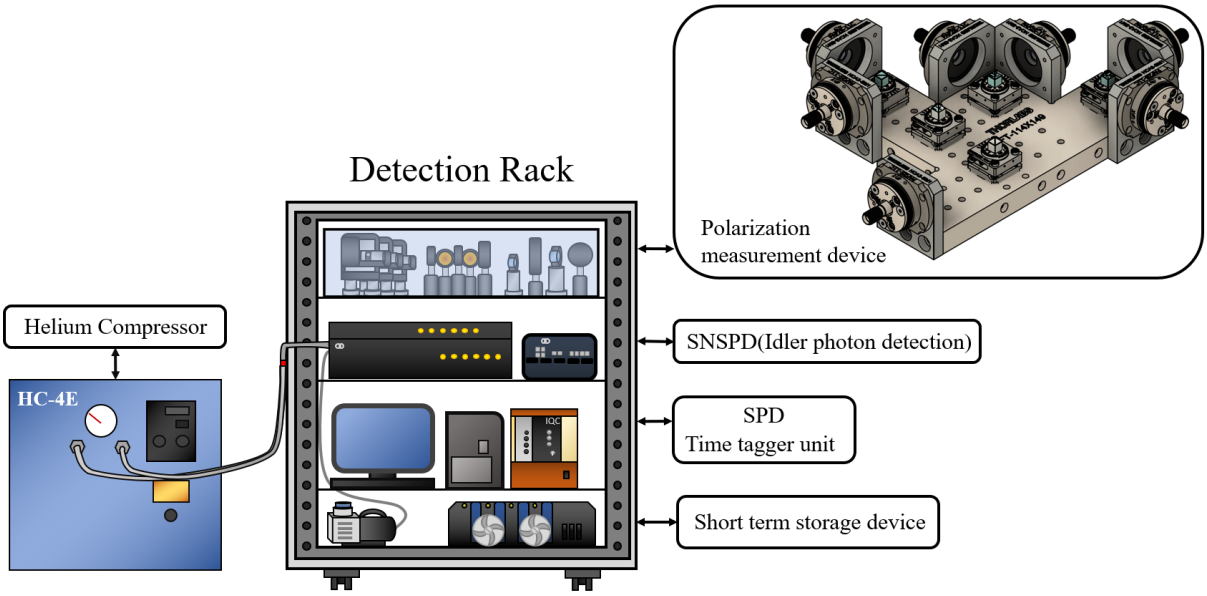

Figure 5.2: Schematic diagram detailing the construction plan for the detection rack.

The 19"×19" detection rack will serve as the platform for the measurement system responsible for detecting the idler photons with a wavelength of 1550 nm using a 6-state analyzer, as illustrated in Figure 5.2. The rack will also be equipped with SNSPD necessary for photodetection, along with a time-tagging unit capable of capturing coincidence events between signals sent from the satellite and those detected by the SNSPD. These coincidence detections captured by the time tagger will be sent to a computer installed inside the rack, used as quantum information for performing QKD. Furthermore, we plan to have a short-term storage device in the rack for temporarily storing data needed during the satellite pass. The SNSPD requires a helium compressor to maintain low temperatures, but the current model we are using is too bulky to be accommodated within the rack. Therefore, alternatives will be explored, such as installing the compressor adjacent to the rack or seeking out other options that demonstrate sufficient performance while being sized to fit within the rack. We aim to establish these systems by the end of this year (2024), with the belief that this thesis will contribute significantly.

References

[1] Laboratory spectra - noaa, online source (last accessed in april 2024): $ngdc.noaa.gov/eog/night_sat/spectra.html$.

[2] Mgo:ppln - covesion ltd., online source (last accessed in april 2024): $www.neotron.co.jp/covesion/ppln_catal.pdf$.

[3] Optical fiber channel loss - thorlab.inc, online source (last accessed in april 2024) : $www.thorlabs.com/newgrouppage9.cfm?objectgroup_id = 1362$.

[4] Qeyssat mission - canadian space agency, online source (last accessed in april 2024) : $www.asc - csa.gc.ca/eng/satellites/qeyssat.asp$.

[5] Satellite drag - noaa, online source (last accessed in april 2024) : $www.swpc.noaa.gov/impacts/satellite - drag$.

[6] Spec sheet of snspd - quantum opus, online source (last accessed in april 2024) : $www.quantumopus.com/web/product - info$.

[7] Spec sheet of spad - excelitas technologies, online source (last accessed in april 2024) : $www.excelitas.com/product - category/low - light - level - detection - modules$.

[8] Two line element - celestrak, online source (last accessed in april 2024) : $celestrak.org/norad/elements/$.

[9] Viirs data catalog - earthdata, online source (last accessed in april 2024) : $rammb.cira.colostate.edu/projects/npp/viirs_bands_and_bandwidths.pdf$.

[10] Viirs day/night band spectrum - earthdata, online source (last accessed in april 2024) : $www.earthdata.nasa.gov/learn/find - data/near - real - time/viirs$.

[11] Viirs satellite - earthdata, online source (last accessed in april 2024) : $www.earthdata.nasa.gov/learn/find-data/near-real-time/viirs$.

[12] Sascha Agne, Thomas Kauten, Jeongwan Jin, Evan Meyer-Scott, Jeff Z. Salvail, Deny R. Hamel, Kevin J. Resch, Gregor Weihs, and Thomas Jennewein. Observation of genuine three-photon interference. *Physical Review Letters*, 118(15), April 2017.

[13] Dwight E. Andersen. Computing norad mean orbital elements from a state vector, Dec 1994.

[14] J. S. Bell. On the einstein podolsky rosen paradox. *Physics Physique Fizika*, 1:195–200, Nov 1964.

[15] Charles H. Bennett and Gilles Brassard. Quantum cryptography: Public key distribution and coin tossing. *Theoretical Computer Science*, 560:7–11, December 2014.

[16] Ryan S. Bennink. Optimal collinear gaussian beams for spontaneous parametric down-conversion. *Physical Review A*, 81(5), May 2010.

[17] C Bonato, A Tomaello, V Da Deppo, G Naletto, and P Villoresi. Feasibility of satellite quantum key distribution. *New Journal of Physics*, 11(4):045017, apr 2009.

[18] Max Born. *Statistical Interpretation of Quantum Mechanics*, pages 89–99. Springer Berlin Heidelberg, Berlin, Heidelberg, 1969.

[19] J-P Bourgoin, E Meyer-Scott, B L Higgins, B Helou, C Erven, H Hübel, B Kumar, D Hudson, I DSouza, R Girard, R Laflamme, and T Jennewein. A comprehensive design and performance analysis of low earth orbit satellite quantum communication. *New Journal of Physics*, 15(2):023006, February 2013.

[20] J-P Bourgoin, E Meyer-Scott, B L Higgins, B Helou, C Erven, H Hübel, B Kumar, D Hudson, I DSouza, R Girard, R Laflamme, and T Jennewein. Corrigendum: A comprehensive design and performance analysis of low earth orbit satellite quantum communication (2013 new j. phys. 15 023006). *New Journal of Physics*, 16(6):069502, jun 2014.

[21] Jean-Philippe Bourgoin, Nikolay Gigov, Brendon L. Higgins, Zhizhong Yan, Evan Meyer-Scott, Amir K. Khandani, Norbert Lütkenhaus, and Thomas Jennewein. Experimental quantum key distribution with simulated ground-to-satellite photon losses and processing limitations. *Phys. Rev. A*, 92:052339, Nov 2015.

[22] GD Boyd and DA Kleinman. Parametric interaction of focused gaussian light beams. *Journal of Applied Physics*, 39(8):3597–3639, 1968.

[23] Robert W. Boyd. *Nonlinear Optics, Third Edition*. Academic Press, Inc., USA, 3rd edition, 2008.

[24] Gilles Brassard, Norbert Lütkenhaus, Tal Mor, and Barry C. Sanders. Limitations on practical quantum cryptography. *Physical Review Letters*, 85(6):1330–1333, August 2000.

[25] H.-J. Briegel, W. Dür, J. I. Cirac, and P. Zoller. Quantum repeaters: The role of imperfect local operations in quantum communication. *Phys. Rev. Lett.*, 81:5932–5935, Dec 1998.

[26] Dagmar Bruß, David P. DiVincenzo, Artur Ekert, Christopher A. Fuchs, Chiara Macchiavello, and John A. Smolin. Optimal universal and state-dependent quantum cloning. *Physical Review A*, 57(4):2368–2378, April 1998.

[27] Changyong Cao, Bin Zhang, Frank Xia, and Yan Bai. Exploring viirs night light long-term time series with cnn/si for urban change detection and aerosol monitoring. *Remote Sensing*, 14(13), 2022.

[28] Silvia Carrasco, Alexander V. Sergienko, Bahaa E. A. Saleh, Malvin C. Teich, Juan P. Torres, and Lluis Torner. Spectral engineering of entangled two-photon states. *Phys. Rev. A*, 73:063802, Jun 2006.

[29] B. S. Cirel'son. Quantum generalizations of bell's inequality. *Letters in Mathematical Physics*, 4:93–100, 1980.

[30] John F. Clauser, Michael A. Horne, Abner Shimony, and Richard A. Holt. Proposed experiment to test local hidden-variable theories. *Phys. Rev. Lett.*, 23:880–884, Oct 1969.

[31] R. S. Coetzee, S. Duzellier, J. B. Dherbecourt, A. Zukauskas, M. Raybaut, and V. Pasiskevicius. Gamma irradiation-induced absorption in single-domain and periodically-poled ktiopo4 and rb:ktiopo4. *Opt. Mater. Express*, 7(11):4138–4146, Nov 2017.

[32] Shabtai Cohen and Gerald Stanhill. Chapter 32 - changes in the sun's radiation: the role of widespread surface solar radiation trends in climate change: dimming and brightening. In Trevor M. Letcher, editor, *Climate Change (Third Edition)*, pages 687–709. Elsevier, third edition edition, 2021.

[33] Arthur H. Compton. A quantum theory of the scattering of x-rays by light elements. *Phys. Rev.*, 21:483–502, May 1923.

[34] H.D. Curtis. *Orbital Mechanics for Engineering Students*. Elsevier aerospace engineering series. Elsevier Science & Technology Books, 2010.

[35] H.D. Curtis. *Orbital Mechanics: For Engineering Students*. Aerospace Engineering. Elsevier Science, 2015.

[36] P. Ben Dixon, Danna Rosenberg, Veronika Stelmakh, Matthew E. Grein, Ryan S. Bennink, Eric A. Dauler, Andrew J. Kerman, Richard J. Molnar, and Franco N. C. Wong. Heralding efficiency and correlated-mode coupling of near-ir fiber coupled photon pairs, 2014.

[37] Ido Dolev, Ayelet Ganany-Padowicz, Ofer Gayer, and Ady Arie. Temperature and wavelength dependent refractive index equation for stochiometric lithium tantalite. In *2008 IEEE 25th Convention of Electrical and Electronics Engineers in Israel*, pages 308–312, 2008.

[38] Hillger Don. Viirs information - viirs , online source (last accessed in april 2024) : *www.star.nesdis.noaa.gov/data/star*$_d$*ocs/meetings/*2017*jpssannual/cloudsimg/imagery.pdf*, 2017.

[39] A. Einstein. Über einen die Erzeugung und Verwandlung des Lichtes betreffenden heuristischen Gesichtspunkt. *Annalen der Physik*, 322(6):132–148, January 1905.

[40] Artur K. Ekert. Quantum cryptography based on bell's theorem. *Phys. Rev. Lett.*, 67:661–663, Aug 1991.

[41] Christopher D. Elvidge, Feng Chi Hsu, Mikhail Zhizhin, Tilottama Ghosh, and Tamara Sparks. Statistical moments of viirs night-time lights. *International Journal of Remote Sensing*, 0(0):1–25, 2023.

[42] Miao Er-long, Han Zheng-fu, Gong Shun-sheng, Zhang Tao, Diao Da-sheng, and Guo Guang-can. Background noise of satellite-to-ground quantum key distribution. *New Journal of Physics*, 7(1):215, oct 2005.

[43] David L. Fried and Jeffrey L. Vaughn. Branch cuts in the phase function. *Appl. Opt.*, 31(15):2865–2882, May 1992.

[44] Marissa Giustina, Marijn A. M. Versteegh, Sören Wengerowsky, Johannes Handsteiner, Armin Hochrainer, Kevin Phelan, Fabian Steinlechner, Johannes Kofler, Jan-Åke Larsson, Carlos Abellán, Waldimar Amaya, Valerio Pruneri, Morgan W. Mitchell, Jörn Beyer, Thomas Gerrits, Adriana E. Lita, Lynden K. Shalm, Sae Woo Nam, Thomas Scheidl, Rupert Ursin, Bernhard Wittmann, and Anton Zeilinger. Significant-loophole-free test of bell's theorem with entangled photons. *Phys. Rev. Lett.*, 115:250401, Dec 2015.

[45] O.L. Guerreau, F.J. Malassenet, S.W. McLaughlin, and J.-M. Merolla. Quantum key distribution without a single-photon source using a strong reference. *IEEE Photonics Technology Letters*, 17(8):1755–1757, 2005.

[46] Michael Hentschel, Hannes Hübel, Andreas Poppe, and Anton Zeilinger. Three-color sagnac source of polarization-entangled photon pairs. *Optics Express*, 17(25):23153, December 2009.

[47] M.V. Hobden and J. Warner. The temperature dependence of the refractive indices of pure lithium niobate. *Physics Letters*, 22(3):243–244, 1966.

[48] D. H. Höhn. Depolarization of a laser beam at 6328 å due to atmospheric transmission. *Appl. Opt.*, 8(2):367–369, Feb 1969.

[49] Masayuki Hojo, Shuntaro Tani, Yohei Kobayashi, and Koichiro Tanaka. Coincidence measurements of two quantum-correlated photon pairs widely separated in the frequency domain. *Scientific Reports*, 13(1):8520–, 5 2023.

[50] Felix R. Hoots and Ronald L. Roehrich. Models for propagation of norad element sets, Dec 1980.

[51] Won-Young Hwang. Quantum key distribution with high loss: Toward global secure communication. *Physical Review Letters*, 91(5), August 2003.

[52] Takahiro Inagaki, Nobuyuki Matsuda, Osamu Tadanaga, Masaki Asobe, and Hiroki Takesue. Entanglement distribution over 300 km of fiber. *Opt. Express*, 21(20):23241–23249, Oct 2013.

[53] Tanvirul Islam, Jasminder S. Sidhu, Brendon L. Higgins, Thomas Brougham, Tom Vergoossen, Daniel K. L. Oi, Thomas Jennewein, and Alexander Ling. Finite resource performance of small satellite-based quantum key distribution missions, 2024.

[54] Adarsh Jain, Parthkumar V Sakhiya, and R K Bahl. Design and development of weak coherent pulse source for quantum key distribution system. In *2020 IEEE International Conference on Electronics, Computing and Communication Technologies (CONECCT)*, pages 1–5, 2020.

[55] Thomas Jennewein, J. Bourgoin, B. Higgins, C. Holloway, Evan Meyer-Scott, Chris Erven, Bettina Heim, Zhizhong Yan, Hannes Hübel, Gregor Weihs, Enosh Choi, I. D'Souza, D. Hudson, and R. Laflamme. Qeyssat: A mission proposal for a quantum receiver in space. *Proceedings of SPIE - The International Society for Optical Engineering*, 8997, 01 2014.

[56] W. A. Joye and E. Mandel. New Features of SAOImage DS9. In H. E. Payne, R. I. Jedrzejewski, and R. N. Hook, editors, *Astronomical Data Analysis Software and Systems XII*, volume 295 of *Astronomical Society of the Pacific Conference Series*, page 489, January 2003.

[57] Richard Jozsa. A stronger no-cloning theorem, 2002.

[58] Yoon-Ho Kim, Sergei P. Kulik, and Yanhua Shih. Bell-state preparation using pulsed nondegenerate two-photon entanglement. *Physical Review A*, 63(6), May 2001.

[59] Boris Korzh, Charles Ci Wen Lim, Raphael Houlmann, Nicolas Gisin, Ming Jun Li, Daniel Nolan, Bruno Sanguinetti, Rob Thew, and Hugo Zbinden. Provably secure and practical quantum key distribution over 307km of optical fibre. *Nature Photonics*, 9(3):163–168, February 2015.

[60] Michel Kruglanski, N. Messios, Erwin De Donder, E. Gamby, Stijn Calders, Laszlo Hetey, and Hugh Evans. Space environment information system (spenvis). pages 7457–, 04 2009.

[61] Krynski, Joanna. Estimating and mitigating effects of space radiation damage in single-photon avalanche diodes. Master's thesis, 2022.

[62] Chiang KwoFu. Zwo camera specification sheet - zwo, online source (last accessed in april 2024) : $astronomy - imaging - camera.com/product/asi183mm - mono/$.

[63] Chiang KwoFu. Nasa revision to the joint polar satellite system (jpss) viirs radiometric calibration algorithm theoretical basis document (atbd), 2014.

[64] Christopher C. M. Kyba, Theres Kuester, Alejandro Sánchez de Miguel, Kimberly Baugh, Andreas Jechow, Franz Hölker, Jonathan Bennie, Christopher D. Elvidge,

Kevin J. Gaston, and Luis Guanter. Artificially lit surface of earth at night increasing in radiance and extent. *Science Advances*, 3(11):e1701528, 2017.

[65] Youn Seok Lee, Mengyu Xie, Ramy Tannous, and Thomas Jennewein. Sagnac-type entangled photon source using only conventional polarization optics, 2020.

[66] Debbie Leung and John Watrous. On the complementary quantum capacity of the depolarizing channel. *Quantum*, 1:28, September 2017.

[67] Alexander Ling, Antía Lamas-Linares, and Christian Kurtsiefer. Absolute emission rates of spontaneous parametric down-conversion into single transverse gaussian modes. *Physical Review A*, 77(4), April 2008.

[68] Hoi-Kwong Lo. Quantum key distribution with vacua or dim pulses as decoy states. In *International Symposium onInformation Theory, 2004. ISIT 2004. Proceedings.*, pages 137–, 2004.

[69] Alexander Lohrmann, Chithrabhanu Perumangatt, Aitor Villar, and Alexander Ling. Broadband pumped polarization entangled photon-pair source in a linear beam displacement interferometer. *Applied Physics Letters*, 116(2), January 2020.

[70] Robert L. Lucke. Rayleigh-sommerfeld fraunhofer diffraction, 2006.

[71] Norbert Lütkenhaus. Security against individual attacks for realistic quantum key distribution. *Physical Review A*, 61(5), April 2000.

[72] Grant Matthews. Celestial body irradiance determination from an underfilled satellite radiometer: application to albedo and thermal emission measurements of the moon using ceres. *Appl. Opt.*, 47(27):4981–4993, Sep 2008.

[73] Christopher Mertens, John Wilson, Steve Blattnig, Brian Kress, John Norbury, Michael Wiltberger, Stanley Solomon, and W Kent Tobiska. Influence of space weather on aircraft ionizing radiation exposure. *46th AIAA Aerospace Sciences Meeting and Exhibit*, 01 2008.

[74] Evan Meyer-Scott, Zhizhong Yan, Allison MacDonald, Jean-Philippe Bourgoin, Hannes Hübel, and Thomas Jennewein. How to implement decoy-state quantum key distribution for a satellite uplink with 50-db channel loss. *Physical Review A*, 84(6), December 2011.

[75] F. Miller. *Telegraphic Code to Insure Privacy and Secrecy in the Transmission of Telegrams*. C.M. Cornwell, 1882.

[76] Alicia Negre, Renaud Mathevet, Benoit Chalopin, and Sebastien Massenot. Unexpected optimal measurement protocols in bell's inequality violation experiments. *American Journal of Physics*, 91:64–73, 01 2023.

[77] James L. Park. The concept of transition in quantum mechanics. *Foundations of Physics*, 1:23–33, 1970.

[78] Brett J. Pearson and David P. Jackson. A hands-on introduction to single photons and quantum mechanics for undergraduates. *American Journal of Physics*, 78(5):471–484, May 2010.

[79] Cheng-Zhi Peng, Jun Zhang, Dong Yang, Wei-Bo Gao, Huai-Xin Ma, Hao Yin, He-Ping Zeng, Tao Yang, Xiang-Bin Wang, and Jian-Wei Pan. Experimental long-distance decoy-state quantum key distribution based on polarization encoding. *Phys. Rev. Lett.*, 98:010505, Jan 2007.

[80] Chithrabhanu Perumangatt, Alexander Lohrmann, and Alexander Ling. Experimental conversion of position correlation into polarization entanglement. *Physical Review A*, 102(1), July 2020.

[81] G. Peruzzo and S.P. Sorella. Entanglement and maximal violation of the chsh inequality in a system of two spins j: A novel construction and further observations. *Physics Letters A*, 474:128847, June 2023.

[82] Max Planck. On the Law of Distribution of Energy in the Normal Spectrum. *Annalen Phys.*, 4:553, 1901.

[83] Max Planck. On the theory of the energy distribution law of the normal spectrum†. 1967.

[84] Christopher J Pugh, Sarah Kaiser, Jean-Philippe Bourgoin, Jeongwan Jin, Nigar Sultana, Sascha Agne, Elena Anisimova, Vadim Makarov, Eric Choi, Brendon L Higgins, and Thomas Jennewein. Airborne demonstration of a quantum key distribution receiver payload. *Quantum Science and Technology*, 2(2):024009, June 2017.

[85] Jennifer C. Ricklin, Stephen M. Hammel, Frank D. Eaton, and Svetlana L. Lachinova. *Atmospheric channel effects on free-space laser communication*, pages 9–56. Springer New York, New York, NY, 2008.

[86] Ulrich Roth, Michael Tröbs, Thomas Graf, Jürg E. Balmer, and Heinz P. Weber. Proton and gamma radiation tests on nonlinear crystals. *Appl. Opt.*, 41(3):464–469, Jan 2002.

[87] Bahaa E A Saleh and Malvin Carl Teich. *Fundamentals of photonics; 2nd ed.* Wiley series in pure and applied optics. Wiley, New York, NY, 2007.

[88] Nicolas Sangouard, Christoph Simon, Hugues de Riedmatten, and Nicolas Gisin. Quantum repeaters based on atomic ensembles and linear optics, 2009.

[89] Valerio Scarani, Antonio Acín, Grégoire Ribordy, and Nicolas Gisin. Quantum cryptography protocols robust against photon number splitting attacks for weak laser pulse implementations. *Physical Review Letters*, 92(5), February 2004.

[90] Valerio Scarani, Helle Bechmann-Pasquinucci, Nicolas J. Cerf, Miloslav Dušek, Norbert Lütkenhaus, and Momtchil Peev. The security of practical quantum key distribution. *Reviews of Modern Physics*, 81(3):1301–1350, September 2009.

[91] Tobias Schmitt-Manderbach, Henning Weier, Martin Fürst, Rupert Ursin, Felix Tiefenbacher, Thomas Scheidl, Josep Perdigues, Zoran Sodnik, Christian Kurtsiefer, John G. Rarity, Anton Zeilinger, and Harald Weinfurter. Experimental demonstration of free-space decoy-state quantum key distribution over 144 km. *Phys. Rev. Lett.*, 98:010504, Jan 2007.

[92] E. Schrödinger. An undulatory theory of the mechanics of atoms and molecules. *Phys. Rev.*, 28:1049–1070, Dec 1926.

[93] Lijiong Shen, Chang Hoong Chow, Justin Yu Xiang Peh, Xi Jie Yeo, Peng Kian Tan, and Christian Kurtsiefer. Distributing polarization-entangled photon pairs with high rate over long distances through standard telecommunication fiber. *Physical Review Applied*, 18(4), October 2022.

[94] Yicheng Shi, Soe Moe Thar, Hou Shun Poh, James A. Grieve, Christian Kurtsiefer, and Alexander Ling. Stable polarization entanglement based quantum key distribution over a deployed metropolitan fiber. *Applied Physics Letters*, 117(12), September 2020.

[95] Justin B. Spring, Paolo L. Mennea, Benjamin J. Metcalf, Peter C. Humphreys, James C. Gates, Helen L. Rogers, Christoph Söller, Brian J. Smith, W. Steven Kolthammer, Peter G. R. Smith, and Ian A. Walmsley. Chip-based array of near-identical, pure, heralded single-photon sources. *Optica*, 4(1):90, January 2017.

[96] Larry B. Stotts and Larry C. Andrews. Improving the hufnagel-andrews-phillips refractive index structure parameter model using turbulent intensity. *Opt. Express*, 31(9):14265–14277, Apr 2023.

[97] Ramy Tannous. Advancing the robustness of polarization and time bin quantum key distribution for free-space channels - phd thesis, 2023.

[98] C. Tranquille and E. J. Daly. An evaluation of solar-proton event models for ESA missions. *ESA Journal*, 16(3):275–297, January 1992.

[99] Ravitej Uppu, Freja T. Pedersen, Ying Wang, Cecilie T. Olesen, Camille Papon, Xiaoyan Zhou, Leonardo Midolo, Sven Scholz, Andreas D. Wieck, Arne Ludwig, and Peter Lodahl. Scalable integrated single-photon source. *Science Advances*, 6(50):eabc8268, 2020.

[100] D.A. Vallado and W.D. McClain. *Fundamentals of Astrodynamics and Applications*. Fundamentals of Astrodynamics and Applications. Microcosm Press, 2001.

[101] Zhipeng Wang, Xiaoxiong Xiong, Jon Fulbright, and Ning Lei. Viirs day/night band radiometric calibration stability monitoring using the moon. *Journal of Geophysical Research: Atmospheres*, 122(11):5616–5624, 2017.

[102] David R. Williams. Planetary fact sheet - nasa, online source (last accessed in april 2024) : $nssdc.gsfc.nasa.gov/planetary/factsheet/$, Nov 2022.

[103] Mujtaba Zahidy, Mikkel T. Mikkelsen, Ronny Müller, Beatrice Da Lio, Martin Krehbiel, Ying Wang, Nikolai Bart, Andreas D. Wieck, Arne Ludwig, Michael Galili, Søren Forchhammer, Peter Lodahl, Leif K. Oxenløwe, Davide Bacco, and Leonardo Midolo. Quantum key distribution using deterministic single-photon sources over a field-installed fibre link, 2023.

[104] Chun-Hui Zhang, Xing-Yu Zhou, Hua-Jian Ding, Chun-Mei Zhang, Guang-Can Guo, and Qin Wang. Proof-of-principle demonstration of passive decoy-state quantum digital signatures over 200 km. *Phys. Rev. Appl.*, 10:034033, Sep 2018.

APPENDICES

Appendix A

Coherence Time

As a wave packet travels through space, its wave components gradually shift out of phase, a phenomenon known as dispersion. In Quantum Mechanics, coherence time refers to the duration over which a wave packet (i.e, a quantum state) maintains a consistent phase relationship. After a time longer than the coherence time has passed, the information about the wave or system is said to be lost. This is because if the wave components of the wave packet are too off-phase, precise predictions and measurements become very challenging. Hence, it is crucial to understand the coherence time of the waves used when aiming to implement quantum technologies. Suppose we have a wave packet that can be described

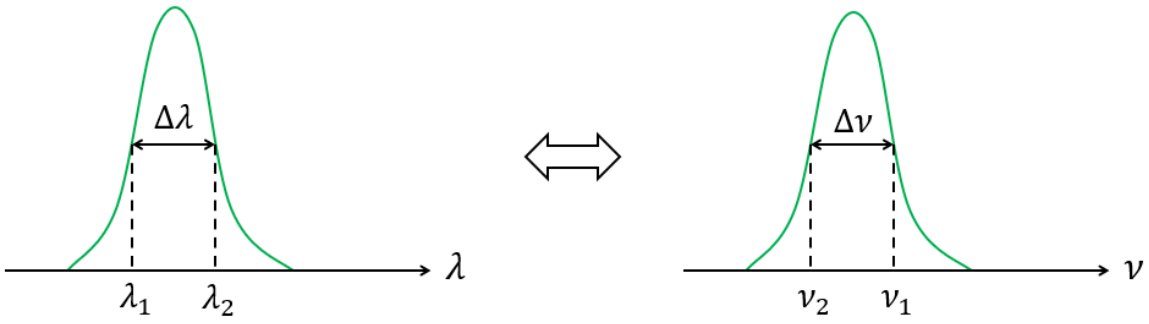

Figure A.1: Gaussian distributions of a wave packet. Note that the wavelength and the frequency are inversely proportional to each other such that the order is flipped when one is transformed to the other. Nonetheless, the relationship of the two different types of bandwidth is consistent.

with a Gaussian distribution (FigureA.1). We consider two wavelength components λ_1 and λ_2, that are close to the central wavelength λ, so that the following assumption is possible.

$$\lambda_1 \lambda_2 \approx \lambda^2 \tag{A.1}$$

Since the speed of light $c = \lambda\nu$ relates the wavelength and the frequency, the relationship between the bandwidths of the wavelength and the frequency is

$$\Delta\nu = \frac{c}{\lambda^2}\Delta\lambda \tag{A.2}$$

Such an approximation is typically employed when dealing with laser beams which normally have sharp distributions.

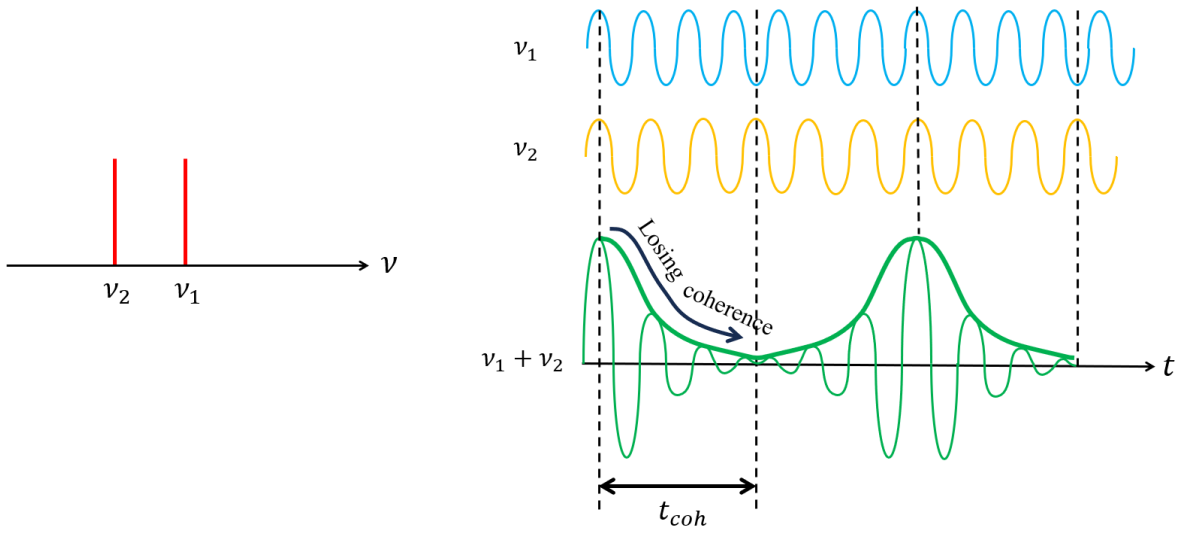

Figure A.2: Left : Two distinct frequency modes. Right : The two frequency modes expanded in time domain. The coherence time, denoted as t_{coh}, represents the duration for which the two frequency modes maintain coherence.

When two different wave components with frequencies ν_1 and ν_2 travel together, they create a wave packet (shown in the Figure A.2). At times, they create constructive and destructive interferences. One occurance of fully constructive and one occurance of fully destructive interference complete a cycle which corresponds to $1/\Delta\nu$. The coherence time is then $t_{coh} = 1/(2\Delta\nu)$. This means the wave packet retrieves its coherence after $2t_{coh}$. Coherence length is simply $L_{coh} = ct_{coh}$. Figure A.3 shows different cases, each with a different outcome. The more wave components a wave packet has, the harder it becomes to maintain coherence. This is because each wave is influenced by many other waves, leading to rapid overall destruction. On the other hand, the narrower the bandwidth, the longer the overall phase is maintained. A narrower bandwidth also results in the overall phase taking longer to recover, but by that time, the wave packet will no longer be useful anyway. $2\pi n$ of phase shifts may create other constructive interferences, but the wave packet will no longer be exactly the same as the original one. According to these analyses, we can conclude that a single frequency implies permanent coherence (Figure A.4). However, a perfect single frequency is not realistically achievable. Instead, we normally have a wave packet that contains different wave components (Figure A.5). Because coherence time really depends on the chosen bandwidth, it is important to make a reasonable choice. The Full-Width-Half-Maximum of the wave packet is normally chosen.

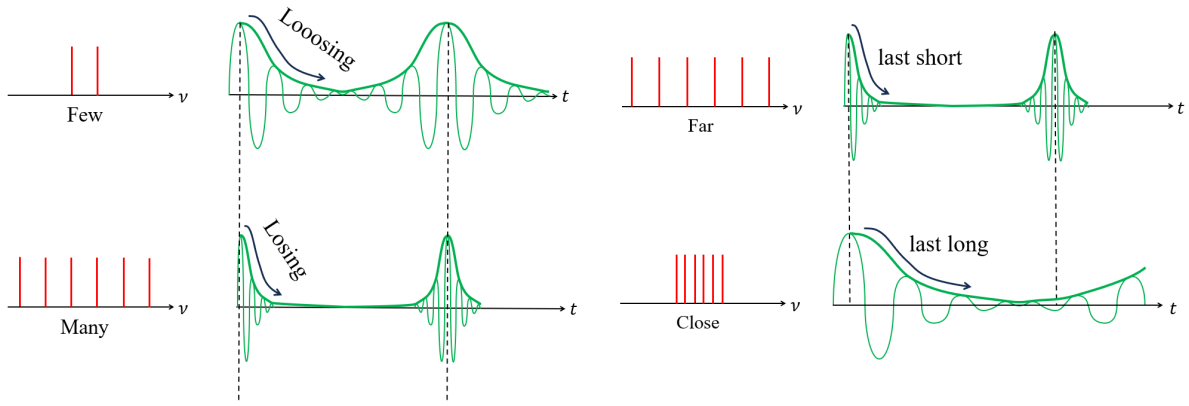

Figure A.3: Graphs illustrating how coherence time changes with frequency modes in different combinations.

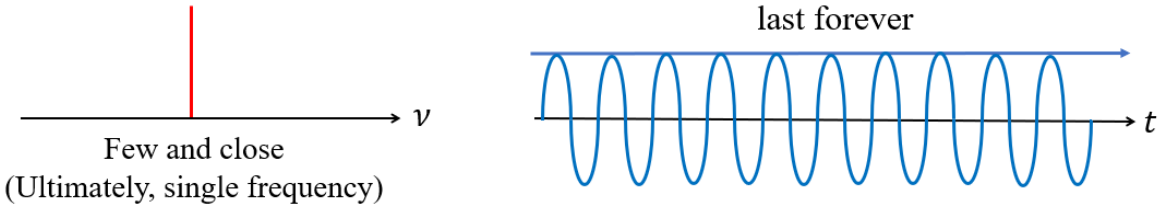

Figure A.4: Single frequency mode shown in the frequency domain (left) and time domain (right).

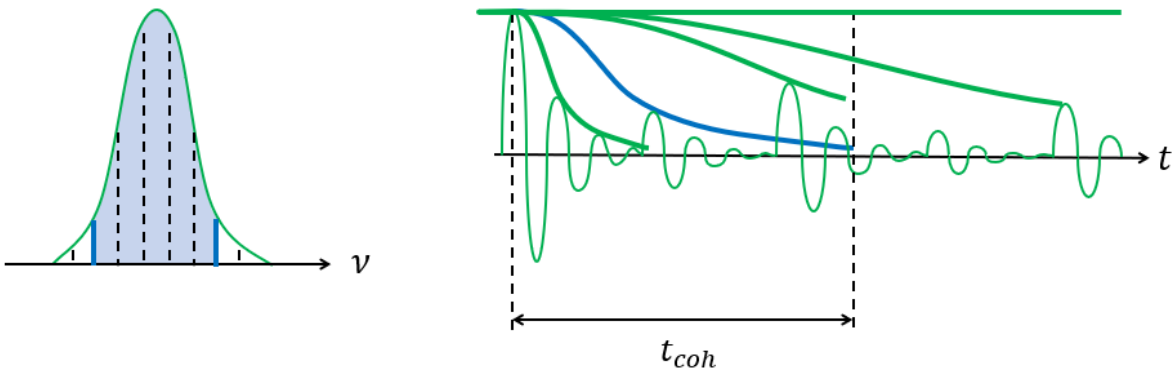

Figure A.5: Left : A typical mode spectrum. Right : Expansion of the mode spectrum in time domain.

Appendix B

Specifications of Nonlinear Materials

5% MgO doped Periodically Poled Lithium Niobate (Covesion Ltd.)

- d_{33} (nonlinear coefficient) : 25 pm/V
- Dimensions (L× W× H) : 10 mm × 10 mm × 0.5 mm
- Contains 9 gratings (in μm) : $6.00, 6.26, 6.53, 6.81, 7.10, 7.40, 7.71, 8.03, 8.36$
- Both sides are AR-coated ($R < 1\%$ at 523 nm and $R < 1.6\%$ at 791/1550nm)

The temperature-dependent Sellmeier equation (λ in μm) and the coefficients for ordinary and extraordinary refractive indices provided by the company are

$$n^2(\lambda, T) = a_1 + b_1 f + \frac{a_2 + b2f}{\lambda^2 - (a_3 + b_3 f)^2} + \frac{a_4 + b_4 f}{\lambda^2 - a_5^2} - a_6 \lambda^2 \tag{B.1}$$

where there exists a termperature dependent parameter, $f = (T - (298.15K))(T + (298.15K))$ [37]. Assuming room temperature, temperature-dependent poling period and length of the crystal are characterized by

$$\begin{aligned} \text{Poling period} : \Lambda(T) &= \Lambda_0 \left(1 + \alpha(T - 298.15K) + \beta(T - 298.15K)^2\right) \\ \text{Crystal Length} : L(T) &= L_0 \left(1 + \alpha(T - 298.15K) + \beta(T - 298.15K)^2\right) \end{aligned} \tag{B.2}$$

where we have the thermal expansion coefficients, $\alpha = 1.54 \times 10^{-5}$ and $\beta = 5.3 \times 10^{-9}$.

Refractive index	n_o	n_e
a_1	5.653	5.756
a_2	0.1185	0.0983
a_3	0.2091	0.2020
a_4	89.61	189.32
a_5	10.85	12.52
a_6	0.0197	0.0132
b_1	7.941×10^{-7}	2.860×10^{-6}
b_2	3.134×10^{-8}	4.700×10^{-8}
b_3	-4.641×10^{-9}	6.113×10^{-8}
b_4	-2.188×10^{-6}	1.516×10^{-4}

α-BBO Beam Displacer (Newlight Photonics inc.)

- Dimensions (L$\times$ W$\times$ H) : 39.4 mm $\times$ 10 mm $\times$ 10 mm
- First Beam Displacer : AR-coated ($R < 1\%$ at 523 nm)
- Second Beam Displacer : AR-coated $R < 1.6\%$ at 791/1550nm)
- Optic Angle : 45^o

Sellmeier equation (λ in μm) for ordinary and extreaordinary indices provided by the company.

$$\begin{aligned} n_o^2(\lambda) &= 2.67579 + \frac{0.02099}{(\lambda^2 - 0.00470)} - 0.00528\lambda^2 \\ n_e^2(\lambda) &= 2.31197 + \frac{0.01184}{(\lambda^2 - 0.01607)} - 0.00400\lambda^2 \end{aligned} \tag{B.3}$$

The thermo-optic coefficients $dn_o/dT = -9.3 \times 10^{-6}/C^o$ and $dn_e/dT = -16.6 \times 10^{-6}/C^o$ are provided. The thermal expansion coefficients $\alpha_o = 4 \times 10^{-6}/K$ and $\alpha_e = 36 \times 10^{-6}/K$ are provided.

Calcite Compensators (Newlight Photonics inc.)

- Face Dimensions (W$\times$ H) : 10 mm $\times$ 10 mm
- Wedge Thickness : Minimum 1 mm , Maximum 3.68 mm.

- Wedge angle : 15^o from the face
- AR-coated ($R < 0.2\%$ at 1550 nm and $R < 0.5\%$ at 791nm)
- Optic Angle : Perpendicular to the 10×1mm face.

Sellmeier equation (λ in μm) for ordinary and extreaordinary indices provided by the company.

$$\begin{aligned} n_o^2(\lambda) &= 2.69705 + \frac{0.0192064}{(\lambda^2 - 0.01820)} - 0.0151624\lambda^2 \\ n_e^2(\lambda) &= 2.18438 + \frac{0.0087309}{(\lambda^2 - 0.01018)} - 0.0024411\lambda^2 \end{aligned} \tag{B.4}$$

The thermo-optic coefficients $dn_o/dT = 2.7 \times 10^{-6}/C^o$ and $dn_e/dT = 12.3 \times 10^{-6}/C^o$ are provided. The thermal expansion coefficients $\alpha_o = 4.9 \times 10^{-6}/K$ and $\alpha_e = 25.1 \times 10^{-6}/K$ are provided.

Appendix C

Single/Multi mode electric fields

$$\begin{aligned} (i) \quad & \nabla \cdot \vec{E} = \frac{\rho}{\epsilon_0} \\ (ii) \quad & \nabla \cdot \vec{B} = 0 \\ (iii) \quad & \nabla \times \vec{E} = -\frac{\partial \vec{B}}{\partial t} \\ (iv) \quad & \nabla \times \vec{B} = \mu_0 \vec{J} + \mu_0 \epsilon_0 \frac{\partial \vec{E}}{\partial t} \end{aligned} \tag{C.1}$$

We start from these Maxell's equations which describe the relations between electric fields $\vec{E}$, magnetic fields $\vec{B} = \nabla \times \vec{A}$ (curl of vector potentials), currents $\vec{J}$ and charge densities ρ. The divergence "$\nabla\cdot$" tells whether the vector diverges or not. The curl "$\nabla\times$" tells whether the vector rotates or not. Combine (iii) and (v).

$$\nabla \times \vec{E} = -\frac{\partial}{\partial t}\left(\nabla \times \vec{A}\right) \qquad \rightarrow \qquad \nabla \times \left(\vec{E} + \frac{\partial}{\partial t}\vec{A}\right) = 0 \tag{C.2}$$

A vector field is said to be conservative (irrotational), if its curl is zero. In calculus, a conservative vector field implies that it can be expressed as the gradient of a scalar field. Therefore, we can represent it as $-\nabla V = \vec{E} + \frac{\partial}{\partial t}\vec{A}$ where V is the scalar potential that we all know. This integrates the findings from C.2, combining (iv) and (v).

$$\begin{aligned}\nabla \times \vec{B} = \nabla \times \left(\nabla \times \vec{A}\right) &= \mu_0 \vec{J} + \mu_0 \epsilon_0 \frac{\partial}{\partial t}\left(-\nabla V - \frac{\partial}{\partial t}\vec{A}\right) \\ &= \mu_0 \vec{J} - \mu_0 \epsilon_0 \nabla\left(\frac{\partial V}{\partial t}\right) - \mu_0 \epsilon_0 \frac{\partial^2 \vec{A}}{\partial t^2}\end{aligned} \tag{C.3}$$

Next, we use one of the known vector identities : $\nabla \times (\nabla \times \vec{A}) = \nabla(\nabla \cdot \vec{A}) - \nabla^2 \vec{A}$

$$\longrightarrow \qquad \nabla\left(\nabla \cdot \vec{A}\right) - \nabla^2 \vec{A} = \mu_0 \vec{J} - \mu_0 \epsilon_0 \nabla\left(\frac{\partial V}{\partial t}\right) - \mu_0 \epsilon_0 \frac{\partial^2 \vec{A}}{\partial t^2} \tag{C.4}$$

Then we apply the Coulomb (transverse) gauge ($\nabla \cdot \vec{A} = 0$). By assuming that fields are in free space (i.e, no charges $V = 0$ and no currents $\vec{J} = 0$),

$$\begin{aligned}\longrightarrow \qquad & \nabla\cancelto{0}{\left(\nabla \cdot \vec{A}\right)} - \nabla^2 \vec{A} = \cancelto{0}{\mu_0 \vec{J}} - \mu_0 \epsilon_0 \nabla\cancelto{0}{\left(\frac{\partial V}{\partial t}\right)} - \mu_0 \epsilon_0 \frac{\partial^2 \vec{A}}{\partial t^2} \\ \longrightarrow \qquad & \nabla^2 \vec{A} - \mu_0 \epsilon_0 \frac{\partial^2 \vec{A}}{\partial t^2} = 0\end{aligned} \tag{C.5}$$

This is precisely the Laplace's wave equation ($c^2 \nabla^2 \psi = \partial^2 \psi / \partial t^2$), which implies that the vector potential is a wave. A solution for the differential equation can be the following

$$\therefore \quad \vec{A} = C e^{i(k \cdot r - \omega t)} + C^\star e^{-i(k \cdot r - \omega t)} \tag{C.6}$$

where C and its complex conjugate $C^\star$ are both constant. Coulomb gauge also allows the expression for the scalar potential (from equation C.2) become $\vec{E} = -\partial \vec{A}/\partial t$. By considering an eletromagnetic field (light) propagating in z-direction, we can have the following three expressions :

$$\vec{A} = \left(C e^{i(kz - \omega t)} + C^\star e^{-i(kz - \omega t)}\right) \hat{x} \tag{C.7}$$

$$\vec{E} = -\frac{\partial}{\partial t}\vec{A} = i\omega \left(C e^{i(kz - \omega t)} - C^\star e^{-i(kz - \omega t)}\right) \hat{x} \tag{C.8}$$

$$\vec{B} = \nabla \times \vec{A} = det \begin{bmatrix} \hat{x} & \hat{y} & \hat{z} \\ \frac{d}{dx} & \frac{d}{dy} & \frac{d}{dz} \\ A & 0 & 0 \end{bmatrix} = ik \left(C e^{i(kz-\omega t)} - C^{\star} e^{-i(kz-\omega t)} \right) \hat{y} \tag{C.9}$$

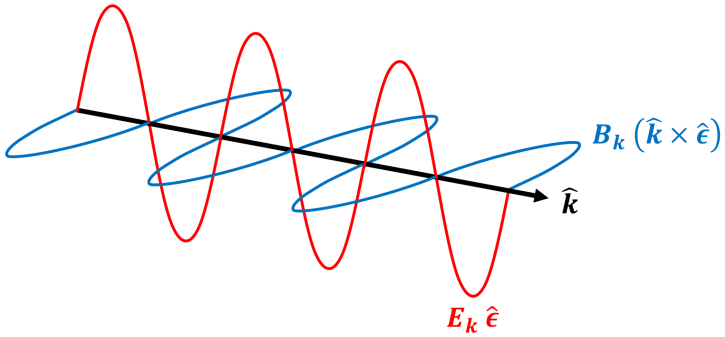

Figure C.1: Electromagnetic wave. $\hat{k}$ is the propagation direction of the light, $\hat{\epsilon}$ is the transverse polarization direction of the electric field. Hence, we can say the transverse polarization direction of the magnetic field can be expressed in terms of the two other vectors, $(\hat{k} \times \hat{\epsilon})$.

We see that directions of the electric field, magnetic field and propagation are mutually perpendicular. Additionally, the magnetic field can be expressed in terms of the electric field using the relation $k = \omega/c$. Different values of k (or $\omega = ck$) correspond to different frequency (or temporal) modes of the fields. For instance, the multi-frequency mode (or multimode) electric and magnetic fields can be written as

$$\begin{aligned} \vec{E} &= \sum_k \vec{E}_k \qquad \cdots \hat{\epsilon}_{\mathbf{k}} \\ \vec{B} &= \sum_k \frac{1}{c} \vec{E}_k \quad \cdots (\hat{\mathbf{k}} \times \hat{\epsilon}_{\mathbf{k}}) \end{aligned} \tag{C.10}$$

where $\vec{E}_k$ is the single frequency mode (or single mode) electric field. $\hat{k}$ is the propagation vector that is perpendicular to the polarization vectors, $\hat{\epsilon}_k$ and $\hat{k} \times \hat{\epsilon}_k$. To obtain the coefficients shown in equations C, C.8 and C.9, we examine the total energy (Hamiltonian) of

the electrimagnetic field within an arbitrary volume, V.

$$H = \frac{1}{2}\int_V \left(\epsilon_0 \left|\vec{E}_k \cdot \vec{E}^{\star}_{k'}\right| + \frac{1}{\mu_0}\left|\vec{B}_k \cdot \vec{B}^{\star}_{k'}\right|\right) dV \tag{C.11}$$

We typically study the interactions (or quantizations) of the electromagnetic field. Therefore, this arbitrary volume could correspond to a cavity space where such interactions occur. By using the periodic boundary condition,

$$\int_V e^{i(k-k')\cdot r} dV = \delta_{kk'} V \tag{C.12}$$

the first term becomes

$$\frac{\epsilon_0}{2}\int_V \left|\vec{E}_k \cdot \vec{E}^{\star}_{k'}\right| dV \tag{C.13}$$

$$= \frac{\epsilon_0}{2}\int_V \left|(i\omega)\left(C_k e^{i(kz-\omega t)} - C^{\star}_k e^{-i(kz-\omega t)}\right)\hat{\epsilon}_k\,(-i\omega')\left(C^{\star}_{k'} e^{-i(k'z-\omega' t)} - C_{k'} e^{i(k'z-\omega' t)}\right)\hat{\epsilon}_{k'}\right|$$

$$= \frac{\epsilon_0}{2}\int_V \omega\omega' \Big|C_k C^{\star}_{k'} e^{i(k-k')z} e^{-i(\omega-\omega')t}\hat{\epsilon}_k\cdot\hat{\epsilon}_{k'} + C^{\star}_k C_{k'} e^{-i(k-k')z} e^{i(\omega-\omega')t}\hat{\epsilon}_k\cdot\hat{\epsilon}_{k'}$$

$$-C_k C_{\boxed{k'}} e^{i\left(k\,\boxed{+k'}\right)z} e^{-i\left(\omega+\,\boxed{\omega'}\right)t}\hat{\epsilon}_k\cdot\hat{\epsilon}_{\boxed{k'}} - C^{\star}_k C^{\star}_{\boxed{k'}} e^{-i\left(k\,\boxed{+k'}\right)z} e^{i\left(\omega+\,\boxed{\omega'}\right)t}\hat{\epsilon}_k\cdot\hat{\epsilon}_{\boxed{k'}}\Big|\, dV$$

$$= \frac{\epsilon_0}{2}\int_V \omega\omega' \Big|C_k C^{\star}_{k'} e^{i(k-k')z} e^{-i(\omega-\omega')t}\hat{\epsilon}_k\cdot\hat{\epsilon}_{k'} + C^{\star}_k C_{k'} e^{-i(k-k')z} e^{i(\omega-\omega')t}\hat{\epsilon}_k\cdot\hat{\epsilon}_{k'}$$

$$-C_k C_{\boxed{-k'}} e^{i\left(k\,\boxed{-k'}\right)z} e^{-i\left(\omega\,\boxed{-\omega'}\right)t}\hat{\epsilon}_k\cdot\hat{\epsilon}_{\boxed{-k'}} - C^{\star}_k C^{\star}_{\boxed{-k'}} e^{-i\left(k\,\boxed{-k'}\right)z} e^{i\left(\omega\,\boxed{-\omega'}\right)t}\hat{\epsilon}_k\cdot\hat{\epsilon}_{\boxed{-k'}}\Big|\, dV$$

$$= \frac{1}{2}\epsilon_0\omega\omega' V\Big(C_k C^{\star}_{k'}\delta_{kk'} e^{-i(\omega-\omega')t}\hat{\epsilon}_k\cdot\hat{\epsilon}_{k'} + C^{\star}_k C_{k'}\delta_{kk'} e^{i(\omega-\omega')t}\hat{\epsilon}_k\cdot\hat{\epsilon}_{k'}$$

$$-C_k C_{-k'}\delta_{kk'} e^{-i(\omega-\omega')t}\hat{\epsilon}_k\cdot\hat{\epsilon}_{-k'} - C^{\star}_k C^{\star}_{-k'}\delta_{kk'} e^{i(\omega-\omega')t}\hat{\epsilon}_k\cdot\hat{\epsilon}_{-k'}\Big)$$

We have renamed one of our dummy variables, $k' \to -k'$ (shown in the yellow boxes),which also means $\omega' \to -\omega'$, in order to get rid of the exponential terms by using Eq C.12. For a single mode ($k = k'$), we then have

$$\frac{\epsilon_0}{2}\int_V \left|\vec{E}_k \cdot \vec{E}^{\star}_{k'}\right| dV = \frac{1}{2}\epsilon_0\omega^2 V\left(2C_k C^{\star}_k - C_k C_{-k}\hat{\epsilon}_k\cdot\hat{\epsilon}_{-k} - C^{\star}_k C^{\star}_{-k}\hat{\epsilon}_k\cdot\hat{\epsilon}_{-k}\right) \tag{C.14}$$

For the second term, the result is slightly different.
We use another vector identity : $(A\times B)\cdot(C\times D) = (A\cdot C)(B\cdot D) - (A\cdot D)(B\cdot C)$

which gives what we need to derive for the second term.

$$\frac{1}{2\mu_0}\int_V \left|\vec{B}_k \cdot \vec{B}^\star_{k'}\right| dV \tag{C.15}$$

$$\begin{aligned}
&= \frac{1}{2\mu_0}\int_V \frac{\omega\omega'}{c^2}\left|\left(C_k e^{i(kz-\omega t)} - C^\star_k e^{-i(kz-\omega t)}\right)\left(\hat{k}\times\hat{\epsilon}_k\right)\left(C^\star_{k'} e^{-i(k'z-\omega' t)} - C_{k'} e^{i(k'z-\omega' t)}\right)\left(\hat{k}'\times\hat{\epsilon}_{k'}\right)\right| dV \\
&= \frac{1}{2\mu_0}\int_V \frac{\omega\omega'}{c^2}\Big|C_k C^\star_{k'} e^{i(k-k')z} e^{-i(\omega-\omega')t}\left(\hat{k}\times\hat{\epsilon}_k\right)\left(\hat{k}'\times\hat{\epsilon}_{k'}\right) \\
&\qquad + C^\star_k C_{k'} e^{-i(k-k')z} e^{i(\omega-\omega')t}\left(\hat{k}\times\hat{\epsilon}_k\right)\left(\hat{k}'\times\hat{\epsilon}_{k'}\right) \\
&\qquad - C_k C_{\boxed{k'}} e^{i\left(k\boxed{+k'}\right)z} e^{-i\left(\omega\boxed{+\omega'}\right)t}\left(\hat{k}\times\hat{\epsilon}_k\right)\left(\boxed{k'}\times\hat{\epsilon}_{\boxed{k'}}\right) \\
&\qquad - C^\star_k C^\star_{\boxed{k'}} e^{-i\left(k\boxed{+k'}\right)z} e^{i\left(\omega\boxed{+\omega'}\right)t}\left(\hat{k}\times\hat{\epsilon}_k\right)\left(\boxed{k'}\times\hat{\epsilon}_{\boxed{k'}}\right)\Big| dV
\end{aligned} \tag{C.16}$$

We can rename one of the dummy variables just as before ($k' \to -k'$ and $\omega' \to -\omega'$).

$$\begin{aligned}
&= \frac{1}{2\mu_0}\int_V \frac{\omega\omega'}{c^2}\Big|C_k C^\star_{k'} e^{i(k-k')z} e^{-i(\omega-\omega')t}\delta_{kk'} + C^\star_k C_{k'} e^{-i(k-k')z} e^{i(\omega-\omega')t}\delta_{kk'} \\
&\qquad - C_k C_{\boxed{-k'}} e^{i\left(k\boxed{-k'}\right)z} e^{-i\left(\omega\boxed{-\omega'}\right)t}\left(\hat{k}\times\hat{\epsilon}_k\right)\left(\boxed{-k'}\times\hat{\epsilon}_{\boxed{-k'}}\right) \\
&\qquad - C^\star_k C^\star_{\boxed{-k'}} e^{-i\left(k\boxed{-k'}\right)z} e^{i\left(\omega\boxed{-\omega'}\right)t}\left(\hat{k}\times\hat{\epsilon}_k\right)\left(\boxed{-k'}\times\hat{\epsilon}_{\boxed{-k'}}\right)\Big| dV \\
&= \frac{1}{2}\epsilon_0\omega\omega' V\Big(C_k C^\star_{k'}\delta_{kk'} e^{-i(\omega-\omega')t}\hat{\epsilon}_k\cdot\hat{\epsilon}_{k'} + C^\star_k C_{k'}\delta_{kk'} e^{i(\omega-\omega')t}\hat{\epsilon}_k\cdot\hat{\epsilon}_{k'} \\
&\qquad + C_k C_{-k'}\delta_{kk'} e^{-i(\omega-\omega')t}\hat{\epsilon}_k\cdot\hat{\epsilon}_{-k'} + C^\star_k C^\star_{-k'}\delta_{kk'} e^{i(\omega-\omega')t}\hat{\epsilon}_k\cdot\hat{\epsilon}_{-k'}\Big) \quad \cdots \quad c^2 = \frac{1}{\epsilon_0\mu_0}
\end{aligned}$$

Again, for a single mode we have

$$\frac{1}{2\mu_0}\int_V \left|\vec{B}_k \cdot \vec{B}^{\star}_{k'}\right| dV = \frac{1}{2}\epsilon_0\omega^2 V\left(2C_kC_k^{\star} + C_kC_{-k}\hat{\epsilon}_k\cdot\hat{\epsilon}_{-k} + C_k^{\star}C_{-k}^{\star}\hat{\epsilon}_k\cdot\hat{\epsilon}_{-k}\right) \tag{C.17}$$

Using Eq **??** and Eq C, we find that the result for Eq [**??**] is

$$H = 2\epsilon_0\omega^2 V C_k C_k^{\star} \tag{C.18}$$

A quantized EM field could simply be driven from $H|\psi\rangle = \hbar\omega(n+1/2)|\psi\rangle$. Thus,

$$C_k = \sqrt{\frac{\hbar}{2\omega\epsilon_0 V}}\ \hat{a} \quad , \quad C_k^{\star} = \sqrt{\frac{\hbar}{2\omega\epsilon_0 V}}\ \hat{a}^{\dagger} \tag{C.19}$$

Finally we have full expressions for the two single mode fields.

$$\vec{E}_k = i\sqrt{\frac{\hbar\omega}{2\epsilon_0 V}}\left(\ \hat{a}e^{i(kz-\omega t)} - \ \hat{a}^{\dagger}e^{-i(kz-\omega t)}\right)\hat{\epsilon}$$

$$\vec{B}_k = i\sqrt{\frac{\hbar\omega}{2\epsilon_0 c^2 V}}\left(\ \hat{a}e^{i(kz-\omega t)} - \ \hat{a}^{\dagger}e^{-i(kz-\omega t)}\right)\hat{\epsilon}\times\hat{k} \tag{C.20}$$

Appendix D

Paraxial Gaussian Wave

Beam diverges. It can also be focused or defocused, reflected or refracted using variety of optics. For this reason, the interaction space described by the unit volume V (from the equations C.20) does not remain constant but evolves along the direction of the beam propagation unless it is the case where one can simply consider a plane wave to describe the beam. We must further develop the equations C.20) to describe propagation of a beam. Assuming that the beam is propagating along z-axis, we will first recall the electric field expression (from the equation C.20) and divide it into two frequency terms, $\vec{E} = \vec{E}^{(+)} + \vec{E}^{(-)}$.

$$\begin{aligned} \vec{E}^{(+)}(\vec{r},t) &= \; i\sqrt{\frac{\hbar\omega}{2\epsilon_0 V(\vec{r})}}\; \hat{a}e^{i(kz-\omega t)}\; \hat{\epsilon} \\ \vec{E}^{(-)}(\vec{r},t) &= -\,i\sqrt{\frac{\hbar\omega}{2\epsilon_0 V(\vec{r})}}\; \hat{a}^{\dagger}e^{-i(kz-\omega t)}\; \hat{\epsilon} \end{aligned} \tag{D.1}$$

where the volume constant became a function $\frac{1}{\sqrt{V(\vec{r})}} = \frac{1}{\sqrt{V_0}} g(\vec{r})$. Such a wave well-describes laser beam in optical experiments. Let us examine the negative frequency term, which is responsible for photon creation, as an example. For simplicity, we can separate the spatial and temporal terms of the complex amplitude function.

$$\vec{E}^{(-)}(\vec{r},t) = \boxed{-i\sqrt{\frac{\hbar\omega}{2\epsilon_0 V_0}}}\; \hat{a}^{\dagger}E^{(-)}(\vec{r})E^{(-)}(t)\; \hat{\epsilon} \tag{D.2}$$

such that $E^{(-)}(\vec{r}) = g(\vec{r})e^{-ikz}$. The blue box in the equation D.2 corresponds to E_0.

In ray optics, a light ray is paraxial when the ray remains nearly parallel and close to the optical axis. This means $g(\vec{r})$ should be considered as a slowly varying complex envelope. We apply Helmholtz equation to develop a new version for the paraxial wave.

$$Helmholtz\ equation \quad : \quad \left(\nabla^2 + k^2\right) E(\vec{r}) = 0 \tag{D.3}$$

$$\begin{aligned}
\longrightarrow \quad & \nabla^2 \left[g(\vec{r})e^{-ikz}\right] + k^2 \left[g(\vec{r})e^{-ikz}\right] \\
=& \nabla \left[\left(\nabla g(\vec{r})\right) e^{-ikz} - ikg(\vec{r})e^{-ikz}\right] + k^2 g(\vec{r})e^{-ikz} \\
=& \left(\nabla^2 g(\vec{r})\right) e^{-ikz} - ik\left(g(\vec{r})\right) e^{-ikz} - ik\left(g(\vec{r})\right) e^{-ikz} - k^2 g(\vec{r})e^{-ikz} + k^2 g(\vec{r})e^{-ikz} \\
=& \left(\nabla^2 g(\vec{r})\right) e^{-ikz} - 2ik\left(g(\vec{r})\right) e^{-ikz}
\end{aligned}$$

Slowly varying within a wavelength period ($\Delta z = \lambda$) : $\Delta E \ll E$

$$\Delta E = \frac{dE}{dz}\Delta z \ \rightarrow \ \frac{dE}{dz} = \frac{\Delta E}{\Delta z} \ \rightarrow \ \frac{dE}{dz} \ll \frac{E}{\lambda} = \frac{kE}{2\pi} \quad \frac{dE}{dz} \ll kE \tag{D.4}$$

which means $\dfrac{d^2E}{dz^2} \ll k^2 E$.

$$\longrightarrow \quad \left(\nabla_T^2 g(\vec{r})\right) e^{-ikz} + \cancelto{0}{\left(\frac{d^2}{dz^2} g(\vec{r})\right)} e^{-ikz} - 2ik\left(\frac{d}{dz} g(\vec{r})\right) e^{-ikz} = 0$$

$$\nabla_T^2 = \frac{d^2}{dx^2} + \frac{d^2}{dy^2}$$

$$\frac{d}{dz} = \frac{d}{dx} = \frac{d}{dy} = 0$$

We come up with a new version of Helmholtz equation.

$$\therefore \quad \nabla_T^2 g(\vec{r}) - 2ik\frac{d}{dz} g(\vec{r}) = 0 \quad \cdots\cdots \quad Paraxial\ Helmholtz\ equation \tag{D.5}$$

A paraxial ray solution to Eq. D.5 could be a **paraboloidal wave**.

$$g(\vec{r}) = \frac{1}{z} e^{-ik\frac{\rho^2}{2z}} \quad , \quad \rho^2 = x^2 + y^2 \tag{D.6}$$

$$E^{(-)}(\vec{r}) = \frac{1}{z} e^{-ik\frac{\rho^2}{2z} - ikz} \tag{D.7}$$

By adding the Gaussian wave property by replacing $z \rightarrow z+iz_R$ (complex envelope), where z_R is the Rayleigh length, the expression becomes

$$E^{(-)}(\vec{r}) = \underbrace{\frac{1}{(z+iz_R)}}_{\text{I}} e^{-ik\underbrace{\frac{\rho^2}{2(z+iz_R)}}_{\text{II}}-ikz} \tag{D.8}$$

Using the trigonometric identity $\frac{1}{1-ix} = \frac{1}{\sqrt{1+ix}} e^{i\ tan^{-1}x}$

$$\text{I} \quad \frac{1}{z+iz_R} = \frac{1}{iz_R\left(1-\frac{z}{z_R}\right)} = \frac{exp\left[i\ tan^{-1}\left(\frac{z}{z_R}\right)\right]}{iz_R\sqrt{1+\frac{z^2}{z_R^2}}} = \frac{W_0}{iz_RW(z)} exp\left[i\ tan^{-1}\left(\frac{z}{z_R}\right)\right] \tag{D.9}$$

$$\begin{aligned}\text{II} \quad \frac{1}{z+iz_R} &= \frac{1}{z+iz_R}\frac{z-iz_R}{z-iz_R} = \frac{z}{z^2+z_R^2} - \frac{iz_R}{z^2+z_R^2} = \frac{z}{z^2\left(1+\frac{z_R^2}{z^2}\right)} - \frac{iz_R}{z_R^2\left(1+\frac{z^2}{z_R^2}\right)} \\ &= \frac{z}{z^2\frac{R(z)}{z}} - \frac{iz_R}{z_R^2\frac{W^2(z)}{W_0^2}} = \frac{1}{R(z)} - \frac{iW_0^2}{z_RW^2(z)} \\ &= \frac{1}{R(z)} - \frac{i\lambda z_R}{\pi z_RW^2(z)} = \underbrace{\frac{1}{R(z)} - i\frac{2}{kW^2(z)}}_{k=\frac{2\pi}{\lambda}}\end{aligned} \tag{D.10}$$

We now have an expression for the complex amplitude by re-writting the equation D.8 as follows.

$$E^{(-)}(\vec{r}) = \frac{W_0}{W(z)} e^{-ik\frac{\rho^2}{2R(z)} - \frac{\rho^2}{W^2(z)} - ikz + i\ tan^{-1}\left(\frac{z}{z_R}\right)} \tag{D.11}$$

Note that the constant factor $\frac{1}{iz_R}$ at the front was taken out and absorbed by the volume constant for convenience. The normalization volume constant from the equation D.1 could

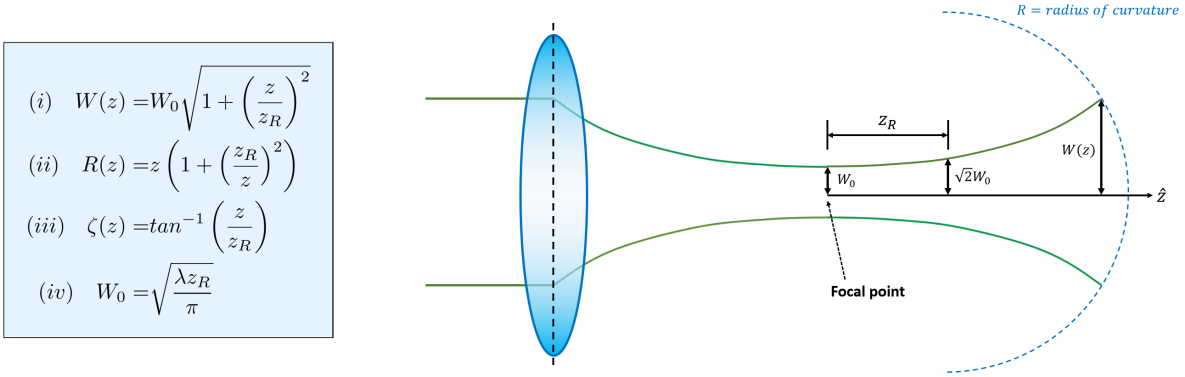

Figure D.1: Ray diagram. The figure shows a beam, initially focused by a lens to the focal point, propagating along the z-axis. Its width increases as it propagates, and becomes $\sqrt{2}$ times the original width W_0, at the distance which is defined as Rayleigh length z_R. The factor $\sqrt{2}$ times its original width means 2 times its original area.

be split into the area (A_0) and the length (L_0) terms as $V_0 = A_0 L_0$. The length would simply correspond to the length of the interaction region we are interested in. In order to find the area of the beam, we simply integrate the optical intensity $I(\vec{r}) = |E(\vec{r})^2|$ over the transverse (x,y) plane.

$$\int_0^\infty \left|E(\vec{r})^2\right| 2\pi\rho d\rho = \frac{1}{2}\pi W_0^2 \tag{D.12}$$

Thus, giving us $\frac{1}{\sqrt{A_0}} = \sqrt{\frac{2}{\pi W_0^2}}$. In fact, this is exactly the normalization constant for the Gaussian wave function which its standard deviation is half of the beam radius $\sigma = 2W$.

$$G(r) = \frac{1}{\sqrt{2\pi\sigma^2}} e^{-\frac{r^2}{2\sigma^2}} \tag{D.13}$$

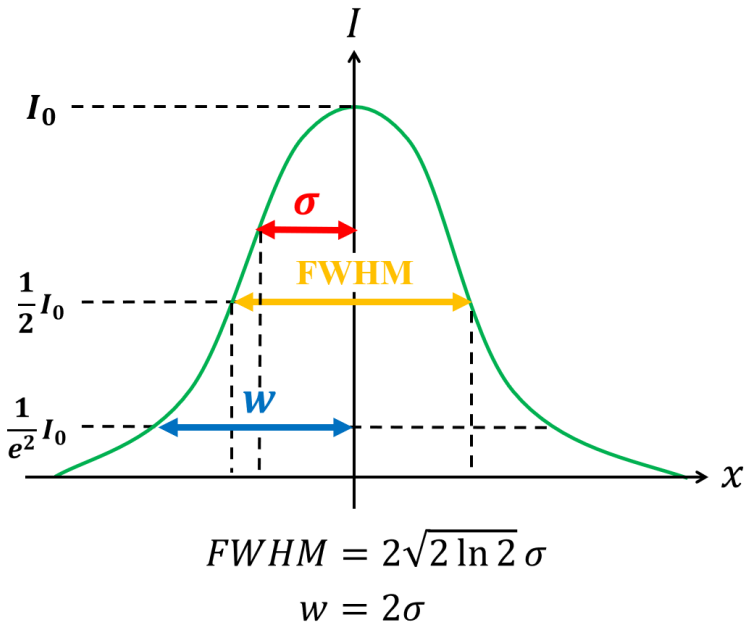

Figure D.2: Definition of the intensity profile of a Gaussian beam.

The definitions of a Full-Width-Half-Maximum (FWHM), the standard deviation (σ) and the beam radius is shown in the Figure D.2. We finally have an expression for the **paraxial gaussian wave**.

$$\vec{E}^{(-)}(\vec{r},t) = -i\sqrt{\frac{\hbar\omega}{2\epsilon_0 L_0}}\sqrt{\frac{2}{\pi W_0^2}}\frac{W_0}{W(z)}e^{-ik\frac{\rho^2}{2R(z)} - \frac{\rho^2}{W^2(z)} - ikz + i\ tan^{-1}\left(\frac{z}{z_R}\right) + i\omega t}\hat{\epsilon} \tag{D.14}$$

D.0.1 Fiber Coupling

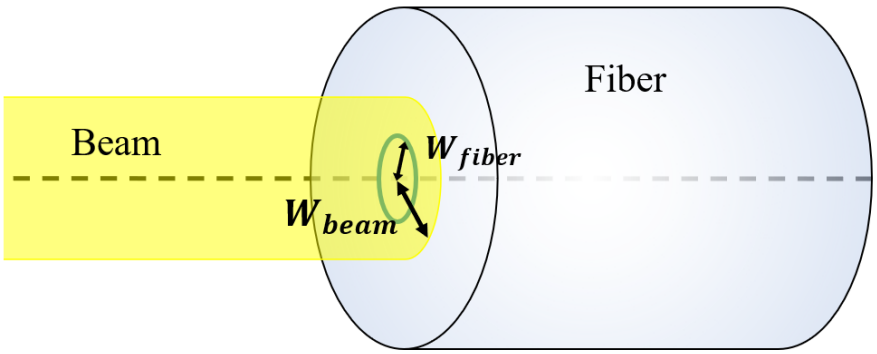

Figure D.3: Fiber-coupling. The figure shows a beam, initially focused by a lens to the focal point, propagating along the z-axis. Its width increases as it propagates, and becomes $\sqrt{2}$ times the original width W_0, at the distance which is defined as Rayleigh length z_R. The factor $\sqrt{2}$ times its original width means 2 times its original area.

The fiber-coupling efficiency, ν can be computed by the following expression

$$\nu = \frac{\left| \int_{-\infty}^{\infty} \int_{-\infty}^{\infty} \vec{E}_{in} \vec{E}_{out}^{*} dxdy \right|^2}{\left| \int_{-\infty}^{\infty} \int_{-\infty}^{\infty} \vec{E}_{in} \vec{E}_{in}^{*} dxdy \right| \left| \int_{-\infty}^{\infty} \int_{-\infty}^{\infty} \vec{E}_{out} \vec{E}_{out}^{*} dxdy \right|} \tag{D.15}$$

We favorably consider the paraxial gaussian wave expression that we have derived. All the normalization constants vanish as they would cancel each other. We assume that the beam is perfectly aligned with the fiber core (i.e $\int d\theta = 2\pi$). Lastly, we assume that the fiber is located at the focal point of the objective lens (i.e $z = 0$ and $R = \infty$). Hence, the expression can be simplifeid as

$$\nu = \frac{\left| \int_{-\infty}^{\infty} e^{-\rho^2 \left(\frac{1}{W_{in}^2} + \frac{1}{W_{out}^2} \right)} \rho d\rho \right|^2}{\left| \int_{-\infty}^{\infty} e^{-\frac{2\rho^2}{W_{in}^2}} \rho d\rho \right| \left| \int_{-\infty}^{\infty} e^{-\frac{2\rho^2}{W_{out}^2}} \rho d\rho \right|} = 4 \left(\frac{W_{in} W_{out}}{W_{in}^2 + W_{out}^2} \right)^2 \tag{D.16}$$

in case of $W_{in} = W_{out}$, the fiber coupling efficiency is $\nu = 1$ as expected.

Appendix E

Fermi's Golden Rule

Transition state.

$$Perturbed\ Hamiltonian : H(t) = H_0 + H_1(t) + H_2(t) + H_3(t)\ \cdots \tag{E.1}$$

Spontaneous parametric downconversion happens in first-order hamiltonian interaction. We simplify the perturbation by neglecting all the other higher-orders : $H(t) = H_0 + H_1(t)$. Consider a state $|\psi(t)\rangle = \sum_n C_n(t)\,|\psi(t)\rangle = \sum_n C_n(t)\,|\phi_n\rangle\, exp(-iE_nt/\hbar)$. According to Schrödinger's equation, our expression becomes

$$Schrödinger's\ equation : (H_0 + H_1(t))\,|\psi(t)\rangle = i\hbar\frac{d}{dt}\,|\psi(t)\rangle \tag{E.2}$$

$$\longrightarrow \sum_n C_n(t)\,(H_0 + H_1(t))\,|\phi_n\rangle\, e^{-\frac{iE_nt}{\hbar}} = i\hbar\frac{d}{dt}\sum_n C_n(t)\,|\phi_n\rangle\, e^{-\frac{iE_nt}{\hbar}}$$

$$\longrightarrow \cancel{\sum_n C_n(t)E_n\,|\phi_n\rangle\, e^{\frac{-iE_nt}{\hbar}}} + \sum_n C_n(t)H_1(t)\,|\phi_n\rangle\, e^{-\frac{-iE_nt}{\hbar}} =$$

$$\cancel{\sum_n C_n(t)E_n\,|\phi_n\rangle\, e^{\frac{-iE_nt}{\hbar}}} + i\hbar\left(\sum_n \frac{d}{dt}C_n(t)\right)|\phi_n\rangle\, e^{-\frac{-iE_nt}{\hbar}}$$

Projecting to the final state $\langle\phi_f| H_{fn}(t) |\phi_n\rangle$

$$\sum_n \underbrace{C_n(t)}_{\uparrow}H_{fn}(t) \langle\phi_f|\phi_{n=f}\rangle e^{-\frac{-iE_nt}{\hbar}} = i\hbar \left(\frac{d}{dt}\underbrace{C_f(t)}_{\uparrow}\right) \langle\phi_f|\phi_{n=f}\rangle e^{-\frac{-iE_ft}{\hbar}}$$

$\uparrow$ $H_{fn}(t)$ allows all C_n to survive

$\uparrow$ only C_f survives and the rest C_n disappear

$$\longrightarrow \quad \frac{1}{i\hbar}C_n(t)H_{fn}(t)e^{-\frac{i(E_f-E_n)t}{\hbar}} = \frac{d}{dt}C_f(t)$$

There are two assumptions to be made :

- at $t = 0$, only the initial state exists $\rightarrow \quad C_i(0) = 1 \quad , \quad C_f(0) = 0$
- at $t = t$, the initial state is weakly perturbed $\rightarrow \quad C_i(t) \approx 1 \quad , \quad C_f(t) \ll 1$

only $n = i$ term survives since everything else is nearly unchanged.

$$\underbrace{\frac{1}{i\hbar}C_i(t)}_{\uparrow}H_{fi}(t)\ e^{-\frac{i(E_f-E_i)t}{\hbar}} = \frac{d}{dt}C_f(t) \ \longrightarrow \ \frac{1}{i\hbar}H_{fi}(t)\ e^{-\frac{i(E_f-E_i)t}{\hbar}} = \frac{d}{dt}C_f(t)$$

$\uparrow$ $C_i(t) \approx 1$

(E.3)

$$\therefore \quad C_f(t) = \frac{1}{i\hbar}\int_0^t H_{fi}(t')\ e^{i\omega_{fi}t'}dt'$$

where $\omega_{fi} = (E_f - E_i)/\hbar$. Hence, probability of finding the system in $|\phi_f\rangle$ is

$$P_{if}(t) = |\langle\phi_f|\psi(t)\rangle|^2 = \frac{1}{\hbar^2}\left|\int_0^t H_{fi}(t')\ e^{i\omega_{fi}t'}dt'\right|^2 \tag{E.4}$$

$$
\begin{aligned}
P_{if}(t) =& \frac{H_{fi}^2}{\hbar^2}\left|\int_0^t \left(e^{i\omega t'}+e^{-i\omega t'}\right)e^{i\omega_{fi}t'}dt'\right|^2 \\
=& \frac{H_{fi}^2}{\hbar^2}\left|\int_0^t \; e^{i(\omega+\omega_{fi})t'}+e^{i(\omega_{fi}-\omega)t'}\; dt'\right|^2 = \frac{H_{fi}^2}{\hbar^2}\left(\left|\; \frac{e^{i(\omega+\omega_{fi})t'}}{i(\omega+\omega_{fi})}+\frac{e^{i(\omega_{fi}-\omega)t'}}{i(\omega_{fi}-\omega)}\right|_0^t\right)^2 \\
=& \frac{H_{fi}^2}{\hbar^2}\left|\; \frac{e^{i(\omega+\omega_{fi})t}-1}{i(\omega+\omega_{fi})}+\frac{e^{i(\omega_{fi}-\omega)t}-1}{i(\omega_{fi}-\omega)}\right|^2
\end{aligned}
\tag{E.5}
$$

ω is near resonance with ω_{fi} such that the 2^{nd} term becomes dominant. Hence,

$$
\begin{aligned}
\approx& \frac{H_{fi}^2}{\hbar^2}\left|\; \frac{e^{i(\omega_{fi}-\omega)t}-1}{i(\omega_{fi}-\omega)}\right|^2 \\
=& \frac{H_{fi}^2}{\hbar^2}\left|\; e^{i(\omega_{fi}-\omega)\frac{t}{2}}\left(\frac{e^{i(\omega_{fi}-\omega)\frac{t}{2}}-e^{-i(\omega_{fi}-\omega)\frac{t}{2}}}{i(\omega_{fi}-\omega)}\right)\right|^2 = \frac{H_{fi}^2}{\hbar^2}\left|\; e^{i(\omega_{fi}-\omega)\frac{t}{2}}\frac{t\; sin\left((\omega_{fi}-\omega)\frac{t}{2}\right)}{(\omega_{fi}-\omega)\frac{t}{2}}\right|^2 \\
=& \frac{H_{fi}^2}{\hbar^2}\left(\cancel{e^{-i(\omega_{fi}-\omega)\frac{t}{2}}}t\; sin\left((\omega_{fi}-\omega)\frac{t}{2}\right)}{(\omega_{fi}-\omega)\frac{t}{2}}\right)\left(\frac{\cancel{e^{i(\omega_{fi}-\omega)\frac{t}{2}}}t\; sin\left((\omega_{fi}-\omega)\frac{t}{2}\right)}{(\omega_{fi}-\omega)\frac{t}{2}}\right) \\
=& \frac{H_{fi}^2}{\hbar^2}t^2\left|sinc\left((\omega_{fi}-\omega)\frac{t}{2}\right)\right|^2
\end{aligned}
\tag{E.6}
$$

We call $\Delta = \omega_{fi} - \omega$ as detuning. If $\Delta = 0$, it is at resonance.

Transition probability : $P(t) = \int P_{fi}(t)\rho(E)dE$. The density of the energy states could be considered as a constant, if its energy range is very narrow.

$$
\begin{aligned}
P(t) =& \int \frac{H_{fi}^2}{\hbar^2}\left|t\cdot sinc\left((\omega_{fi}-\omega)\frac{t}{2}\right)\right|^2\; \rho(E)\; dE \\
=& \frac{H_{fi}^2}{\hbar^2}\rho(E)\int\left|t\cdot\frac{sin\left((\omega_{fi}-\omega)\frac{t}{2}\right)}{(\omega_{fi}-\omega)\frac{t}{2}}\right|^2\; d\hbar\omega \\
=& \frac{H_{fi}^2}{\hbar}\rho(E)\int\left|t^2\cdot\frac{sin^2\left((\omega_{fi}-\omega)\frac{t}{2}\right)}{\left((\omega_{fi}-\omega)\frac{t}{2}\right)}\right|^2\; d\omega
\end{aligned}
\tag{E.7}
$$

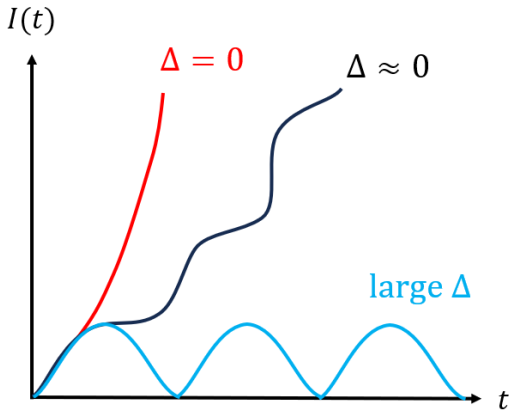

Figure E.1: Comparison of the intensity of the wave generated by a periodically poled nonlinear crystal for different phase matching conditions. A phase mismatch (blue) makes the intensity oscillates periodically in time. A perfect phase-matching condition (red) is the ideal case where the intensity increases quadratically. A quasi-phase-matching condition (black) might not be ideal, but achievable by a periodically poloed nonlinear medium.

By letting $x = (\omega_{fi} - \omega)\frac{t}{2}$ and $dx = -\frac{t}{2}d\omega$,

$$\begin{aligned} &= \frac{H_{fi}^2}{\hbar}\rho(E) \int \left| -\frac{2}{t}\, t^2\, \frac{sin^2(x)}{x^2} \right| \quad dx \quad \cdots \int sinc^2(x)dx = \pi \\ &= \frac{2\pi}{\hbar} H_{fi}^2 \rho(E) t \end{aligned} \tag{E.8}$$

We finally arrive at the Fermi's golden rule.

$$\Gamma_{i\to f} = \frac{d}{dt}P(t) = \frac{2\pi}{\hbar}H_{fi}^2\rho(E) \tag{E.9}$$

Appendix F

Matlab Code - Quasi-Phase-Matching Condition

```
% 2020/05/05 written by Sungeun (Paul) Oh -University of Waterloo, CANADA
%------------[Inputs]--------------
Temp_Start=107; % (in degC)
Temp_End=108; % (in degC)
Lambda_End=2000e-9; % (in meters)

Decimal_Temp = 1; % number of decimals for temperature array (degC)
Decimal_Lambda = 1; % number of decimals for wavelength arrays (nm)

Crystal = "PPLN";
CT_ref=107.6; % crystal temperature (in degC)
CL=1e-2; % crystal length (in meters)
CP=7.10e-6; % crystal poling periods (in meters)
    6.00,6.26,6.53,6.81,7.10,7.40,7.71,8.03,8.36
d_eff=25e-12; % Nonlinear coefficient (m/V)

Lambda_P = 523.64e-9; % Pump wavelength (in meters)
dLambda_P=0.01e-9; % Pump bandwidth (in meters)

%----------Preparations------------
cLight=299792458; % Speed of light (in m/s)

Lambda_P_Front = Lambda_P - 10^(-9-Decimal_Lambda); % To calculate the propagation
    constant of the pump
Lambda_P_Back = Lambda_P + 10^(-9-Decimal_Lambda); % To calculate the propagation constant
     of the pump

Lambda_Start = (1/Lambda_P-1/Lambda_End)^(-1); % starting wavelength from the array (in
    meters)
Length_Temp = (round(Temp_End,Decimal_Temp)-round(Temp_Start,Decimal_Temp))*10^
    Decimal_Temp ;
Length_Lambda = (round(Lambda_End*10^9,Decimal_Lambda) - round(Lambda_Start*10^9,
    Decimal_Lambda))*10^Decimal_Lambda;
```

```
28
29 Array_Lambda_S = linspace(Lambda_Start,Lambda_End,Length_Lambda+1);
30 Array_Lambda_I = (1/Lambda_P-1./Array_Lambda_S).^(-1);
31
32 Array_Temp = linspace(Temp_Start,Temp_End,Length_Temp+1);
33 Array_QPM_S = zeros(Length_Temp+1,1);
34 Array_QPM_I = zeros(Length_Temp+1,1);
35 Array_QPM_dS = zeros(Length_Temp+1,1);
36 Array_QPM_dI = zeros(Length_Temp+1,1);
37
38 PolyTerm = 10;
39 for i=1:length(Array_Temp+1)
40     [no_P,ne_P,no_group_P(j),ne_group_P(j),CLT,CPT] = Function20_Crystalinfo(Lambda_P,
    Crystal,CL,CP,Array_Temp(i));
41     QPM = zeros(length(Array_Lambda_S),1);
42     for j=1:length(Array_Lambda_S)
43         [no_S(j),ne_S(j),no_group_S(j),ne_group_S(j),CLT,CPT] = Function20_Crystalinfo(
    Array_Lambda_S(j),Crystal,CL,CP,Array_Temp(i));
44         [no_I(j),ne_I(j),no_group_I(j),ne_group_I(j),CLT,CPT] = Function20_Crystalinfo(
    Array_Lambda_I(j),Crystal,CL,CP,Array_Temp(i));
45         QPM(j) = 2*pi*CLT*((ne_P-ne_I(j))/Lambda_P+(ne_I(j)-ne_S(j))/Array_Lambda_S(j)-1/
    CPT);
46     end
47     QPMCurve = polyfit(Array_Lambda_S,QPM,PolyTerm);
48     warning('off','all');
49
50     Optimal_S=sort(roots(QPMCurve)); % roots coorespond to possible signal wavelengths for
     the deltaK(quasi-Phase)=0 % (in meters)
51     Optimal_I=(1/Lambda_P-1./(Optimal_S)).^(-1); % (in meters)
52     for p=1:PolyTerm
53         if isreal(Optimal_S(p))==1 && Optimal_S(p)>=Lambda_Start && Optimal_S(p)<=
    Lambda_End % allow only signal and idler positive-real, and higher than pump
    wavelength
54             Optimal_S(p)=Optimal_S(p); % (in meters)
55             Optimal_I(p)=Optimal_I(p); % (in meters)
56         else
57             Optimal_S(p)=0; % non-positive-real, or lower than pump wavelength = erased
58             Optimal_I(p)=0; % non-positive-real, or lower than pump wavelength = erased
59         end
60     end
61     if sum(Optimal_S)==0
62         Optimal_S(1)=NaN;
63         Optimal_I(1)=NaN;
64     else
65     end
66     MultipleRoots_S = round(nonzeros(Optimal_S)*10^9,Decimal_Lambda)*10^(-9);
67     MultipleRoots_I = round(nonzeros(Optimal_I)*10^9,Decimal_Lambda)*10^(-9);
68     % Signal will go something like 700,800,900,1000,1100, when Idler goes
    1100,1000,900,800,700.
69     % To avoid double calculations, we only take the first half of the signal and idler.
70     if mod(length(MultipleRoots_S),2)==0 && length(MultipleRoots_S)~=1
71         Candidate=length(MultipleRoots_S)/2;
72     elseif mod(length(MultipleRoots_S),2)==1 && length(MultipleRoots_S)~=1
73         Candidate=(length(MultipleRoots_S)-1)/2;
74     else
75         Candidate=length(MultipleRoots_S); % which should be 1
76     end
```

```
    % re-analyze the candidates
    CanQPM=zeros(Candidate,1);
    for C=1:Candidate
        [Can_no_S(C),Can_ne_S(C),Can_no_group_S(C),Can_ne_group_S(C),CLT,CPT] =
    Function20_Crystalinfo(MultipleRoots_S(C),Crystal,CL,CP,Array_Temp(i));
        [Can_no_I(C),Can_ne_I(C),Can_no_group_I(C),Can_ne_group_I(C),CLT,CPT] =
    Function20_Crystalinfo(MultipleRoots_I(C),Crystal,CL,CP,Array_Temp(i));
        CanQPM(C)=2*pi*CLT.*((Can_ne_I(C)-Can_ne_S(C))./(MultipleRoots_S(C)*10^(-9))+((
    ne_P-Can_ne_I(C))./Lambda_P)-(1./CPT));
    end
    BestQuasiPhase=min(abs(CanQPM)); % whichever among the candidates is the closest to
    deltaK=0
    Best_S=find(abs(CanQPM)==BestQuasiPhase); % whichever among the candidates is the
    closest to deltaK=0
    Final_S=MultipleRoots_S(Best_S); % I choose you ! (in nanometers)
    Final_I=MultipleRoots_I(Best_S); % I choose you ! (in nanometers)
    if sum(Final_S)==0
        Final_S=NaN;
        Final_I=NaN;
    else
    end
    Array_QPM_S(i) = Final_S(1);
    Array_QPM_I(i) = Final_I(1);
    %--------------------- Bandwidth calculations ------------------------
    Final_S_Front = Array_QPM_S(i) - 10^(-9-Decimal_Lambda);
    Final_S_Back = Array_QPM_S(i) + 10^(-9-Decimal_Lambda);

    Final_I_Front = Array_QPM_I(i) - 10^(-9-Decimal_Lambda);
    Final_I_Back = Array_QPM_I(i) + 10^(-9-Decimal_Lambda);

    [no_P_Front,ne_P_Front,no_group_P_Front,ne_group_P_Front,CLT,CPT] =
    Function20_Crystalinfo(Lambda_P_Front,Crystal,CL,CP,Array_Temp(i));
    [no_P_Back,ne_P_Back,no_group_P_Back,ne_group_P_Back,CLT,CPT] = Function20_Crystalinfo
    (Lambda_P_Back,Crystal,CL,CP,Array_Temp(i));

    [no_S_Final,ne_S_Final,no_group_S_Final,ne_group_S_Final,CLT,CPT] =
    Function20_Crystalinfo(Array_QPM_S(i),Crystal,CL,CP,Array_Temp(i));
    [no_S_Front,ne_S_Front,no_group_S_Front,ne_group_S_Front,CLT,CPT] =
    Function20_Crystalinfo(Final_S_Front,Crystal,CL,CP,Array_Temp(i));
    [no_S_Back,ne_S_Back,no_group_S_Back,ne_group_S_Back,CLT,CPT] = Function20_Crystalinfo
    (Final_S_Back,Crystal,CL,CP,Array_Temp(i));

    [no_I_Final,ne_I_Final,no_group_I_Front,ne_group_I_Front,CLT,CPT] =
    Function20_Crystalinfo(Array_QPM_I(i),Crystal,CL,CP,Array_Temp(i));
    [no_I_Front,ne_I_Front,no_group_I_Final,ne_group_I_Final,CLT,CPT] =
    Function20_Crystalinfo(Final_I_Front,Crystal,CL,CP,Array_Temp(i));
    [no_I_Back,ne_I_Back,no_group_I_Back,ne_group_I_Back,CLT,CPT] = Function20_Crystalinfo
    (Final_I_Back,Crystal,CL,CP,Array_Temp(i));

    dndLambda_P = (((ne_P-ne_P_Front)/(Lambda_P-Lambda_P_Front))+((ne_P_Back-ne_P)/(
    Lambda_P_Back-Lambda_P)))/2;
    Beta_P(i) = (ne_P_Front-Lambda_P*dndLambda_P)/cLight; % propagation constant
    dndLambda_S = (((ne_S_Final-ne_S_Front)/(Array_QPM_S(i)-Final_S_Front))+((ne_S_Back-
    ne_S_Final)/(Final_S_Back-Array_QPM_S(i))))/2;
    Beta_S(i) = (ne_S_Front-Array_QPM_S(i)*dndLambda_S)/cLight; % propagation constant
    dndLambda_I = (((ne_I_Final-ne_I_Front)/(Array_QPM_I(i)-Final_I_Front))+((ne_I_Back-
    ne_I_Final)/(Final_I_Back-Array_QPM_I(i))))/2;
```

```
118     Beta_I(i) = (ne_I_Front-Array_QPM_I(i)*dndLambda_I)/cLight; % propagation constant
119     Array_QPM_dS(i) = abs(Array_QPM_S(i).^2/cLight*(1/CLT/(Beta_I(i)-Beta_S(i))-(Beta_P(i)
        -Beta_I(i))/(Beta_I(i)-Beta_S(i))*cLight*dLambda_P/Lambda_P^2)); % signal BW
120     Array_QPM_dI(i) = abs(Array_QPM_I(i).^2/cLight*(1/CLT/(Beta_S(i)-Beta_I(i))-(Beta_P(i)
        -Beta_S(i))/(Beta_S(i)-Beta_I(i))*cLight*dLambda_P/Lambda_P^2)); % idler BW
121     fprintf('%.2f%sC done\n',Array_Temp(i),char(186));
122 end
```

Appendix G

Matlab Code - Phase variation

```
% 2022/02/19 written by Sungeun (Paul) Oh -University of Waterloo, CANADA
% Temperature fluctuation
Lambda_P = 523.64e-9; % pump wavelength (in meters)
Lambda_S = 790.8e-9; % signal wavelength (in meters)
Lambda_I = 1550e-9; % idler wavelength (in meters)

BD = "BBO";
OpticAngle = pi/4;
Accuracy = 2;
alpha_o = 4e-6; % Thermal expansion coefficients of o-ray (in K^-1) in BBO
alpha_e = 36e-6; % Thermal expansion coefficients of e-ray (in K^-1) in BBO
dno_dT = -9.3e-6; % Thermo-optic coefficients of o-ray (in K^-1) in BBO
dne_dT = -16.6e-6; % Thermo-optic coefficients of e-ray (in K^-1) in BBO
L = 39.4e-3; % length of the BBO beam displacer (in meters)
T = 20; % room temperature (in degC)
dT = 1; % temperature fluctuation (in K)

[no_P,ne_P,neff_P,AOR_P,Vgroup_o_P,Vgroup_e_P,Vgroup_eff_P] = Function1_BDinfo(BD,
    OpticAngle,Lambda_P,Accuracy);
[no_S,ne_S,neff_S,AOR_S,Vgroup_o_S,Vgroup_e_S,Vgroup_eff_S] = Function1_BDinfo(BD,
    OpticAngle,Lambda_S,Accuracy);
[no_I,ne_I,neff_I,AOR_I,Vgroup_o_I,Vgroup_e_I,Vgroup_eff_I] = Function1_BDinfo(BD,
    OpticAngle,Lambda_I,Accuracy);

TK = T + 273.15; % temperature (in K)
theta_eff_P = OpticAngle + AOR_P;
dneff_dT_P = (no_P*dne_dT+ne_P*dno_dT)/sqrt(no_P^2*sin(theta_eff_P)^2+ne_P^2*cos(
    theta_eff_P)^2) + 2*no_P*ne_P*(no_P*dno_dT*sin(theta_eff_P)^2+ne_P*dne_dT*cos(
    theta_eff_P)^2)/(no_P^2*sin(theta_eff_P)^2+ne_P^2*cos(theta_eff_P)^2)^1.5;
theta_eff_S = OpticAngle + AOR_S;
dneff_dT_S = (no_S*dne_dT+ne_S*dno_dT)/sqrt(no_S^2*sin(theta_eff_S)^2+ne_S^2*cos(
    theta_eff_S)^2) + 2*no_S*ne_S*(no_S*dno_dT*sin(theta_eff_S)^2+ne_S*dne_dT*cos(
    theta_eff_S)^2)/(no_S^2*sin(theta_eff_S)^2+ne_S^2*cos(theta_eff_S)^2)^1.5;
theta_eff_I = OpticAngle + AOR_I;
dneff_dT_I = (no_I*dne_dT+ne_I*dno_dT)/sqrt(no_I^2*sin(theta_eff_I)^2+ne_I^2*cos(
    theta_eff_I)^2) + 2*no_I*ne_I*(no_I*dno_dT*sin(theta_eff_I)^2+ne_I*dne_dT*cos(
    theta_eff_I)^2)/(no_I^2*sin(theta_eff_I)^2+ne_I^2*cos(theta_eff_I)^2)^1.5;
```

```
29
30 dPhi_o_P = 2*pi*L/Lambda_P*(dno_dT+no_P*alpha_o)*dT;
31 dPhi_e_P = 2*pi*L/Lambda_P*(dne_dT+ne_P*alpha_e)*dT;
32 dPhi_P = dPhi_e_P - dPhi_o_P
33 dPhi_o_S = 2*pi*L/Lambda_S*(dno_dT+no_S*alpha_o)*dT;
34 dPhi_e_S = 2*pi*L/Lambda_S*(dne_dT+ne_S*alpha_e)*dT;
35 dPhi_S = dPhi_e_S - dPhi_o_S
36 dPhi_o_I = 2*pi*L/Lambda_I*(dno_dT+no_I*alpha_o)*dT;
37 dPhi_e_I = 2*pi*L/Lambda_I*(dne_dT+ne_I*alpha_e)*dT;
38 dPhi_I = dPhi_e_I - dPhi_o_I
39
40 dPhi = dPhi_P - dPhi_S - dPhi_I;
41 dPhi_no = dPhi_P + dPhi_S + dPhi_I;
42
43 fprintf('\n\nphi_P = %.4f pi\n',dPhi_P/pi);
44 fprintf('phi_S = %.4f pi\n',dPhi_S/pi);
45 fprintf('phi_I = %.4f pi\n',dPhi_I/pi);
46 fprintf('\nBD : dPhi = %.4f pi\n',dPhi/pi);
47 fprintf('MZ : dPhi = %.4f pi\n',dPhi_no/pi);
48 %================================================================================
```

Appendix H

Matlab Code - Nonlinear Susceptibility

```
% 2022/02/02 written by Sungeun (Paul) Oh -University of Waterloo, CANADA
% susceptibility
d_eff = 25e-12; % Nonlinear coefficient (m/V)
CP = 7.1e-6; % (in meters) Poling Period
CL = 1e-2; % (in meters) Crystal Length
z = linspace(0,CL,round(CL/CP,0)*10);
Crystal = 'PPLN';
CT = 107.6;
Sumstart = 1;
Sumsize = 100;

Lambda_P = 523.64e-9;
Lambda_S = 790.8e-9;
Lambda_I = 1550e-9;
cLight = 299792458; % Speed of Light (in m/s)
[no_P,ne_P,no_group_P,ne_group_P,CLT,CPT] = Function20_Crystalinfo(Lambda_P,Crystal,CL,CP,
    CT);
[no_S,ne_S,no_group_S,ne_group_S,CLT,CPT] = Function20_Crystalinfo(Lambda_S,Crystal,CL,CP,
    CT);
[no_I,ne_I,no_group_I,ne_group_I,CLT,CPT] = Function20_Crystalinfo(Lambda_I,Crystal,CL,CP,
    CT);
k_P=2*pi*ne_P/Lambda_P; % Wave Number (in rad/m)
k_S=2*pi*ne_S/Lambda_S; % Wave Number (in rad/m)
k_I=2*pi*ne_I/Lambda_I; % Wave Number (in rad/m)
deltak = k_P-k_S-k_I;

for l=1:length(z)
    SUM = 0;
    SUMfactor = 0;
    expterm = 0;
    for i=Sumstart:Sumsize
        SUM = SUM + 4/(i*2-1)/pi.*sin((i*2-1)*pi/2).*exp(1j*2*pi*(i*2-1)/CPT*z(l));
    end
```

```
31      Chi(l) = d_eff*SUM;
32  end
```

Appendix I

Matlab Code - EPS Pair Rate

```
% 2022-01-29 Sungeun (Paul) Oh
% Calculating "Heralding Efficiency" and "Pair Rate" with all lenses given.
Lambda_P = 523.64e-9; % in meters
Lambda_S = 790.8e-9; % in meters
Lambda_I = 1550e-9; % in meters
dLambda_P = 0.01e-9; % spectral bandwidth of the pump (in meters)
dLambda_S = 0.66e-9; % spectral bandwidth of the signal (in meters)
dLambda_I = 2.61e-9; % spectral bandwidth of the idler (in meters)

Crystal = 'PPLN';
CL = 0.010013082006280; % in meters
CP = 7.109288224458798e-06; % in meters
T = 107.6; % in degreeC
d_eff=25e-12; % Nonlinear coefficient (m/V)

cLight=299792458; % speed of light (in m/s)
hbar=1.0545718*10^(-34); % (in kgm^2/s)
epsilon0=8.8541878*10^(-12); % (in F/m) = (in J/m^3) = (in C/V/m)   ,   V x C = J

% %------------------------ Fiber Information -------------------------
Mode = 1; % 1 : MFD, 2 : NA
info_P=3.95e-6;%0.12;%  % numerical aperture (P3-488PM-FC-2) MFD : (3.95+-0.5)e-6, NA :
    0.12
info_S=5.3e-6;%0.13;%  % numerical aperture MFD : (5.3+-1)e-6, NA : 0.13
info_I=9.3e-6;%0.14;%  % numerical aperture MFD : (9.3+-0.5)e-6, NA : 0.13
% %------------------------------- Lens --------------------------------
% % P_obj : 8mm , S_obj : 11mm , I_obj : 15mm
Obj_P = 0.011; % Objective lens (in meters)  %miniature :  11mm
Mag_P = 0.30; % Magnifying lens (in meters)  %miniature : 300mm
Obj_S = 0.01825; % Objective lens (in meters)
Mag_S = 0.35; % Magnifying lens (in meters)  %miniature : 350mm
Obj_I = 0.01825; % Objective lens (in meters)
Mag_I = 0.30; % Magnifying lens (in meters)  %miniature : 300mm
% %---------------------------------------------------------------------
S_eff = 0.4745; % at the crystal
I_eff = 0.3937; % at the crystal
```

```
% %%%%%%%%%%%%%%%%%%%%%%%%%%%%%%%%%%%%%%%%%%%%%%%%%%%%%%%%%%%%%%%%%%%%%%%%%%%%%%%%%%%%%%%%%%%%%%%%%%%
% calculate the spot size of each beam at the crystal
W_P = Function21_SpotSizeWithGivenLenses(Lambda_P,Mode,info_P,Obj_P,Mag_P); % Spot size of the pump in meters
W_S = Function21_SpotSizeWithGivenLenses(Lambda_S,Mode,info_S,Obj_S,Mag_S); % Spot size of the signal in meters
W_I = Function21_SpotSizeWithGivenLenses(Lambda_I,Mode,info_I,Obj_I,Mag_I); % Spot size of the idler in meters
% calculate the pair rate given the spot sizes
[R_S,R_I,R_c] = Function30_PairRate(Lambda_P,Lambda_S,Lambda_I,dLambda_P,dLambda_S,dLambda_I,Crystal,CL,CP,T,W_P,W_S,W_I);
R_Snew = R_S*S_eff;
R_Inew = R_I*I_eff;
R_cnew = R_c*S_eff*I_eff;
Pair = R_Snew*R_Inew/R_cnew;
H_S = R_cnew/R_Inew;
H_I = R_cnew/R_Snew;
```

Appendix J

Matlab Code - Compensations

```
% 2022/08/02 written by Sungeun (Paul) Oh -University of Waterloo, CANADA
%================================[ Input ]================================
Lambda_P = 523.64e-9; % central wavelength of the pump (in meters)
WavelengthEnd = 2000e-9; % (in meters)
Accuracy = 1; % ex ) 1 = 0.1nm, 2 = 0.01nm
BD = "BBO"; % Type of Beam Displacer
OpticAngle = pi/4; % Optic angle of the Beam Displacer (in radians)
BD_length = 39.7 * 10^(-3); % Beam Displacer length (in meters)
cLight = 299792458; % Speed of Light (in m/s)
TargetSignal = 790.8*10^-9;% central wavelength of the signal (in meters)
TargetIdler = 1550*10^-9;% central wavelength of the idler (in meters)
TargetSBW = 0.66e-9; % spectral bandwidth of the signal (in meters)
TargetIBW = 2.61e-9; % spectral bandwidth of the idler (in meters)
Compensator = "Calcite"; % Compensator for walk-off : 'aBBO' 'Quartz' 'Calcite'
WedgeAngle = 15/180*pi; % angle of the wedges, in radians
%=========================================================================
% Providing wavelength domains for signal and idler.
[Lambda_S,WavelengthStart_S] = Function3_SPDCwavelengths(Lambda_P,WavelengthEnd,Accuracy);
[Lambda_I,WavelengthStart_I] = Function3_SPDCwavelengths(Lambda_P,WavelengthEnd,Accuracy);

% Obtain the refractive indices (no,ne,neff), the angle of refraction (AOR) and the group
    velocities (Vgroup_o,Vgroup_e,Vgroup_eff) in the Beam Displacer
[P1_BD_no,P1_BD_ne,P1_BD_neff,P1_AOR,P1_Vgroup_o,P1_Vgroup_e,P1_Vgroup_eff] =
    Function1_BDinfo(BD,OpticAngle,Lambda_P,Accuracy);
[S2_BD_no,S2_BD_ne,S2_BD_neff,S2_AOR,S2_Vgroup_o,S2_Vgroup_e,S2_Vgroup_eff] =
    Function1_BDinfo(BD,OpticAngle,Lambda_S,Accuracy);
[I2_BD_no,I2_BD_ne,I2_BD_neff,I2_AOR,I2_Vgroup_o,I2_Vgroup_e,I2_Vgroup_eff] =
    Function1_BDinfo(BD,OpticAngle,Lambda_I,Accuracy);

% Spatial and temporal walk-off calculations
[S_D_Walkoff, S_T_Walkoff] = Function2_Walkoffs(P1_Vgroup_o,P1_Vgroup_eff,S2_Vgroup_o,
    S2_Vgroup_eff,BD_length,BD_length,P1_AOR,S2_AOR);
[I_D_Walkoff, I_T_Walkoff] = Function2_Walkoffs(P1_Vgroup_o,P1_Vgroup_eff,I2_Vgroup_o,
    I2_Vgroup_eff,BD_length,BD_length,P1_AOR,I2_AOR);

% Find the signal and idler wavelengths that we are interested in.
```

```
SignalIndex = find(Lambda_S==TargetSignal);
IdlerIndex = find(Lambda_I==TargetIdler);

% Determine the walk-offs at the target wavelengths.
Signal_D_Walkoff = S_D_Walkoff(SignalIndex)+ 0.04747*10^(-3); % An extra walk-off (0.04747 mm) from the dichroic mirrors is manually added
Idler_D_Walkoff = I_D_Walkoff(IdlerIndex)+ 0.15835*10^(-3); % An extra walk-off (0.15835mm ) from the dichroic mirrors is manually added
Signal_T_Walkoff = S_T_Walkoff(SignalIndex);
Idler_T_Walkoff = I_T_Walkoff(IdlerIndex);
%================================================
% Preparing the spatial mode Gaussian functions
% Signal : FWHM = 0.6mm
% So the standard deviation is FWHM/(2sqrt(2ln2)) = 0.255mm MFR
SBeam_o_MFD = 0.51e-3;
SBeam_e_MFD = 0.51e-3;
SD_Walkoff = Signal_D_Walkoff;

% Idler : FWHM = 0.8mm
% So the standard deviation is FWHM/(2sqrt(2ln2)) = 0.34mm MFR
IBeam_o_MFD = 0.68e-3;
IBeam_e_MFD = 0.68e-3;
ID_Walkoff = Idler_D_Walkoff;
%================================================
% Preparing the temporal mode Gaussian functions
[SBeam_o_TW] = Function8_TemporalWidth(TargetSignal, TargetSBW); % temporal width of signal (in meters)
[SBeam_e_TW] = Function8_TemporalWidth(TargetSignal, TargetSBW); % temporal width of signal (in meters)
ST_Walkoff = Signal_T_Walkoff;
[IBeam_o_TW] = Function8_TemporalWidth(TargetIdler, TargetIBW); % temporal width of idler (in meters)
[IBeam_e_TW] = Function8_TemporalWidth(TargetIdler, TargetIBW); % temporal width of idler (in meters)
IT_Walkoff = Idler_T_Walkoff;
%================================================
TWidth_o_S = SBeam_o_TW/(2*sqrt(2*log(2))); % convert FWHM into standard deviation, 1sigma
TWidth_e_S = SBeam_e_TW/(2*sqrt(2*log(2))); % convert FWHM into standard deviation, 1sigma
TWidth_o_I = IBeam_o_TW/(2*sqrt(2*log(2))); % convert FWHM into standard deviation, 1sigma
TWidth_e_I = IBeam_e_TW/(2*sqrt(2*log(2))); % convert FWHM into standard deviation, 1sigma
[Spatial_Overlap_S] = Function4_SpatialOverlap(SBeam_o_MFD,SBeam_e_MFD,SD_Walkoff);
[Temporal_Overlap_S] = Function5_TemporalOverlap(TWidth_o_S,TWidth_e_S,ST_Walkoff)
[Spatial_Overlap_I] = Function4_SpatialOverlap(IBeam_o_MFD,IBeam_e_MFD,ID_Walkoff);
[Temporal_Overlap_I] = Function5_TemporalOverlap(TWidth_o_I,TWidth_e_I,IT_Walkoff)

[Compensator_no_S,Compensator_ne_S,CVgroup_oS,CVgroup_eS] = Function9_Compensator(TargetSignal,Compensator);
[Compensator_no_I,Compensator_ne_I,CVgroup_oI,CVgroup_eI] = Function9_Compensator(TargetIdler,Compensator);
CompensatorN_S = CVgroup_eS-CVgroup_oS;
CompensatorN_I = CVgroup_eI-CVgroup_oI;
CompensatorSignal = abs((ST_Walkoff-IT_Walkoff).*CompensatorN_S)*1000 % size of the signal compensator crystal (in meters)
CompensatorIdler = abs(CompensatorN_I) % size of the idler compensator crystal (in meters)
```

Appendix K

Matlab Code - PairRate Calculations

```
% 2022/02/04 written by Sungeun (Paul) Oh -University of Waterloo, CANADA
%================================[input]==================================
% Wavelengths (in meters)
clear;
Lambda_P=523.64e-9;
Lambda_S=790.8e-9;
Lambda_I=1550e-9;
% Frequency bandwidths (in Hz) This is not FWHM but 1 standard deviation
domega_P=4.6429874e9;
domega_S=2.4230264e10;
domega_I=2.4941619e10;
% Crystal info
Crystal = "PPLN";
CL = 1e-2; % crystal length (in meters)
CP = 7.10e-6; % crystal poling period (in meters)
T = 107.6; % crystal temperature (degC)
d_eff=25*10^(-12); % Nonlinear coefficient (in m/V)
Power=0.001; % Pump power (in Watts)
%=========================================================================
epsilon0=8.8541878*10^(-12); % (in F/m) = (in J/m^3) = (in C/V/m)   ,   V x C = J
cLight=299792458; % Speed of light (in m/s)
hbar=1.0545718*10^(-34); % Planck constant (in kgm^2/s)
% Extraordinary refractive indices (obtained from Sellmeier eq)
[no_P,ne_P,no_group_P,ne_group_P,CLT,CPT] = Function20_Crystalinfo(Lambda_P,Crystal,CL,CP,
    T);
[no_S,ne_S,no_group_S,ne_group_S,CLT,CPT] = Function20_Crystalinfo(Lambda_S,Crystal,CL,CP,
    T);
[no_I,ne_I,no_group_I,ne_group_I,CLT,CPT] = Function20_Crystalinfo(Lambda_I,Crystal,CL,CP,
    T);
%=========================================================================
% Wave numbers (in rad/m)
k_P=2*pi*ne_P/Lambda_P;
k_S=2*pi*ne_S/Lambda_S;
k_I=2*pi*ne_I/Lambda_I;
omega_P = 2*pi*cLight/Lambda_P; % Pump Frequency (in rad Hz)
deltak = k_P-k_S-k_I; % Wave number mismatch without QPM
mK=2*pi/CPT; % Wave number of poling (First order of Taylor series)
```

```
N_P=2*pi*Power/hbar/omega_P; % number of pump photons at the given pump power
Phase= (k_P-k_S-k_I-(mK))*CLT; % Phase = (deltak)L
%
    ------------------------------------------------------------------------------------------------------------

% Find optimal spot sizes
logstart=-2; % pump array start
logend=2; % pump array end
increment=20; % only positive integers should be used for this.
% Arrays of Focal parameters
Candidate_Length=(logend-logstart)*increment; % Size of the arrays.
Xsi_P=logspace(logstart,logend,Candidate_Length);
Xsi_S=logspace(logstart,logend,Candidate_Length);
Xsi_I=logspace(logstart,logend,Candidate_Length);
Xsi=logspace(logstart,logend,Candidate_Length);
% Combination Arrays of candidate Signal and Idler Spotsize.
% 1: Optimal Xsi_P, 2: Optimal Xsi_S, 3: Optimal Xsi_I, 4: Optimal overall Xsi, 5: Upper-
    bound coincidence rate, 6: Upper-bound single rate (signal), 7: Upper-bound single
    rate (idler)
Candidate_Combinations=zeros(Candidate_Length,7);
%
    ------------------------------------------------------------------------------------------------------------

% Find the optimal focal parameter. Simulate all possible combinations for each Xsi_P
    value, find and collect only the ones that give the optimal coincidence rate

ProbFactor = Power*64*pi^2*d_eff^2*Lambda_P/epsilon0/ne_P^2/(abs(ne_group_I-ne_group_S))/
    Lambda_S^2/Lambda_I^2; % Same for pair and single rates

for i=1:Candidate_Length
    Candidate_Xsi=zeros(Candidate_Length,Candidate_Length);
    IntegralResult=zeros(Candidate_Length,Candidate_Length);
    ConstantC1_pair=zeros(Candidate_Length,Candidate_Length);
    ConstantC2_pair=zeros(Candidate_Length,Candidate_Length);
    ConstantC3_pair=zeros(Candidate_Length,Candidate_Length);
    for j=1:Candidate_Length % first loop for the candidate SignalXsi
        for k=1:Candidate_Length % second loop for the candidate IdlerXsi
            ConstantC1_pair(j,k)=1+k_S/k_P*Xsi_S(j)./Xsi_P(i)+k_I/k_P*Xsi_I(k)./Xsi_P(i);
            ConstantC2_pair(j,k)=(1-deltak/k_P).*(1+((k_S+deltak).*Xsi_P(i))./((k_P-deltak
    ).*Xsi_S(j))+((k_I+deltak).*Xsi_P(i))./((k_P-deltak).*Xsi_I(k)));
            ConstantC3_pair(j,k)=Xsi_P(i).^2./Xsi_S(j)./Xsi_I(k).*ConstantC1_pair(j,k)./
    ConstantC2_pair(j,k).^2*deltak/k_P;
            Candidate_Xsi(j,k)=ConstantC2_pair(j,k)/ConstantC1_pair(j,k).*Xsi_S(j).*Xsi_I(
    k)./Xsi_P(i);
            % Joint Spectral Function
            F=@(l) 1./(1-1i*Candidate_Xsi(j,k).*l-ConstantC3_pair(j,k).*Candidate_Xsi(j,k)
    .^2.*l.^2)./(1+1i*Candidate_Xsi(j,k).*l-ConstantC3_pair(j,k).*Candidate_Xsi(j,k).^2.*l
    .^2);
            IntegralResult(j,k)=Candidate_Xsi(j,k).*abs(integral(F,-1,1))./(
    ConstantC1_pair(j,k).*ConstantC2_pair(j,k));
        end
    end
    % Identify the combination that gave the maximum value from the integral of the Joint
    Spectral Function.
    IntegralMax=max(max(IntegralResult));
    [FoundSignal,FoundIdler]=find(IntegralResult==IntegralMax);
    Candidate_Combinations(i,1)=Xsi_P(i);
```

```
77      Candidate_Combinations(i,2)=Xsi_S(FoundSignal);
78      Candidate_Combinations(i,3)=Xsi_I(FoundIdler);
79      ConstantC1_pair_Win=ConstantC1_pair(FoundSignal,FoundIdler); % Optimal C1
80      ConstantC2_pair_Win=ConstantC2_pair(FoundSignal,FoundIdler); % Optimal C2
81      Candidate_Combinations(i,4)=Candidate_Xsi(FoundSignal,FoundIdler);
82      Candidate_Combinations(i,5)=2*ProbFactor*atan(Candidate_Combinations(i,4))./
        ConstantC1_pair_Win./ConstantC2_pair_Win; % pair rate
83      fprintf('%d done \n',i);
84  end
85  % ---------------Single rates-----------------------------
86  for i=1:Candidate_Length
87      ConstantC1_S=2*sqrt((1+k_S/k_P.*Candidate_Combinations(i,2)./Xsi_P(i))*k_I/k_P);
88      ConstantC2_S=2*(1-deltak/k_P).*sqrt((1+((k_S+deltak).*Xsi_P(i))./((k_P-deltak).*
        Candidate_Combinations(i,2)))*(k_I+deltak)/(k_P-deltak));
89      ConstantC1_I=2*sqrt((1+k_I/k_P.*Candidate_Combinations(i,3)./Xsi_P(i))*k_S/k_P);
90      ConstantC2_I=2*(1-deltak/k_P).*sqrt((1+((k_I+deltak).*Xsi_P(i))./((k_P-deltak).*
        Candidate_Combinations(i,3)))*(k_S+deltak)/(k_P-deltak));
91      Candidate_Combinations(i,6)=ProbFactor*atan(ConstantC2_S/ConstantC1_S.*
        Candidate_Combinations(i,2))/ConstantC1_S/ConstantC2_S;
92      Candidate_Combinations(i,7)=ProbFactor*atan(ConstantC2_I/ConstantC1_I.*
        Candidate_Combinations(i,3))/ConstantC1_I/ConstantC2_I;
93  end
94  SpotSize_P=sqrt(CLT/k_P./Candidate_Combinations(:,1)); % Spot radius of the pump (in
        meters)
95  SpotSize_S=sqrt(CLT/k_S./Candidate_Combinations(:,2)); % Spot radius of the signal (in
        meters)
96  SpotSize_I=sqrt(CLT/k_I./Candidate_Combinations(:,3)); % Spot radius of the idler (in
        meters)
97
98  semilogx(SpotSize_P*10^6,Candidate_Combinations(:,5)*10^-6,'k','LineWidth',1.5);
```

Appendix L

Matlab Code - Other Functions

Listing L.1: Function1_BDinfo

```
% 2021/01/24 written by Sungeun (Paul) Oh -University of Waterloo, CANADA
% This function generates refractive indices of the crystal.
%------------------------------[input]--------------------------------
% Name of the crystal (BD) : "BBO", "Calcite", "YVO4' available at this moment
% Optic Angle (Optic Angle) : in radians
% Array of Wavelengths (Lambda): in meters
% Accuracy (Accuracy) : number of decimal
%------------------------------[output]-------------------------------
% BD_no    : ordinary refractive index
% BD_ne    : extraordinary refractive index
% BD_neff  : effective refractive index
% AOR      : angle of refraction
% Vgroup_o : ordinary group velocity
% Vgroup_e : extraordinary group velocity
% Vgroup_eff : effective group velocity
%------------------------------[function]-----------------------------
function [BD_no,BD_ne,BD_neff,AOR,Vgroup_o,Vgroup_e,Vgroup_eff] = Function1_BDinfo(BD,
    OpticAngle,Lambda,Accuracy)
    c = 299792458; % speed of light (m/s)
    if length(Lambda)==1
        LambdaNext = Lambda+10^(-Accuracy-9);
        LambdaPrevious = Lambda-10^(-Accuracy-9);
    else
        LambdaNext = Lambda(2);
        LambdaPrevious = Lambda(end-1);
    end
    if BD == "BBO"
        LambdaFront = Lambda(1)-(LambdaNext-Lambda(1)); % very front
        LambdaBack = Lambda(end)+(Lambda(end)-LambdaPrevious); % very back
        ExtendedLambda = cat(2,LambdaFront,Lambda,LambdaBack);
        ExtendedBD_no = sqrt(2.67579+0.02099./((ExtendedLambda*10^6).^2-0.00470)
    -0.00528.*(ExtendedLambda*10^6).^2);
        ExtendedBD_ne = sqrt(2.31197+0.01184./((ExtendedLambda*10^6).^2-0.01607)
    -0.00400.*(ExtendedLambda*10^6).^2);
```

```
        Extended_dLambda = ExtendedLambda(2:end)-ExtendedLambda(1:end-1);
        Extended_dno = ExtendedBD_no(2:end)-ExtendedBD_no(1:end-1);
        Extended_dne = ExtendedBD_ne(2:end)-ExtendedBD_ne(1:end-1);
        ExtendedtanAOR = (1-(ExtendedBD_no./ExtendedBD_ne).^2).*(tan(OpticAngle)./(1+(ExtendedBD_no./ExtendedBD_ne).^2.*tan(OpticAngle).^2));
        ExtendedAOR = atan(ExtendedtanAOR); % angle of refraction
        ExtendedBD_neff = ExtendedBD_no.*ExtendedBD_ne./sqrt((ExtendedBD_no.^2).*sin(OpticAngle+ExtendedAOR).^2+(ExtendedBD_ne.^2).*cos(OpticAngle+ExtendedAOR).^2);
        Extended_dneff = ExtendedBD_neff(2:end)-ExtendedBD_neff(1:end-1);
        for i=1:length(Lambda)
            d_Lambda(i) = (Extended_dLambda(i)+Extended_dLambda(i+1))/2;
            d_no(i) = (Extended_dno(i)+Extended_dno(i+1))/2;
            d_ne(i) = (Extended_dne(i)+Extended_dne(i+1))/2;
            d_neff(i) = (Extended_dneff(i)+Extended_dneff(i+1))/2;
        end
        AOR = ExtendedAOR(2:end-1);
        BD_no = ExtendedBD_no(2:end-1);
        BD_ne = ExtendedBD_ne(2:end-1);
        BD_neff = ExtendedBD_neff(2:end-1);
        Vgroup_o = c./(BD_no-Lambda.*(d_no./d_Lambda));
        Vgroup_e = c./(BD_ne-Lambda.*(d_ne./d_Lambda));
        Vgroup_eff = c./(BD_neff-Lambda.*(d_neff./d_Lambda));
%-------------------------------------------------------------------------
    elseif BD == "Calcite"
        LambdaFront = Lambda(1)-(LambdaNext-Lambda(1));
        LambdaBack = Lambda(end)+(Lambda(end)-LambdaPrevious);
        ExtendedLambda = cat(2,LambdaFront,Lambda,LambdaBack);
        ExtendedBD_no = sqrt(2.69705+0.0192064./((ExtendedLambda*10^6).^2-0.01820)-0.0151624.*(ExtendedLambda*10^6).^2);
        ExtendedBD_ne = sqrt(2.18438+0.0087309./((ExtendedLambda*10^6).^2-0.01018)-0.0024411.*(ExtendedLambda*10^6).^2);
        Extended_dLambda = ExtendedLambda(2:end)-ExtendedLambda(1:end-1);
        Extended_dno = ExtendedBD_no(2:end)-ExtendedBD_no(1:end-1);
        Extended_dne = ExtendedBD_ne(2:end)-ExtendedBD_ne(1:end-1);
        ExtendedtanAOR = (1-(ExtendedBD_no./ExtendedBD_ne).^2).*(tan(OpticAngle)./(1+(ExtendedBD_no./ExtendedBD_ne).^2.*tan(OpticAngle).^2));
        ExtendedAOR = atan(ExtendedtanAOR); % angle of refraction
        ExtendedBD_neff = ExtendedBD_no.*ExtendedBD_ne./sqrt((ExtendedBD_no.^2).*sin(OpticAngle+ExtendedAOR).^2+(ExtendedBD_ne.^2).*cos(OpticAngle+ExtendedAOR).^2);
        Extended_dneff = ExtendedBD_neff(2:end)-ExtendedBD_neff(1:end-1);
        for i=1:length(Lambda)
            d_Lambda(i) = (Extended_dLambda(i)+Extended_dLambda(i+1))/2;
            d_no(i) = (Extended_dno(i)+Extended_dno(i+1))/2;
            d_ne(i) = (Extended_dne(i)+Extended_dne(i+1))/2;
            d_neff(i) = (Extended_dneff(i)+Extended_dneff(i+1))/2;
        end
        AOR = ExtendedAOR(2:end-1);
        BD_no = ExtendedBD_no(2:end-1);
        BD_ne = ExtendedBD_ne(2:end-1);
        BD_neff = ExtendedBD_neff(2:end-1);
        Vgroup_o = c./(BD_no-Lambda.*(d_no./d_Lambda));
        Vgroup_e = c./(BD_ne-Lambda.*(d_ne./d_Lambda));
        Vgroup_eff = c./(BD_neff-Lambda.*(d_neff./d_Lambda));
%-------------------------------------------------------------------------
    elseif BD == "YVO4"
        LambdaFront = Lambda(1)-(LambdaNext-Lambda(1));
        LambdaBack = Lambda(end)+(Lambda(end)-LambdaPrevious);
```

```
        ExtendedLambda = cat(2,LambdaFront,Lambda,LambdaBack);
        ExtendedBD_no = sqrt(3.77834+0.069736./((ExtendedLambda*10^6).^2-0.04724)
    -0.0108133.*(ExtendedLambda*10^6).^2);
        ExtendedBD_ne = sqrt(4.59905+0.110534./((ExtendedLambda*10^6).^2-0.04813)
    -0.0122676.*(ExtendedLambda*10^6).^2);
        Extended_dLambda = ExtendedLambda(2:end)-ExtendedLambda(1:end-1);
        Extended_dno = ExtendedBD_no(2:end)-ExtendedBD_no(1:end-1);
        Extended_dne = ExtendedBD_ne(2:end)-ExtendedBD_ne(1:end-1);
        ExtendedtanAOR = (1-(ExtendedBD_no./ExtendedBD_ne).^2).*(tan(OpticAngle)./(1+(
    ExtendedBD_no./ExtendedBD_ne).^2.*tan(OpticAngle).^2));
        ExtendedAOR = atan(ExtendedtanAOR); % angle of refraction
        ExtendedBD_neff = ExtendedBD_no.*ExtendedBD_ne./sqrt((ExtendedBD_no.^2).*sin(
    OpticAngle+ExtendedAOR).^2+(ExtendedBD_ne.^2).*cos(OpticAngle+ExtendedAOR).^2);
        Extended_dneff = ExtendedBD_neff(2:end)-ExtendedBD_neff(1:end-1);
        for i=1:length(Lambda)
            d_Lambda(i) = (Extended_dLambda(i)+Extended_dLambda(i+1))/2;
            d_no(i) = (Extended_dno(i)+Extended_dno(i+1))/2;
            d_ne(i) = (Extended_dne(i)+Extended_dne(i+1))/2;
            d_neff(i) = (Extended_dneff(i)+Extended_dneff(i+1))/2;
        end
        AOR = ExtendedAOR(2:end-1);
        BD_no = ExtendedBD_no(2:end-1);
        BD_ne = ExtendedBD_ne(2:end-1);
        BD_neff = ExtendedBD_neff(2:end-1);
        Vgroup_o = c./(BD_no-Lambda.*(d_no./d_Lambda));
        Vgroup_e = c./(BD_ne-Lambda.*(d_ne./d_Lambda));
        Vgroup_eff = c./(BD_neff-Lambda.*(d_neff./d_Lambda));
%-------------------------------------------------------------------------
    elseif BD == "Quartz"
        LambdaFront = Lambda(1)-(LambdaNext-Lambda(1));
        LambdaBack = Lambda(end)+(Lambda(end)-LambdaPrevious);
        ExtendedLambda = cat(2,LambdaFront,Lambda,LambdaBack);
        ExtendedBD_no = sqrt(2.3573-0.01170.*(ExtendedLambda*10^6).^2+0.01054./(
    ExtendedLambda*10^6).^2+1.3414*10^(-4)./(ExtendedLambda*10^6).^4-4.4537*10^(-7)./(
    ExtendedLambda*10^6).^6+5.9236*10^(-8)./(ExtendedLambda*10^6).^8);
        ExtendedBD_ne = sqrt(2.3849-0.01259.*(ExtendedLambda*10^6).^2+0.01079./(
    ExtendedLambda*10^6).^2+1.6518*10^(-4)./(ExtendedLambda*10^6).^4-1.9474*10^(-7)./(
    ExtendedLambda*10^6).^6+9.3648*10^(-8)./(ExtendedLambda*10^6).^8);
        Extended_dLambda = ExtendedLambda(2:end)-ExtendedLambda(1:end-1);
        Extended_dno = ExtendedBD_no(2:end)-ExtendedBD_no(1:end-1);
        Extended_dne = ExtendedBD_ne(2:end)-ExtendedBD_ne(1:end-1);
        ExtendedtanAOR = (1-(ExtendedBD_no./ExtendedBD_ne).^2).*(tan(OpticAngle)./(1+(
    ExtendedBD_no./ExtendedBD_ne).^2.*tan(OpticAngle).^2));
        ExtendedAOR = atan(ExtendedtanAOR); % angle of refraction
        ExtendedBD_neff = ExtendedBD_no.*ExtendedBD_ne./sqrt((ExtendedBD_no.^2).*sin(
    OpticAngle+ExtendedAOR).^2+(ExtendedBD_ne.^2).*cos(OpticAngle+ExtendedAOR).^2);
        Extended_dneff = ExtendedBD_neff(2:end)-ExtendedBD_neff(1:end-1);
        for i=1:length(Lambda)
            d_Lambda(i) = (Extended_dLambda(i)+Extended_dLambda(i+1))/2;
            d_no(i) = (Extended_dno(i)+Extended_dno(i+1))/2;
            d_ne(i) = (Extended_dne(i)+Extended_dne(i+1))/2;
            d_neff(i) = (Extended_dneff(i)+Extended_dneff(i+1))/2;
        end
        AOR = ExtendedAOR(2:end-1);
        BD_no = ExtendedBD_no(2:end-1);
        BD_ne = ExtendedBD_ne(2:end-1);
        BD_neff = ExtendedBD_neff(2:end-1);
```

```
        Vgroup_o = c./(BD_no-Lambda.*(d_no./d_Lambda));
        Vgroup_e = c./(BD_ne-Lambda.*(d_ne./d_Lambda));
        Vgroup_eff = c./(BD_neff-Lambda.*(d_neff./d_Lambda));
%-------------------------------------------------------------------------
    else
        disp(' ');
        disp('Unknown beam displacer. Type again.');
        disp(' ');
        return
    end
    if Lambda(1)<400*10^-9
        disp(' ');
        disp('The wavelength range should be longer than 400nm');
        disp(' ');
        return
    end
end
```

Listing L.2: Function2_Walkoffs

```
% 2021/01/25 written by Sungeun (Paul) Oh -University of Waterloo, CANADA
% This function generates spatial and temporal walkoffs after two beam displacers
%---------------------------------[input]---------------------------------
% Ordinary/Extraordinary group velocities in two beam displacers
% Length of the two beam displacers (BD1_length, BD2_length): in meters
% Angle of refractions of the two beam displacers (AOR1, AOR2): in radians
%--------------------------------[output]---------------------------------
% D_Walkoff : Spatial walkoff ( in meters )
% T_Walkoff : Temporal Walkoff ( in seconds )
%-------------------------------[function]--------------------------------
function [D_Walkoff, T_Walkoff] = Function2_Walkoffs(BD1_Vgroup_o,BD1_Vgroup_eff,
    BD2_Vgroup_o,BD2_Vgroup_eff,BD1_length,BD2_length,AOR1,AOR2)
    % Spatial Walkoff (D_Signal, D_idler) in meters
    D_Walkoff = BD2_length.*tan(AOR2)-BD1_length.*tan(AOR1);
    % Temporal Walkoff (T_Signal, T_idler) in seconds
    T_Walkoff_oe = BD1_length./BD1_Vgroup_o + BD2_length./cos(AOR2)./BD2_Vgroup_eff;
    T_Walkoff_eo = BD1_length./cos(AOR1)./BD1_Vgroup_eff + BD2_length./BD2_Vgroup_o;
    T_Walkoff = T_Walkoff_oe-T_Walkoff_eo; %"delay of final e - delay of final o"
end
```

Listing L.3: Function3_SPDCwavelengths

```
% 2021/01/25 written by Sungeun (Paul) Oh -University of Waterloo, CANADA
% This function generates arrays of signal/idler wavelengths
%-------------------------------[input]---------------------------------
% Pump wavelength       : in meters
% Wavelength Range(end) : in meters
% Accuracy              : number of intervals for 1 nm , in number of digits
%-------------------------------[output]--------------------------------
% Lambda_S  : Signal wavelengths (in meters)
%-----------------------------[function]--------------------------------
function [Lambda_S,WavelengthStart] = Function3_SPDCwavelengths(Lambda_P,WavelengthEnd,
    Accuracy)
    Lambda_P2 = round(Lambda_P*10^9,Accuracy);
    WavelengthEnd2 = round(WavelengthEnd*10^9,Accuracy);
    WavelengthStart2 = round((1/Lambda_P2-1/WavelengthEnd2)^(-1),Accuracy); %signal/idler
```

```
    WavelengthStart = WavelengthStart2*10^(-9);
    WavelengthBins = (WavelengthEnd2-WavelengthStart2)*10^Accuracy;
    Lambda_S2 = linspace(WavelengthStart2+10^(-Accuracy),WavelengthEnd2,WavelengthBins);
    Lambda_S = Lambda_S2*10^(-9);
end
```

Listing L.4: Function4_SpatialOverlap

```
% 2022/01/27 written by Sungeun (Paul) Oh -University of Waterloo, CANADA
% This function calculates spatial overlap of two beams (ordinary, extraordinary)
% Gaussian functions are used (FWHM @ 1/e^2, intensity profile)
%------------------------------[input]--------------------------------
% Ordinary beam's mode-field diameter      : in meters
% Extraordinary beam's mode-field diameter : in meters
% Spatial Walkoff                          : in meters
%------------------------------[output]-------------------------------
% Spatial overlap: in fraction
%-----------------------------[function]-------------------------------

function [Spatial_Overlap] = Function4_SpatialOverlap(Beam_o_MFD,Beam_e_MFD,D_Walkoff)  % mode field diameter (in meters)
    sigma_o = Beam_o_MFD/4*10^3; % SD (in mm)
    sigma_e = Beam_e_MFD/4*10^3; % SD (in mm)
    D_Walkoffmm = D_Walkoff*10^3; % SD (in mm)
    pos_o = 0;
    pos_e = 0;
    NormalizingGaussian = @(pos_x,pos_y) exp(-(pos_o-pos_x).^2./2/sigma_o.^2-(pos_o-pos_y).^2./2/sigma_o.^2-(pos_e-pos_x).^2./2/sigma_e.^2-(pos_e-pos_y).^2./2/sigma_e.^2);
    Normalization = integral2(NormalizingGaussian,-inf,inf,-inf,inf); % normalization constant
    Gaussian = @(pos_x,pos_y) 1/Normalization.*exp(-(pos_o-pos_x).^2./2/sigma_o.^2-(pos_o-pos_y).^2./2/sigma_o.^2-(pos_e-pos_x-D_Walkoffmm).^2./2/sigma_e.^2-(pos_e-pos_y-D_Walkoffmm).^2./2/sigma_e.^2);
    Spatial_Overlap = integral2(Gaussian,-inf,inf,-inf,inf);
end
```

Listing L.5: Function5_TemporalOverlap

```
% 2022/01/27 written by Sungeun (Paul) Oh -University of Waterloo, CANADA
% This function calculates temporal overlap of two beams (ordinary, extraordinary)
% Gaussian functions are used (FWHM @ 1/e^2 intensity overlap)
% temporal radius = 1 standard deviation
%------------------------------[input]--------------------------------
% Ordinary beam's temporal width      : in meters
% Extraordinary beam's temporal width : in meters
% Temporal Walkoff                    : in meters
%------------------------------[output]-------------------------------
% Temporal overlap   : in fraction
%-----------------------------[function]-------------------------------
function [Temporal_Overlap] = Function5_TemporalOverlap(Beam_o_TW,Beam_e_TW,T_Walkoff)
    sigma_o = Beam_o_TW*10^12; % SD (in ps)
    sigma_e = Beam_e_TW*10^12; % SD (in ps)
    T_Walkoffps = T_Walkoff*10^12;
    pos_o = 0;
    pos_e = 0;
    NormalizingGaussian = @(pos_x,pos_y) exp(-(pos_o-pos_x).^2./2/sigma_o.^2-(pos_o-pos_y).^2./2/sigma_o.^2-(pos_e-pos_x).^2./2/sigma_e.^2-(pos_e-pos_y).^2./2/sigma_e.^2);
```

```
    Normalization = integral2(NormalizingGaussian,-inf,inf,-inf,inf); % normalization
    constant
    Gaussian = @(pos_x,pos_y) 1/Normalization.*exp(-(pos_o-pos_x).^2./2/sigma_o.^2-(pos_o-
    pos_y).^2./2/sigma_o.^2-(pos_e-pos_x-T_Walkoffps).^2./2/sigma_e.^2-(pos_e-pos_y-
    T_Walkoffps).^2./2/sigma_e.^2);
    Temporal_Overlap = integral2(Gaussian,-inf,inf,-inf,inf);
end
```

Listing L.6: Function8_TemporalWidth

```
% 2022/02/21 written by Sungeun (Paul) Oh -University of Waterloo, CANADA
% This function computes Temporal width (or Pulse Duration)
%------------------------------[input]------------------------------
% Central Wavelength (in meters)
% Bandwidth (in meters) from FWHM
%------------------------------[output]-----------------------------
% Temporal Width or Pulse Duration (in seconds) as FWHM
%-----------------------------[function]----------------------------
function [TW] = Function8_TemporalWidth(CW, BW)
    cLight = 299792458; % in m/s
    BW_freq = BW*cLight/(CW^2);
    TW = 1/BW_freq;
end
```

Listing L.7: Function9_Compensator

```
% 2022/05/09 written by Sungeun (Paul) Oh -University of Waterloo, CANADA
% This function generates refractive indices of quartz.
%------------------------------[input]------------------------------
% Array of Wavelengths : in meters
% Name of the material : Calcite, Quartz
%------------------------------[output]-----------------------------
% Compensator_no    : ordinary refractive index
% Compensator_ne    : extraordinary refractive index
%-----------------------------[function]----------------------------
function [Compensator_no,Compensator_ne,CVgroup_o,CVgroup_e] = Function9_Compensator(
    Lambda,Material)
    Lambda2=1.01*Lambda;
    cLight=299792458; % speed of light (m/s)
    %  Alpha-BBO
    aBBO_Ao = 2.67579;
    aBBO_Bo = 0.02099;
    aBBO_Co = 0.00470;
    aBBO_Do = 0.00528;
    aBBO_Ae = 2.31197;
    aBBO_Be = 0.01184;
    aBBO_Ce = 0.01607;
    aBBO_De = 0.00400;
    aBBO_no=sqrt(aBBO_Ao+aBBO_Bo/((Lambda*10^6)^2-aBBO_Co)-aBBO_Do*(Lambda*10^6)^2);
    aBBO_ne=sqrt(aBBO_Ae+aBBO_Be/((Lambda*10^6)^2-aBBO_Ce)-aBBO_De*(Lambda*10^6)^2);
    aBBO_no2=sqrt(aBBO_Ao+aBBO_Bo/((Lambda2*10^6)^2-aBBO_Co)-aBBO_Do*(Lambda2*10^6)^2);
    aBBO_ne2=sqrt(aBBO_Ae+aBBO_Be/((Lambda2*10^6)^2-aBBO_Ce)-aBBO_De*(Lambda2*10^6)^2);
    %  Quartz
    Quartz_no=sqrt(2.3573-0.01170*(Lambda*10^6)^2+0.01054/(Lambda*10^6)^2+0.00013414/(
    Lambda*10^6)^4-0.000000445337/(Lambda*10^6)^6+0.000000059236/(Lambda*10^6)^8);
    Quartz_ne=sqrt(2.3849-0.01259*(Lambda*10^6)^2+0.01079/(Lambda*10^6)^2+0.00016518/(
    Lambda*10^6)^4-0.0000019474/(Lambda*10^6)^6+0.000000093648/(Lambda*10^6)^8);
```

```
    Quartz_no2=sqrt(2.3573-0.01170*(Lambda2*10^6)^2+0.01054/(Lambda2*10^6)^2+0.00013414/(
    Lambda2*10^6)^4-0.000000445337/(Lambda2*10^6)^6+0.000000059236/(Lambda2*10^6)^8);
    Quartz_ne2=sqrt(2.3849-0.01259*(Lambda2*10^6)^2+0.01079/(Lambda2*10^6)^2+0.00016518/(
    Lambda2*10^6)^4-0.0000019474/(Lambda2*10^6)^6+0.000000093648/(Lambda2*10^6)^8);
    %  Calcite
    Ao = 2.69705;
    Bo = 0.0192064;
    Co = 0.01820;
    Do = 0.0151624;
    Ae = 2.18438;
    Be = 0.0087309;
    Ce = 0.01018;
    De = 0.0024411;
    Calcite_no=sqrt(Ao+Bo/((Lambda*10^6)^2-Co)-Do*(Lambda*10^6)^2);
    Calcite_ne=sqrt(Ae+Be/((Lambda*10^6)^2-Ce)-De*(Lambda*10^6)^2);
    Calcite_no2=sqrt(Ao+Bo/((Lambda2*10^6)^2-Co)-Do*(Lambda2*10^6)^2);
    Calcite_ne2=sqrt(Ae+Be/((Lambda2*10^6)^2-Ce)-De*(Lambda2*10^6)^2);
    if Material == "aBBO"
        Compensator_no = aBBO_no;
        Compensator_ne = aBBO_ne;
        Compensator_no2 = aBBO_no2;
        Compensator_ne2 = aBBO_ne2;
    else
    end
    if Material == "Calcite"
        Compensator_no = Calcite_no;
        Compensator_ne = Calcite_ne;
        Compensator_no2 = Calcite_no2;
        Compensator_ne2 = Calcite_ne2;
    else
    end
    if Material == "Quartz"
        Compensator_no = Quartz_no;
        Compensator_ne = Quartz_ne;
        Compensator_no2 = Quartz_no2;
        Compensator_ne2 = Quartz_ne2;
    else
    end
    CVgroup_o = cLight./(Compensator_no-Lambda.*((Compensator_no2-Compensator_no)/0.01./
    Lambda));
    CVgroup_e = cLight./(Compensator_ne-Lambda.*((Compensator_ne2-Compensator_ne)/0.01./
    Lambda));

end
```

Listing L.8: Function20_Crystalinfo

```
% 2022/05/16 written by Sungeun (Paul) Oh -University of Waterloo, CANADA
% This function provides information about the crystal at the given temperature
%---------------------------------[input]---------------------------------
% Lambda : wavelength (in meters)
% Crystal : PPLN(covesion)
% CL : Crystal's length (in meters)
% CP : Crystal's poling period (in meters)
% T  : Temperature (in degrees Celcius)
%--------------------------------[output]---------------------------------
% no,ne : Refractive indices
```

```
% no_group,ne_group : Group indices
% CLT   : Crystal's length at the temperature (in meters)
% CPT   : Crystal's poling period at the temperature (in seconds)
%------------------------------[function]---------------------------------

function [no,ne,no_group,ne_group,CLT,CPT] = Function20_Crystalinfo(Lambda,Crystal,CL,CP,T
    )
    if length(Lambda)==1
        LambdaNext = Lambda+Lambda*0.001;
        LambdaPrevious = Lambda-Lambda*0.001;
    else
        LambdaNext = Lambda(2);
        LambdaPrevious = Lambda(end-1);
    end
    if Crystal == "PPLN"
    ea1=5.756;
    ea2=0.0983;
    ea3=0.2020;
    ea4=189.32;
    ea5=12.52;
    ea6=1.32*10^(-2);
    eb1=2.860*10^(-6);
    eb2=4.700*10^(-8);
    eb3=6.113*10^(-8);
    eb4=1.516*10^(-4);
    oa1=5.653;
    oa2=0.1185;
    oa3=0.2091;
    oa4=89.61;
    oa5=10.85;
    oa6=1.97*10^(-2);
    ob1=7.941*10^(-7);
    ob2=3.134*10^(-8);
    ob3=-4.641*10^(-9);
    ob4=-2.188*10^(-6);
    ThermalExp1=1.54*10^(-5); % thermal expansion coefficient : alpha
    ThermalExp2=5.3*10^(-9); % thermal expansion coefficient : beta
    end
    coef_factor=10^(-6); % desired unit
    CT=T+273.15; % in Kelvin
    CTEff=(CT-(24.5+273.16)).*(CT+(24.5+273.16)); % this is used for calculating
    refractive indices

    LambdaFront = Lambda(1)-(LambdaNext-Lambda(1)); % very front
    LambdaBack = Lambda(end)+(Lambda(end)-LambdaPrevious); % very back
    ExtendedLambda = cat(2,LambdaFront,Lambda,LambdaBack);
    Extended_no = sqrt(oa1+ob1*CTEff+(oa2+ob2*CTEff)./(((ExtendedLambda/coef_factor).^2)-(
    oa3+ob3*CTEff)^2)+(oa4+ob4*CTEff)./(((ExtendedLambda/coef_factor).^2)-oa5^2)-oa6*(
    ExtendedLambda/coef_factor).^2); % extraordinary refractive index for the pump
    Extended_ne = sqrt(ea1+eb1*CTEff+(ea2+eb2*CTEff)./(((ExtendedLambda/coef_factor).^2)-(
    ea3+eb3*CTEff)^2)+(ea4+eb4*CTEff)./(((ExtendedLambda/coef_factor).^2)-ea5^2)-ea6*(
    ExtendedLambda/coef_factor).^2); % extraordinary refractive index for the pump
    Extended_dLambda = ExtendedLambda(2:end)-ExtendedLambda(1:end-1);
    Extended_dno = Extended_no(2:end)-Extended_no(1:end-1);
    Extended_dne = Extended_ne(2:end)-Extended_ne(1:end-1);
    for i=1:length(Lambda)
        d_Lambda(i) = (Extended_dLambda(i)+Extended_dLambda(i+1))/2;
```

```
        d_no(i) = (Extended_dno(i)+Extended_dno(i+1))/2;
        d_ne(i) = (Extended_dne(i)+Extended_dne(i+1))/2;
    end
    no = Extended_no(2:end-1);
    ne = Extended_ne(2:end-1);
    no_group = no-Lambda.*(d_no./d_Lambda);
    ne_group = ne-Lambda.*(d_ne./d_Lambda);
    CPT=CP.*(1+ThermalExp1.*(CT-298.15)+ThermalExp2.*(CT-298.15).^2); % thermally expanded poling period (in meters)
    CLT=CL.*(1+ThermalExp1.*(CT-298.15)+ThermalExp2.*(CT-298.15).^2); % thermally expanded length (in meters)
end
```

Listing L.9: Function21_SpotSizeWithGivenLenses

```
% 2021/05/16 written by Sungeun (Paul) Oh -University of Waterloo, CANADA
% Expected spot size with given aspheric and magnifying lenses
% Fiber -> Focused beam (by aspheric lens) -> Collimated beam (by magnifying lens) -> Diverging beam (with spotsize)

%-----------------[input]------------------
% Wavelength : Lambda (in meters)
% Fiber's numerical aperture : FiberNA (unitless)
% aspheric lens focal length : ObjLens (in meters)
% magnifying lens focal length : MagLens (in meters)
%-----------------[output]-----------------
% Spot size (in meters) waist radius
% FWHM (in meters) diameter
%------------------------------------------
% numerical aperture : NA=sqrt(n_core^2-n_clad^2)  <<==========this is not for single mode fiber
% mode field diameter = sqrt(2)/sqrt(ln(2))*FWHM   -> MFD = 1.699 FWHM

function [W] = Function21_SpotSizeWithGivenLenses(Lambda,Mode,Information,ObjLens,MagLens)

% Mode 1 : Information = Mode Field Diameter (in meters)
% Mode 2 : Information = Numerical Aperture (dimensionless)

if Mode == 1
    FiberMFR = Information/2; % mode field radius
    zR = pi*(FiberMFR^2)/Lambda;
    CollimatedMFR = FiberMFR*sqrt(1+(ObjLens/zR)^2); % radius (in meters)
    CollimatedMFD = CollimatedMFR*2; % diameter (in meters) spot size after the objective lens
    CollimatedFWHM = 0.5887*CollimatedMFD; % FWHM (in meters)
elseif Mode == 2
    FiberNA = Information; % numerical aperture
    CollimatedMFR = ObjLens*tan(asin(FiberNA)); % radius (in meters)
    CollimatedMFD = CollimatedMFR*2; % diameter (in meters)
    CollimatedFWHM = 0.5887*CollimatedMFD; % (FWHM in meter)
else
end
W = sqrt((CollimatedMFR^2-sqrt(CollimatedMFR^4-4*MagLens^2*Lambda^2/pi^2))/2); % spot size at the crystal
end
```

Listing L.10: Function30_PairRate

```
% 2022-02-14 Sungeun (Paul) Oh
% Pair rate and Heralding efficiency calculations at 1mW of power with spot sizes and the crystal given
%------------------------------[input]------------------------------
% Lambda_P,S,I : wavelengths (in meters)
% dLambda_P,S,I : bandwidths (in meters)
% Crystal : 'PPLN'
% CL : Crystal length (in meters)
% CL : Crystal poling period (in meters)
% T : Crystal temperature (in degree celsius)
% W_P,S,I : Beam spotsize (in meters)
%------------------------------[output]------------------------------
% R_S, R_I : Single counts (in Hz)
% R_C : Coincidences (in Hz)
%------------------------------[function]------------------------------
[R_S,R_I,R_C] = Function30_PairRate2(523.64e-9,790.8e-9,1550e-9,0.01e-9,0.66e-9,2.61e-9,'PPLN',1e-2,7.1e-6,107.6,11.9e-6,17.6e-6,28.8-6)

function [R_S,R_I,R_C] = Function30_PairRate2(Lambda_P,Lambda_S,Lambda_I,dLambda_P,dLambda_S,dLambda_I,Crystal,CL,CP,T,W_P,W_S,W_I)
    cLight=299792458; % speed of light (in m/s)
    hbar=1.0545718e-34; % (in kgm^2/s)
    epsilon0=8.8541878e-12; % (in F/m) = (in J/m^3) = (in C/V/m)    ,   V x C = J
    Power = 1e-3; % Power in Watts
    omega_P = 2*pi*cLight/Lambda_P;
    omega_S = 2*pi*cLight/Lambda_S;
    omega_I = 2*pi*cLight/Lambda_I;
    domega_S = cLight/Lambda_S^2*dLambda_S;
    domega_I = cLight/Lambda_I^2*dLambda_I;
    if Crystal == 'PPLN'
        d_eff = 25e-12; % (in pm/V)
    else
        d_eff = 0; % need more information about other crystals
    end
    % refractive indices and group indices
    ------------------------------------------------------

    [no_P,ne_P,no_group_P,ne_group_P,CLT,CPT] = Function20_Crystalinfo(Lambda_P,Crystal,CL,CP,T);
    [no_S,ne_S,no_group_S,ne_group_S,CLT,CPT] = Function20_Crystalinfo(Lambda_S,Crystal,CL,CP,T);
    [no_I,ne_I,no_group_I,ne_group_I,CLT,CPT] = Function20_Crystalinfo(Lambda_I,Crystal,CL,CP,T);
    N_P = Power/hbar/omega_P; % number of pump photons
    k_P=2*pi*ne_P/Lambda_P; % Wave Number (in rad/m)
    k_S=2*pi*ne_S/Lambda_S; % Wave Number (in rad/m)
    k_I=2*pi*ne_I/Lambda_I; % Wave Number (in rad/m)
    Xsi_P = CLT/k_P/W_P^2;
    Xsi_S = CLT/k_S/W_S^2;
    Xsi_I = CLT/k_I/W_I^2;
    deltak=k_P-k_S-k_I; % without poling period
    % for pair rate-------------------------------------------------------------------
    C_1 = 1+(k_S*Xsi_S)/(k_P*Xsi_P)+(k_I*Xsi_I)/(k_P*Xsi_P);
    C_2 = (1-deltak/k_P)*(1+((k_S+deltak)*Xsi_P)/((k_P-deltak)*Xsi_S)+((k_I+deltak)*Xsi_P)/((k_P-deltak)*Xsi_I));
```

```
    Xsi = (C_2/C_1)*(Xsi_S*Xsi_I/Xsi_P);
    C_3 = (Xsi_S*Xsi_I/Xsi^2)*deltak/k_P/C_1;
    F = @(l) Xsi./(1-1i*Xsi*l-C_3*Xsi^2*l.^2)./(1+1i*Xsi*l-C_3*Xsi^2*l.^2); % Overlap
    function
    IntResult=abs(integral(F,-1,1));
    % for single rate-------------------------------------------------------------------
    C_S4 = 2*sqrt((1+k_S*Xsi_S/k_P/Xsi_P)*k_I/k_P);
    C_S5 = 2*(1-deltak/k_P)*sqrt((1+(k_S+deltak)/(k_P-deltak)*Xsi_P/Xsi_S)*(k_I+deltak)/(
    k_P-deltak));
    C_I4 = 2*sqrt((1+k_I*Xsi_I/k_P/Xsi_P)*k_S/k_P);
    C_I5 = 2*(1-deltak/k_P)*sqrt((1+(k_I+deltak)/(k_P-deltak)*Xsi_P/Xsi_I)*(k_S+deltak)/(
    k_P-deltak));
    % assumes the photons are collected through singlemode fiber (R_S=R_I=R_C). Otherwise,
     C_S4/C_S5/C_I4/C_I5 should be used for the single counts.
    EstProbFactor = 64*pi^2*Lambda_P*Power/epsilon0/ne_P^2/abs(ne_group_I-ne_group_S)*(
    d_eff/Lambda_S/Lambda_I)^2; % This is a factor that applies to all R_c R_S R_I.
    R_S = EstProbFactor.*IntResult;
    R_I = EstProbFactor.*IntResult;
    R_C = EstProbFactor.*IntResult;
    fprintf('\n Paul   Single (Signal)      =   %.2f KHz\n',R_S/1000);
    fprintf(' Paul   Single  (Idler)      =   %.2f KHz\n',R_I/1000);
    fprintf(' Paul   Coincidence        =   %.2f KHz\n',R_C/1000);
end
```

Listing L.11: Function31_FriedParam

```
% 2023/03/30 written by Sungeun (Paul) Oh -University of Waterloo, CANADA
% This function calculates the Fried parameter.
%------------------------------[input]-------------------------------
% Lambda : signal wavelength (in meters)
% elev : elevation angle of the satellite (in radians)
% alt : altitude of the satellite (in meters)
%------------------------------[output]------------------------------
% r_0 : Fried parameter (in meters)
%------------------------------[function]----------------------------
function [r_0] = Function31_FriedParam(Lambda,elev,alt)
    altkm = alt/1000; % in kilometers
    C2 = @(z) ((altkm-z)./altkm).^(5/3)*1.7e-14.*exp(-z./100)+0.00359*(z*1e-5).^10.*exp(-z
    ./1000)+2.7e-16.*exp(-z./1500);
    C2intResult = integral(C2,0,altkm);
    r_0 = (C2intResult*(2*pi./Lambda).^2./sin(elev)*0.424).^(-3/5);
end
```

Appendix M

Data - SGP4 (ISS-2019-Oct-28)

y	m	d											
19	10	28	SGP4		Actual								
h	m	s	Azi	Alt	Azi	Alt	h	m	s	Azi	Alt	Azi	Alt
22	58	30	263.853	9.52515	263.85	9.54358	22	59	58	277.993	22.4835	276.828	21.1522
22	58	32	266.891	6.78955	264.034	9.74294	23	0	0	278.476	22.8351	277.306	21.505
22	58	34	267.083	6.99829	264.222	9.94449	23	0	2	278.948	23.1812	277.797	21.8627
22	58	36	267.27	7.19604	264.413	10.1483	23	0	4	279.448	23.5437	278.302	22.2253
22	58	38	267.468	7.40479	264.607	10.3544	23	0	6	279.965	23.9117	278.821	22.5929
22	58	40	267.665	7.61902	264.805	10.5628	23	0	8	280.393	24.2084	279.354	22.9654
22	58	42	267.863	7.82227	265.007	10.7736	23	0	10	280.953	24.5929	279.902	23.3428
22	58	44	268.033	8.00354	265.212	10.9868	23	0	12	281.508	24.9719	280.465	23.7252
22	58	46	268.193	8.15735	265.421	11.2025	23	0	14	282.101	25.3674	281.045	24.1124
22	58	48	268.407	8.38257	265.634	11.4208	23	0	16	282.673	25.7465	281.641	24.5046
22	58	50	268.621	8.60229	265.851	11.6416	23	0	18	283.288	26.1475	282.254	24.9015
22	58	52	268.846	8.82751	266.072	11.8652	23	0	20	283.931	26.554	282.885	25.3032
22	58	54	269.072	9.05273	266.298	12.0914	23	0	22	284.573	26.9604	283.535	25.7095
22	58	56	269.302	9.28345	266.528	12.3204	23	0	24	285.244	27.3724	284.204	26.1203
22	58	58	269.533	9.51416	266.763	12.5522	23	0	26	285.914	27.7789	284.893	26.5355
22	59	0	269.764	9.73938	267.002	12.7869	23	0	28	286.617	28.1964	285.602	26.955
22	59	2	270.011	9.98108	267.246	13.0245	23	0	30	287.358	28.6304	286.333	27.3785
22	59	4	270.264	10.2283	267.495	13.2652	23	0	32	288.111	29.0588	287.086	27.8058
22	59	6	270.522	10.4755	267.749	13.5089	23	0	34	288.853	29.4763	287.861	28.2367
22	59	8	270.775	10.7117	268.009	13.7558	23	0	36	289.666	29.9213	288.661	28.6708
22	59	10	271.038	10.9644	268.274	14.0059	23	0	38	290.319	30.2618	289.484	29.108
22	59	12	271.313	11.2225	268.545	14.2593	23	0	40	291.165	30.7013	290.333	29.5477
22	59	14	271.533	11.4203	268.821	14.516	23	0	42	292.006	31.1298	291.208	29.9897
22	59	16	271.719	11.5906	269.103	14.7761	23	0	44	292.939	31.5912	292.11	30.4334
22	59	18	272.01	11.8542	269.392	15.0397	23	0	46	293.829	32.0251	293.039	30.8783
22	59	20	272.307	12.1289	269.687	15.3068	23	0	48	294.791	32.4701	293.997	31.324
22	59	22	272.609	12.3981	269.988	15.5776	23	0	50	295.774	32.9205	294.985	31.7698
22	59	24	272.917	12.6727	270.296	15.8521	23	0	52	296.812	33.3765	296.002	32.215
22	59	26	273.23	12.9474	270.612	16.1303	23	0	54	297.834	33.8159	297.05	32.659
22	59	28	273.483	12.7167	270.934	16.4123	23	0	56	298.932	34.2664	298.129	33.1009
22	59	30	273.735	12.9309	271.264	16.6983	23	0	58	300.02	34.7003	299.241	33.5401
22	59	32	274.005	13.5736	271.602	16.9883	23	1	0	301.163	35.1398	300.386	33.9755
22	59	34	274.087	19.1656	271.947	17.2823	23	1	2	302.333	35.5682	301.563	34.4062
22	59	36	274.103	18.9844	272.301	17.5804	23	1	4	303.569	36.0077	302.775	34.8312
22	59	38	273.829	19.2041	272.664	17.8828	23	1	6	304.761	36.4142	304.021	35.2495
22	59	40	274.213	19.5227	273.035	18.1894	23	1	8	305.799	36.7438	305.301	35.6599
22	59	42	274.592	19.8303	273.415	18.5004	23	1	10	307.117	37.1558	306.616	36.0613
22	59	44	274.966	20.1324	273.805	18.8157	23	1	12	308.491	37.5568	307.966	36.4524
22	59	46	275.372	20.4565	274.205	19.1356	23	1	14	309.869	37.9413	309.35	36.832
22	59	48	275.79	20.7916	274.614	19.46	23	1	16	311.292	38.3148	310.768	37.1988
22	59	50	276.191	21.1047	275.035	19.789	23	1	18	312.742	38.6719	312.221	37.5514
22	59	52	276.625	21.4398	275.466	20.1227	23	1	20	314.231	39.0125	313.706	37.8886
22	59	54	277.07	21.7859	275.908	20.461	23	1	22	315.753	39.342	315.223	38.209
22	59	56	277.52	22.1265	276.362	20.8042	23	1	24	317.269	39.6442	316.772	38.5113

h	m	s	Azi	Alt	Azi	Alt	h	m	s	Azi	Alt	Azi	Alt
23	1	26	318.856	39.9353	318.351	38.7941	23	2	58	23.3679	30.2234	23.9069	28.7565
23	1	28	320.493	40.2045	319.957	39.0561	23	3	0	24.1864	29.7839	24.7104	28.3222
23	1	30	322.119	40.4517	321.591	39.2963	23	3	2	24.9719	29.35	25.4901	27.891
23	1	32	323.718	40.6714	323.248	39.5132	23	3	4	25.7465	28.916	26.2468	27.4634
23	1	34	325.432	40.8746	324.928	39.706	23	3	6	26.4276	28.5315	26.9814	27.0396
23	1	36	327.134	41.0449	326.628	39.8736	23	3	8	26.9659	28.2129	27.6945	26.6198
23	1	38	328.326	41.1438	328.345	40.0151	23	3	10	27.6361	27.8119	28.3869	26.2042
23	1	40	330.046	41.2646	330.076	40.1298	23	3	12	28.3228	27.3944	29.0593	25.7929
23	1	42	331.809	41.358	331.819	40.217	23	3	14	29.0094	26.9714	29.7124	25.3861
23	1	44	333.545	41.424	333.57	40.2763	23	3	16	29.6466	26.5704	30.3469	24.984
23	1	46	335.319	41.4624	335.326	40.3073	23	3	18	30.2454	26.1804	30.9635	24.5866
23	1	48	337.11	41.4734	337.084	40.3098	23	3	20	30.8661	25.7794	31.5626	24.1939
23	1	50	338.868	41.4569	338.841	40.2839	23	3	22	31.4594	25.3839	32.1451	23.8061
23	1	52	340.637	41.4075	340.593	40.2297	23	3	24	32.0361	24.9994	32.7115	23.4232
23	1	54	342.339	41.3361	342.337	40.1474	23	3	26	32.5854	24.6259	33.2622	23.0452
23	1	56	344.064	41.2317	344.07	40.0376	23	3	28	33.1293	24.2413	33.798	22.6722
23	1	58	345.811	41.0999	345.79	39.9009	23	3	30	33.6676	23.8623	34.3193	22.304
23	2	0	347.536	40.9406	347.493	39.7379	23	3	32	34.173	23.5052	34.8266	21.9408
23	2	2	349.222	40.7593	349.176	39.5496	23	3	34	34.6674	23.1482	35.3205	21.5826
23	2	4	350.903	40.5505	350.838	39.3369	23	3	36	35.1013	22.8351	35.8013	21.2292
23	2	6	352.529	40.3308	352.475	39.1009	23	3	38	35.4474	22.5769	36.2696	20.8806
23	2	8	353.606	40.155	354.086	38.8428	23	3	40	35.9143	22.2253	36.7258	20.5369
23	2	10	355.21	39.8749	355.669	38.5637	23	3	42	36.3647	21.8848	37.1703	20.198
23	2	12	356.836	39.5673	357.223	38.265	23	3	44	36.7932	21.5497	37.6035	19.8637
23	2	14	358.369	39.2596	358.746	37.9479	23	3	46	37.2217	21.2201	38.0259	19.5342
23	2	16	359.841	38.9355	0.23648	37.6138	23	3	48	37.6392	20.8905	38.4377	19.2092
23	2	18	1.30737	38.5895	1.69419	37.264	23	3	50	38.0457	20.5719	38.8393	18.8888
23	2	20	2.75208	38.2269	3.11825	36.8998	23	3	52	38.4467	20.2478	39.2311	18.5729
23	2	22	4.13086	37.8589	4.50813	36.5227	23	3	54	38.8257	19.9402	39.6135	18.2614
23	2	24	5.49866	37.4689	5.86352	36.1338	23	3	56	39.2047	19.6271	39.9866	17.9543
23	2	26	6.828	37.0734	7.18426	35.7344	23	3	58	39.5728	19.3195	40.3509	17.6514
23	2	28	8.13538	36.6614	8.47036	35.3258	23	4	0	39.9353	19.0173	40.7067	17.3528
23	2	30	9.40979	36.2439	9.72194	34.9092	23	4	2	40.2759	18.7317	41.0541	17.0583
23	2	32	10.6348	35.8209	10.9393	34.4856	23	4	4	40.6274	18.4296	41.3936	16.7678
23	2	34	11.8268	35.3925	12.1227	34.0561	23	4	6	40.9076	18.1879	41.7252	16.4814
23	2	36	12.9474	34.9805	13.2728	33.6219	23	4	8	41.1548	17.9791	42.0494	16.1988
23	2	38	13.7769	34.6509	14.3899	33.1837	23	4	10	41.4734	17.699	42.3663	15.9201
23	2	40	14.8315	34.2279	15.4748	32.7425	23	4	12	41.792	17.4133	42.6762	15.6452
23	2	42	15.8917	33.783	16.528	32.2992	23	4	14	42.0886	17.1552	42.9793	15.374
23	2	44	16.9299	33.338	17.5504	31.8545	23	4	16	42.3853	16.8805	43.2758	15.1064
23	2	46	17.9736	32.8766	18.5426	31.4091	23	4	18	42.6874	16.6113	43.5659	14.8424
23	2	48	18.924	32.4371	19.5054	30.9638	23	4	20	42.973	16.3477	43.8498	14.5819
23	2	50	19.8853	31.9812	20.4397	30.519	23	4	22	43.2477	16.095	44.1277	14.3248
23	2	52	20.7916	31.5417	21.3461	30.0754	23	4	24	43.5223	15.8368	44.3998	14.071
23	2	54	21.676	31.1023	22.2256	29.6335	23	4	26	43.797	15.5841	44.6663	13.8205
23	2	56	22.5165	30.6738	23.0789	29.1937							

Appendix N

Data - Pair Rate (dark subtracted)

Lens Analysis										
Sungeun (Paul) Ol										
2021-05-21			Signal		Idler		Coincidence		Signal efficiency	Idler efficiency
P (cm)	S (cm)	I (cm)	Hz	2SD	Hz	2SD	Hz	2SD	fraction	fraction
50	15	10	217391	1119	194462	1077	63094	696	0.4745	0.3937
50	15	12.5	214101	1347	183172	972	63771	1109	0.4745	0.3937
50	15	15	224759	4471	187310	3705	65441	1558	0.4745	0.3937
50	15	17.5	212115	2650	169043	1601	55441	1258	0.4745	0.3937
50	15	20	213942	1302	163589	906	50927	763	0.4745	0.3937
50	15	25	212299	3470	147029	2534	38458	781	0.4745	0.3937
50	17.5	10	198932	1694	191582	1123	57294	903	0.4745	0.3937
50	17.5	12.5	200367	1360	185481	1204	64384	809	0.4745	0.3937
50	17.5	15	204482	1970	187653	1723	65620	1163	0.4745	0.3937
50	17.5	17.5	198309	1660	170503	1480	59998	738	0.4745	0.3937
50	17.5	20	204439	2670	171879	1894	55752	967	0.4745	0.3937
50	17.5	25	198370	1165	149101	936	45095	584	0.4745	0.3937
50	20	10	201353	939	194672	754	59631	714	0.4745	0.3937
50	20	12.5	205413	1207	190905	920	72803	1123	0.4745	0.3937
50	20	15	204840	964	186091	1024	72314	1084	0.4745	0.3937
50	20	17.5	204806	992	179920	892	67589	809	0.4745	0.3937
50	20	20	208857	4229	175550	3593	63649	1460	0.4745	0.3937
50	20	25	203321	1218	153455	700	51501	6781	0.4745	0.3937
50	25	10	199966	4625	199469	4734	53115	1518	0.4745	0.3937
50	25	12.5	201439	1016	190082	1037	63325	598	0.4745	0.3937
50	25	15	204795	1799	188402	1671	66910	1114	0.4745	0.3937
50	25	17.5	201177	1580	178032	1361	71847	1027	0.4745	0.3937
50	25	20	201377	3540	173365	3546	69507	1529	0.4745	0.3937
50	25	25	195680	1773	148082	1352	58735	915	0.4745	0.3937
40	15	10	327065	2747	280830	2221	92479	1075	0.4745	0.3937
30	15	10	492090	2807	386148	2195	117777	1337	0.4745	0.3937
20	15	10	742722	36949	599213	31279	136514	6304	0.4745	0.3937

Experiment					Theory			
	At the detector		At the crystal					
Pair rate	Signal Herald	Idler Herald	Signal Herald	Idler Herald	Pair rate	Signal Herald	Idler Herald	Pair Herald
Hz	%	%	%	%	Hz	%	%	%
670020.7	32.4%	29.0%	68.38%	73.72%	778323.27	86.19%	84.95%	85.57%
614970.9	34.8%	29.8%	73.37%	75.66%	740389.43	90.61%	86.41%	88.48%
643321.6	34.9%	29.1%	73.63%	73.95%	754118.77	88.96%	80.96%	84.87%
646751.6	32.8%	26.1%	69.12%	66.39%	794060.48	84.48%	72.70%	78.37%
687229.9	31.1%	23.8%	65.61%	60.46%	847720.37	79.14%	63.96%	71.14%
811641.5	26.2%	18.1%	55.12%	46.01%	970807.03	69.10%	48.61%	57.96%
665196.9	29.9%	28.8%	63.03%	73.15%	767242.7	84.67%	86.18%	85.42%
577228.4	34.7%	32.1%	73.15%	81.62%	698571.9	92.99%	91.58%	92.28%
584755.6	35.0%	32.1%	73.70%	81.51%	685544.37	94.76%	89.06%	91.87%
563556.8	35.2%	30.3%	74.16%	76.85%	700187.71	92.78%	82.45%	87.46%
630269.2	32.4%	27.3%	68.36%	69.27%	729411.4	89.06%	74.33%	81.36%
655885.7	30.2%	22.7%	63.74%	57.74%	806424.65	80.56%	58.52%	68.66%
657339.2	30.6%	29.6%	64.56%	75.22%	782184.23	80.05%	84.53%	82.26%
538636.7	38.1%	35.4%	80.37%	90.02%	685298.93	91.36%	93.35%	92.35%
527130.0	38.9%	35.3%	81.90%	89.67%	650221.38	96.29%	93.90%	95.09%
545187.8	37.6%	33.0%	79.17%	83.82%	645559	96.99%	89.43%	93.13%
576047.5	36.3%	30.5%	76.41%	77.41%	657036.71	95.29%	82.52%	88.68%
605825.6	33.6%	25.3%	70.73%	64.34%	701945.54	89.20%	67.23%	77.44%
750955.8	26.6%	26.6%	56.12%	67.47%	853815.15	67.36%	77.44%	72.23%
604657.4	33.3%	31.4%	70.21%	79.85%	703394.23	81.77%	90.95%	86.24%
576652.0	35.5%	32.7%	74.85%	82.99%	631042.15	91.14%	96.75%	93.91%
498503.0	40.4%	35.7%	85.05%	90.71%	596778.35	96.37%	96.73%	96.55%
502276.4	40.1%	34.5%	84.49%	87.67%	582928.95	98.66%	93.01%	95.79%
493346.1	39.7%	30.0%	83.59%	76.24%	584958.24	98.32%	80.67%	89.06%
993194.8	32.9%	28.3%	69.40%	71.82%	1142740.5	87.04%	85.26%	86.15%
1613384.4	30.5%	23.9%	64.28%	60.79%	1793597.9	88.16%	85.49%	86.81%
3260095.5	22.8%	18.4%	48.01%	46.69%	3074933.1	88.00%	84.09%	86.03%

Appendix O

Data - Bell measurement (dark subtracted)

V basis						H basis					
Signal	SD	Idler	SD	Coin	SD	Signal	SD	Idler	SD	Coin	SD
452550	2822	206845	905	33029	414	457213	3074	213453	1303	243	17
457159	2891	206021	788	30946	185	460697	3588	215860	978	2826	63
459385	2964	204856	1023	24730	267	462773	4069	217568	883	9192	159
465237	3438	204829	1080	16338	459	467348	2340	216147	1230	17407	190
466308	3395	205894	596	8234	120	468545	4289	216155	709	25275	367
469506	3585	204699	1161	2197	104	468358	1397	216913	863	31332	298
467383	3838	206115	1111	193	20	472866	4981	216842	856	33752	177
464324	4006	205280	951	2560	56	466677	5225	216557	1123	31133	343
463057	4168	205852	904	8786	180	466942	3650	217778	667	24403	176
460027	4398	205797	571	17494	273	463050	4644	215662	1539	15776	247
450792	4645	203648	1294	25558	463	460640	1742	217047	460	7786	150
452307	2909	203175	1037	31779	584	461302	4007	216686	1014	2024	44
460478	5258	203810	1014	33335	561	454421	4398	217240	335	236	32
A basis						**D basis**					
Signal	SD	Idler	SD	Coin	SD	Signal	SD	Idler	SD	Coin	SD
449112	3124	207964	1820	16465	73	457748	3478	212461	354	17032	198
451545	3193	210281	636	24491	233	454563	2211	209970	1018	8750	54
456161	3747	211013	1088	30548	307	455246	3032	208122	1525	2854	160
461502	2521	208318	754	32338	335	461133	4002	210842	666	754	60
463825	3843	211854	677	30729	71	462658	3065	210016	1303	2672	52
466941	1991	211672	1555	24717	415	467603	2786	210123	1395	8278	150
460333	3088	206843	994	16651	374	465119	3178	210171	1027	16312	232
465771	3560	212789	1452	8341	153	464592	4572	209886	1474	24815	281
466288	3070	214247	594	2830	110	462260	4401	211268	329	30441	318
457881	2624	213477	924	738	92	456791	3182	210985	1003	32339	259
456253	3883	212759	1139	2864	117	455823	2332	210689	1230	30236	406
456024	3025	213249	705	9136	120	455567	4273	210043	772	24433	184
451335	2014	207264	1270	17025	135	453618	4292	209265	761	16686	213

Appendix P

Design - Crystal Oven (in millimeters)

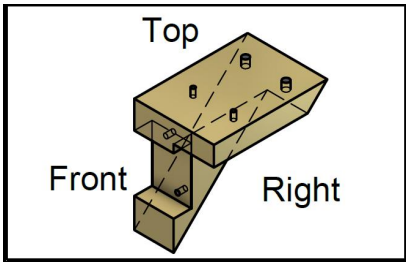

Top Copper Slider

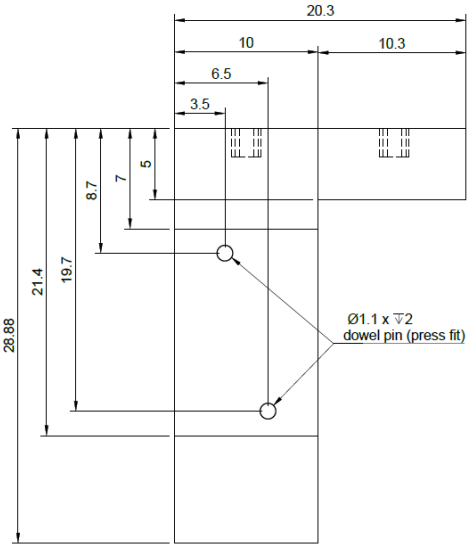

Front

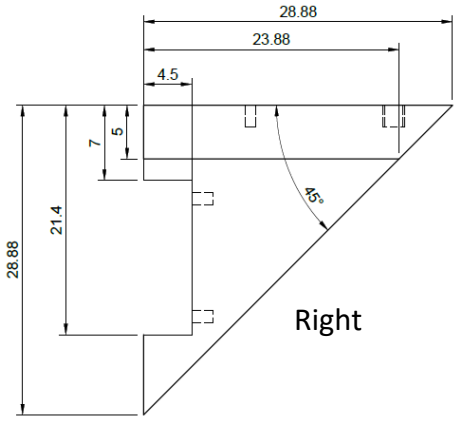

Right

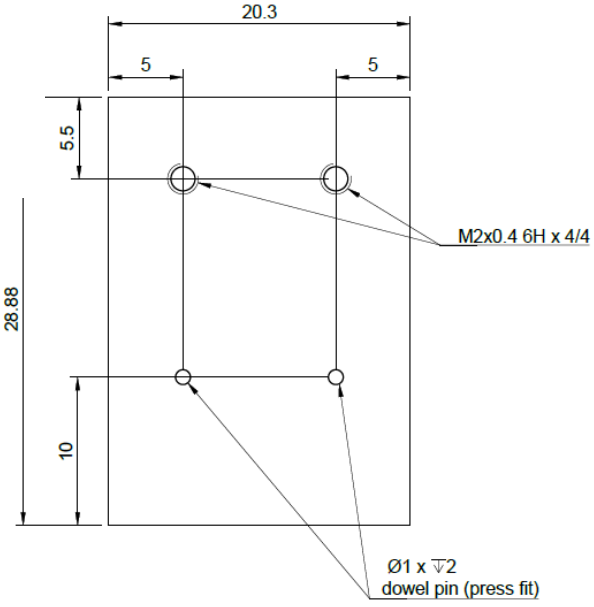

Top

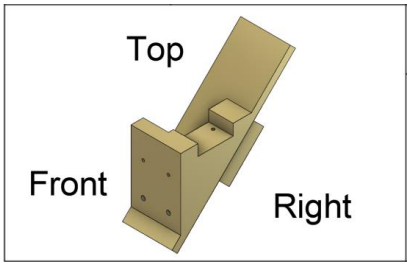

Bottom Copper Slider

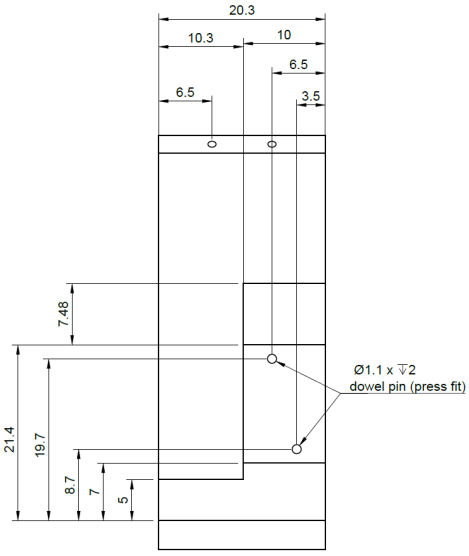

Top

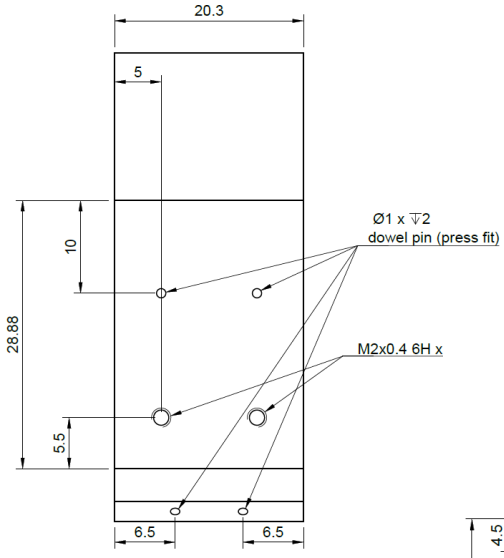

Front

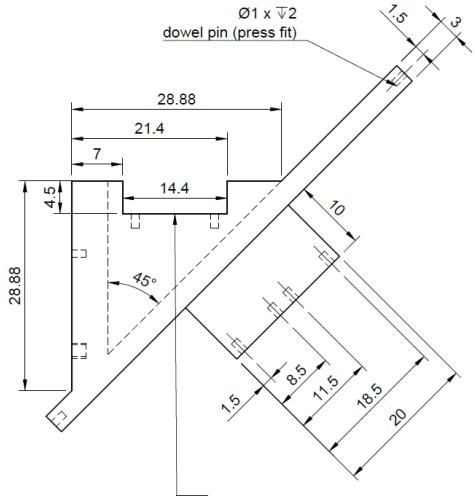

The 14.4mm space is where the crystal kit is going to be placed. The crystal kit is known to have the width of 14.4mm. However, it is very important to know the actual width so the crystal exactly fits into this space. In case we expand the width, it should be expanded from the center. Also, please be aware of the respective changes of the pinhole positions.

Right

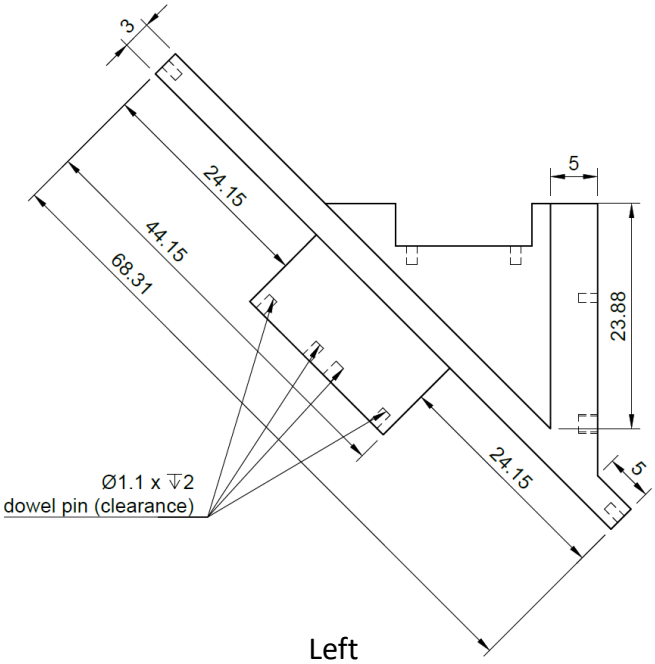
3
24.15
44.15
68.31
5
23.88
24.15
5
Ø1.1 x ⩛2
dowel pin (clearance)

Left

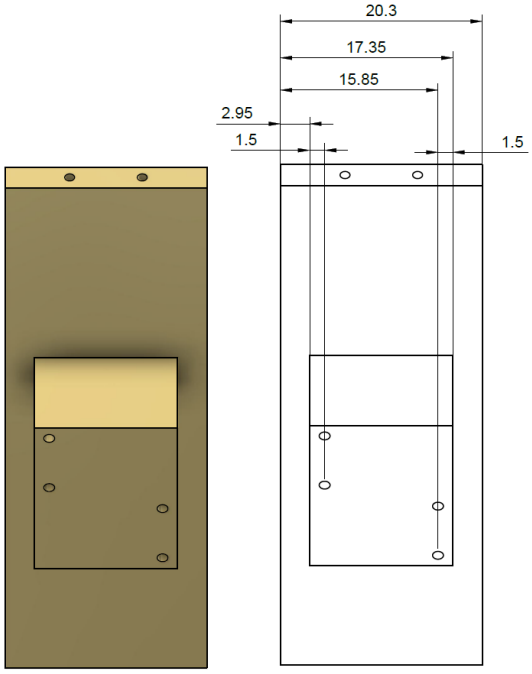
20.3
17.35
15.85
2.95
1.5
1.5

Bottom

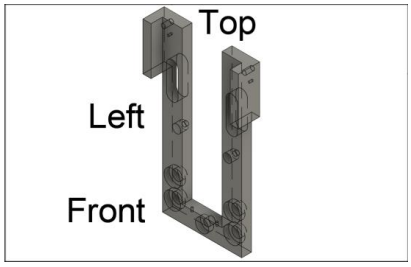

Aluminum Plate

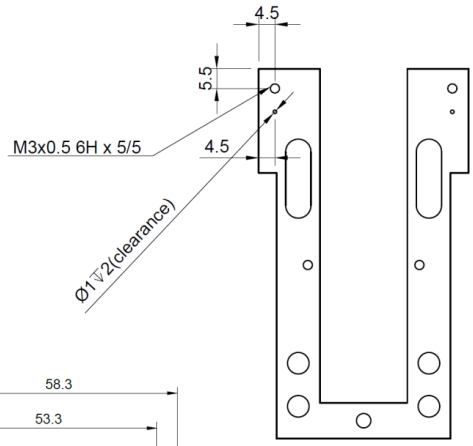

Bottom

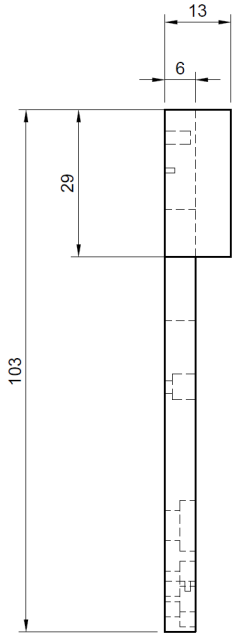

Left

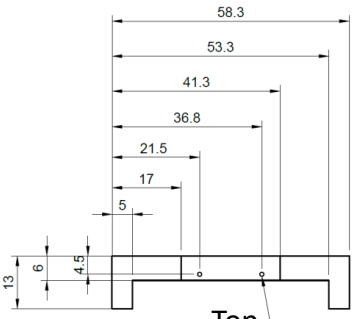

Top

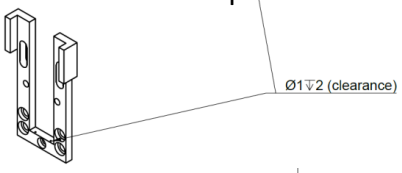

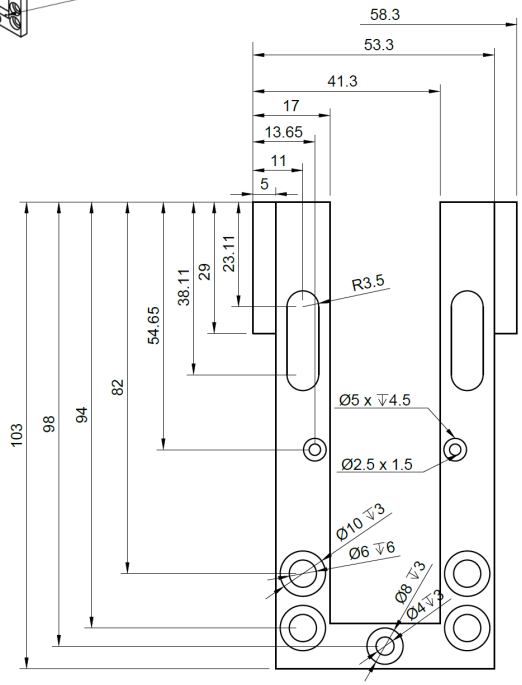

Front

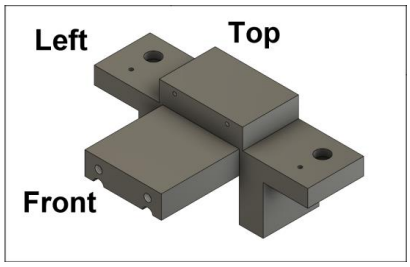

Aluminum Plate2

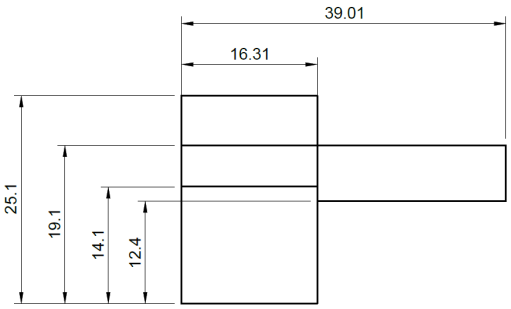

Left

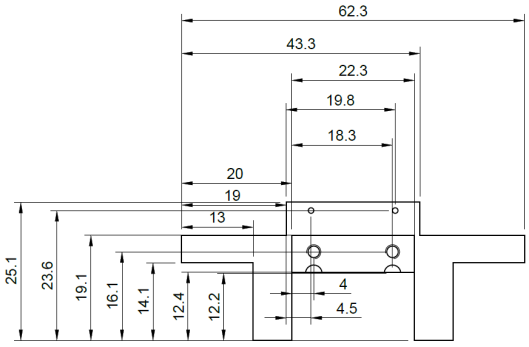

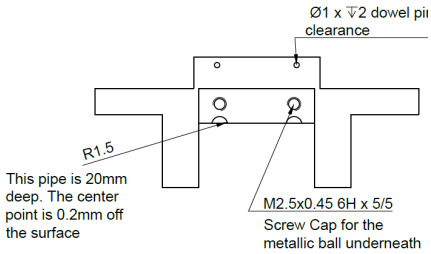

Front

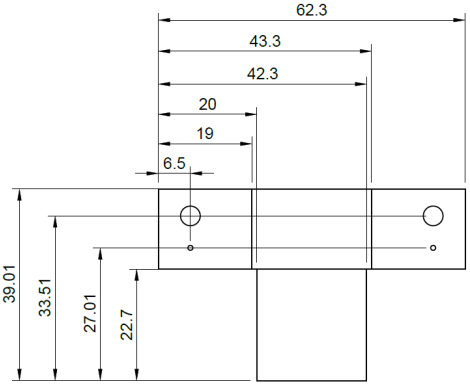

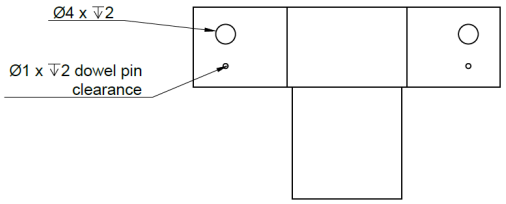

Top

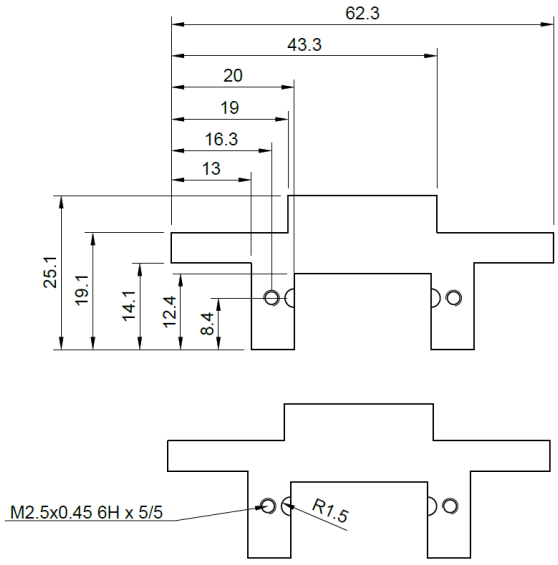
62.3
43.3
20
19
16.3
13
25.1
19.1
14.1
12.4
8.4
M2.5x0.45 6H x 5/5
R1.5

Back

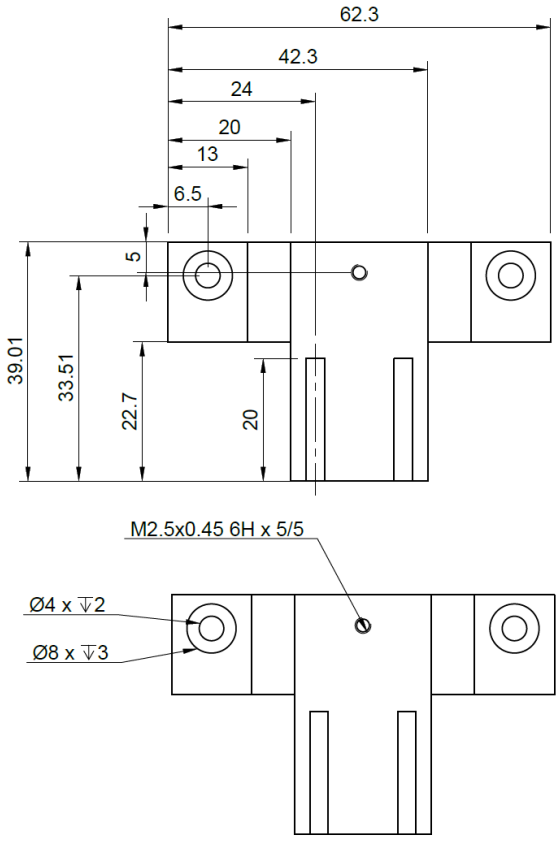
62.3
42.3
24
20
13
6.5
5
39.01
33.51
22.7
20
M2.5x0.45 6H x 5/5
Ø4 x ↧2
Ø8 x ↧3

Bottom

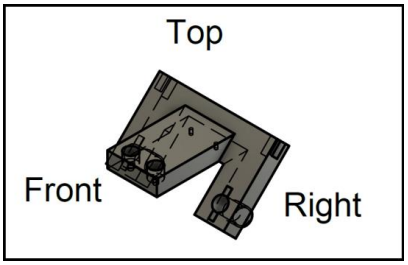

Aluminum Slider

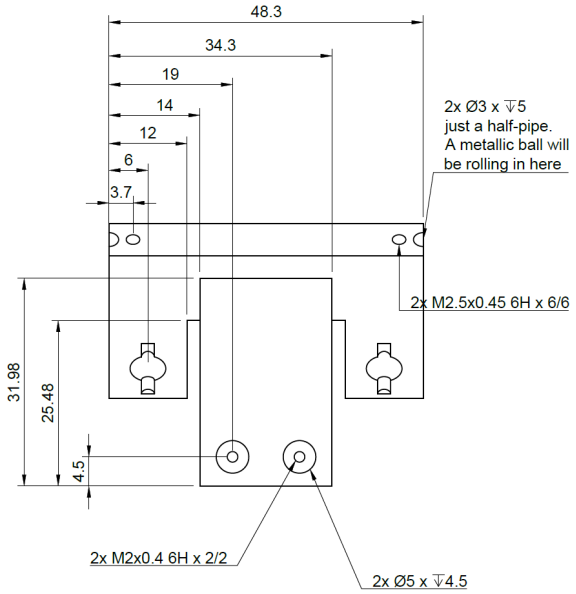

Top

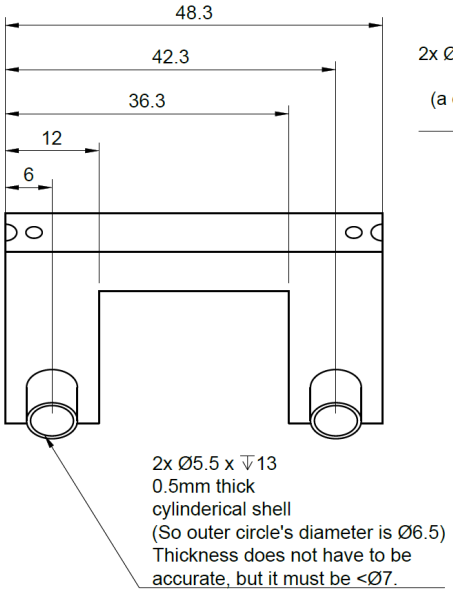

Back

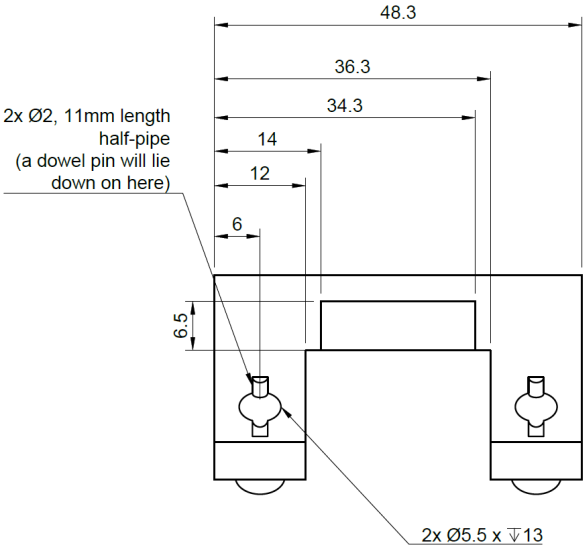

Front

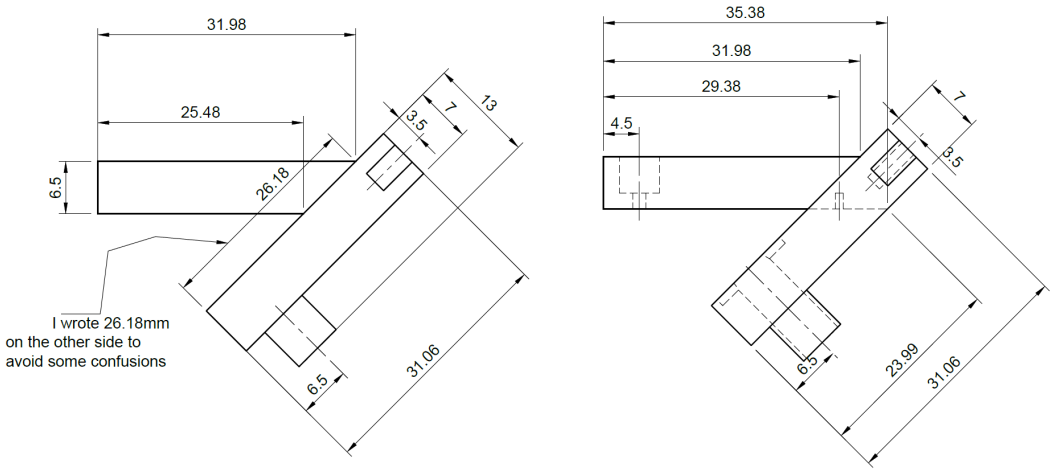

Right

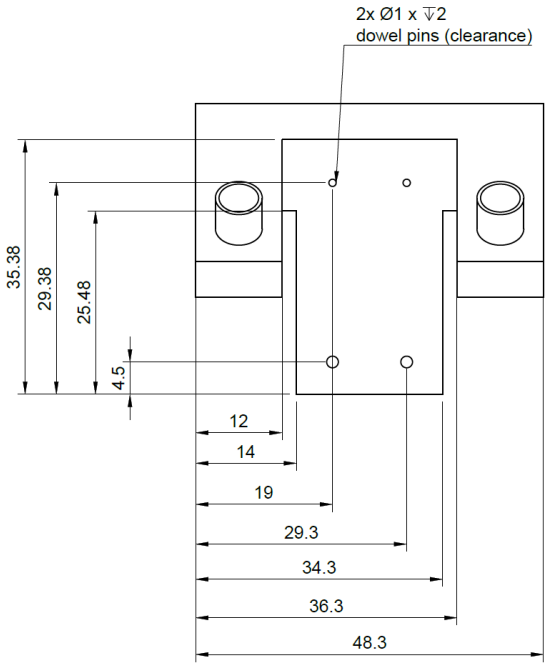

Bottom

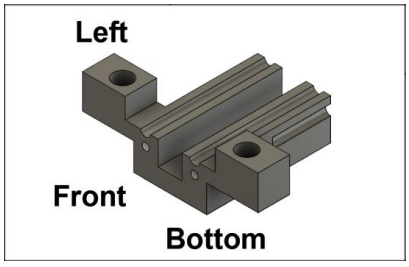

Aluminum Bottom Slider

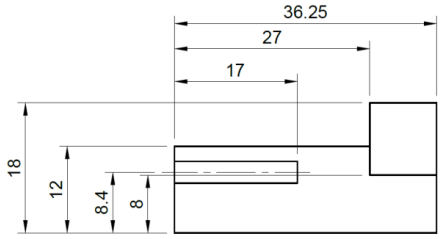

Left

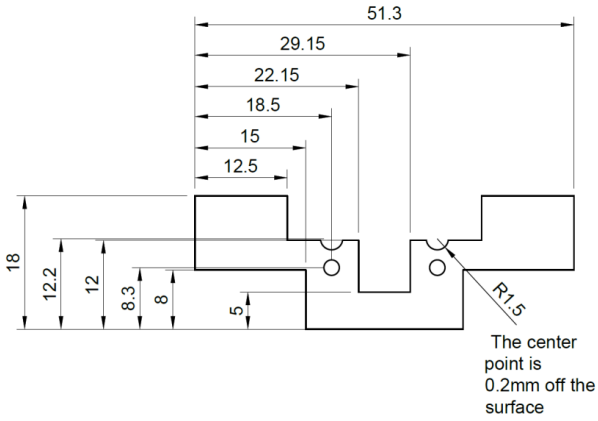

Front

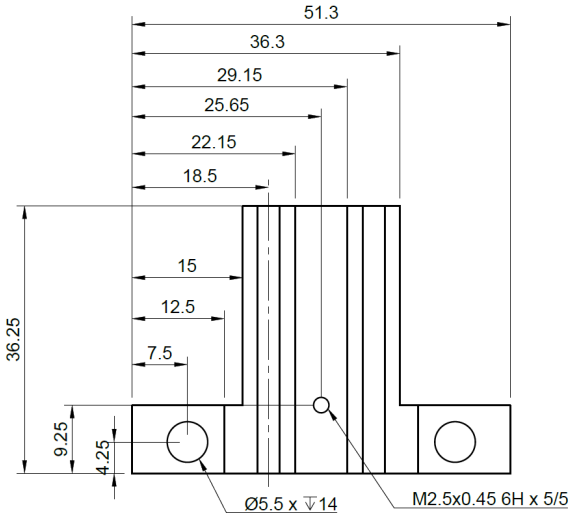

Top

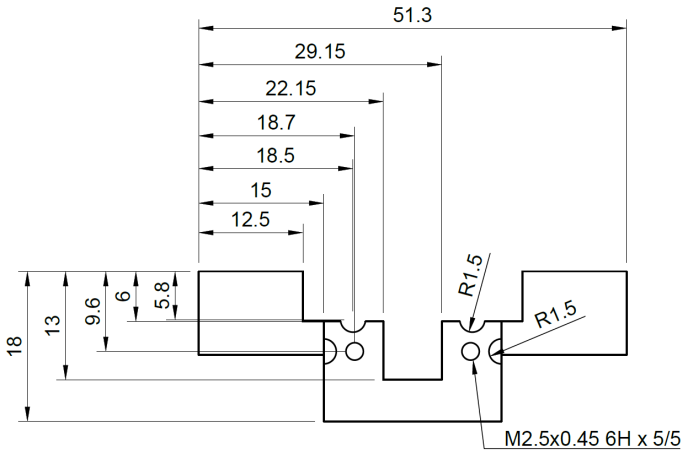
51.3
29.15
22.15
18.7
18.5
15
12.5
R1.5
R1.5
18
13
9.6
6
5.8
M2.5x0.45 6H x 5/5

Back

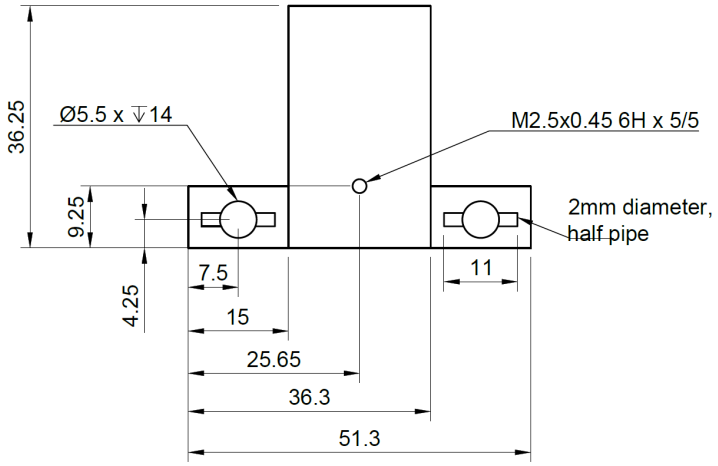
36.25
Ø5.5 x ⌵14
M2.5x0.45 6H x 5/5
9.25
2mm diameter,
half pipe
7.5
11
4.25
15
25.65
36.3
51.3

Bottom

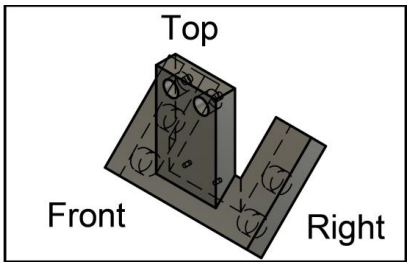

Aluminum Wall

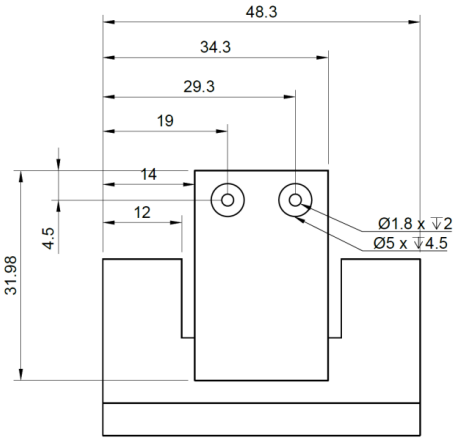

Front

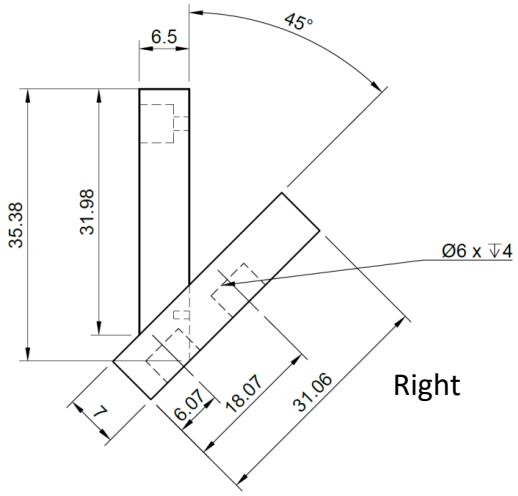

Right

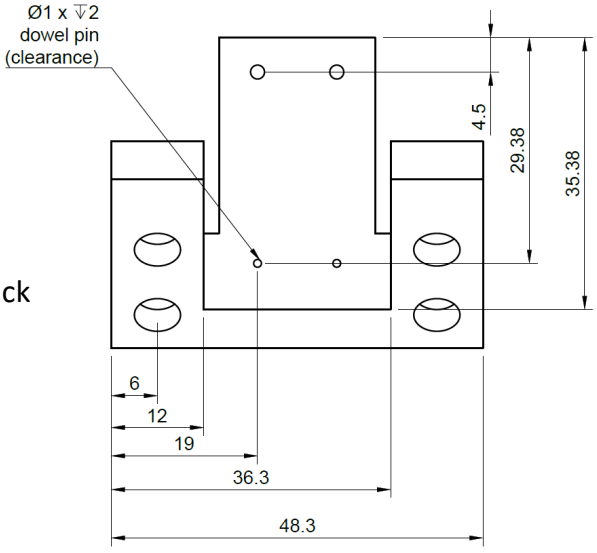

Back

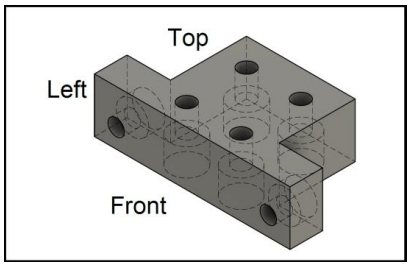

Micrometer Plate

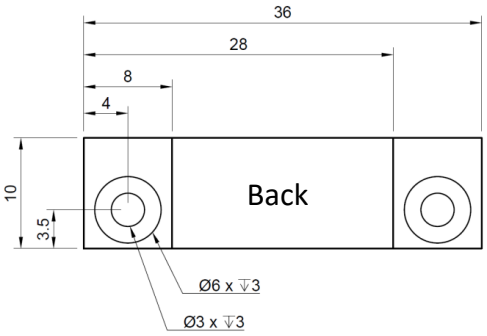

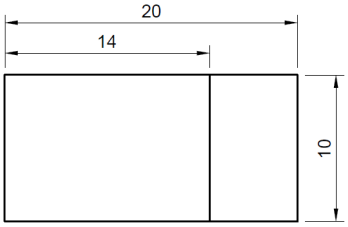

Left

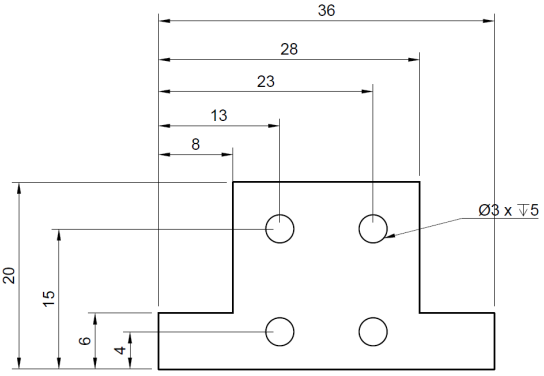

Top

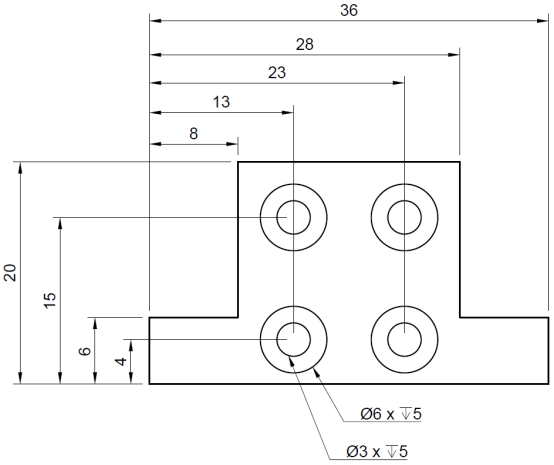

Bottom

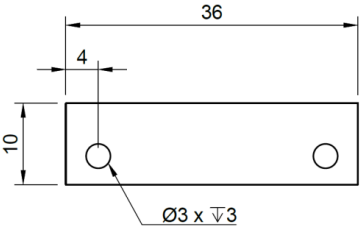

Front

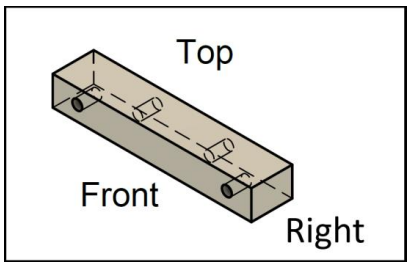

PEEK spacer

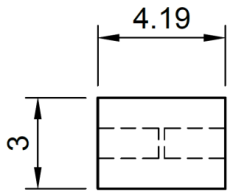

Right

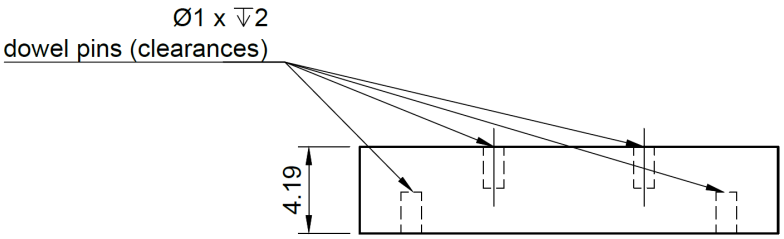

Top

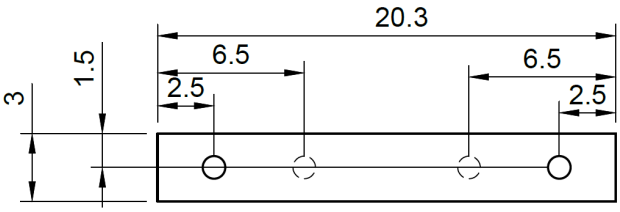

Front

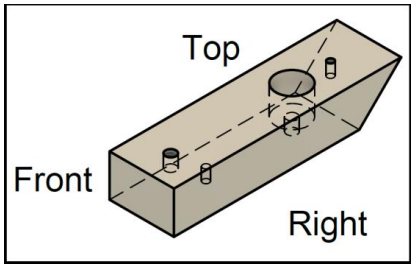

PEEK spacer2

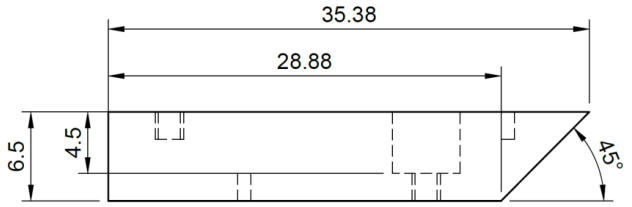

Right

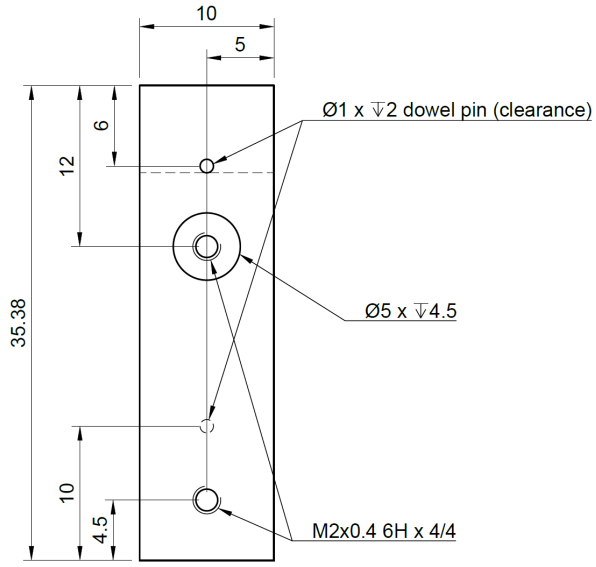

Top

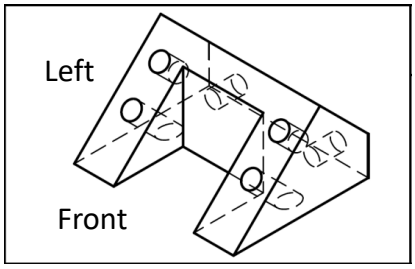

Oven Mount (Ver.1)

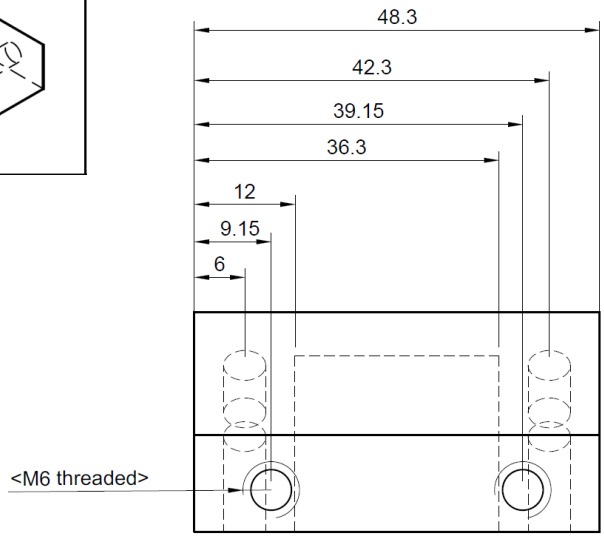

Back

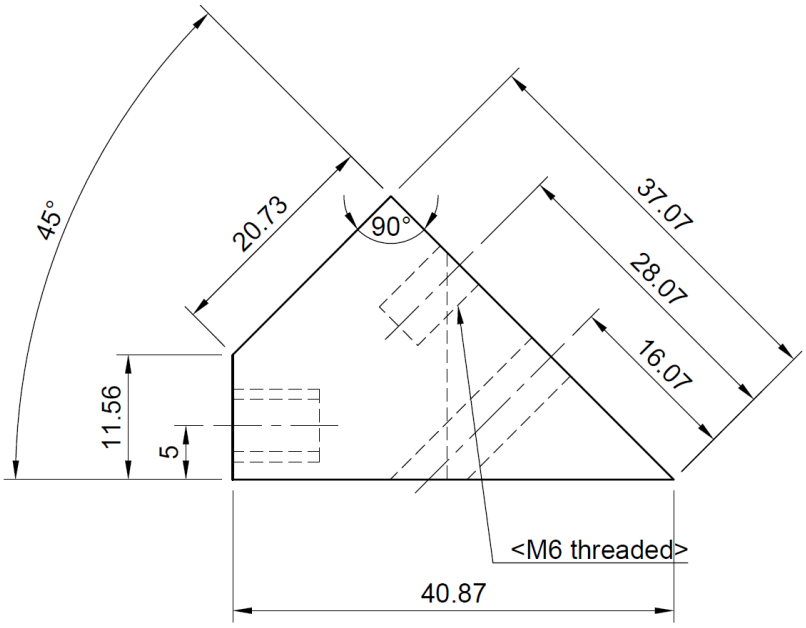

Left

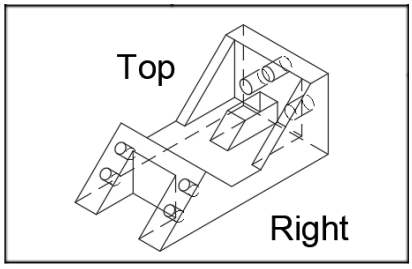

Oven Mount (Ver.2)
3-D printing

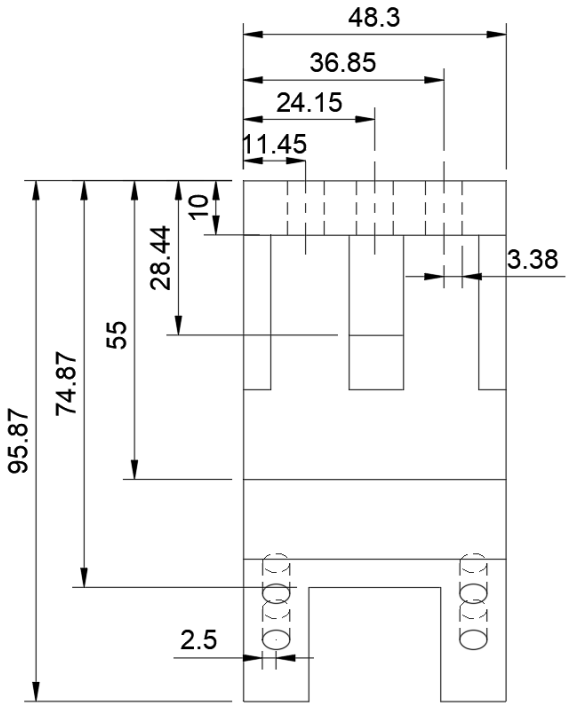

Top

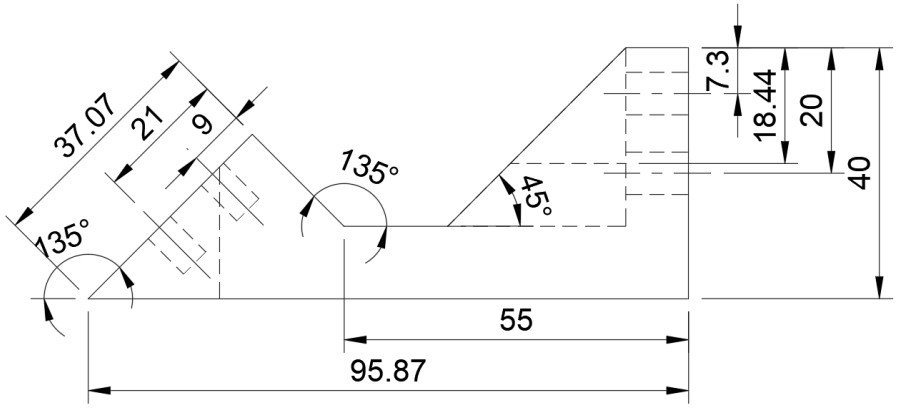

Right

Appendix Q

Design - Crystal Holder (in millimeters)

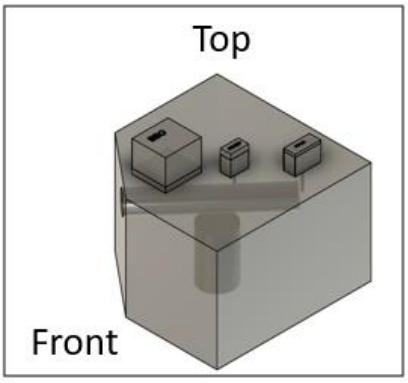

Crystal Holder

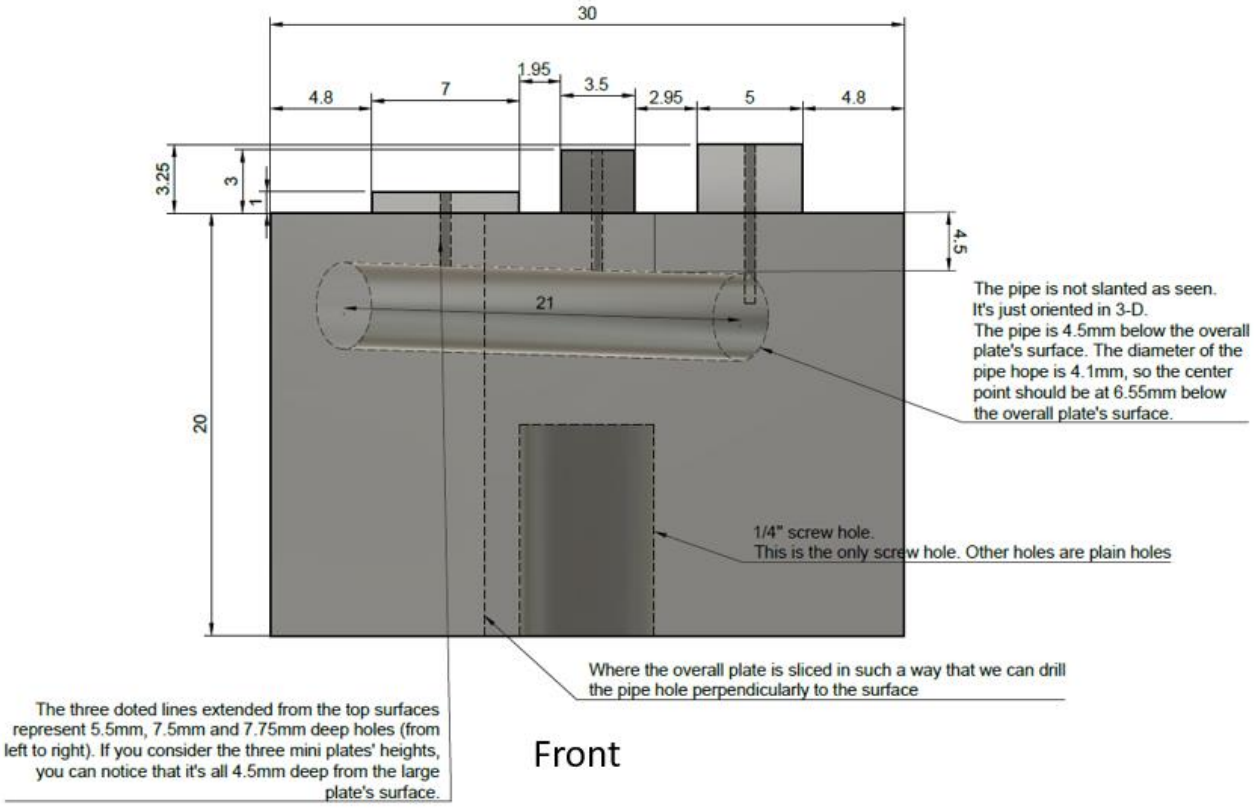

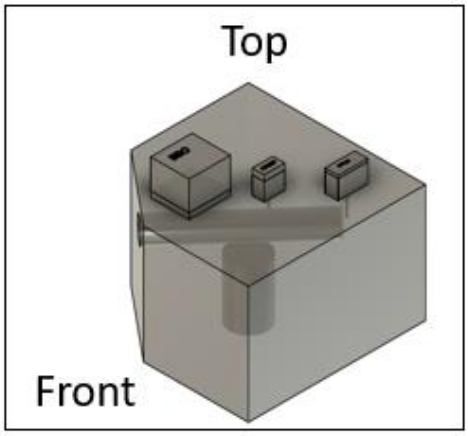

Crystal Holder